Improving the Radial Velocity Precision of the HERMES Spectrograph to Enable Exoplanet Detection

By

Carlos Bacigalupo

A thesis submitted to Macquarie University
for the degree of Doctor of Philosophy
Department of Physics and Astronomy
April 2018

MACQUARIE
University
SYDNEY·AUSTRALIA

Disclaimer

I hereby declare that the work in this thesis is that of the candidate alone, except where indicated below or in the text of the thesis.

The discussion of the Australian Astronomical Observatory (AAO) Starbugs software control, described in Chapter 1, is published in Lorente et al. (2016) where I am a co-author.

In addition to the publication of my Honours Thesis (Bacigalupo, 2013), I have contributed as a co-author to the papers Bento et al. (2013), Feger et al. (2016) and Sheinis et al. (2015), which include results of my analysis of the RHEA spectrograph and HERMES spectrograph Point Spread Function (PSF) as described in Chapter 2.

The details of the GALAH survey science, the survey data and survey data reduction described in various parts of Chapters 1, 2 and 4 are based on the original publications De Silva et al. (2015), Kos et al. (2017) and Martell et al. (2017) where I am a co-author contributing to the GALAH radial velocity determination, data quality testing and as a GALAH observing team member.

Carlos Bacigalupo
December 2017

For Sue, Hannah and Luca

Acknowledgements

This work could not have been done without the outstanding help of my supervisor Gayandhi De Silva. Without her, this project would have simply not happened. I owe her my endless gratitude for being my coach, my mentor, my supervisor and my friend. Gayandhi, I lack the capacity to express what your support has meant to me and I'll be forever grateful.

I was lucky enough to have Duncan Wright cross my path at the right time to take my thesis to the next level. His wealth of knowledge and experience combined with his selfless human quality made HARPY what it is. Thank you Duncan, I have become a more knowledgeable man thanks to you.

I'm grateful to my supervisor, Dan Zucker, who has been the constant amongst the variables, never failing to help me at the right times. Orsola De Marco, who has been available for support whenever I needed her and Mike Ireland who set in motion many of the ideas in this work.

Scott Smedley has been an unconditional friend and supporter during the last year of this work. He brought a clean view with a full commitment to the highest quality. His patient proof-reading eye, enhanced by his years as an avid programmer, took this thesis to where it is. Thank you Scott, may this be the beginning of many adventures to come.

Joao Bento has been there since the beginning. He helped me find my way during the difficult early stages of my thesis. He has invested endless hours in me without asking anything in return. Joao, I'm glad you are in my life.

To the Macquarie Physics and Astronomy Department, in particular to Dave Spence and Rich Mildren who were available to help during the changes and the many turns of my PhD.

I'd like to thank Tony Farrell and Nuria Lorente, from the AAO software team, for being very understanding of my limited availability during the write up of this thesis. I will repay you in software and humour.

Above all, I want to thank my family; my wife Susan, my daughter Hannah and my son Luca. You define everything that is important in my life. Sue, you gave me the space to focus on this project. Thank you for your patience during these periods of intense absence. I love you guys. Family...,family...

To my mother, whose great cooking keeps increasing my radial velocity signature.

And to Gustavo Cerati, you know why.

Abstract

The evolution of modern astronomical instruments and their capacity to produce useful data has advanced in tandem with, and benefited from, the development of software to optimally analyse those data. In particular, recent developments in the analysis of high resolution spectroscopic data have yielded unique insights on a wide range of astronomical phenomena. As we develop instruments capable of achieving higher spectral resolution and greater wavelength stability, the techniques necessary to produce successful measurements become increasingly challenging.

The goal of this thesis is to develop a wavelength solution with an aim to maximise the instrumental performance. For that purpose, we developed a complete reduction pipeline and demonstrate the improvement that it achieves. We show how it produces results that enable new range of scientific goals that were not achievable using the previous methods.

We initially investigated the possibility of modelling instrumental wavelength calibration from physical principles, an effort which we applied to the small high-resolution spectrograph RHEA. However we found that a model based only on optical principles was unable to generate a wavelength solution superior to a purely mathematical approach.

Taking the lessons learned from RHEA, we then set out to develop a precision radial velocity pipeline for the high-resolution HERMES spectrograph recently commissioned at the 3.9m Anglo-Australian Telescope (AAT). First we characterised the behaviour of the spectrograph PSF across all four channels. Then we undertook a series of observations of stellar targets - some with known radial velocity variability, others as yet unstudied in the time domain - in order to test the radial velocity precision achievable with HERMES.

We found that 2dfdr, the standard spectroscopic data reduction package provided by theAAO, was unable to reduce the uncertainty in radial velocity measurements below $400\,\mathrm{m\,s^{-1}}$, due to a combination of PSF effects and the wavelength solution applied by the software. Tests indicated that the extraction method employed by 2dfdr prevented a significant reduction in radial velocity measurement uncertainties; this fundamental limitation led us to develop HARPY, a new radial velocity determination software package that can independently reduce the data produced by HERMES. It calculates a wavelength solution that is stable across observations and performs radial velocity calculations from extracted, calibrated spectra.

The final version of HARPY, presented in this thesis, shows radial velocity uncertainties on the order of $70\,\mathrm{m\,s^{-1}}$ with HERMES data. Applying HARPY to our observations, we demonstrate its capabilities on both a binary star and a hot Jupiter system. Proving that HERMES can reach such radial velocity precision, opens a large range of scientific projects to investigation, previously unable to be considered. Its highly multiplexed capability and wide field of view, in combination with its 4 cameras, can be used for large exoplanet surveys, once the lessons learned from this study are adapted to both observing and reduction procedures.

Contents

List of Figures

List of Tables

1 Introduction

The night sky has been a source of fascination since long before we began trying to decipher its wonders. A seemingly unchanging pattern, transiting every night, has inspired curiosity and mythology since humanity's earliest days. With time, we discovered that the immutable background wasn't quite so fixed; night after night, careful observers noticed that at least 5 wandering stars didn't follow the background pattern. It has been a long journey of discovery since those days. We now understand that even the background is not static. The thousands of stars that we can see every night, and the billions that we don't, are in constant motion in seemingly limitless space. But, what does the motion of a star tell us? What can we learn from the changes in that motion?

From a static background to an immensely complex dynamic system, the development of our understanding of the universe around us has been rooted in observations. At every point of the journey, the precision of our measurements has been a key limiting factor in the level of scientific understanding achievable. This limit is intimately linked to the instruments used to make observations and the analysis techniques employed to extract measurements from those observations. Today, as in the past, we strive to maximise the results obtainable using the current state of technological development, and in doing so, advance our understanding even as we prompt the next steps toward technological advances.

The goal of this thesis is to fully exploit the precision limits attainable using the High-Efficiency and Resolution Multi-Element Spectrograph (HERMES). For that purpose, we developed a superior solution to the standard reduction pipeline. We demonstrate how it produces results that enable HERMES to pursue a new range of scientific goals that were not achievable using the pre-existing methods. Using our software, we present new measurements of stellar targets, some with known radial velocity variability, others as yet unstudied in the time domain, demonstrating the instrument's new capacity to engage in this level of analysis. We review the past and present state of astronomical measurements, analysing scientific motivations and linking them to instrumental and software development. Our scientific focus in this work is almost exclusively on what can be determined from radial velocity measurements, see Section 1.1.

In keeping with the scientific focus, this chapter describes the science attainable from radial velocity measurements, followed by a brief overview of the evolution of spectrographs,

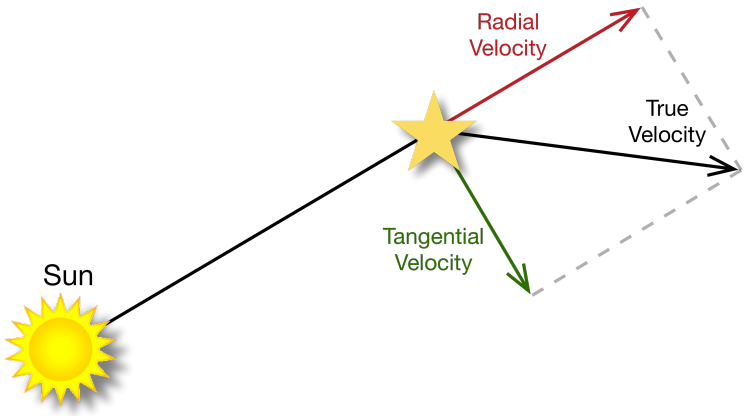

Figure 1.1: Schematic diagram of the radial and tangential components of stellar motion.

a description of astronomical software and concludes with an outline of the thesis.

1.1 Radial Velocity Science

The component of an object's velocity in the direction of the line of sight is referred to as the radial velocity, while the component of motion perpendicular to the radial direction is called the tangential velocity (see Figure 1.1). Measuring the radial velocity of a star (or any astronomical object) is based on the Doppler effect on the spectral features, in which the wavelength associated to a given feature is shifted as a function of velocity.

Current technology makes radial velocity generally the easiest component of motion to measure. These measurements give insight into many astrophysical phenomena. In a star, the change in its radial velocity component can indicate the presence of a companion, either stellar or planetary in nature. It can also provide information on the intrinsic behaviour of the star's outer layers. The global radial velocity distributions of groups or large samples of objects (whether stars or galaxies) can describe the kinematics of large galactic structures or clusters of galaxies, helping us map the large scale structure of the universe.

1.1.1 Exoplanets

The existence of planetary systems beyond our solar system is an intriguing concept that excites the imagination of professional astronomers and the general public alike. There are

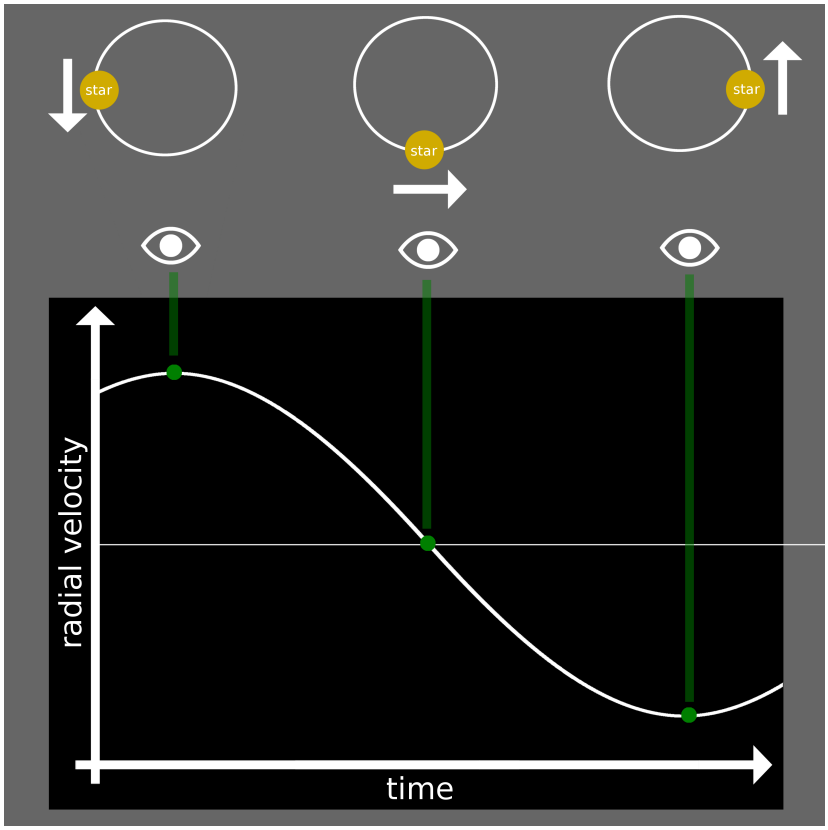

Figure 1.2: Schematic figure showing the motion of a star and the effect of that motion on its measured radial velocity.

several methods of detecting planets around other stars. The so-called radial velocity method hinges on the fact that a star with a planet, or planetary system, will display periodic variations in its radial velocity over time. The telltale signature of a planet orbiting another star detected using the radial velocity method is an oscillatory radial velocity curve, see Figure 1.2. The amplitude and period of the radial velocity curve relates to the mass ratio and distance between the planet and its host star.

In 1992, a new era in astronomy began with the detection of the first accepted planet outside our Solar System (Wolszczan and Frail, 1992). This was soon followed by (Mayor and Queloz, 1995), the first exoplanet discovery by the radial velocity method, with an amplitude of $59 \pm 3\,\mathrm{m\,s^{-1}}$ measured using the highly stable ELODIE spectrograph (Baranne et al., 1996) at the Haute-Provence Observatory in France, see Figure 1.3. Numerous additional discoveries followed, and established the radial velocity method as the primary exoplanet detection method until the launch of orbital observatories like Kepler, which have made an unprecedented number of planetary discoveries using the transit method (i.e., measuring the dip in a star's brightness due to a planet transiting its disk). The radial velocity method has produced over 450 candidate exoplanet detections to date (Han et al., 2014), including a claimed Earth-mass planet around our closest star system (Dumusque et al., 2012), later proved to a be spurious detection Rajpaul et al. (2016). The radial velocity method has also yielded further information to characterise some 1000 exoplanet systems, making it not only a primary source of detection of planetary candidates, but a great technique for producing complementary data on detections from other methods. An example of this is the quantification of planetary mass limits that, in combination with transit information, can produce constraints on planetary densities.

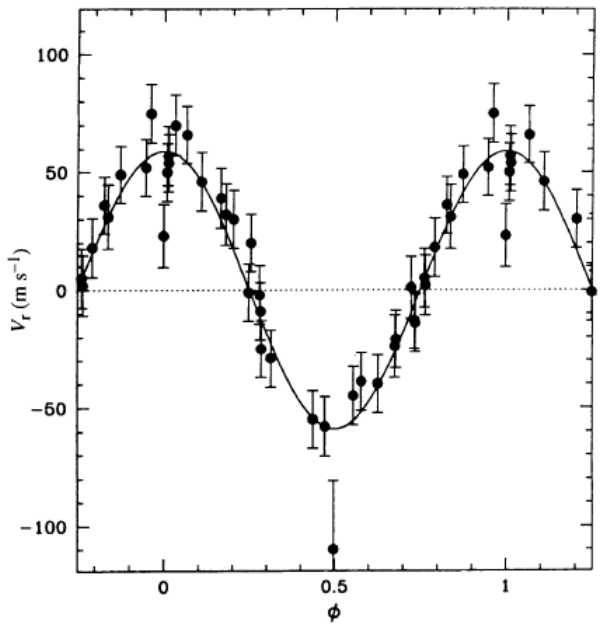

Figure 1.3: 51 Peg, the first Sun-like star with an identified planet-sized companion discovered by the radial velocity method (Mayor and Queloz, 1995).

A large number of extrasolar planets have been detected since 1992. Organising these discoveries into classes of planets is a process in continuous evolution. As is often the case with new discoveries, it is impossible to know in advance the types of objects that the research will produce. It is the incremental understanding of their common properties that allows us to classify them. Although there is not yet a formal list of "types" of exoplanets, certain common groups of characteristics are slowly becoming standard use.

An Earth-like planet is a planet that will be approximately 1 $R_\oplus$ and 1 $M_\oplus$, orbiting a Sun-like star. The term super-Earth is used for rocky planets that are larger than Earth with masses $< 10M_\oplus$ and radii ≤ 1.6 $R_\oplus$ (Rogers, 2015). Planets with higher masses are likely to capture gas during formation and develop into giants. Planets that range between $10M_\oplus$ and $< 25M_\oplus$ are sometimes referred to as Exo-Neptunes. Hot Jupiters are planets orbiting close to their host star with masses ranging from $1M_{Jup}$ to $13M_{Jup}$. The upper limit of this definition is set by the deuterium-burning limit (Hubbard et al., 2002), at which a planet could potentially have enough mass to start energy production at the early stages of its life, effectively qualifying it as a brown-dwarf. This effect is highly dependant on metallicity, and planets with still higher masses are thought to be possible (Sato et al., 2010). The area around the star where liquid water could be maintained on a planet's surface is known as the habitable zone, popularly referred to as the Goldilocks zone, in analogy to the classic children's tale.

The combination of stellar and planetary masses and the distance between the objects will determine the amplitude and period of the radial velocity variations that the star will exhibit. These elements are related by

$$RV = \sqrt{\frac{G}{(m_1 + m_2)a(1 - e^2)}} m_2 \sin\theta \tag{1.1}$$

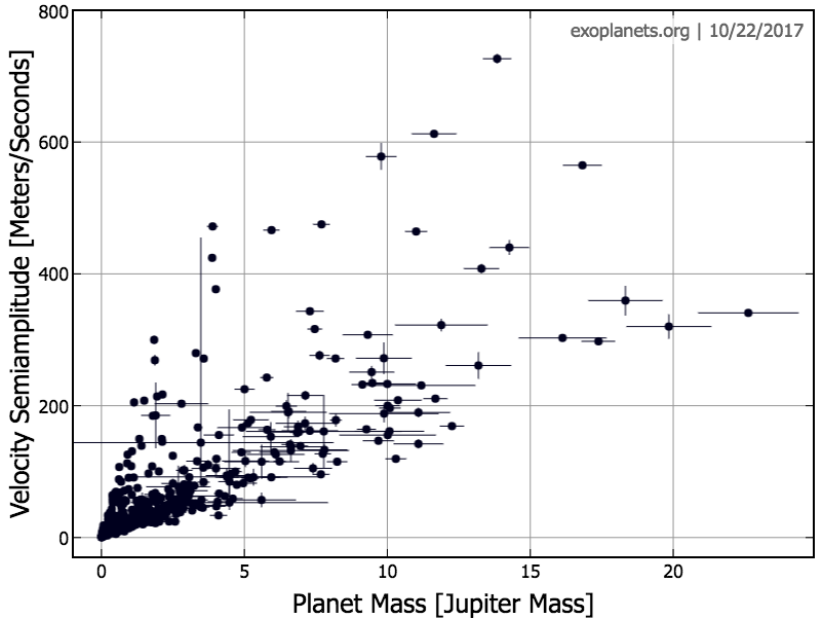

Figure 1.4: Detectable radial velocity as a function of planetary mass. The void area on the bottom right corner shows that, as planetary masses increase, so does the minimum distance from its host star. Planets at closer distances would be in cataclysmic configurations, reducing the chances of being detected due to their relatively short lifespans. The void on the left side shows the maximum radial velocity amplitude as a function of planetary mass. Credit: Exoplanets.org (Han et al., 2014).

where m_1 and m_2 are the mass of the 2 bodies, a is the semi-major axis, e is the system's eccentricity and θ is the angle between the line of sight and the vector normal to the orbital plane, known as the inclination of the orbit. See Appendix B for the formal derivation.

The radial velocity precision limit of an instrument determines the range of targets that will be detectable with it. Most planets detected by the radial velocity method show a radial velocity semi-amplitude under $200\,\mathrm{m\,s^{-1}}$, see Figure 1.4. An instrumental uncertainty of that order or higher will limit its capacity for planet detection.

In addition to the limits imposed by the instruments, there is an intrinsic limitation to the radial velocity method itself. Planetary masses derived from detections by this method can only be expressed as minimum masses; the limitation stems from the fact that the observer doesn't know the angle between the orbital plane and the line of sight. The radial velocity amplitude calculated is thus only an unknown fraction of the total velocity amplitude. The coefficient $\sin\theta$ is introduced to account for this unknown angle. Without an upper limit for the mass of the detected object, the type of object detected cannot be conclusively determined. Some constraints to a companion's mass range could be set, based on the absence of flux from the companion, however it could still be a planet or a larger object. Hence the radial velocity method can only identify planetary candidates due to this intrinsic limitation, and any such detection needs to be confirmed by another observational method.

The spectroscopic data used for radial velocity calculations can also provide information on the physical parameters and chemical abundances of a star. These data allow studies such as Johnson et al. (2010) and Santos et al. (2004), that show a statistical link on the likelihood of giant planets as a function of host stellar mass and metallicity.

The precision of a spectrograph can also confirm or refute, to a higher level of confidence

than previous studies, the presence of a companion. Queloz et al. (2001) conducted a follow-up study to lower precision observations which had hinted at a potential companion to HD166435. The new observations refuted this claim, incidentally proposing the idea of a spatially static magnetic field locking the position of stellar spots having misled the initial observations. This is an example of the incremental scientific results that a high resolution spectrograph can produce, and conversely how low resolution observations can yield erroneous results. One of the goals of this thesis is to maximise the science obtainable from a given instrument by increasing the efficiency of its data reduction.

The search for exoplanets generally requires observations to be carried out over long periods. Most radial velocity planet search programs are carried out as large surveys. The Anglo-Australian Planet Search (Tinney et al., 2001) is a long term survey that has been carried out at the Anglo-Australian Telescope since 1998. It uses the UCLES echelle spectrograph (Diego et al., 1990) and has discovered over 45 planet candidates, including multiple-planet systems. The Extrasolar Planet Search Programme at Haute-Provence Observatory employs the ELODIE spectrograph. It uses 25 % of the telescope time and was responsible for the discovery of 51 Peg, the first exoplanet around a Sun-like star. The Southern Sky extrasolar Planet search program uses 50 % of the available time at the 1.2m "Leonard Euler" Swiss Telescope at ESO-La Silla Observatory in Chile with CORALIE (Udry et al., 1999), an echelle fibre-fed spectrograph modelled after ELODIE.

The continuous improvement in instrumental precision and data reduction techniques is paving the way for the detection of still smaller radial velocity amplitudes, allowing the measurement of even more subtle phenomena. This may potentially include the detection of exomoons, i.e., moons orbiting extra-solar planets (Rauer et al., 2014; Kipping et al., 2012; Heller et al., 2014).

Other Methods of Exoplanet Detection

The methods of exoplanet detection are in constant development, either through the exploration of new techniques to trace the signatures of a planetary presence or by the improvement of existing methods. The radial velocity method produced the highest number of results until the Kepler space telescope was launched. This was due to the Kepler mission being designed for unprecedented photometric stability, enabling it to produce a large number of detections using the transit method. By this technique, the light curve of the star is analysed for periodic changes produced by the transit of a planet, which temporarily decreases the amount of light observed from the star. The method known as microlensing, uses the lensing effect of a foreground star when it's almost aligned with a background star. During the alignment event, lasting from days to weeks, the presence of a planet orbiting the foreground star can contribute to this lensing effect in a unique way that can trigger a detection. Direct imaging aims to produce actual photometric images of exoplanets, and pulsar timing relies on the changes in the precise signal cycles of pulsars to detect a companion.

The chances of observing a transit are inversely proportional to the star-planet separation. Figure 1.5 shows the areas where transits have been successfully detected. In addition to the Kepler space telescope (Borucki et al., 2010), there are several large scale surveys that aim to systematically search for exoplanets using the transit method; PSST: The Planet Search Survey Telescope (Dunham et al., 2004), WASP (Pollacco et al., 2006), HAT (Bakos et al., 2013), and TESS (Ricker et al., 2014).

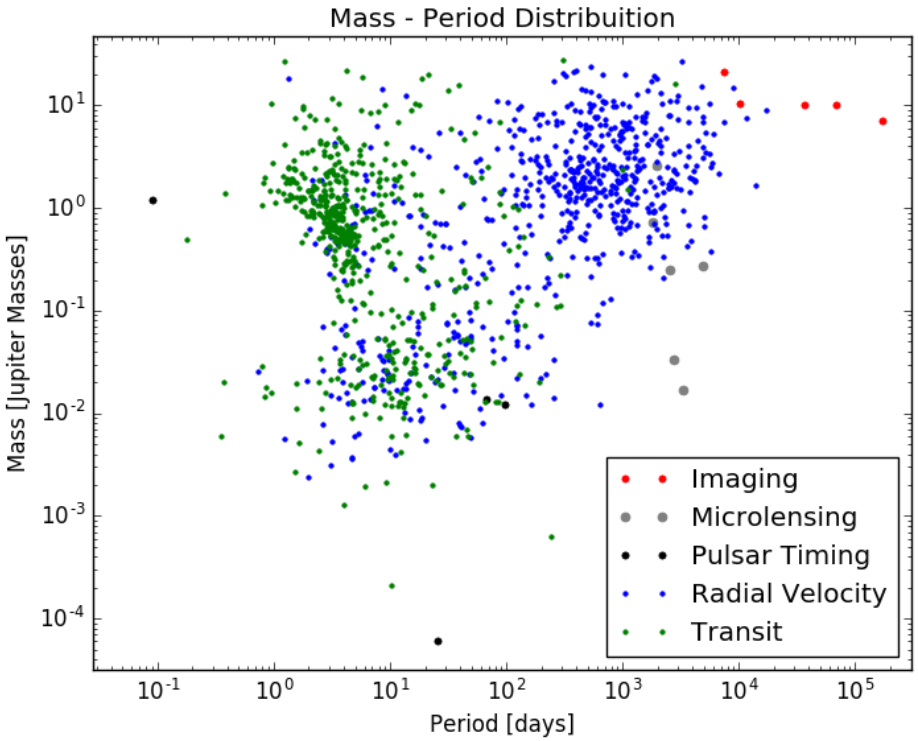

Figure 1.5: Mass vs. period of exoplanets, colour-coded by method of discovery. Note the areas defined by the different method biases. Transits are more likely at closer distances, radial velocities are easier to detect at higher masses and imaging benefits from some significant orbital separation from the host star to allow subtraction. Data: NASA Exoplanet Archive.

1.1.2 Stellar Oscillations

Another major area of research based on radial velocity measurements is the detection of stellar pulsations. These periodic radial velocity variations are caused by intrinsic oscillations found in stars, which in turn give us information on their internal structure. This is the realm of asteroseismology, the branch of astronomy that studies the interior structure of stars by using their oscillations as seismic waves.

Stellar oscillations can be grouped by their driving mechanisms. The ϵ mechanism depends on changes in the energy production rate as the source of instability. The $\kappa - \gamma$ mechanism points to increases in opacity to temporarily store energy; upon release, the energy will expand the radius of the star beyond the equilibrium point. This is also known as the Eddington Valve mechanism, and explains most of the variabilities observed in pulsating stars. A similar case aims at regions in the interior of the star where convective motion is temporarily blocked, creating a store and release effect. Finally, the turbulence in the convective layers of stars produce stochastically excited waves. These are sometimes referred to as solar-like oscillations (Uytterhoeven et al., 2011; Catelan and Smith, 2015; Charpinet et al., 2001; Breger et al., 1995; Istrate et al., 2016).

Oscillations can span varying time-scales or periods with different radial velocity amplitudes. When comparing these results with planetary searches, there is a range of values where the two phenomena can overlap. Table 1.1 shows the wide range of periods that asteroseismological oscillations can have and Figure 1.6 shows where these groups fit in a

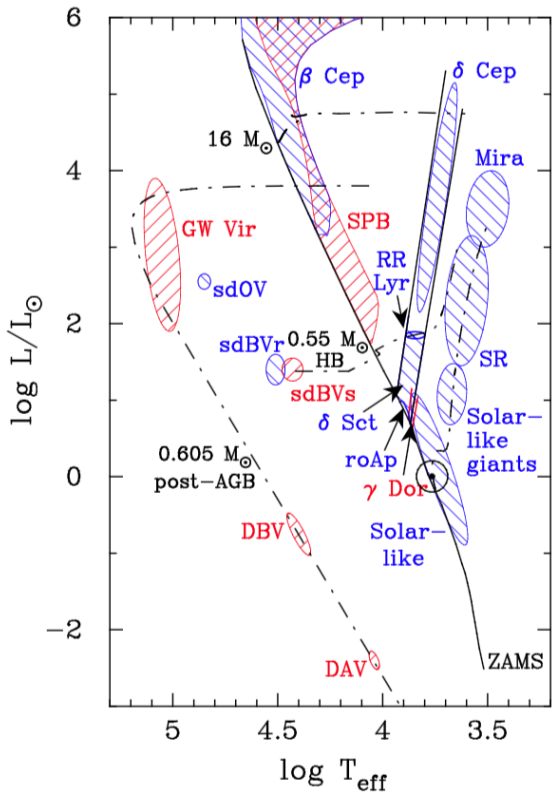

Figure 1.6: Types of stars with similar variability parameters in the HR diagram (Handler, 2013).

colour-magnitude diagram. As an example, the period of a Keplerian orbit around a ≈ 1 $M_\odot$ star at 0.1 au is ≈6.7 days. Without further information, radial velocity variations with this period could either represent a δ Cephei type star or the presence of a companion. Understanding the properties of a star can constrain its stellar parameters, and thus potentially distinguish between these two scenarios.

Radial velocity measurements have contributed to the characterisation of stellar oscillations. Hatzes and Cochran (1998) analysed the K-type star Arcturus. The different oscillations detected were grouped based on their periods, with main groups of oscillations identified. Only 4 years later, HD209295 became the first star to be classified as a γ Doradus and a δ Scuti simultaneously (Handler et al., 2002). The former type exhibits non-radial oscillations with periods $\approx$ 1 day and the latter are either radial or non-radial oscillations with periods of the order of hours. Both types are used as standard candles due to their period-luminosity relation. On a larger scale, a catalogue of radial velocity variations of 2000 evolved stars (de Medeiros and Mayor, 1999) was used to constrain the expected rotational behaviour of evolved stars and helped to build the link between rotation, chemical abundance and stellar activity.

The Goettingen Solar Radial Velocity project (Lemke and Reiners, 2016) aims to produce extremely high precision radial velocity measurements of the Sun, on the order of 0.3 m s^{-1}. This is in principle achievable, as it is calculated from the photon noise limit, yet still dominated by instrumental systematics as a result of an unmodeled instability – a similar limitation to the one encountered in this thesis. A more recent project, the HARPS-N solar RV project (Dumusque et al., 2015), has been running since 2015.

Name	Approx. Periods	Discovery/Definition
Mira variables	100 - 1000 d	Fabricius (1596)
Semiregular (SR) variables	20 - 2000 d	Herschel (1782)
δ Cephei stars	1 - 100 d	1784, Pigott, Goodricke (1786)
RR Lyrae stars	0.3 - 3 d	Fleming (1899)
δ Scuti stars	0.3 - 6 h	Campbell and Wright (1900)
β Cephei stars	2 - 7 h	Frost (1902)
ZZ Ceti stars (DAV)	2 - 20 min	1964, Landolt (1968)
GW Virginis stars (DOV)	5 - 25 min	McGraw et al. (1979)
Rapidly oscillating Ap (roAp) stars	5 - 25 min	1978, Kurtz (1982)
V777 Herculis stars (DBV)	5 - 20 min	Winget et al. (1982)
Slowly Pulsating B (SPB) stars	0.5 - 3 d	Waelkens and Rufener (1985)
Solar-like oscillators	3 - 15 min	Kjeldsen et al. (1995)
V361 Hydrae stars (sdBVr)	2 - 10 min	1994, Kilkenny et al. (1997)
γ Doradus stars	0.3 - 1.5 d	1995, Kaye et al. (1999)
Solar-like giant oscillators	1 - 18 hr	Frandsen et al. (2002)
V1093 Herculis stars (sdBVs)	1 - 2 hr	Green et al. (2003)
Pulsating subdwarf O star (sdOV)	1 - 2 min	Woudt et al. (2006)

Table 1.1: Different types of stellar radial velocity variables and their respective radial velocity periods. (Handler, 2013)

It is important to note that stellar radial velocity variations can also be due to multiple stellar systems. Sometimes the multiple components are visible in the spectrum; for example Niemela et al. (2002) discovered a massive binary system by disentangling the overlapping spectra of the two stars, such that the individual radial velocities could be measured and an orbital model fitted. The brown dwarf mass companion of a intermediate mass giant was also detected by this technique (Liu et al., 2008).

There are also the cases of single lined binaries, where a secondary stellar spectrum cannot be detected. However, the presence of the stellar companion(s) is detectable from the radial velocity variations. This is similar to the case of exoplanets described in Section 1.1.1. Generally, because a secondary stellar companion is much more massive than a planetary companion, the radial velocity amplitudes are much larger and easier to detect (Pourbaix et al., 2004).

For example, a white dwarf companion to the star KR Aurigae was detected by radial velocity measurements after variations were observed photometrically. The orbital period was calculated to be under 4 hours, suggesting that mass is being transferred between the two bodies and thus making this system a likely cataclysmic variable (Shafter, 1983). There are many other examples of such exotic objects and phenomena that are detectable via radial velocity variations in stellar targets, and it is an active field of stellar astrophysics.

The story of precision astronomical radial velocity measurement is the story of precision instrumentation and the parallel development of the software to run it; software is required to run complex hardware and is also an essential part of the data reduction process. This parallel evolution continues today, as massive astronomical surveys produce increasingly large datasets that require several software layers for processing, from the initial data reduction, to

'intelligent' pipelines using emerging technologies like neural networks and other types of machine learning algorithms.

1.2 Spectrographs

Although the word spectrum wasn't used until the 1600s, the use of dispersing optical elements to separate light into its components can be traced back to the Romans(Lucretius, 9BCE). The publication of Opticks (Newton, 1730) included the understanding of spectroscopy at the time, based on the author's work and that of others before him. The solar spectrum was often observed, and by the early 1800s it became clear that some colours were "missing" from the spectrum. This was formalised by the work of Fraunhofer (1817), who published the list of wavelengths absent from the solar spectrum.

Ongoing work over the 19th century led to the link between spectroscopic features and the chemical composition of the source. In 1860 spectra were used to determine that the elements found in the Sun were also found on Earth. Only a few years later the first radial velocity shift was measured in Sirius, marking the beginning of an era.

There are several types of dispersing optical elements, but they all share a key characteristic, spectral resolution. This value quantifies the ability to resolve spectral features by measuring how close two parts of a spectrum can be, while still being individually identifiable, see Figure 1.8. This is closely linked to the concept of resolving power represented by

$$R = \frac{\lambda}{\Delta\lambda} \tag{1.2}$$

where λ represents the location in the spectrum, in wavelength, where the measurement is performed and $\Delta\lambda$ the minimum separation measurable between adjacent spectral features. The resolving power of a spectrograph has been one of its most important features since the early days of spectroscopic research. This was matched only recently by the need for thermal stabilisation, a requirement particularly driven by high precision radial velocity studies.

1.2.1 Spectral Resolution

Since the first applications of dispersing optical elements to separate the wavelengths that compose light, spectrographs have achieved several major advances. The collimator, making the incoming beam parallel in a given direction, and the slit, constraining the beam to an elongated shape, were introduced around 1840 (Simms, 1840). The goal of focusing the incoming light and creating a beam shape that would favour the prism as a dispersing optical element led to an increase in spectral resolution. These elements were used in addition to a rotating table that would allow the collimator and telescope to rotate around the prism, thereby allowing the observer to select what section of the spectrum to focus on. The addition of a second prism allowed a simultaneous source to act as a calibration lamp. This brought large improvements to the study of solar spectra.

In the latter part of the 19^{th} century, several technical improvements to spectrograph design had a great impact in astronomical research. In particular, the addition of more prisms in the dispersed light path allowed for even higher spectral resolution, see Figure 1.7.

Figure 1.7: Angelo Secchi's multi-prism, double-pass spectrograph. (Hearnshaw, 2009)

The next step in the evolution of spectrograph design was the use of the same prism twice in the light path. This type of arrangement would also use the collimator twice, the second time as a focusing element on the light's returning path, sometimes referred to as automatic spectroscopes. The standardisation of this design became known as Littrow configuration. This name remains in use today, even for dispersing elements other than prisms. A slight modification later allowed the returning path to be slightly offset from the incoming beam, and hence, while still travelling through the initial prism, now somewhat longer. The slight difference in the returning path allows a separate lens to be the focuser, eliminating the reflection of waves in the returning path (known as back-scatter).

Slits were used to narrow the width of the incoming beam, minimising the range of incident angles hitting the prism surface. This increased the spectral resolution of the spectrograph, at the cost of illumination. As the ideal angle is measured from the middle of the slit, the edges add an extra length to the incident beam, curving the image produced and reducing the spectral resolution. The solution to this issue was to create curved slits to counteract the effect. This was successful in cases where the source beams were large enough, particularly used with solar spectra.

In parallel to the improvements in spectral resolution, work was being done to accurately identify the observed wavelengths. The first attempts aimed at having simultaneous fiducial spectra, or spatial markers that would provide a relative reference to the observed spectra. This took the form of projected crosses and micrometers, allowing observers to inscribe marks on the back of a glass to record line positions for later analysis.

The use of diffraction gratings, initially built from parallel wires placed at increasingly higher densities, developed quickly, primarily driven by Fraunhofer's work. The groove density increased from 1 wire/mm to 800 grooves/mm by the end of the 19^{th} century. By the mid 20^{th} century, gratings had surpassed prisms as dispersing objects both in efficiency and spectral resolution. This was achieved primarily due to the work of Henry Rowland, who

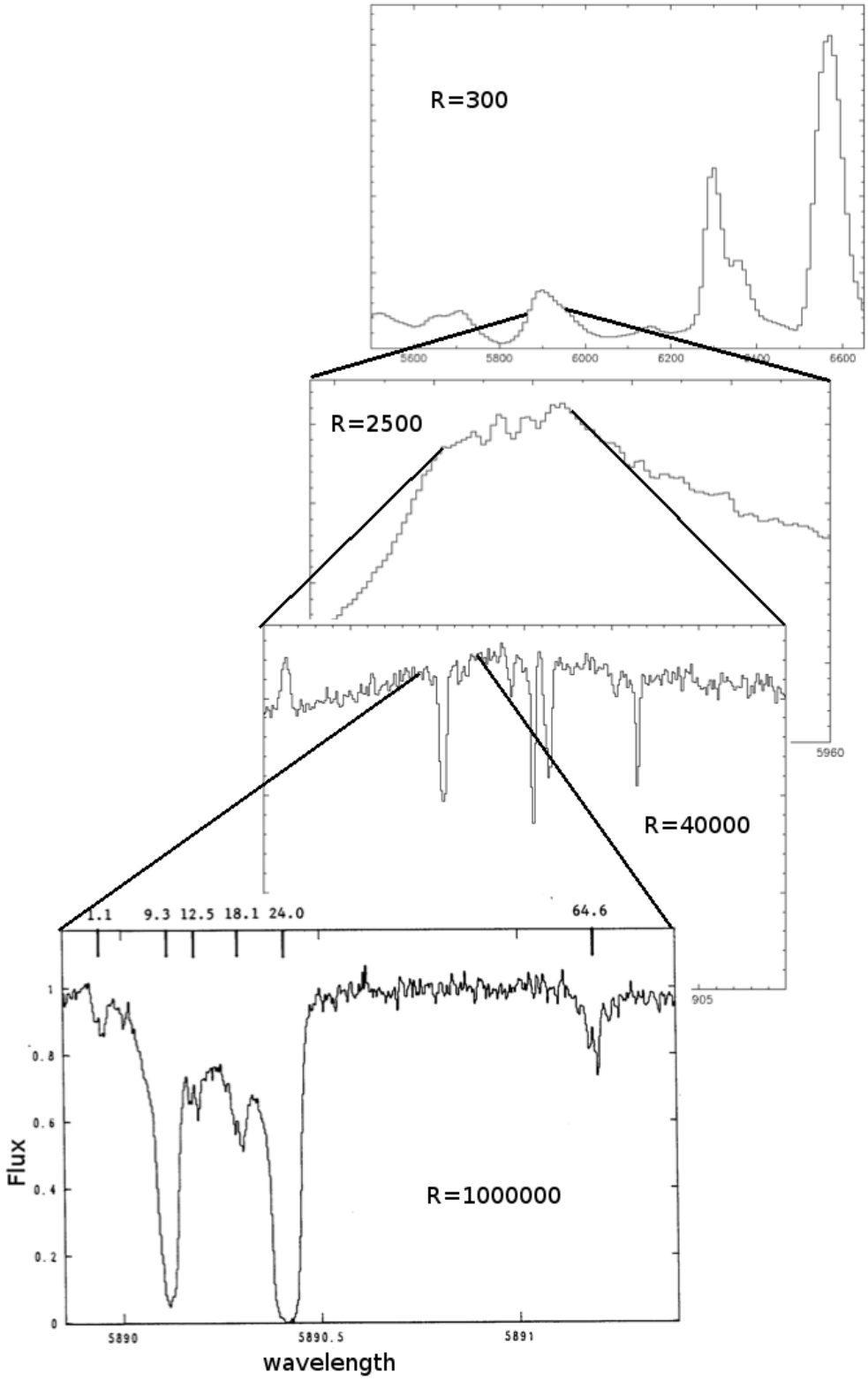

Figure 1.8: Normalised flux vs. wavelength on a schematic plot of stellar spectra as an example of how the spectral resolution of a spectrograph determines the level of detail that the spectrum will yield. Credit: UHRF/UCLES - AAO.

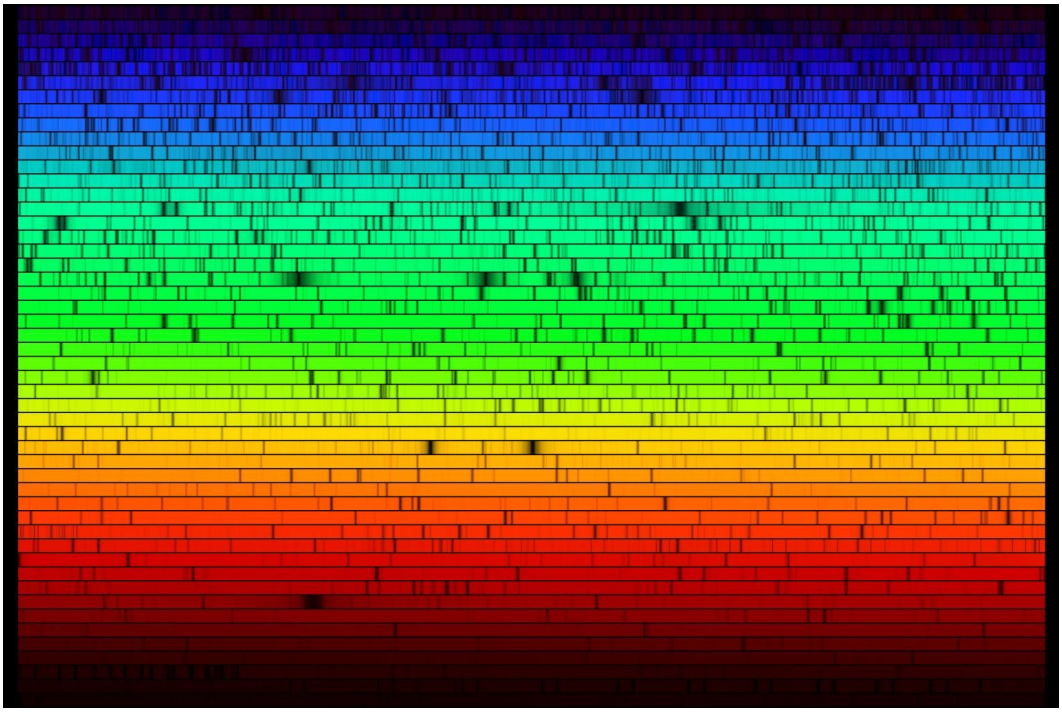

Figure 1.9: Fraunhofer's lines in the solar spectrum. The colours are artificially added based on the corresponding known wavelength colours. Credit: N.A. Sharp NOAO/NSO/Kitt Peak FTS.

focused on the manufacturing process of the gratings and particularly on the avoidance of periodic errors that could potentially lead to ghosts in the resulting spectra.

Although a slit would help to increase the spectral resolution by reducing the size of the source to a convenient scale, it would also mean that part of the incoming light would be lost. A mechanism to avoid this effect is to use an image slicer. This allows the incoming beam to be re-arranged into a collection of vertical slices along the slit width, lining-up vertically and minimising the loss of signal.

The use of echelle gratings was initiated by Harrison (1949). Soon after its publication, there were applications to laboratory and solar spectroscopy. Echelle spectrographs were positioned in a Coudé or Cassegrain focus, allowing relatively small telescopes to use a high resolution spectrograph for the first time.

The installation of an echelle spectrograph at the Cassegrain focus of a telescope sometimes led to flexure in the instrument due to the extra weight. In the 1980s, the use of fibre-fed spectrographs became an appealing alternative to avoid telescope flexure issues. It also provided a way to remove the instrument from the main body of the telescope and avoid forcing the telescope design to include a Coudé focus. Pioneered by the Pennsylvania State fibre-coupled echelle (Barden et al., 1987), and followed by devices built by Heidelberg, Kitt Peak and Mt John in New Zealand, this technology opened the door to a wealth of engineering possibilities. Its main advantage was freeing the spectrograph from the telescope, allowing for bench-mounting and temperature stabilisation. In addition, as the light is scrambled in the fibre, small guiding errors did not affect performance, an important feature for precision radial velocity measurements.

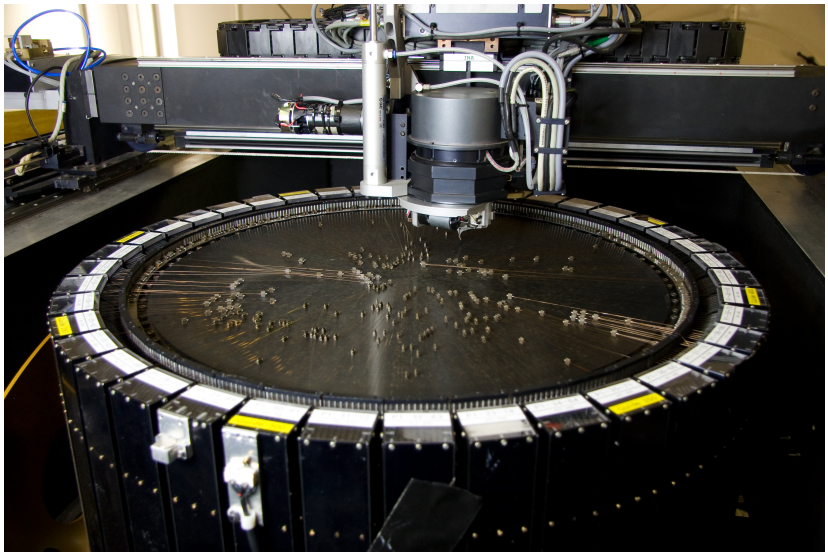

Figure 1.10: The 2dF fibre positioner working at the Anglo Australian Telescope. Image Credit: Angel Lopez-Sanchez

Multi-Object Spectroscopy

The ability to observe several objects simultaneously is an obvious advantage. However, since the first spectrographs and for almost a century thereafter, the only option to record data from multiple targets was to produce a field with multiple objects in it and let the objective prism do the dispersion. Because the spatial distribution of the objects can't be changed, the risk of overlapping spectra was a real risk. In addition, the spectral resolutions of the spectra vary as a function of position in the field, leading to a range of spectral resolutions within the same field.

There are three alternative solutions to address these issues. An aperture plate, placed at the focal plane, combined with a low dispersing optical element, ensures that only selected points in the field are observed. This allows some control on the layout of the targets on a given field but required fields to be configured ahead of the observation, as the plates needed to be drilled in advance. The second option is movable slits, where a pairs of slitlets driven by a motor can be allocated in different positions in the focal plane (Appenzeller et al., 1998). The third option was the use of optical fibres. An aperture plate at the focal plane would become the attachment on one end of the fibre, freeing the other end to be arranged as convenient (Hill et al., 1980). This technique quickly evolved, increasing performance in reconfiguration times and throughput (Gray, 1984). This is the most widely used method for multi-object spectroscopy. Although aperture plates are still used in some configurations, such as SAMI (Bryant et al., 2015), automated fibre-positioners are playing an increasing role in the development of this technology. The solutions developed evolved from early designs using 1 step motor per fibre (MX spectrometer), to a single arm capable of positioning multiple fibres in systems like Autofib, 2df, Argus, Medisis and Decaspec, see Figure 1.10.

Recent technologies continue to advance the methods for repositioning fibres in multi-object fibre-fed spectrographs. Current instruments include HERMES (Sheinis et al., 2015) and AAOmega on the Anglo-Australian Telescope (AAT) and Fibre Large Array Multi Element Spectrograph (FLAMES) (Pasquini et al., 2002) on the Very Large Telescope (VLT). 4MOST, the 4-metre Multi-Object Spectroscopic Telescope (de Jong et al., 2016), is currently being built using a positioner system based on the tilted spine principle, with individual

Figure 1.11: The starbugs technology is currently being developed with the goal of reducing reconfiguration times.

piezoelectric actuators that tilt each fibre until it finds its position in the field. It can simultaneously reconfigure ≈2400 fibres with separations smaller than 13″. Starbugs (Kuehn et al., 2014) is an alternative technology, in which each fibre "walks" on a glass plate placed at the focal plane, see Figure 1.11. This is currently being tested at the UK Schmidt Telescope in Australia. The development of these 2 fibre positioning methods reflects the need for faster reconfiguration times, driven by a new wave of large astronomical spectroscopic surveys.

1.2.2 Precision and Stability

The evolution of spectrographs in the context of radial velocity measurements required increasingly higher stability and more precise calibration techniques. Reference sources, with known wavelength values, were used from the early days of spectroscopy. The initial solution to this problem was over impose the flux from known sources into the science images or to interleave images of known sources in between science exposures. These images would carry a map of the wavelength distribution as a function of plate position, and later as a function of pixel value. Knowing the initial distribution of the wavelengths allowed scientists to interpolate the wavelength values into a wavelength scale model. Variations of this method are still widely used and it is, in fact, the method used in this thesis. This approach carries the disadvantage of a high dependence on the instrument's stability to keep the reference images from becoming outdated due to changes in the spectrograph. Attempts to improve the identification of wavelengths across the image recently led to the use of laser combs for this purpose; these instruments produce a stable light source that peaks at fixed wavelength gaps, providing a stable reference, evenly spaced in frequency.

An innovative step in the development of calibration techniques was introduced by Butler et al. (1996). In this approach, an iodine cell is introduced in the light path, adding its spectrum to the telescope's target. This has the advantage of not depending on the instrument's stability, as it is recorded at the same time, and in the same light path, as the science exposure. However it also has the disadvantage of reducing the throughput of the system. There is also a limited wavelength range in which the iodine spectrum is useful due to the location of its spectral features. Outside this range, extrapolation is necessary, potentially reducing the effectiveness

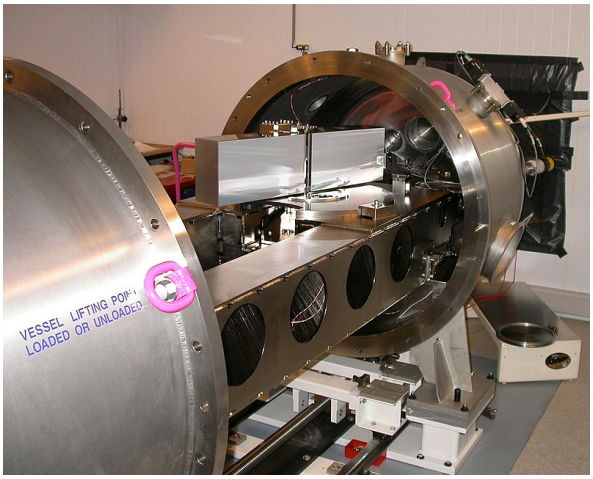

Figure 1.12: HARPS in its temperature stabilised pod.

of the method. This technique, in principle, allows for wavelength calibration with $3\,\mathrm{m\,s^{-1}}$ precision. This has been improved down to $1\,\mathrm{m\,s^{-1}}$ in modern telescopes, but the precision achieved largely remains a function of stellar brightness and quickly decreases with Signal-to-Noise Ratio (SNR).

Thermal stabilisation of the spectrograph is one of the key aspects to control in order to attain high precision spectroscopic measurements. In 1979, CORAVEL (Baranne et al., 1979) could achieve a record breaking precision of $300\,\mathrm{m\,s^{-1}}$ (Udry et al., 1999). This wasn't enough for exoplanet detection, but it set the scene for ELODIE, which had first light in 1993. ELODIE is thermally stabilised, fibre-fed and can measure radial velocities with $7\,\mathrm{m\,s^{-1}}$ precision. It was followed by SOPHIE, with a similar design and improved characteristics, and capable of reaching $\approx 4\,\mathrm{m\,s^{-1}}$ radial velocity precision.

CORALIE, installed on the Swiss EULER Telescope at La Silla Observatory in Chile has reached a $2\,\mathrm{m\,s^{-1}}$ radial velocity precision, and it is the predecessor of one of the most stable spectrographs built to date: High Accuracy Radial velocity Planet Searcher (HARPS) (Pepe et al., 2002) is in a thermally controlled environment (see Figure 1.12) and produces spectra for a single target and a calibration source simultaneously.

Future spectrographs aim to continue increasing stability and spectral resolution. Veloce is a high resolution, R≈80000, multi-object, echelle spectrograph. It uses 26 fibres, 24 for targets and sky and 2 for calibration. It will allow 2 simultaneous calibration sources, with the possibility of making one of them a laser comb for extremely precise wavelength calibration [1].

1.3 Software

The introduction of the Charged Coupled Device (CCD) as an electronic imaging device greatly facilitated the acquisition of data and their subsequent analysis. It allowed a process that previously required manual, repetitive labour to be transformed into an automated reduction pipeline. In addition, it allowed the data extraction process to use much more complex algorithms and to be applied to large volumes of data simultaneously.

In general, we use the term data reduction for the steps that convert the raw data as read out from the CCD into processed information that can then be analysed for scientific purposes. The automation of the data reduction process is known as a pipeline. The creation of a

[1] https://www.aao.gov.au/science/instruments/current/veloce/overview

successful pipeline is essential for the reduction of large volumes of data. This is particularly true in large surveys that require high degrees of automation, not only due to their sheer volume of data, but also because the use of a pipeline can standardise the data output, thereby yielding a consistent dataset.

With instruments on modern telescopes, it has become common practice to develop software packages that standardise the initial steps of the data reduction. The goal is to remove the instrumental signature from the data. The development of these software packages requires a deep understanding of the instruments involved in the data production. There are several widely-used data reduction packages that have been developed by a number of different telescope host institutions. These packages have different levels of flexibility in the features they provide, ranging from single feature modules that simply remove instrumental effects, to more complex features like scripting, spectral cross-correlation, etc.

In every step of the reduction process, decisions are made that affect the output. Different reduction methods use different approaches, with the final result dependent on the sequence of steps taken. Indeed, a given dataset processed by different pipelines can produce slightly, or significantly, different results. Radial velocity measurements can certainly be an example of this.

Reduction Packages

Tody (1993) developed one of the most popularly used packages, Image Reduction and Analysis Facility (IRAF). It was developed by the National Optical Astronomy Observatories (NOAO) of the U.S. and is a flexible platform that allows for the addition of external packages. It has been successful due to its flexibility, and several large surveys have used it as a standard reduction package, including GALAH (Kos et al., 2017). The package benefits from a popular python wrapper that adds further flexibility to the software package. ESO-MIDAS (Warmels, 1992) is a similar package developed by the European Southern Observatory. It has similar flexibility to IRAF and allows a generalised approach to data reduction. Figaro (Shortridge et al., 2004b), falls into the same class of software, with a general solution that allows flexibility in the methods that can be applied to reduce the data.

The Australian Astronomical Observatory (AAO) offers a single package that can reduce data from several of the spectroscopic instruments it supports. 2dfdr (AAO software Team, 2015) is a solution that was originally designed to reduce data from the 2dF fibre positioner, and has subsequently been extended and modified to process data from related instruments, such as AAOmega, 6dF, SAMI, HERMES and Taipan. It doesn't have the broad flexibility of the previously mentioned packages, and it focuses exclusively on removing instrumental signatures from spectroscopic data. The output is a collection of calibrated spectra, see Section 4.1. 2dfdr was used in part of this thesis with only limited success, leading to the decision to write HERMES Automated Radial velocities in PYthon (HARPY) as a more suitable alternative (see Section 4.2).

As the volume of astronomical data continues to grow, fuelled by increasingly large and more detailed surveys, data reduction software is becoming increasingly complex. The demand for astronomical software development has grown in parallel, yet the allocated resources often seem to be less than needed. The tasks required, and corresponding resource allocation, from a software development perspective are not always clear in advance. As a consequence, it isn't uncommon to find extended software development projects that exceed

the originally planned times. The full scope of a project only becomes clear as the research advances.

The development of HARPY is indeed an example of this. In the early stages, HARPY was developed to automate the different cross correlation options of 2dfdr-reduced spectra. Observing the results produced, however, it became clear that the 2dfdr pipeline was not adequate for the task, and a full reduction pipeline needed to be developed for the specific purpose of producing radial velocity measurements from raw data.

The challenge ahead, and the hope of the author of this thesis, is that astronomical software development continues to evolve, facilitating integration with other areas and adopting practices that proved successful across other fields.

1.4 Outline of the thesis

This thesis describes the development of a dedicated reduction pipeline customised for radial velocity precision. We present the challenges found with the existing software solutions and demonstrate how the development of HARPY has increased the instrumental capabilities of HERMES at the AAT as an exoplanet detection instrument. We use the developed pipeline to confirm the discovery of an exoplanet, previously unachievable with the instrument. We apply the developed pipeline to several known targets, confirming its performance. We finally apply HARPY to new targets, identifying objects of interest for follow-up observations.

Chapter 2 is a description of the high-resolution spectrographs used for this thesis. Initially Replicable High-Resolution Exoplanets and Asteroseismology (RHEA) is presented as a starting point to develop a wavelength solution, followed by HERMES. In both cases, a careful analysis of the spectrograph's technical characteristics is presented with a focus on the relevant features that need to be modelled in a software package. The characterisation of the Point Spread Function (PSF) of HERMES, developed for this thesis, is presented at the end of this chapter.

The approach to selecting a wide range of targets to apply the reduction pipeline developed for this thesis is presented in Chapter 3. We start with the high level decisions that narrow the types of targets considered. We describe the large dataset obtained by the Galactic Archaeology with HERMES (GALAH) survey, partially used in this thesis, and conclude with the detailed list of the targets used.

Chapter 4 introduces the two existing software solutions initially used for data reduction and describes HARPY, the software package developed from the ground up for this thesis to reach higher precision levels than the previously tested software packages. We describe the theory behind radial velocity calculations and introduce the 3 data reduction methods used in this thesis

In Chapter 5, we apply the three methods to the core targets and we provide a comparison of the performance of each of them. We confirm HARPY as the approach that produces the best results. We also use this method on selected new targets and present the most promising results.

Chapter 6 summarises the achievements presented across this thesis. We also focus on the lessons learned at different stages of this study. We present alternative approaches applying the currently used reduction pipeline. We look at new features that could improve HARPY in the future. Using the results presented in Chapter 5, and the larger dataset analysed in this thesis, we identify a number of follow-up research paths that we consider worth pursuing.

2 High-Resolution Spectrographs

In this chapter we describe the physical aspects of the main instruments employed for this thesis, HERMES and RHEA. HERMES is the newest facility class instrument commissioned on the AAT. When this thesis project began, HERMES was expected to be on-line by early 2013; however, the instrument was delayed by approximately 1 year. HERMES was finally commissioned over the summer 2013/2014, and made available for community use in early 2014

Due to this delay, the first year of the thesis focused on developing software capable of producing a physically driven wavelength scale model for any spectrograph. The test instruments used were the RHEA spectrograph, co-developed by the author, and IR-RHEA, an infra-red version of the RHEA spectrograph. The initial version of the spectrograph formed part of my Honours thesis (Bacigalupo, 2013). Part of the information previously published is included here as a background to the early development stages of this thesis work. In particular, parts of section 2.1 and 2.1.1, including the figures, are based on my Honours thesis.

2.1 RHEA

The RHEA project, (Feger et al., 2014), aimed to build the simplest spectrograph that would reach the level of precision necessary for the detection of exoplanets. The approach was "from-the-ground-up" in which, after a design period, an initial spectrograph setup would be constructed and any problems noted for improvement in subsequent versions. The goal of this approach was to ensure that the most basic configuration capable of achieving the science goals would become the standard.

The search for exoplanets around giant stars requires long term observations over periods ranging from months to years. The intrinsic oscillations of giants can mimic the signature of an exoplanet when observations are limited to a short time period, potentially producing misleading results. As a consequence, searches for planets around giant stars are mainly conducted as part of large, long term studies. In order to carry out long term observations at a modest cost, the RHEA project was conceived as a comprehensive design that included dome

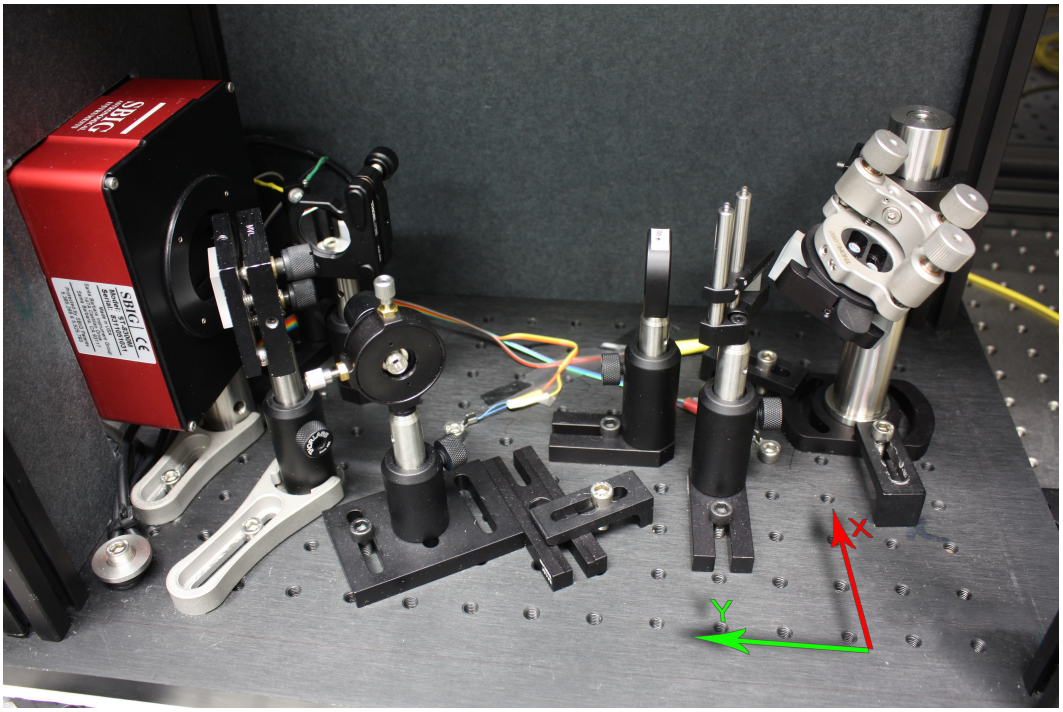

Figure 2.1: The RHEA spectrograph. The reference frame for the model is indicated by the arrows. The components are described in Section 2.1.1.

and remote / automated telescope operation, in addition to the spectrograph itself. It is the unmanned observing operations and minimal maintenance that makes long term observations cost effective.

As the complete setup includes the RHEA spectrograph and the support systems that make the observations possible, the long term vision is to create an instrument that in its final version would reduce production costs increasing potential interest for replicability. The initial steps of this project were tested at Macquarie University using a Meade LX200 16 inch telescope in a Schmidt Cassegrain configuration. The latest version of this spectrograph, RHEA@subaru, is currently being tested on the Subaru telescope.

2.1.1 The Spectrograph

RHEA is a cross-dispersed echelle spectrograph. Its compact design yields a spectral resolution of R≈50000 at 550nm. It operates over a wavelength range between 390 nm and 795 nm. Its optical design is a near-Littrow configuration, and is adapted to work with a 0.4m telescope working at F/10 focal ratio.

The spectrograph is designed to minimise size and cost. It relays light from the telescope by the use of a single mode fibre with a $\phi = 1/2''$ lens at the fibre attachment (Figure 2.2(c)). The 3.5μm fibre core creates an 18.33μm size image that becomes the entrance slit. The beam is collimated by a 200 mm focal length lens (see Figure 2.2(a)) at f/8 and sent to the prism. This is where the pupil of the system is defined. The prism is 9 mm in aperture. The light horizontally dispersed by the prism is dispersed vertically by the R2 echelle grating (Figure 2.2(e)) with a ≈63.43 ° blaze angle and 31.6 grooves/mm, placed at near-Littrow configuration. The light returning from the grating is dispersed once again by the prism acting as a cross-disperser, effectively separating overlapping orders. The prism is made of

N-KZFS8 glass, has an 8 mm base and a 30 ° apex angle (see Figure 2.2(d)). The collimating lens becomes the camera lens on the return beam as the final optical element focuses the spectrum onto the detector. The sensor is a CCD Kodak KAF-8300 3326 × 2504 with 5.4 μm pixels (Figure 2.2(b)). It includes a thermal stabilisation system. The spectrograph is enclosed by 5 mm lightweight polystyrene foam and surrounded by a thermal insulator. All the components are off-the-shelf, making it relatively inexpensive and simple to replicate. Note that the camera shutter is the only moving part.

RHEA components

(a) The collimating/camera lens (AC254-200-A) has a focal length of 200 mm and a diameter of 25 mm. It's an achromat and operates at wavelength range of 400-700 nm.

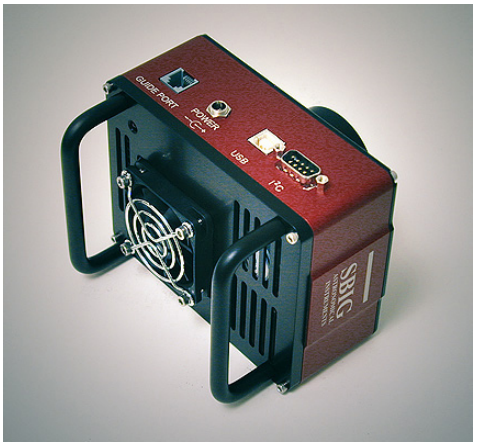

(b) The SBIG STT-8300M **camera** has a Kodak KAF-8300 sensor with an array of 3326 × 2504 pixels, each measureing 5.4 μm.

(c) The LM05XY/M **fibre optic attachment** is connected to a translating lens mount for $\phi 1/2''$ optics. It works with a sensitivity of 250μm/rev and it has a FC/PC connector.

(d) The PS873-A **prism** operates over a wavelength range of 350-700 nm and has an apex angle of 30deg. It's made of N-KZFS8 with a refractive index of 1.7249 @ 550nm.

(e) The GE2550-0363 **echelle grating** has 31.6 grooves/mm and a 63 ° blaze angle. The size is $25 \times 50 \times 9.5$ mm.

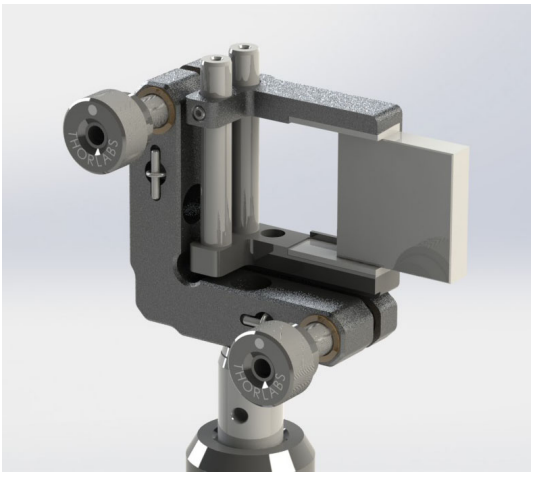

(f) The PFSQ10-03-F01 UV enhanced aluminium **mirror** is 25.4×25.4 mm in size.

2.1.2 RHEA Performance

Using the expected efficiency values for each of the optical components of the RHEA spectrograph, combined with the camera's quantum efficiency, the theoretical throughput of the spectrograph was calculated. The results show that the system's highest sensitivity is found between 0.4 and 0.64 μm (see Figure 2.2). These results match the design specifications. However, a first on-sky test showed a large discrepancy between the expected values and the measured ones, namely that only $\approx$20% of the expected flux at 550 μm could be detected. This problem was attributed to the fibre injection system, which was later replaced when the second version of the spectrograph was developed, as per the iterative improvement approach outlined in Section 2.1.

2.1.3 Wavelength Scale Model

Accurate wavelength measurement of spectral features in extracted data is the result of a successful wavelength scale model calculation. The development of wavelength scale model software began during the design phase of RHEA. The initial proof of concept was completed by the author in the year prior to the commencement of this thesis, and was applied to solar spectra, successfully identifying Fraunhofer lines.

Using part of the purpose-written data pipeline as a springboard, a new version of the wavelength scale model was attempted in the early stages of this thesis work. The key changes were a spectrograph independent design, allowing the software to produce a wavelength scale model given any optical configuration. The core algorithms were refactored as part of a redesign of the software architecture. This included the organisation of the existing scripts into classes. The resulting code was tested not only with RHEA, but also with the IR-RHEA spectrograph. An attempt was also made to adapt the software to produce a wavelength solution for HERMES. This effort was suspended when it was realised that the wavelength precision obtainable was limited by the accuracy with which the reference wavelengths of the Thorium-Xenon emission lines visible in the HERMES calibration spectrum were known (see Section 4.1).

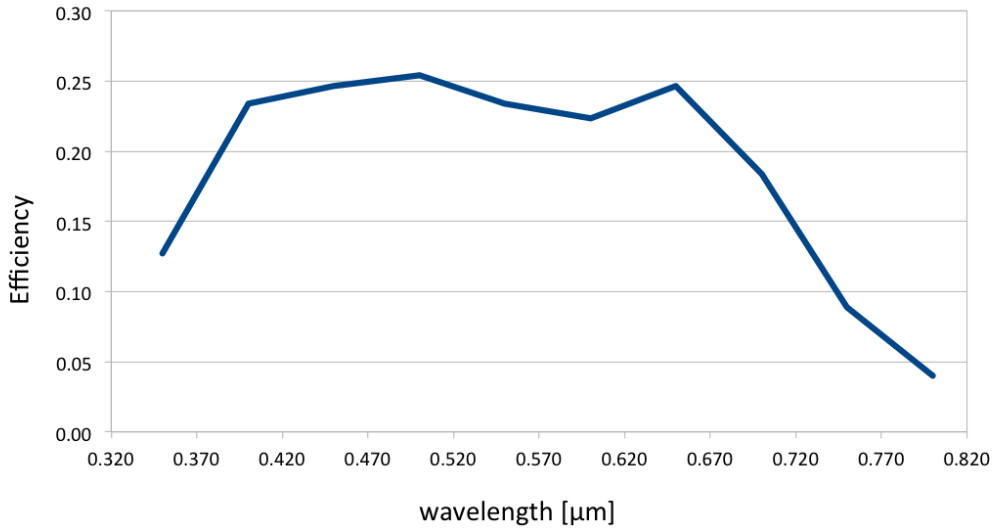

Figure 2.2: Theoretical efficiency of the RHEA spectrograph based on the expected combined throughput values of the optical components and detector sensitivity.

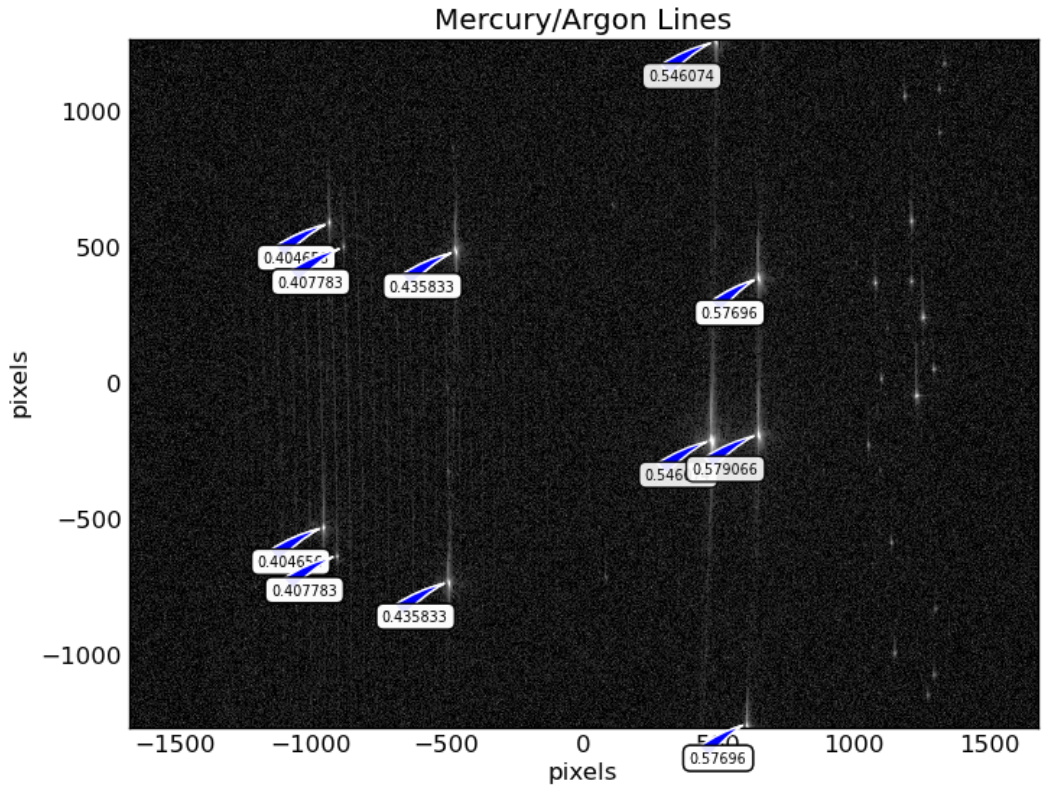

Figure 2.3: Mercury lines identified by the wavelength solution of the RHEA spectrograph. The label overlay is automatically produced by the software at the predicted points of the image, based on the eleven parameter physical spectrograph model.

Software Architecture

All processes in the Wavelength Scale Model (WSM) are consolidated in a single class. This allows the software to be easily embedded as part of larger projects. It also facilitates its usage by adding a well-structured layout of algorithms, variables and related objects, such as input images and external files. The main goal of the WSM is to provide an accurate map that links coordinates on the CCD with the corresponding wavelength. The WSM calculates the distortions that the spectrograph produces on a beam of light from a given source. It traces the path of a monochromatic beam and computes its final location on the CCD detector. It uses a forward model based on an adjustable number of input parameters. The number of parameters depends on the optical configuration being simulated; in the case of RHEA, 11 parameters were necessary.

The simulation of the light path as it travels through the spectrograph is done in a single reference frame and in 3-dimensions. This required the use of equations to describe the behaviour of light as it passes through each optical element. Snell's law and the grating equation were adapted to a 3-dimensional environment; as both equations are ultimately 2-dimensional equations, the incidence plane had to be identified and the beam projected onto it.

The optical elements of the spectrograph were described as matrix transformations of the vector representation of the beam. The innovation of this approach lies in the fact that the optical dispersion arises naturally from the physical description of the transformations on the incoming beam. In addition to the physical description of the spectrograph, optical distortion parameters were added to the model to optimise the fit to the observed spectrum.

The correct value of the input parameters is found by a least-squares method. The process uses the known emission lines of an arc lamp and minimises the difference between the observed lines and the simulation. This method finds the best set of input parameters. The ideal set of input parameters is effectively the parametrisation of the model at a given point in time, and it is used to extract the flux from the source and link each flux measurement to a given wavelength range.

This exercise provided a good basis for generating a global framework to create a wavelength scale model for precision radial velocity work, one applicable to a wide range of different spectrographs. It gave hands-on experience integrating the software and hardware components, and understanding their interdependencies. No on-sky data were collected with the RHEA spectrograph before HERMES became available for continuing the rest of this thesis.

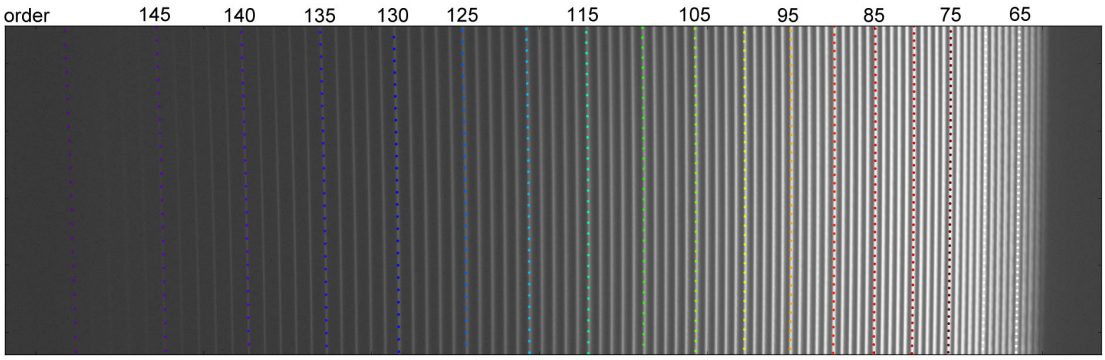

Figure 2.4: Automatic detection of the orders produced by the RHEA spectrograph. Calculated by the Wavelength Scale Model.

Channel	Min Wavelength	Max Wavelength
Blue	471.8 nm	490.3 nm
Green	564.9 nm	587.3 nm
Red	648.1 nm	673.9 nm
IR	759.0 nm	789.0 nm

Table 2.1: Nominal ranges of the 4 HERMES channels.

2.2 HERMES

HERMES is a major facility-class optical spectrograph. Developed by the Instrumentation Group at the AAO and commissioned for the AAT, HERMES is designed to provide multi-object, high-resolution optical spectra; it can target up to 392 simultaneous objects at a spectral resolving power of R≈28,000 within a 2 degree field of view., and it also has a higher resolution mode (R≈45,000). Its spectral range is divided into 4 non-contiguous bands, totalling ≈100 nm within a 370-1000 nm window (see Table 2.1). The spectrograph is fed by the existing 2dF robotic fibre positioning system at the telescope's prime focus.

The spectrograph's primary goal is Galactic archaeology (Freeman and Bland-Hawthorn, 2002). That is, detailed abundances of up to 29 elements will be used to chemically tag stars in order to understand their origin and formation history. This work is being conducted under the auspices of the GALAH survey (see Section 3.3); GALAH's goal is to measure the chemical abundances of 1,000,000 stars in the Milky Way.

A new fibre cable bundle combines fibres from the new HERMES spectrograph with those from the older, lower resolution AAOmega (Brzeski et al., 2012). This design allows each magnetic button of the 2dF robotic positioner system to contain both a fibre for HERMES and one for AAOmega. This approach was introduced to allow for quick instrument changes, without the need to remove the fibre system from the telescope. Each spectrograph has 2 slits, with 392 science fibres per slit; this allows one slit to collect science data while the 2dF robot configures the fibres feeding the other slit for the next observation (Heijmans et al., 2011).

The sensitivity of HERMES yields SNR≈100 per resolution element for a star of V=14 in 60 minutes of integration. This corresponds to an overall system efficiency of 0.1 – a typical value for this type of instrument – and includes telescope, fibre system, spectrograph and detector. HERMES is housed in a clean, temperature-controlled room and mounted on vibration isolators in an effort to maintain long term stability. Based on optical system simulations and early stability analyses, the quoted stability of HERMES corresponds to 0.1 pixels. This translates to roughly to 300 $\mathrm{m\,s^{-1}}$ precision in radial velocity.

After completing assembly, integration and testing, the AAO delivered the instrument to the AAT site in August 2013 and fully commissioned the instrument in the last months of 2013. HERMES became available to the astronomical community in early 2014.

2.2.1 Optical Components

The four cameras in HERMES are an F/1.67 refractive design with a 380 mm diameter first element and an entrance pupil of 190 mm located at the grating. The camera assembly contains a doublet, with an aspheric first surface, and then 3 additional lens elements (see Figure 2.5). The dewar optics are just above the detector and consist of 2 windows and a field flattener.

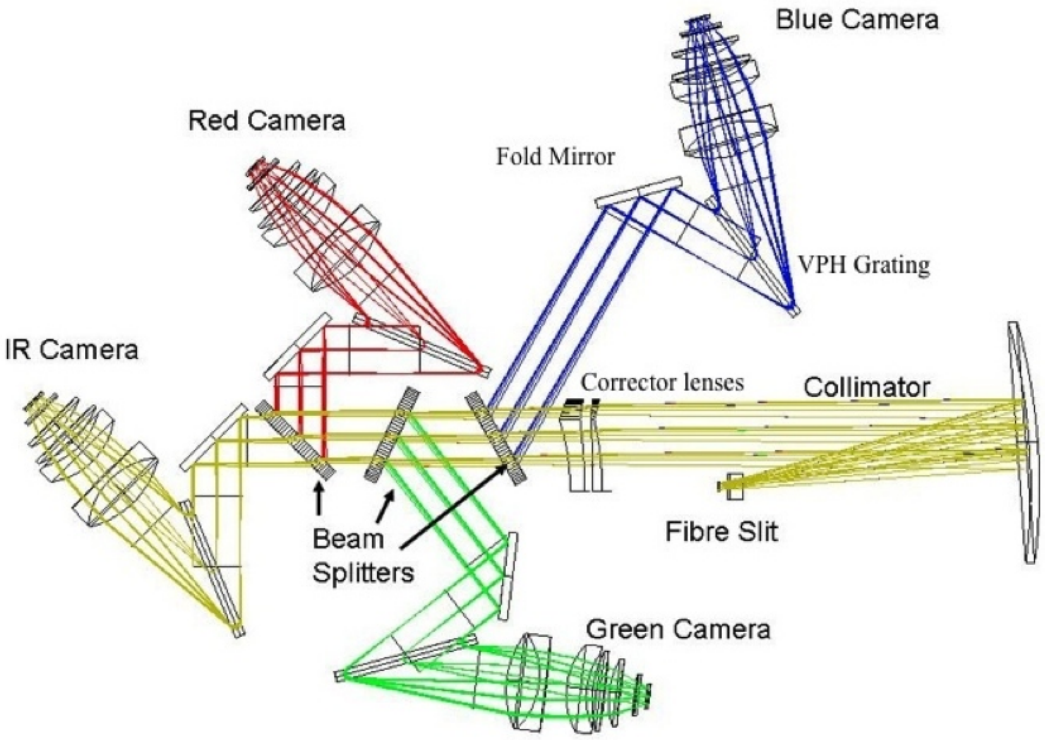

Figure 2.5: Optical layout of the HERMES spectrograph (Sheinis et al., 2015).

The collimator of the HERMES spectrograph is based on an off-axis Houghton design. It is curved to match the radius of the focal surface and also curved in the perpendicular direction to compensate for the otherwise curved distribution of spectral features at the detector focal plane. The assembly is made from 3 optical components: the spherical collimator mirror and 2 off-axis corrector lenses. The diameter of the collimator mirror is 960mm and its thickness 150mm. Only the central, almost rectangular, area of the mirror (350 x 910 mm) is used.

The Volume Phase Holographic (VPH) gratings in HERMES are 550 x 220 x 40 mm in size. There is one grating per channel,i.e., there are four in total. The line frequencies vary from 3827 to 2378 lines/mm. All gratings operate at a 67.2 degree angle of incidence. These are amongst the largest, highest frequency, and tightest tolerance VPH gratings yet produced for astronomy and the development process required several iterations modifying a single variable at a time to meet the specifications of HERMES.

HERMES uses 4 CCD Sensors, all variations of e2v CCD231-84 back illuminated scientific CCD sensor. Each CCD has 4112 by 4096 pixels and 15 μm pixel size. The cryostat shell is based on an Infrared Laboratories cryostat with a Polycold PCC cryocooler cold head. Added to this assembly, a Pfeiffer PKR full range vacuum gauge head was fitted. Each detector is enclosed by a custom made shell extension. The connectors for the detectors and thermal control are mounted through the wall of the shell extension (see Figure 2.6).

Figure 2.6: The 4 cryostats and detectors assembled on HERMES. (Sheinis et al., 2015)

As noted above, with the development of HERMES a new combined HERMES/AAOmega fibre bundle was constructed (Brzeski et al., 2011), allowing the attachment of two fibres to each of the 392 magnetic buttons. The 2dF robot positions the magnetic button on the field plate, (see Figure 1.10), so that any allocated fibre is feeding one spectrograph or the other. This arrangement minimises the need for any instrument changeovers.

The structure of the 2dF buttons is shown in Figure 2.8 and can be seen on the plate in Figure 2.9. The fibres from AAOmega and HERMES – along with a dummy fibre, to align the other fibres – are covered with a polyamide jacket and terminate in a glass ferrule coupled to a prism. Each ferrule is glued into a magnetic button that allows it to be moved by the positioner arm and to remain attached to the 2dF field plate.

At the spectrograph end, the fibres are assembled in slitlets that locate 10 fibres in v-grooves at the slit entrance (see Figure 2.7). The combination of 40 slitlets yields 400 fibres in total, including 8 fibres used for guiding. The average end-to-end throughput for the HERMES fibres is 62% at 505 nm. The predicted throughput was 66%; the discrepancy is primarily attributed to focal ratio degradation due to fibre stress.

Reversed fibre IDs

The identification of the fibres in the CCD has been somewhat complicated by a reversal in the position of the slitlets in HERMES. This section aims to clarify a simple problem that requires a careful approach to avoid erroneously identifying fibres.

The fibre identification starts with the initial target list (.fld file). The program CONFIGURE assigns a fibre number based on a series of algorithms and priorities. Up to 392 fibres are

Figure 2.7: Curved slit assemblies on the translation stage of HERMES. This allows the light from the 2 sets of 400 fibres to be correctly injected and exchanged, increasing observational efficiency (Sheinis et al., 2015).

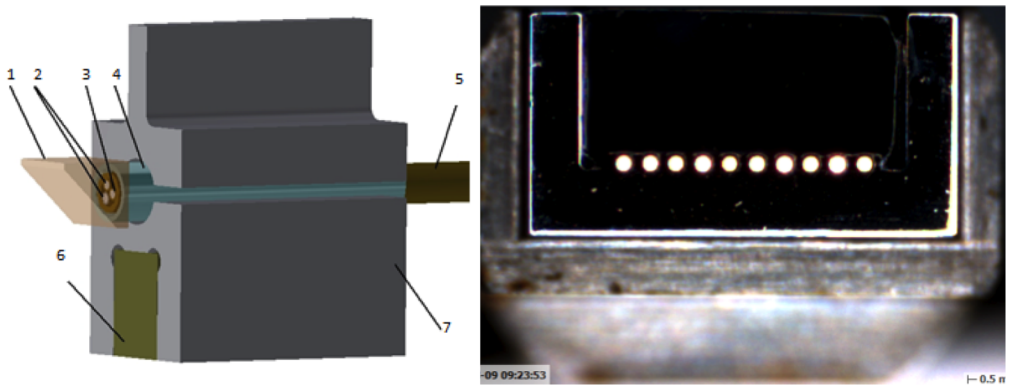

Figure 2.8: Left: Schematic of a 2dF button and its parts. 1-Prism. 2-AAOmega/HERMES science fibres. 3-Dummy fibre. 4-Glass ferrule. 5-Polyimide tube. 6-Magnet. 7-Button body. Right: 10 fibres in a slitlet (Sheinis et al., 2015).

allocated. The 8 remaining fibres are used for guiding and have reserved the numbers 50, 100, 150, 200, 250, 300, 350, 400.

On the other end, the fibres are aligned in groups of ten, forming 40 slitlets. This is the arrangement that sets the location on the CCD. Fibre numbering within these slitlets is inverted, which is the cause of the cross labelling.

2.2.2 Control software

The software architecture chosen for the operation of HERMES relied on the existing software developed earlier for 2dF/AAOmega. This software was originally written using the Distributed Real-time AAO Monitor for Astronomy (DRAMA) API developed by the AAO(Bailey et al., 1995). It has been modified over the years for new instruments.

The software for HERMES is divided into five areas:

- The Observing System is responsible for overall control of observations in real time

Figure 2.9: Magnetic buttons attached to the field plate on the 2df positioner that feeds HERMES.

(including 2dF robot and CCD operations) and provides the main GUI.

- The HERMES Spectrograph Control task is responsible for control of the spectrograph itself.
- The AAO2 CCD detector software(Shortridge et al., 2004a) is used to run the detector systems.
- The fibre Configuration software is responsible for allocating fibres to objects as part of target preparation.
- A separate Data Reduction package provides pipeline reduction to the point of producing calibrated spectra.

The pre-existing 2dF Observing System was modified to add control of HERMES. The Observing System is responsible for controlling the 2dF fibre positioner, the spectrograph, the detector systems, the 2dF calibration system and atmospheric dispersion corrector, the telescope and other minor components.

Each sub-system is run by one or more Distributed Real-time AAO Monitor for Astronomy (DRAMA) tasks. Overall control, software interlocking and synchronisation are provided by the 2dF Control Task. Although the core part of the Observing System remains from the original version written in 1994, the CCD, Telescope and Spectrographs sub-systems have been changed. A new control task has been written to operate in HERMES mode and the detector software has been adapted to control the 4 HERMES CCD systems.

The original version of the CCD Control software was designed for 2 detectors with 2 readouts each. Major changes focused on updating these capabilities to 4 detectors with 4

readouts each. Other changes included the capacity to manage the larger, 4096×4112 pixel detector size.

The fibres for each field observed with 2df must be positioned in advance. The fields are prepared beforehand using a proprietary software package called "AAO Configure". Since its initial development, it has been adapted to support other instruments. The main HERMES-related changes were instrument support, the use of proper motions and modifications to the fibre allocation algorithm to optimise fibre efficiency due to location effects such as cross talk.

2.2.3 Spectrograph Performance

The initial set of HERMES on-sky tests was carried out during the commissioning phase in October, November and December 2013. The objective was to measure the settings necessary for optimal use of the spectrograph and to quantify key instrument performance indicators, such as readout speeds and amplifier combinations, required calibrations and their exposure times, PSF variations, fibre cross talk and scattered light levels, and overall instrumental resolution and throughput.

During the almost 3 subsequent years of operations, a broader set of measurements could be performed, allowing us to gain better insight into the intrinsic behaviour of the instrument. The results presented in the rest of this chapter, and throughout this thesis, are the summary of this analysis.

Spectral Resolution

The nominal spectral resolution for each HERMES channel is R≈28000. This resolution was measured by fitting Gaussian profiles to ThXe calibration arc lamp exposures. Typical values, measured from the central fibre, are presented in Figure 2.10. The combined range of variations in resolving power are represented by the error bars. Note the resolving power varies between fibres and between the four channels (see Section 2.2.4 on PSF variations).

HERMES also offers a higher resolution mode of R≈42000 using a slit-mask on kinematic mounts, the trade-off being that the slit-mask effectively cuts out about 50% of incoming light. However during commissioning it was found that the mask's manufacturing and alignment were faulty, and hence it was not suitable for general scientific use.

Throughput

A range of standard stars, with well-measured fluxes, were used to determine the system's throughput, including telescope, fibre-positioner and spectrograph. The flux transformation equations and magnitude limits are presented in Table 2.2. These values correspond to the Johnson B,V, R and I filters, which are the nearest photometric bands to the four HERMES channels. Observations are based on the median seeing (1.5″) conditions at Siding Spring Observatory, where the spectrograph resides.

A long term analysis using GALAH data, after 2 years of operation, showed no significant change in fibre throughput. Only 2.5 % of the fibres show a consistently low throughput when compared to the average. Variations within groups of fibres and channels have been detected (Simpson et al., 2016), these relative variations have not affected the radial velocity precision work contained in this thesis, however, as the changes are stable from epoch to epoch for a given fibre.

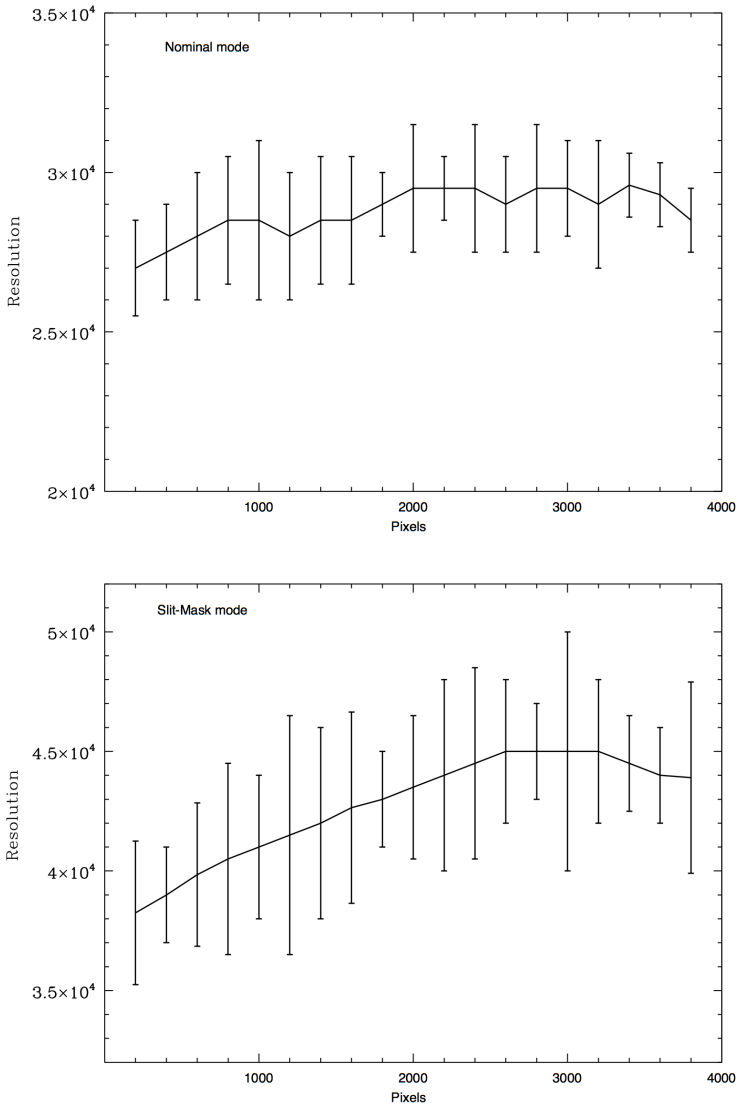

Figure 2.10: Resolving power of HERMES in normal(top) and high(bottom) resolution mode. Measurements were taken on the central fibre. Error bars represent the differences between channels and fibres.

Channel	e-/RE/hr	mag limit
Blue	$10^{-0.4(0.993*B-24.05)}$	B=14.2
Green	$10^{-0.4(1.18*V-26.25)}$	V=13.8
Red	$10^{-0.4(1.07*R-24.98)}$	R=14.0
IR	$10^{-0.4(0.89*I-22.33)}$	I=13.8

Table 2.2: The flux transformation equations in electrons per resolution element per hour. The magnitude limits shown are for each HERMES channel to achieve SNR=100 in one hour, in the normal HERMES resolution mode (Sheinis et al., 2015).

2.2.4 PSF Variations and Fibre Cross-Talk

The response of an optical system to a point source is characterised by its PSF. The resolution achieved by an optical arrangement is directly linked to the structure of the PSF in the focal surface. Variations can be noticed in the optical PSF across the detectors in HERMES. These variations can be seen both in the spatial and spectral direction, and in all channels. For the central fibres, the PSF is circular in the centre and elliptical at the edges. For the top and bottom fibres, the central shape of the PSF is elliptical and becomes inclined in opposite directions at the edges (see Figure 2.11).

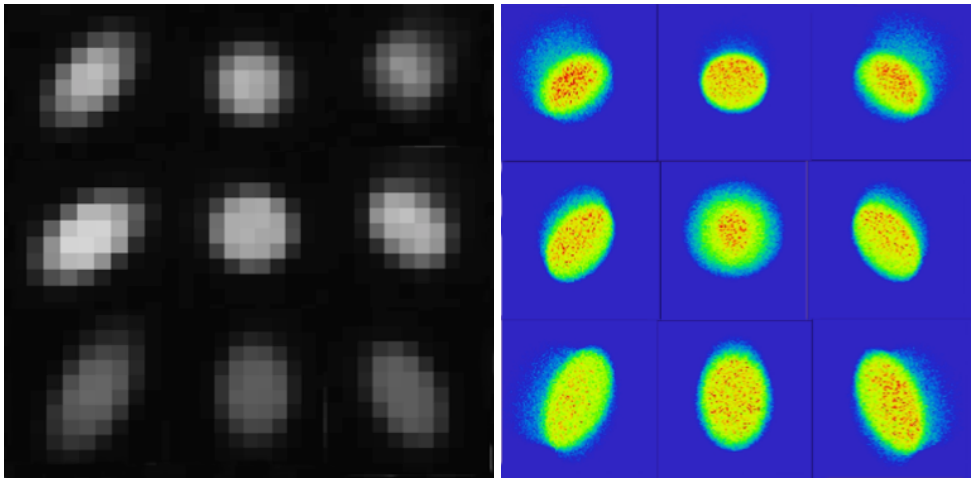

Figure 2.11: The HERMES Point Spread Function at different positions across the CCD. Left: Examples of the PSF at the centre and along the edges of the CCD. Right: Zemax model of the corresponding expected PSF shapes calculated during instrument development.(Sheinis et al., 2015).

The variations of the PSF in the spatial direction produces inter-fibre cross-talk (see Figure 2.11). That is, flux is transferred from neighbouring fibres, contaminating the extracted data. The resulting influx affects spectral resolution as it adds a layer of noise that changes from epoch to epoch independently of the fibre being measured.

In order to quantify the effects of the changing PSF across the CCD, a set of measurements on a series of flat exposures were done using purpose-written Python code. This software module was written in the early stages of this thesis to gain understanding on the PSF sizes that we could expect as a function of CCD position.

The PSF is calculated by taking individual columns of pixels across the full length of the CCD. An initial analysis of each column identifies missing fibres that produce no flux and determines the pixel value where the flux from each detected fibre peaks.

Using this information, a parametrised version of the array is attempted. The number of parameters used to create this version of the array depends on the shape of the curve to be fitted. Gaussian, Voigt and Lorentzian shapes were tested, with the Gaussian showing the best fit. Later software versions and similar tests suggested that a better fit could be achieved using a generalised error distribution curve of the form

$$y = Ae^{-(\frac{|(x-\mu)|\sqrt{2\log 2}}{\sigma})^{\beta}} \tag{2.1}$$

where A is the amplitude, x is the pixel range, μ is the displacement, σ is the scale and β the shape (see Figure 4.15). This alternative curve uses the base Gaussian equation but adds

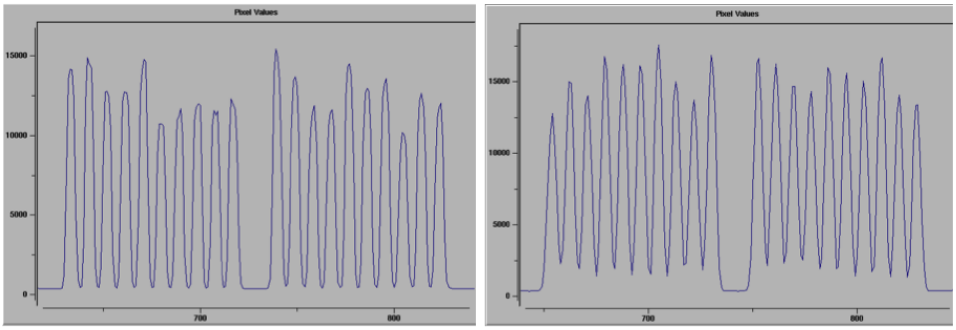

Figure 2.12: Flux vs. pixel position for a vertical cut across a fibre flat field image, zoomed in to the centre column of the detector in the HERMES red channel. Left: At the centre of the CCD, where flux levels drop down to the bias level between fibres. Right: At one of the ends, where flux levels between individual fibres don't reach the bias, indicating there is illumination spilling over from the adjacent fibres (Sheinis et al., 2015).

an extra degree of freedom in the β parameter. It becomes particularly useful when the PSF becomes non-Gaussian, near the edges of the CCD.

Having selected the function and the initial parameters, an array of equal length to the column extracted is created. This array attempts a parametrised version of the extracted column. There are 4 parameters required to create each curve and this scales with the number of peaks. Each column needs ≈1568 input parameters to be created (i.e., 4 parameters × 392 fibres). This step required a special focus in optimisation as it needed to be executed recursively to fit the best parameters.

The programming decision to be taken at this step was to either generate the parametrised curve using a programming loop or by array operations. Quick tests confirmed that the latter was much faster, as expected. The optimisation was achieved taking advantage of the power that the Python language has when operating with arrays; the technical challenge was to translate the recursive approach to an array operation.

In each column of a 2-dimensional array, a curve representing the flux of each fibre is produced. The complete array, finally collapsed, becomes the parametrised column. Both of these steps are fast as they rely on low level functionality rather than on high level programming loops. With the optimised functions created, a least-squares fit was performed to determine the optimal parameters.

The output of this process is a collection of ≈392 parametrised curves that describe the profile of each fibre in the selected column. The parameters include the standard deviation, represented by σ. The Full Width Half-Maximum (FWHM) is calculated by the formula

$$FWHM = 2\sigma\sqrt{2\ln 2}. \tag{2.2}$$

This process is repeated for each column and for each camera. The final result is a 2-dimensional array of values describing the FWHM of the spatial PSF at different points of the CCD for each camera. As the theoretical calculations had demonstrated, the variations of the PSF across the CCD affect the system's resolution (see Figure 2.13).

In order to summarise the 2-dimensional data gathered from each camera, 2 sets of plots were created. The first one presents the data from selected columns as a function of fibre number (see Figure 2.14). The error bars indicate the standard deviation of the data in the

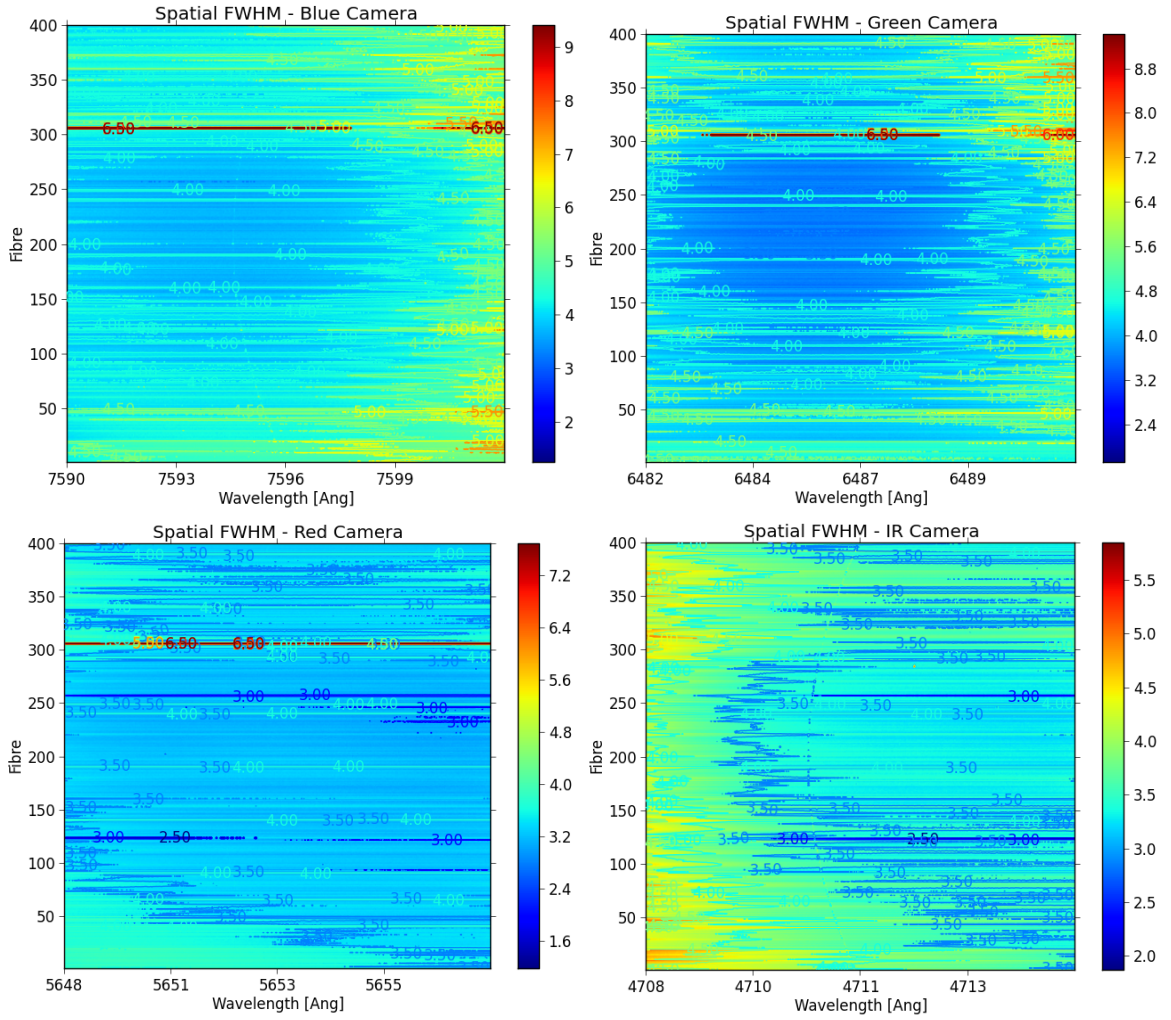

Figure 2.13: Contour plot of the spatial PSF across the 4 HERMES CCDs. PSF FWHM values in pixels are colour coded and added to the plot. The smallest FWHM is found in the central area in all cases and degrades near the edges due to a decrease in resolution and inter-fibre cross talk. Both effects are a consequence of the spatial variation of the PSF.

region sampled. As expected, the central region of all cameras is where the smallest PSF is found.

The second approach to summarising the data collected is to present the value of the FWHM in pixels of the PSF from selected fibres as a function of wavelength. As is the case with the previous set of plots, the error bars indicate the standard deviation of the data in the region sampled. The plots show a more uniform distribution of values for a given fibre and a much larger difference between the values on the central fibres and those near the edges of the CCD (see Figure 2.15).

The analysis of the performance of HERMES helped us gain an understanding of what could be the best possible performance from the instrument. High-impact characteristics, like variations of the PSF across the CCD, and less complex effects, like the numbering system for the fibres, have an important influence on the factors that software has to deal with. The collection of these data proved extremely useful for several aspects of the final versions of the software solutions developed as part of this thesis.

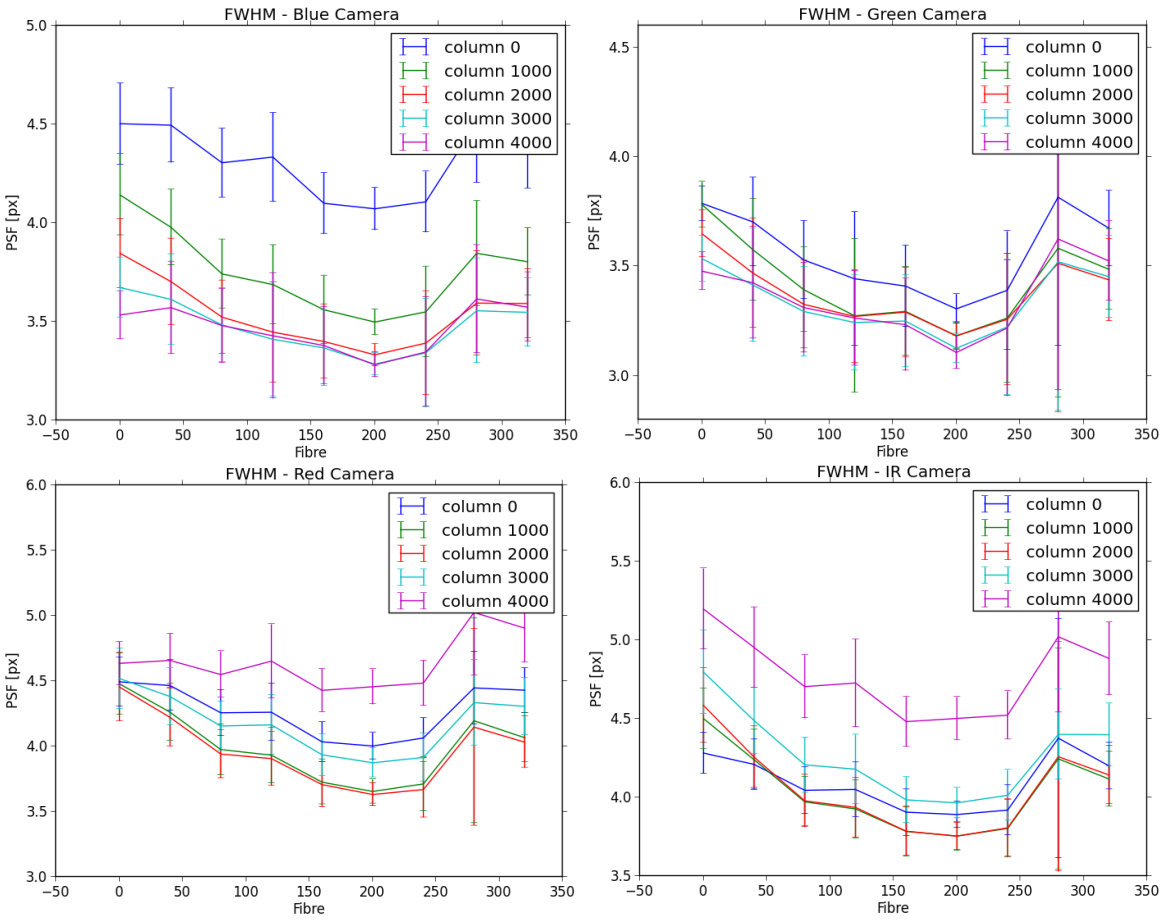

Figure 2.14: The spatial PSF across the 4 HERMES CCDs. Selected columns vs fibre show a decrease in PSF FWHM size in pixels at the edge of the CCD. This effect can be observed on the left side (low pixel value) for cameras Blue and Green, and on the right side (high pixel value) for cameras Red and IR. This is an effect dominated by the instrumental resolution.

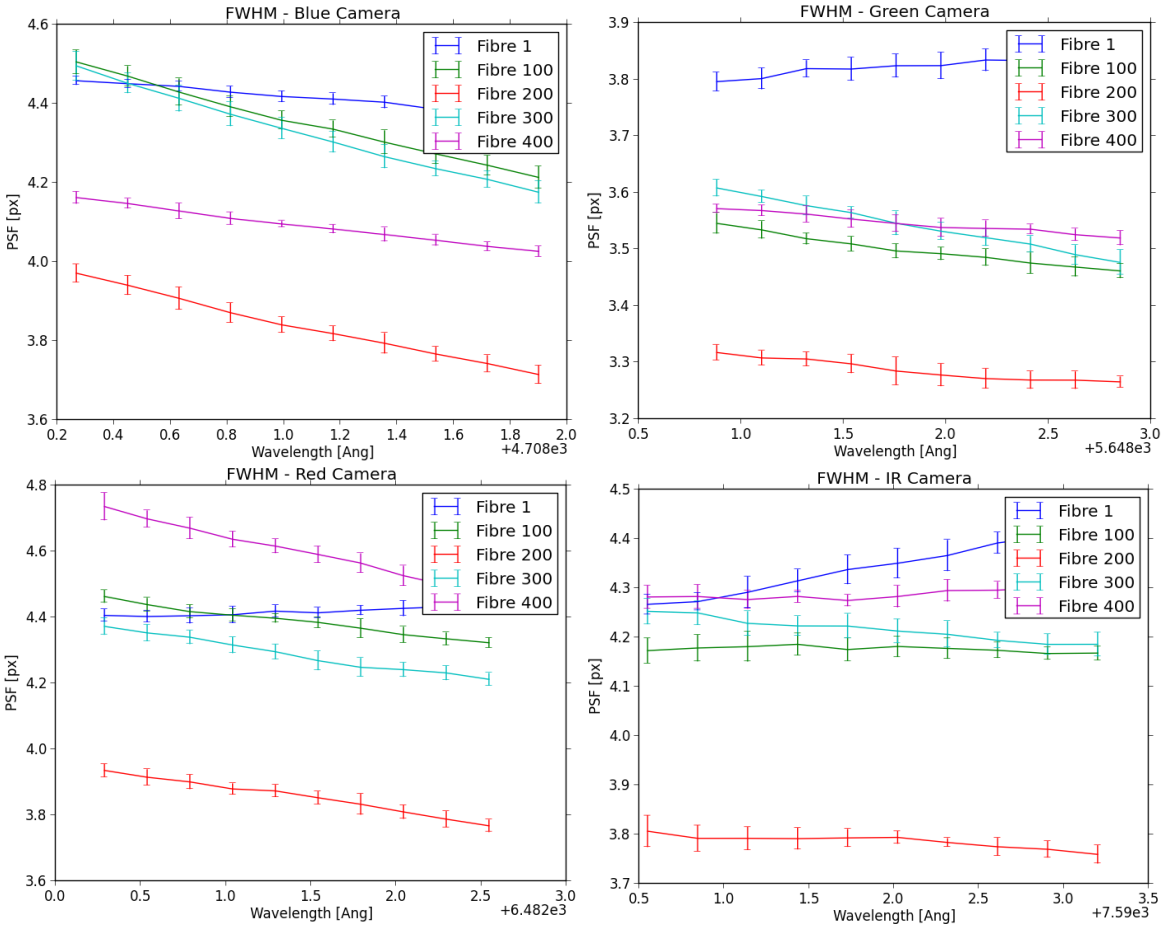

Figure 2.15: The spatial PSF across the 4 HERMES CCDs. The distribution of the PSF vertically shows that the smallest values are found across the central fibres. This is an effect dominated by the inter-fibre cross talk.

3 Data Collection

This chapter describes the different sources of data used in this thesis. Data were sourced from AAT time awarded directly to the author as well as from the GALAH survey. Below, we explain the target selection process and observing methodology used.

3.1 Observations

The expected HERMES radial velocity precision based on early HERMES stability tests by the development team is ~0.1 pixels, which corresponds roughly to 300 $\mathrm{m\,s^{-1}}$ (Sheinis et al., 2015). This sets a limit to the range of radial velocity-derived science that can be carried out with HERMES. It makes exoplanet searches highly challenging, because only a small percentage of planets discovered show a radial velocity semi-amplitude (K) larger than the instrumental limit (see Figure 1.4). The amplitudes of the radial velocity variations due to intrinsic stellar oscillations in giant stars are better matched to the expected radial velocity precision of HERMES. Hence even assuming that this spectrograph stability limit remains, HERMES would still be a suitable instrument to explore the radial velocity variations in binary star systems or make asteroseismological measurements.

3.1.1 Run 1: January 2014

With the purpose of searching for exoplanets in clusters, a proposal was submitted to the Australian Telescope Allocation Committee (ATAC) in September 2013. This proposal was successful, and 3 nights were scheduled for observing on the AAT with HERMES in January 2014. During this run, we targeted 2 open clusters with the aim of searching for evidence of hot Jupiter planets in orbits shorter than 6 days around main sequence stars, and also to observe a sample of cluster giants in order to perform asteroseismological analysis and obtain an unprecedented precision in the age estimate of the clusters from the combined measurements. In the case of positive planet detections, this information could lead to a high precision measurement of the mass of the planet's host stars, thereby linking the two science goals.

Current detection rates suggest that 1.2 ± 0.38% of solar-type stars are predicted to host hot Jupiters (Wright et al., 2012). This translates to 5 to 10 Hot-Jupiters that could be found if ~400 main sequence stars were observed. Any significant deviation from this number could also provide an insight into their formation in a cluster environment. However, this value not only has complex biases, but is also independent of any consideration of the local environment. In particular, a stellar cluster environment may affect the formation process of planetesimals and, hence, the frequency of planets. Thompson (2013) suggested that a relatively high temperature ($> 150K$) of the primordial cloud and unusual gravitational instability can affect the presence of the ice line and inhibit planet formation. An enhanced stellar interaction environment, likely to take place in dense clusters, has also been suggested to trigger scattering events that result in ejected small planets and, hence, in a large free-floating planet population (de Juan Ovelar et al., 2012). On the other hand, in low density clusters, the planet frequency is expected to remain consistent with that of field stars (Chatterjee et al., 2012).Clusters, indeed provide a unique opportunity to obtain a precise estimate of the age of a stellar sample which, in turn, leads to a more accurate estimate of the stellar masses of planet host stars in that cluster (Benomar et al., 2012). This was the core science case of the application.

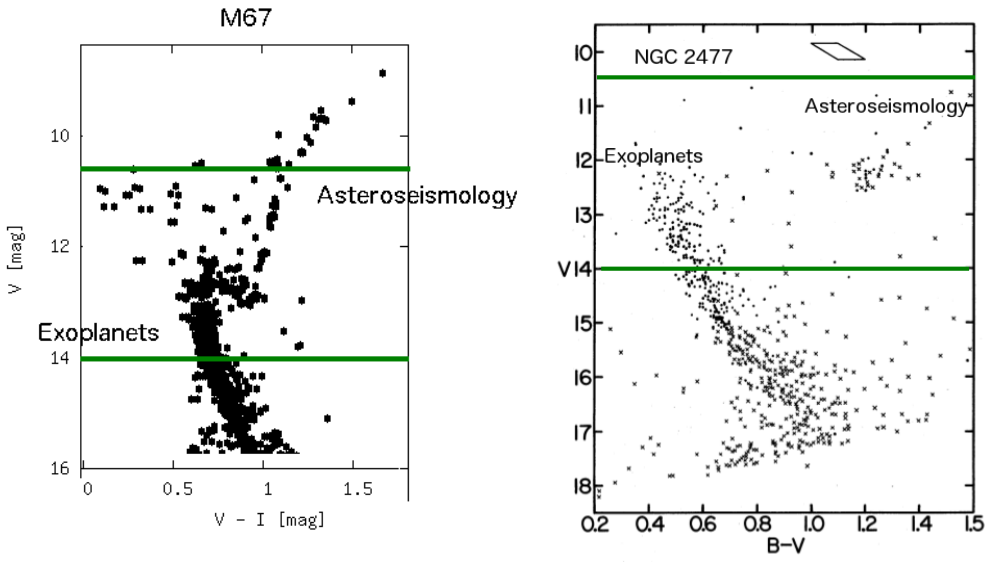

Figure 3.1: Colour-magnitude diagrams of NGC2477 and M67 (Hartwick et al., 1972; Morgan and Eggleton, 1978). Green lines indicate the observed magnitude ranges.

The open clusters M67 and NGC2477 were selected for the January 2014 observations. Their isochronic ages are 4Gyr and 0.7Gyr respectively (Sandage and Eggen, 1969; Magic et al., 2010). The choice was based primarily on their proximity, observability during this period and their relatively high metallicities ($[Fe/H]_{M67} = 0.01 \pm 0.11$ Santos et al. 2009 and $[Fe/H]_{NGC2477} = 0.07 \pm 0.03$ Bragaglia et al. 2008). Each of these clusters has more observable targets than there are HERMES fibres. However, radial velocity measurements on upper main sequence stars are problematic, due to their high temperatures and rotation rates, which lead to fewer and broader visible spectral lines (Santos et al., 2009). Conversely, intermediate mass giants are often cooler and slower and are, hence, better candidates for this type of study. The target sample on each cluster was selected such that each field contains

mostly main sequence stars and a fraction of clump and first-ascent giants. The combination of the intrinsic brightness of the cluster members, the ages of the clusters and their distances, were perfectly suited to observing these types of stars between the magnitudes of V≈10 and 14, for which HERMES can obtain SNR≈100 per resolution element in an hour. Figure 3.1 illustrates how the magnitude limits apply to each colour-magnitude diagram.

Due to the large range of stellar magnitudes in both fields, 2 separate configuration files were prepared for each field. This allowed us to group stars by brightness and decide on exposure times accordingly. The 'long' fields included the fainter stars, with magnitudes V≈12 to ≈14, and the 'short' fields had the brighter stars with magnitudes from V≈10 to ≈12. About 150 stars per field were targeted. Each observation was preceded or followed by standard calibration exposures, as is standard procedure with all HERMES observations. The observations of the 2 clusters were alternated at a sampling rate of one visit every 2 hours over 3 nights. A baseline of 3 nights permits the detection of radial velocity amplitude variations with periods up to 6 days. The second night was unfortunately lost to bad weather.

The primary method for reducing HERMES data is the 2dfdr software[1]. This tool relies on the analysis of exposures from flat and arc lamps to calculate the parameters used to extract science data (see Section 4.1). In the early stages, the version of the software that applies to HERMES was found to have wavelength calibration issues. This seriously impacted the radial velocity precision attainable, as the wavelength scale model calculated by the software carried an uncertainty larger than the expected instrumental limit. It was later discovered that the causes of these issues were the low precision to which the wavelengths of the reference spectral lines were known, in addition to the generalisation of the wavelength solution to fit all fibres in a given field, and the consequent simplification of the wavelength model to accommodate that generalised solution.

The data collected in January 2014 were reduced using this method, and it became evident that this sample alone was not suitable to probe the radial velocity accuracy of HERMES. Two options were presented as a solution: to perform new observations to determine the true radial velocity precision limit attainable or to develop an alternative reduction pipeline. Both options were explored.

3.1.2 Run 2: August 2014

Presented with the need to empirically determine the HERMES instrumental precision limit, we applied for 5 half nights of Director's discretionary time on the AAT. The key technical argument was that the determination of the true limits of the instrument's radial velocity precision could increase the scientific goals achievable. This would apply to both the dataset observed in January 2014 as well as all other HERMES radial velocity studies. The proposal was successful.

The data collected during the month of August 2014 primarily aimed to quantify the HERMES radial velocity limit. In order to maximise the usage of the telescope time granted, these observations were carried out to also potentially allow scientific goals. The main approach to empirically measuring the instrument's radial velocity precision consisted of monitoring bright spectroscopic variables, red giants and a stable star as a reference calibration source. The variable targets were chosen to show radial velocity variations of the magnitude of interest.

The sequence of observations of each night was similar. We started and finished with the outer core of the globular cluster 47 Tucanae. Every night included 1 observation of the stable

[1]https://www.aao.gov.au/science/software/2dfdr

star HD1581 and HD285507, an exoplanet host in the Hyades cluster. ρ Tucanae, a single-lined spectroscopic variable binary system, was observed twice every night, except on the 4th night when weather allowed only a single observation. The field configuration for ρ Tucanae was used to observe HD1581 as an offset field (see Figure 3.2). All observations done during this period kept the same plate, fibre and general configuration parameters for each target, in order to minimise instrumental effects when calculating radial velocity variations. The actual effects of these variations was not quantified at the time of observation and a conservative approach was taken.

Depending on the precision achieved at the end of the analysis, additional science goals could be considered from the data collected from this observing run. The targets were selected in a way that would allow for further scientific investigation, including finding exoplanets in clusters, should higher radial velocity precision levels be achieved. We note that the data from this second run allowed us to quantify the radial velocity precision achievable by HERMES, thereby enabling us to revisit the data collected during the January 2014 observing run for scientific purposes.

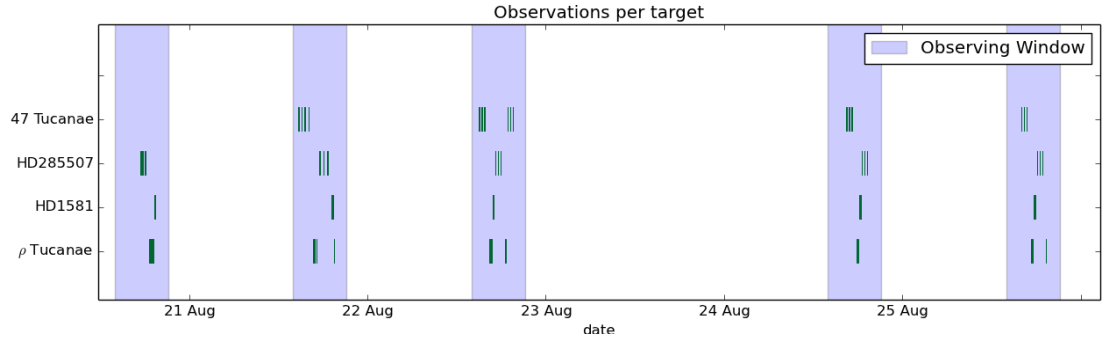

Figure 3.2: The sequence of observations carried out during the August 2014 observing run, as indicated by the green bars. Each bar represents an individual observation.

3.2 Target Selection

The selection of targets for observation during the two telescope runs analysed for this thesis can be organised into several groups. The key factor determining the division of these targets is the differing levels of radial velocity precision required to achieve each scientific goal; i.e., each group is linked to a specific goal and requires a certain level of radial velocity precision. The targets cover a wide range of radial velocity amplitudes, with science goals including the identification of intrinsic oscillations in K–M giants, the follow-up of identified exoplanets, the analysis of globular cluster core dynamics and the potential discovery of binary systems and exoplanets in open clusters. What follows is a description of the different groups considered, with details on the selection criteria and potential scientific goals achievable in each case.

3.2.1 Clusters

The multi-object capability of HERMES makes clusters an ideal choice of target and one prioritised from the beginning of this project. By observing several members of the same

cluster, we can potentially collect a range of radial velocity variability signals, allowing us to determine the instrumental limit.

The approach to selecting stars in the cases of M67 and NGC2477 was similar (see Section 3.1.1). The goal was to maximise the number of cluster members within a given field, giving priority to the giants whose asteroseismological radial velocity oscillations would reach amplitudes detectable by HERMES. Memberships were collected from Geller et al. (2015). A colour cut to the membership list was done based on UCAC4 (Zacharias et al., 2013) magnitudes and the star positions were taken from the same catalogue. Both field centres were decided by the maximum number of giants available in each case.

The Hyades open cluster was observable during August 2014. Its proximity to the Sun has made it a thoroughly studied target with an extensive body of literature. There was a Hot Jupiter planet discovered in the cluster that makes an ideal follow-up target. The approach to determining an ideal field was initially based on the exoplanet host HD285507 (see Section 3.2.2). We tested several possible fields that would include this star and the total amount of additional members found was always low. In addition, no giants could be included in the same field due to their angular separation from the exoplanet host. This was to be expected, as our proximity to this cluster makes its overall angular size, and the consequent angular separation between members, larger than most other clusters.

Being a relatively young cluster (625 ± 50Myr Perryman et al. (1998)), its most evolved stars only reach the bottom of the RGB and there are only a limited number of giants identified, further limiting our chances of combining an exoplanet and a giant in the same field. Based on these facts, an alternative approach to the exoplanet host field was adopted and we concentrated our efforts to create a good field containing a giant. Focusing on the position in the sky of each of the giants, several fields were tested. In all cases only 1 giant star could be included in a given field due to the distance between them. The highest number of members in a field that included a giant was identified, shown in green in Figure 3.3. Despite this approach, the total number of members for the field was under 30. The low number of observable members and the impossibility of observing the exoplanet host and a giant on the same field led to the decision to avoid observations of other cluster member and focus on the exoplanet host (see Section 3.2.2).

The globular cluster 47 Tucanae has been observed by the GALAH survey in several occasions, primarily as a calibrator. The increase in the number density of stars (McLaughlin et al., 2006) with decreasing cluster radius limits the placement of the field if we want to avoid crowding the fibres. Each HERMES fibre maps to 2" on the sky. This limits how close to the core we can observe a star without encountering source confusion. The GALAH survey took this constraint into account when selecting targets near 47 Tuc. We decided to create our fields closer to the core than the limit chosen by the GALAH team, understanding that it would potentially lead to crowding the fibre with more than one source. We expected to overcome this effect by identifying the giants in this part of the cluster that, despite contamination, would outshine other stars due to their larger surface. The targeted stars were chosen from a cone search of the UCAC4 catalogue.

3.2.2 Exoplanets

The confirmation of a previously discovered exoplanet would demonstrate the instrument's capacity to reach the required precision. Even though HERMES is a multiplexed instrument capable of carrying out simultaneous searches for radial velocity variability, it has not been used to search for exoplanets candidates. Furthermore, attempting to rediscover a known

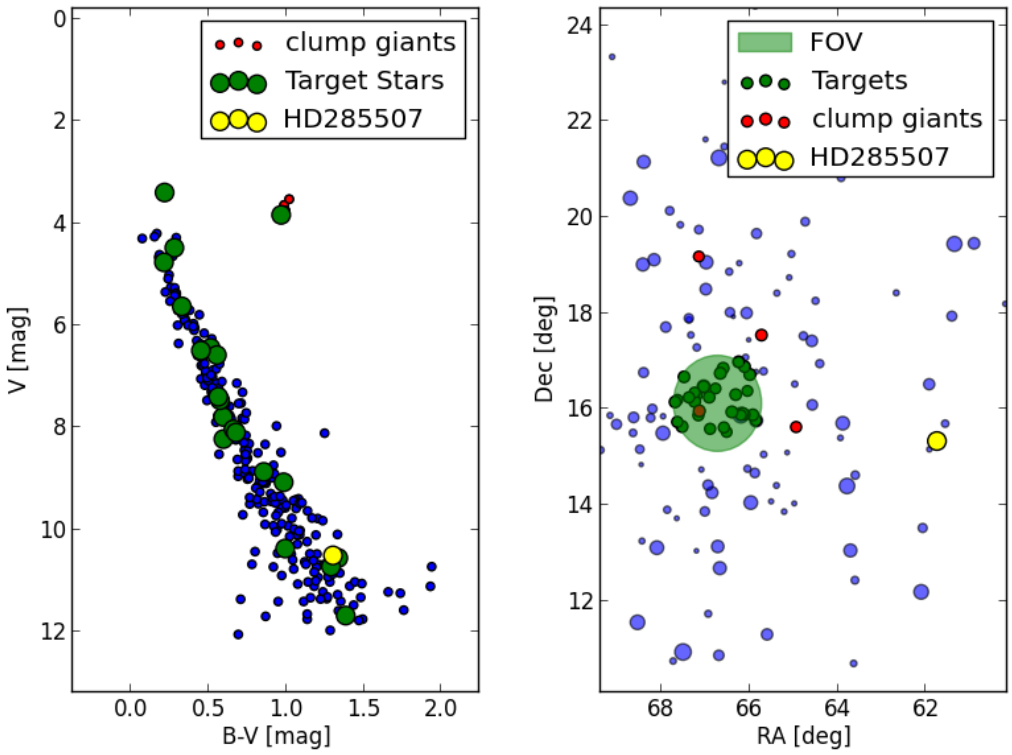

Figure 3.3: Location of the Hyades field planned for observation during the August 2014 observing run. Left: HR diagram. Right: position in the sky. HD285507 is located more than 2 degrees from any known giants.

exoplanet allows us to know in advance the parameters to explore (i.e., period, amplitude and phase) and enables us to fine tune the observations to make the detection.

With this goal in mind we searched the exoplanets.org database[2] for a suitable target based on orbital period, radial velocity amplitude and observability. HD285507 had the right period for the number of observing nights awarded, and the semi-major amplitude was within the potential range achievable by HERMES (see Table 3.1). In addition, HD285507 is a member of the Hyades open cluster. This allowed us to consider including other cluster members in the same field to apply a similar technique as the one originally planned for M67 and NGC2477 (see Section 3.1.1). Unfortunately, as noted in Section 3.2.1, the distance between the exoplanet host and other cluster members, particularly giants, was too large to fit in the same 2 degree field. The final field configuration included the exoplanet host, near the centre, and 72 additional stars. These stars were chosen from the UCAC4 catalogue based on position in the sky. Additional magnitude and J-K colour cuts were applied to select stars in the same brightness range as HD285507 and to try to maximise the number of giants in the sample, in an attempt to identify intrinsic radial velocity variations.

3.2.3 Single-Lined Spectroscopic Binaries

The search for binary stars shares many of the methods applied to exoplanets but the larger masses of the orbiting stellar companions results in a larger range of radial velocity amplitudes.

[2]http://exoplanets.org/

HD285507b	
RA (J2000)	04:07:01.0
Dec (J2000)	+15:20:07
Orbital parameters	
P (days)	6.0881±0.0018
T_c (BJD)	2456263.121±0.029
K ($m\,s^{-1}$)	125.8±2.3
e	0.086±0.019
ω (deg)	182±11
Physical properties	
M_* ($M_\odot$)	0.734±0.034
R_* ($R_\odot$)	0.656±0.054
$T_{eff,*}$ (K)	4503^{+85}_{-61}
log g_* (dex)	$4.670^{+0.051}_{-0.058}$
v sin i (km s^{-1})	3.2±0.5
[Fe/H] (dex)	0.13±0.01
Age (Myr)	0.625±0.050
M_p sin i (M_Jup)	0.917±0.033

Table 3.1: HD285507 Stellar and Planetary Properties(Quinn et al., 2014)

Some binary systems can only be identified by their spectral signature, as they are too close to be separated astrometrically. Their spectrum is then the combination of the spectra of the members, weighted by their relative brightnesses and affected by their relative motions. When one of the members is significantly brighter than the other, only a single spectrum is detectable. This "single-lined" binary spectral signature still carries the relative velocity variations of the brighter member of the star system.

The 9th Catalogue of Spectroscopic Binary Orbits, SB9 (Pourbaix et al., 2004), contains 3994 unique entries. It was the source of data chosen for this search. The selection criteria were based on observability, a period under 5 days and low eccentricity. A constraint of a daily variation in radial velocity between $500\,m\,s^{-1}$ and $10000\,m\,s^{-1}$ was also applied to make sure that the radial velocity variations would fall within the expected ranges. Finally, to simplify the reduction process, no emission lines from the companion should be detectable.

There were 3 candidates within these constraints, shown in Table 3.2 and Figure 3.4. The final choice was HIP 3330 (ρ Tucanae) as we'd be able to capture the largest radial velocity variation during the period of observation in comparison to the others. In order to exploit the multi-object capability of HERMES, another 41 stars where added to the field. These stars were chosen by their location on the sky. A magnitude and colour cut was applied to fit the brightness range close to ρ Tucanae and to maximise the number of potential giants in the sample.

3.2.4 Low RV-variability Stars

The High Accuracy Radial velocity Planet Searcher (HARPS) is a fibre-fed, single-target, high-resolution spectrograph (Pepe et al., 2002). Its stable configuration can measure radial

ID HIP	RA (J2000) hr mm ss	Dec (J2000) Deg mm ss	Spectral Type	Magnitude V	Semi-amplitude (K) km s^{-1}	Period (P) days
3330	00 42 28.373	-65 28 04.91	F6V	5.393	26.10	4.82
11348	02 26 00.349	-15 20 28.49	A3V	5.83	18.42	2.99
10382	02 13 42.226	-03 01 55.3	K1IV	9.27	16.08	2.94

Table 3.2: Single-lined spectroscopic binary candidates from the SB9 catalogue.

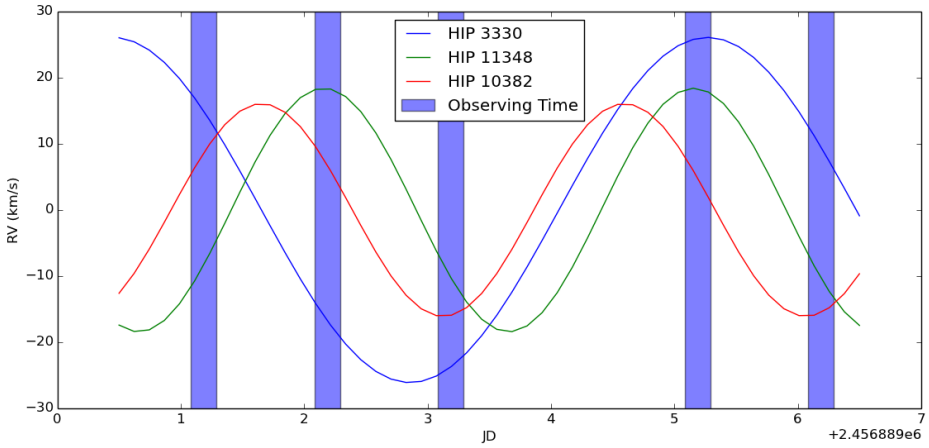

Figure 3.4: Radial velocity variations of the SB9 targets during the observing times allocated in August 2014. The selected target was HIP3330 (ρ Tucanane).

velocity variations to a precision under a metre per second for slowly-rotating stars bright enough to have HD numbers. HD1581 was observed with HARPS in a search for exoplanets. The HARPS observations were performed for over 10 years, collecting 93 data points (Pepe et al., 2011). The search for exoplanets yielded no results in this case and the star showed a scatter $\approx$1.26 m s^{-1}. This makes HD1581 an ideal star to measure instrumental stability as its intrinsic variations are well below the instrumental limit reached by HERMES.

The intrinsic instability of a star due to jitter and granulation that arise from internal stellar activity, combined with its rotation, is the limiting factor to the precision attainable when performing radial velocity measurements. Any radial velocity variations produced by the gravitational effects of a companion that are smaller than the star's intrinsic stability would be rendered undetectable. In this context, the stars with the highest radial velocity stability are slowly rotating K5V stars (Bouchy et al., 2001).

When selecting a host star to search for exoplanets using the radial velocity method, the stellar type is a key constraint if we want to minimise other radial velocity signals. But a selection based on stellar type only would still carry the uncertainties produced by an undetermined rotation velocity and axis inclination ($v \sin(i)$).

In order to build a list of candidate stars, we used the observations of 10 stable stars made over several years with the HARPS spectrograph. There were 5 low mass candidate planets detected by this method in this sample, yet all stars were measured to have less than 2.7 m s^{-1}

Target	Data points	Time span days	RV scatter $m\,s^{-1}$	RA hr mm ss	Dec Deg mm ss
HD 1581	93	2566	1.26	00 20 04	-64 52 29
HD 10700	141	2190	0.92	01 44 04	-15 56 15
HD 20794	187	2610	1.20	03 19 55	-43 04 11
HD 190248	86	2531	1.26	20 08 44	-66 10 55
HD 192310	139	2348	2.62	20 15 17	-27 01 58

Table 3.3: Observed stars by HARPS (Pepe et al., 2011) that were also observable during August 2014.

radial velocity scatter (Pepe et al., 2011). These stars were of particular interest to us, as they are calibrators that show low intrinsic radial velocity scatter. All 5 stars were visible during the August 2014 observing run (see Table 3.3). The final choice was HD1581 due to its particularly low scatter and overall visibility during this period. Being observed as a calibrator star, there was no need to add further stars to the field. This star was observed as an offset field. This means that we used the field configured for the observations of ρ Tucanae, offset to place HD1581 on the corresponding ρ Tucanae-assigned fibre. No other stars were captured in the same exposure.

3.3 GALAH data

The GALAH survey aims to collect spectra of $\approx$1 million stars. This will require approximately 600 nights of telescope time. In practice, GALAH observations are assigned by ATAC. The GALAH large observing program has been granted 75 nights per semester from February 2014 until February 2017. The second phase of GALAH is expected to continue beyond 2017.

The GALAH target selection is simple, the baseline selection being a magnitude-limited sample corresponding to V between 12 and 14, and Galactic latitude $b > 10$ in order to avoid regions of high extinction. The targets are selected from the 2MASS infrared survey (Skrutskie et al., 2006). This forms the main GALAH input catalogue. The input catalogue is divided into 6500 field configurations, each containing over 400 unique stars. The goal of the GALAH observing program is to target at least 3300 different configurations to reach the 1 million star mark.

The GALAH observing strategy is to observe each configuration for 3 consecutive 20 minute exposures. In practice, the total exposure time is dependant on weather conditions such as seeing. An additional 20 minute exposure is taken when the seeing is larger than 2". A further 40 minutes is added if the seeing is larger the 2.5". The nominal SNR for GALAH data is 100 per resolution element.

In the long term, GALAH plans to repeat about 5% of the targets for the purposes of monitoring data quality and determining internal errors in data analysis.

While the repeated observations will also allow variable sources to be identified, it is generally limited to at most one or two epochs. These data alone are insufficient to measure the internal RV variability of HERMES as more data points are needed over a longer baseline. Also, at the moment of writing, GALAH has only taken repeated observations of the clusters M67 and 47 Tucanae. These cluster samples were included in this analysis.

3.4 The final dataset

There were 3 main data sources used for the analysis in this thesis; the observing runs from January and August 2014, and data from the GALAH survey. All the observations have a technical component, aimed at quantifying intrinsic instrumental properties, and a scientific part dependant on the instrumental capabilities. The final dataset consisted of observations of 7 targets: HD1581, HD285507, ρ Tucanae, 47 Tucanae, M67 and NGC2477. Each of these targets plays a role in constraining the RV precision limit of HERMES and thus the subsequent science. What follows is a description of the data observed for each target and their function within the wider research scope of this thesis.

3.4.1 ρ Tucanae - Binary System

The single-lined spectroscopic binary ρ Tucanae has a radial velocity semi-amplitude of 26.1 km s^{-1}. This corresponds to a ≈9 pixel shift in a HERMES spectrum. These observations were aimed to provide a reliable target to test our reduction pipeline. The main target was complemented with 42 other stars selected from a cone search of the UCAC4 catalogue. The returned targets were plotted on a colour-magnitude diagram to identify giant stars. A total of 11 giants were added to the field, as well as 34 dwarfs. There were 24 observations carried out during the observing run of August 2014 spanning a 5.03 day baseline. All observations were based on the same configuration file. The plate and fibre allocations were conserved throughout the observations.

3.4.2 HD285507 - Exoplanet Host

The field prepared to observe HD285507, an exoplanet host in the Hyades open cluster, was originally intended to include other cluster members. The position of the host star, combined with the large spatial extent of the cluster made this impossible. It is for this reason that HD285507 was prepared as a single cluster member observation. Nonetheless, in order to utilise the multi-object capacity of HERMES, an additional 73 stars from the UCAC4 catalogue were added via a cone search. A magnitude and colour cut was applied to accommodate the exposure times constrained by the exoplanet host's brightness and to increase the chances of detecting giants. The target was observed in 3 exposures for every observing session in order to reach a signal-to-noise of 100, totalling 15 exposures over the full period. A total baseline of 5.06 days was reached based on the available observing time. This is an excellent match to the planet's orbital period of 6.09 days. Collecting 5 data points during the ≈5 days allows us, in principle, to characterise the star's radial velocity curve. All observations were carried out with the same field configuration, conserving the fibre allocation and observing plate in order to minimise instrumental effects during the data reduction process.

Obs	Filename	Field Name	Plate	MJD	Day	Exp Time (s)
0	20aug10044.fits	rhoTuc	0	56889.7829	0.0000	300
1	20aug10045.fits	rhoTuc	0	56889.7877	0.0048	360
2	20aug10046.fits	rhoTuc	0	56889.7917	0.0088	120
3	20aug10047.fits	rhoTuc	0	56889.7940	0.0111	120
4	20aug10048.fits	rhoTuc	0	56889.7963	0.0134	120
5	20aug10049.fits	rhoTuc	0	56889.7986	0.0157	120
6	20aug10050.fits	rhoTuc	0	56889.8009	0.0180	120
7	20aug10051.fits	rhoTuc	0	56889.8031	0.0203	120
8	21aug10033.fits	rhoTuc	0	56890.7035	0.9207	600
9	21aug10034.fits	rhoTuc	0	56890.7114	0.9285	600
10	21aug10035.fits	rhoTuc	0	56890.7194	0.9365	600
11	21aug10044.fits	rhoTuc	0	56890.8169	1.0341	360
12	22aug10033.fits	rhoTuc	0	56891.6907	1.9078	360
13	22aug10034.fits	rhoTuc	0	56891.6957	1.9128	360
14	22aug10035.fits	rhoTuc	0	56891.7008	1.9179	360
15	22aug10046.fits	rhoTuc	0	56891.7778	1.9950	360
16	22aug10047.fits	rhoTuc	0	56891.7830	2.0001	360
17	24aug10055.fits	rhoTuc	0	56893.7475	3.9646	360
18	24aug10056.fits	rhoTuc	0	56893.7535	3.9706	360
19	24aug10057.fits	rhoTuc	0	56893.7586	3.9757	360
20	25aug10040.fits	rhoTuc	0	56894.7253	4.9424	360
21	25aug10041.fits	rhoTuc	0	56894.7304	4.9475	360
22	25aug10042.fits	rhoTuc	0	56894.7354	4.9526	360
23	25aug10052.fits	rhoTuc	0	56894.8107	5.0278	360

Table 3.4: All observations carried out for the single-lined binary star ρ Tucanae. The same field plate and fibres were used for each observation. Horizontal lines separate epochs.

Obs	Filename	Field Name	Plate	MJD	Day	Exp Time (s)
0	20aug10039.fits	HD285507	1	56889.7347	0.0000	600
1	20aug10040.fits	HD285507	1	56889.7479	0.0132	1200
2	20aug10041.fits	HD285507	1	56889.7628	0.0281	1200
3	21aug10038.fits	HD285507	1	56890.7449	1.0102	1800
4	21aug10039.fits	HD285507	1	56890.7666	1.0319	1800
5	21aug10040.fits	HD285507	1	56890.7883	1.0536	1800
6	22aug10041.fits	HD285507	1	56891.7283	1.9936	1200
7	22aug10042.fits	HD285507	1	56891.7431	2.0084	1200
8	22aug10043.fits	HD285507	1	56891.7579	2.0232	1200
9	24aug10063.fits	HD285507	1	56893.7812	4.0465	1200
10	24aug10064.fits	HD285507	1	56893.7959	4.0612	1200
11	24aug10065.fits	HD285507	1	56893.8076	4.0729	600
12	25aug10049.fits	HD285507	1	56894.7654	5.0307	1200
13	25aug10050.fits	HD285507	1	56894.7802	5.0455	1200
14	25aug10051.fits	HD285507	1	56894.7950	5.0603	1200

Table 3.5: All observations of the exoplanet host star HD285507. The field and fibre allocation were conserved for the entire period. Horizontal lines separate epochs.

3.4.3 HD1581 - Stable Star

HD1581, an F9.5V star (Pepe et al., 2011), was observed with HERMES as an offset field. This means that the physical position of the fibres on the fibre plate corresponds to a different part of the sky. Keeping that configuration and moving the telescope to aim a single fibre at the selected star allows us to quickly observe a new target without the delays of reconfiguring the field. The negative consequence of this approach is that only 1 star can be observed at a time, as no other star in the field is likely to match the positions of the other fibres. Over the period of 4.94 days, 15 observations were made with this method (see Table 3.6).

All observations were offsets of the same field, rhoTuc.fld, using the same plate and hence HD1581 was always observed with the same fibre. This is a key aspect of the observations, as it minimises instrumental effects that could impact radial velocity measurements due to changes in the fibre throughput or fibre position on the plate.

Obs	Filename	Field Name	Plate	MJD	Day	Exp Time (s)
0	20aug10053.fits	HD1581	0	56889.8107	0.0000	120
1	21aug10041.fits	HD1581	0	56890.8042	0.9935	120
2	21aug10042.fits	HD1581	0	56890.8065	0.9958	120
3	21aug10043.fits	HD1581	0	56890.8088	0.9981	120
4	22aug10036.fits	HD1581	0	56891.7066	1.8959	120
5	22aug10037.fits	HD1581	0	56891.7089	1.8981	120
6	22aug10038.fits	HD1581	0	56891.7112	1.9004	120
7	24aug10058.fits	HD1581	0	56893.7647	3.9539	120
8	24aug10059.fits	HD1581	0	56893.7667	3.9560	80
9	24aug10060.fits	HD1581	0	56893.7682	3.9575	30
10	24aug10061.fits	HD1581	0	56893.7695	3.9587	30
11	24aug10062.fits	HD1581	0	56893.7711	3.9604	30
12	25aug10044.fits	HD1581	0	56894.7427	4.9320	60
13	25aug10045.fits	HD1581	0	56894.7447	4.9340	60
14	25aug10046.fits	HD1581	0	56894.7463	4.9355	60

Table 3.6: All observations of the stable star HD1581. The field configuration was conserved for the entire period. Horizontal lines separate epochs.

3.4.4 47 Tucanae - Globular Cluster

The field arrangement chosen for 47 Tucanae was a doughnut-shaped region around the centre of the cluster. The outer limit of the chosen shape was determined by the region of the cluster where the star density is lower than 2”, effectively aiming at crowding the assigned fibres. The field included 72 stars that set the inner limit of the field. There were 16 observations made of this field over 4.08 days (see Table 3.5). The plate and fibre allocation were conserved over the full data set.

Obs	Filename	Field Name	Plate	MJD	Day	Exp Time (s)
0	21aug10027.fits	47Tuc center	1	56890.6244	0.0000	1200
1	21aug10028.fits	47Tuc center	1	56890.6409	0.0165	1200
2	21aug10029.fits	47Tuc center	1	56890.6570	0.0327	1200
3	21aug10030.fits	47Tuc center	1	56890.6786	0.0542	1200
4	22aug10027.fits	47Tuc center	1	56891.6371	1.0127	1200
5	22aug10028.fits	47Tuc center	1	56891.6518	1.0274	1200
6	22aug10029.fits	47Tuc center	1	56891.6666	1.0422	1200
7	22aug10048.fits	47Tuc center	1	56891.7948	1.1704	1200
8	22aug10049.fits	47Tuc center	1	56891.8096	1.1852	1200
9	22aug10050.fits	47Tuc center	1	56891.8210	1.1966	609
10	24aug10050.fits	47Tuc center	1	56893.6955	3.0711	1200
11	24aug10051.fits	47Tuc center	1	56893.7111	3.0867	1200
12	24aug10052.fits	47Tuc center	1	56893.7267	3.1023	1200
13	25aug10035.fits	47Tuc center	1	56894.6772	4.0528	1200
14	25aug10036.fits	47Tuc center	1	56894.6920	4.0676	1200
15	25aug10037.fits	47Tuc center	1	56894.7069	4.0825	1200

Figure 3.5: All observations made of the globular cluster 47 Tucanae. The field and fibre allocation were conserved for the entire period. Horizontal lines separate epochs.

3.4.5 NGC2477 - Open Cluster

The open cluster NGC2477 was observed during the January 2014 observing run. There were a total of 33 observations over 2.3 days. Targets were organised in 2 different field configurations according to their magnitude (see Table 3.8). The long field grouped magnitudes 12 to 14.5 and the short field grouped magnitudes 9.8 to 12. The same fibres and plates were used during all observations. Targets were selected from the UCAC4 catalogue by applying a colour cut to identify cluster members.

Obs	Filename	Field Name	Plate	MJD	Day	Exp Time (s)
0	07jan10028.fits	NGC2477 Short Field	1	56664.4295	0.0000	600
1	07jan10029.fits	NGC2477 Short Field	1	56664.4374	0.0079	600
2	07jan10030.fits	NGC2477 Short Field	1	56664.4456	0.0161	600
3	07jan10033.fits	NGC2477 Long Field	0	56664.4590	0.0295	600
4	07jan10034.fits	NGC2477 Long Field	0	56664.4671	0.0376	600
5	07jan10035.fits	NGC2477 Long Field	0	56664.4752	0.0456	600
6	07jan10036.fits	NGC2477 Long Field	0	56664.4900	0.0605	1800
7	07jan10039.fits	NGC2477 Short Field	1	56664.5107	0.0811	600
8	07jan10040.fits	NGC2477 Short Field	1	56664.5186	0.0890	600
9	07jan10041.fits	NGC2477 Short Field	1	56664.5264	0.0969	600
10	07jan10042.fits	NGC2477 Short Field	1	56664.5343	0.1047	600
11	07jan10043.fits	NGC2477 Short Field	1	56664.5421	0.1126	600

Obs	Filename	Field Name	Plate	MJD	Day	Exp Time (s)
12	07jan10044.fits	NGC2477 Short Field	1	56664.5502	0.1206	600
13	07jan10045.fits	NGC2477 Short Field	1	56664.5582	0.1286	600
14	07jan10046.fits	NGC2477 Short Field	1	56664.5660	0.1365	600
15	08jan10020.fits	NGC2477 Short Field	1	56665.5877	1.1581	600
16	08jan10021.fits	NGC2477 Short Field	1	56665.5955	1.1660	600
17	09jan10011.fits	NGC2477 Short Field	1	56666.4609	2.0314	600
18	09jan10012.fits	NGC2477 Short Field	1	56666.4688	2.0392	600
19	09jan10013.fits	NGC2477 Short Field	1	56666.4766	2.0471	600
20	09jan10016.fits	NGC2477 Long Field	0	56666.4890	2.0595	600
21	09jan10017.fits	NGC2477 Long Field	0	56666.4973	2.0677	600
22	09jan10018.fits	NGC2477 Long Field	0	56666.5051	2.0756	600
23	09jan10021.fits	NGC2477 Short Field	1	56666.5178	2.0882	600
24	09jan10022.fits	NGC2477 Short Field	1	56666.5256	2.0961	600
25	09jan10023.fits	NGC2477 Short Field	1	56666.5334	2.1039	600
26	09jan10039.fits	NGC2477 Short Field	1	56666.6407	2.2112	600
27	09jan10040.fits	NGC2477 Short Field	1	56666.6486	2.2191	600
28	09jan10041.fits	NGC2477 Short Field	1	56666.6566	2.2270	600
29	09jan10042.fits	NGC2477 Short Field	1	56666.6644	2.2349	600
30	09jan10053.fits	NGC2477 Long Field	0	56666.7231	2.2936	1000
31	09jan10056.fits	NGC2477 Short Field	1	56666.7411	2.3116	600
32	09jan10057.fits	NGC2477 Short Field	1	56666.7489	2.3194	600
33	09jan10058.fits	NGC2477 Short Field	1	56666.7562	2.3267	421

Table 3.8: All observations of the open cluster NGC2477. There were 2 fields created for this target. Each star belonged to a single field and a single fibre. Horizontal lines separate epochs.

3.4.6 M67 - Open Cluster

M67 has been targeted in several observations, both during the GALAH survey and in the observing run of January 2014. In each of these observations, several fields were used to account for the range of brightness in the targeted cluster members (see Figures 3.7 and 3.6). This led to a different approach to the radial velocity curves calculation as the fibres and plates weren't consistent over the full set of observations.

There were 292 stars observed in total over 99 observations, using the HERMES spectrograph in low and high resolution. The observations were carried out using 4 different fields and spanned a 56 day baseline (see Table 3.9. In addition to the difficulties presented due to the range of configurations, Observations 28, 29 and 30 have a failed arc and did not reduce, observations 43 to 48 were saturated and unusable and observations 49 to 73 were done in high resolution, with uncertain effects on how that observing mode would affect the data calibration. These were the only fields observed with HERMES in high resolution mode to date.

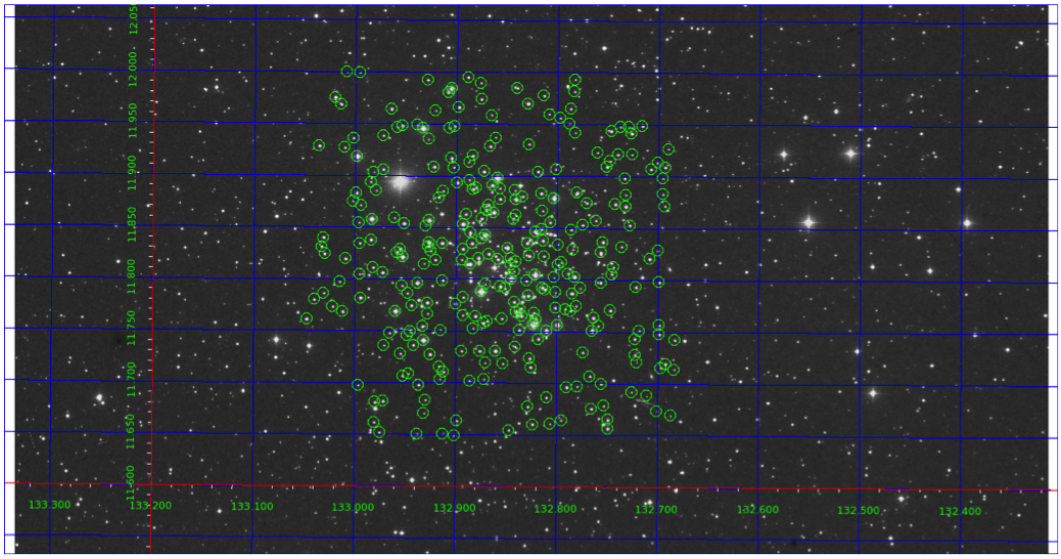

Figure 3.6: Overlay of the observed M67 targets plotted over a SDSS image.

Obs	Filename	Field Name	Plate	MJD	Day	Exp Time (s)
0	17dec10039.fits	M67 12V14	0	56643.6659	0.0000	1200
1	17dec10040.fits	M67 Bright Stars	0	56643.6809	0.0150	1200
2	17dec10041.fits	M67 Bright Stars	0	56643.6957	0.0298	1200
3	17dec10044.fits	M67 Bright Stars	1	56643.7126	0.0467	600
4	17dec10045.fits	M67 Bright Stars	1	56643.7205	0.0545	600
5	17dec10046.fits	M67 Bright Stars	1	56643.7283	0.0624	600
6	18dec10030.fits	M67 Bright Stars	1	56644.6813	1.0154	1200
7	18dec10031.fits	M67 Bright Stars	1	56644.6961	1.0302	1200
8	18dec10032.fits	M67 Bright Stars	1	56644.7109	1.0450	1200
9	18dec10033.fits	M67 Bright Stars	1	56644.7257	1.0597	1200
10	07jan10049.fits	M67 Long Field	0	56664.5809	20.9150	600
11	07jan10050.fits	M67 Long Field	0	56664.5890	20.9231	600
12	07jan10051.fits	M67 Long Field	0	56664.5974	20.9315	600
13	07jan10054.fits	M67 Short Field	1	56664.6103	20.9444	600
14	07jan10055.fits	M67 Short Field	1	56664.6182	20.9523	600
15	07jan10056.fits	M67 Short Field	1	56664.6261	20.9602	600
16	07jan10059.fits	M67 Long Field	0	56664.6388	20.9729	600
17	07jan10060.fits	M67 Long Field	0	56664.6582	20.9923	600
18	07jan10061.fits	M67 Long Field	0	56664.6662	21.0002	600
19	07jan10064.fits	M67 Short Field	1	56664.7310	21.0651	1200
20	09jan10026.fits	M67 Long Field	0	56666.5460	22.8800	600
21	09jan10027.fits	M67 Long Field	0	56666.5539	22.8880	600
22	09jan10030.fits	M67 Short Field	1	56666.5669	22.9009	600
23	09jan10031.fits	M67 Short Field	1	56666.5747	22.9088	600
24	09jan10032.fits	M67 Short Field	1	56666.6029	22.9370	600
25	09jan10033.fits	M67 Short Field	1	56666.6108	22.9449	600
26	09jan10036.fits	M67 Long Field	0	56666.6252	22.9593	950

Obs	Filename	Field Name	Plate	MJD	Day	Exp Time (s)
27	09jan10045.fits	M67 Long Field	0	56666.6786	23.0127	840
28	09jan10048.fits	M67 Short Field	1	56666.6925	23.0266	600
29	09jan10049.fits	M67 Short Field	1	56666.7003	23.0344	600
30	09jan10050.fits	M67 Short Field	1	56666.7082	23.0422	600
31	11jan10028.fits	M67 Bright Stars	1	56668.5921	24.9262	1200
32	11jan10029.fits	M67 Bright Stars	1	56668.6069	24.9410	1200
33	11jan10030.fits	M67 Bright Stars	1	56668.6217	24.9558	1200
34	11jan10033.fits	M67 Bright Stars	1	56668.6413	24.9754	1200
35	11jan10034.fits	M67 Bright Stars	1	56668.6561	24.9902	1200
36	11jan10035.fits	M67 Bright Stars	1	56668.6709	25.0050	1200
37	11jan10038.fits	M67 Bright Stars	1	56668.6900	25.0241	1200
38	11jan10039.fits	M67 Bright Stars	1	56668.7048	25.0389	1200
39	11jan10040.fits	M67 Bright Stars	1	56668.7200	25.0541	1200
40	12jan10030.fits	M67 Bright Stars	1	56669.7056	26.0397	1200
41	12jan10031.fits	M67 Bright Stars	1	56669.7204	26.0545	1200
42	12jan10032.fits	M67 Bright Stars	1	56669.7352	26.0693	1200
43	13jan10039.fits	M67 Bright Stars	0	56670.6155	26.9496	1200
44	13jan10040.fits	M67 Bright Stars	0	56670.6303	26.9644	1200
45	13jan10041.fits	M67 Bright Stars	0	56670.6451	26.9792	1200
46	13jan10042.fits	M67 Bright Stars	0	56670.6599	26.9940	1200
47	13jan10043.fits	M67 Bright Stars	0	56670.6747	27.0087	1200
48	13jan10044.fits	M67 Bright Stars	0	56670.6896	27.0237	1200
49	07feb10022.fits	M67 Bright Stars	0	56695.5298	51.8639	1200
50	07feb10023.fits	M67 Bright Stars	0	56695.5446	51.8787	1200
51	07feb10024.fits	M67 Bright Stars	0	56695.5594	51.8935	1200
52	07feb10027.fits	M67 Bright Stars	1	56695.5808	51.9148	1200
53	07feb10028.fits	M67 Bright Stars	1	56695.5955	51.9296	1200
54	07feb10029.fits	M67 Bright Stars	1	56695.6103	51.9444	1200
55	07feb10030.fits	M67 Bright Stars	1	56695.6251	51.9592	1200
56	07feb10031.fits	M67 Bright Stars	1	56695.6399	51.9740	1200
57	07feb10032.fits	M67 Bright Stars	1	56695.6547	51.9888	1200
58	08feb10027.fits	M67 Bright Stars	0	56696.5525	52.8866	1200
59	08feb10028.fits	M67 Bright Stars	0	56696.5672	52.9013	1200
60	08feb10029.fits	M67 Bright Stars	0	56696.5820	52.9161	1200
61	08feb10032.fits	M67 Bright Stars	1	56696.6040	52.9381	1200
62	08feb10033.fits	M67 Bright Stars	1	56696.6187	52.9528	1200
63	08feb10034.fits	M67 Bright Stars	1	56696.6336	52.9676	1200
64	08feb10035.fits	M67 Bright Stars	1	56696.6483	52.9824	1200
65	08feb10036.fits	M67 Bright Stars	1	56696.6631	52.9972	1200
66	08feb10037.fits	M67 Bright Stars	1	56696.6779	53.0120	1200
67	08feb10040.fits	M67 Bright Stars	0	56696.7023	53.0364	450
68	08feb10041.fits	M67 Bright Stars	0	56696.7120	53.0461	750
69	08feb10042.fits	M67 Bright Stars	0	56696.7221	53.0562	750
70	08feb10043.fits	M67 Bright Stars	0	56696.7317	53.0658	750
71	08feb10046.fits	M67 Bright Stars	0	56696.7477	53.0818	750

Obs	Filename	Field Name	Plate	MJD	Day	Exp Time (s)
72	08feb10047.fits	M67 Bright Stars	0	56696.7497	53.0838	750
73	08feb10048.fits	M67 Bright Stars	0	56696.7506	53.0847	750
74	09feb10029.fits	M67 Bright Stars	1	56697.5496	53.8836	1200
75	09feb10030.fits	M67 Bright Stars	1	56697.5672	53.9013	1200
76	09feb10031.fits	M67 Bright Stars	1	56697.5820	53.9161	1200
77	09feb10034.fits	M67 Bright Stars	0	56697.6106	53.9447	600
78	09feb10035.fits	M67 Bright Stars	0	56697.6185	53.9525	600
79	09feb10036.fits	M67 Bright Stars	0	56697.6263	53.9604	600
80	10feb10027.fits	M67 Bright Stars	0	56698.5445	54.8786	1200
81	10feb10028.fits	M67 Bright Stars	0	56698.5593	54.8934	1200
82	10feb10029.fits	M67 Bright Stars	0	56698.5741	54.9082	1200
83	10feb10030.fits	M67 Bright Stars	0	56698.5889	54.9229	1200
84	10feb10031.fits	M67 Bright Stars	0	56698.6036	54.9377	1200
85	10feb10032.fits	M67 Bright Stars	0	56698.6184	54.9525	1200
86	10feb10033.fits	M67 Bright Stars	0	56698.6332	54.9673	1200
87	11feb10013.fits	M67 Bright Stars	0	56699.4932	55.8273	1200
88	11feb10014.fits	M67 Bright Stars	0	56699.5080	55.8421	1200
89	11feb10015.fits	M67 Bright Stars	0	56699.5228	55.8569	1200
90	11feb10016.fits	M67 Bright Stars	0	56699.5375	55.8716	1200
91	11feb10017.fits	M67 Bright Stars	0	56699.5523	55.8864	1200
92	11feb10018.fits	M67 Bright Stars	0	56699.5671	55.9012	1200
93	11feb10021.fits	M67 Bright Stars	1	56699.5905	55.9246	1200
94	11feb10022.fits	M67 Bright Stars	1	56699.6053	55.9394	1200
95	11feb10023.fits	M67 Bright Stars	1	56699.6201	55.9541	1200
96	11feb10024.fits	M67 Bright Stars	1	56699.6348	55.9689	1200
97	11feb10025.fits	M67 Bright Stars	1	56699.6532	55.9873	1200
98	11feb10026.fits	M67 Bright Stars	1	56699.6680	56.0020	1200

Table 3.9: All observations of the open cluster M67, representing a combination of GALAH survey observations and the January 2014 observing run. Fields, plates and fibres were not conserved across the observations; only a limited number of stars were observed in a consistent configuration. Horizontal lines separate epochs.

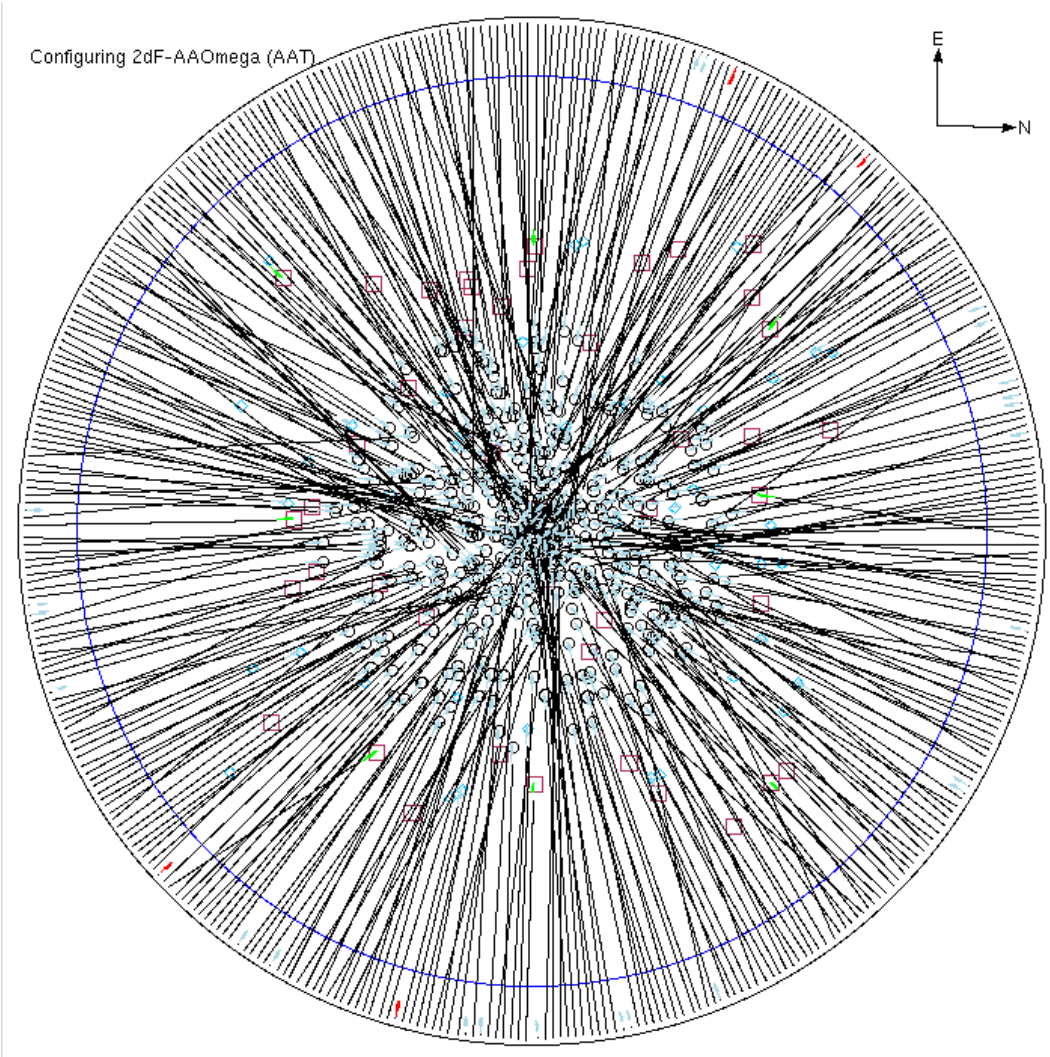

Figure 3.7: One of the M67 fields observed, showing the 2dF fibre allocation and placement as optimised by the *c*onfigure software.

4
Data Reduction

In order to analyse astronomical measurements, instrumental effects need to be removed from the data produced by the telescope. This is accomplished through the data reduction process. There are different ways to achieve this goal but, a common set of steps is typically followed. With the purpose of illustrating this process, a general data reduction flow chart is presented in Figure 4.1.

After standard CCD cosmetic processing with BIAS and DARK frames (to eliminate counts and any spatial patterns due to the bias level and dark current), the data reduction process makes use of 3 main types of input files: FLAT, ARC and SCIENCE. The FLAT is obtained from a quartz lamp that has a smooth spectral illumination with respect to wavelength. An ARC, in contrast, is obtained from an emission-line source that has well defined spectral peaks and can be used as a wavelength calibrator. Finally, a SCIENCE frame is one containing the actual scientific observation.

The basic reduction process starts with the FLAT image used to determine the traces produced by the fibres on the CCD, also known as "tramlines". These are used to extract the flux from the ARC and SCIENCE data. Using the extracted ARC as a reference, and comparing it with known wavelength values of the observed emission lines, a wavelength solution is constructed. This allows us to link wavelengths to extracted 1D pixels, effectively creating a wavelength calibration. The extracted SCIENCE data can now be assigned wavelength values, producing a calibrated SCIENCE frame.

In this chapter, we explore the data reduction software that was available before this thesis and demonstrate the need for an alternative solution. We present HARPY, a new approach to data reduction and radial velocity calculations developed for this thesis that significantly outperforms the precision achievable by the existing software. Specifically, we describe the algorithms that take a set of raw images and reduce them into wavelength-calibrated spectra. We analyse the theory behind radial velocity calculations and explore the steps that convert calibrated spectra into radial velocity measurements via an additional set of algorithms, also developed for this thesis.

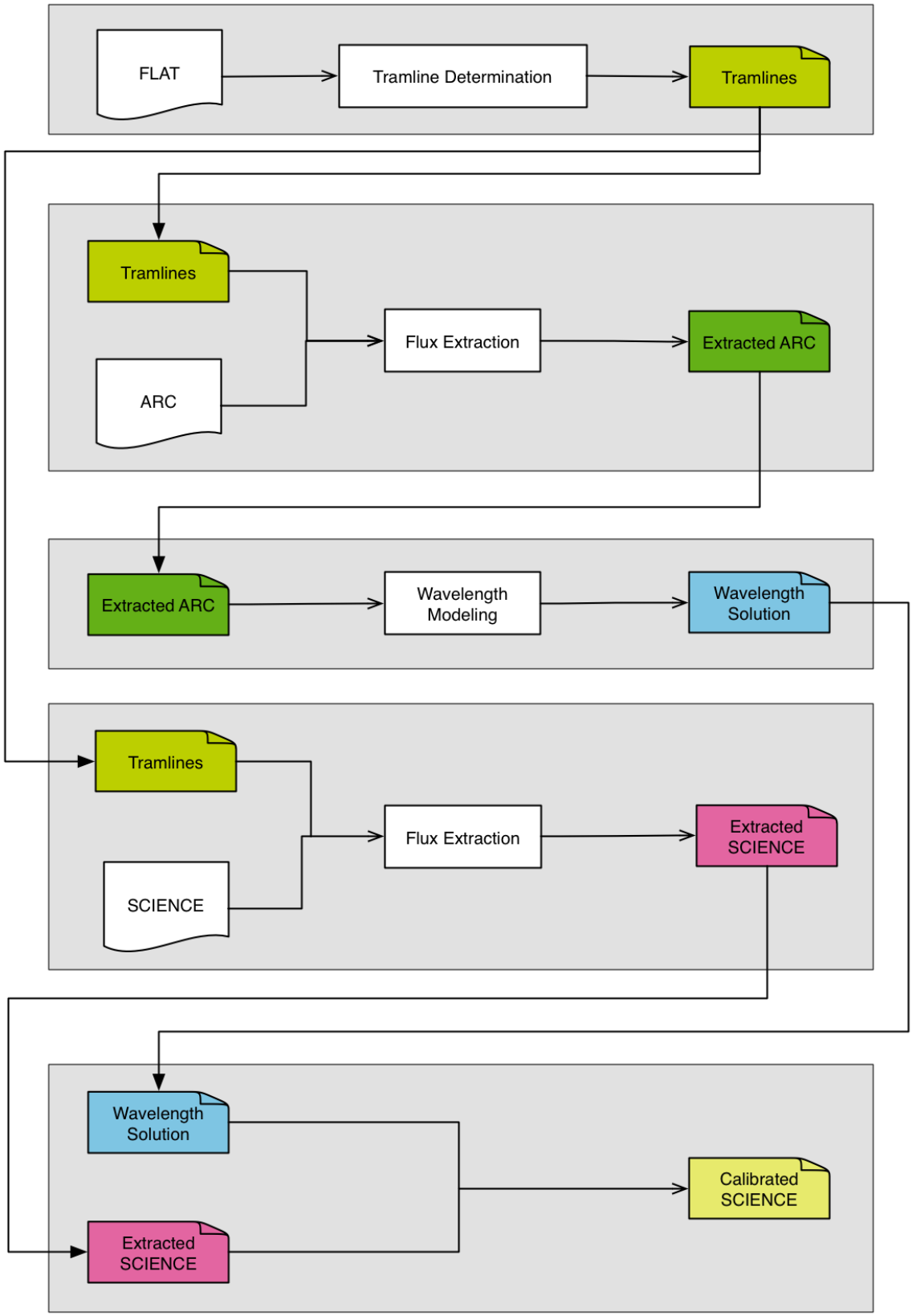

Figure 4.1: Basic data reduction structure. Individual pipelines apply several decisions across this structure. This chart aims to familiarise the reader with the core reduction steps for astronomical spectroscopic data.

4.1 2dfdr

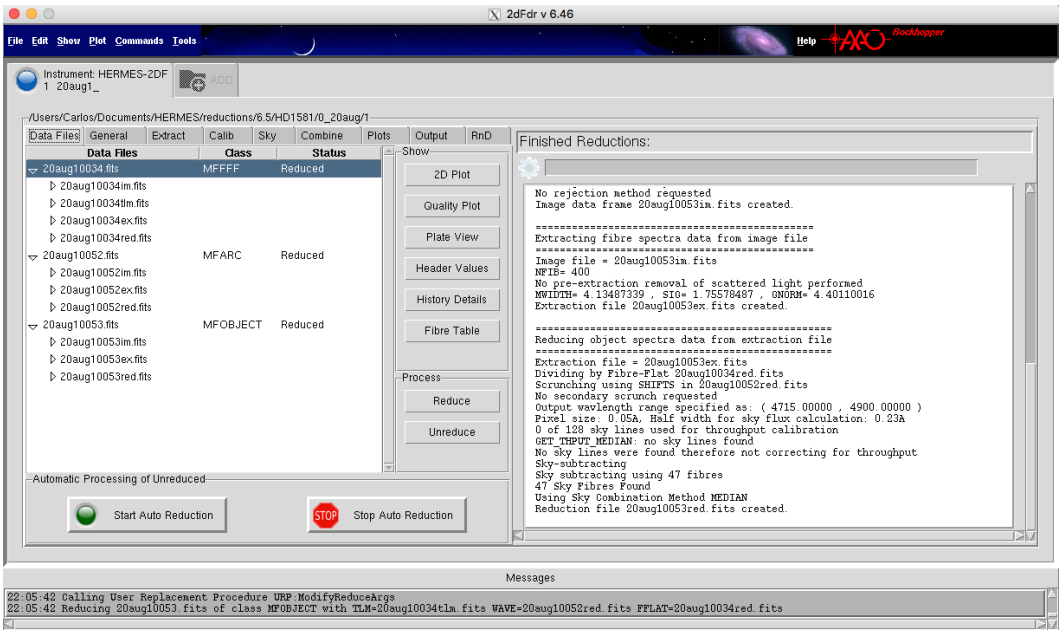

Figure 4.2: The 2dfdr graphical user interface. All functionality of the package can be controlled from this centralised module.

The AAO provides software to reduce the data produced by its instruments. Two Degree Field Data Reduction (2dfdr) is the data reduction package dedicated to reducing multi-fibre spectroscopic data (see Figure 4.2). It has been in development for over 10 years and has several versions supporting a number of the instruments available at the AAT, including a version for HERMES. It is also widely used for the reduction of AAOmega, Sydney-Australian-Astronomical-Observatory Multi-object Integral-Field Spectrograph (SAMI) and Kilofibre Optical AAT Lenslet Array (KOALA) data. 2dfdr was adapted to support HERMES when the instrument was commissioned.

The beginning of this thesis coincided with the development of the HERMES version of 2dfdr. We tested its suitability to reduce HERMES data, and the extensive use that we made of it allowed us to provide extensive feedback towards improving new 2dfdr versions. We started working with 2dfdr version 5.2, and continued our participation until version 6.5, which is the version referenced in this thesis and the one used to produce the results presented here.

4.1.1 File Management

All files used by 2dfdr conform to the Flexible image Transport System (FITS) data format. This standard applies to the input, intermediate and output files (see Table 4.1). Each file contains one or more Header Display Unit (HDU), composed of a header and a data section. The header is organised as a table with 3 columns: keyword, value and comments. 2dfdr uses this structure to store information related to the reduction, in addition to keeping the original information generated during the observations.

The processed files contain several HDU extensions, added by the reduction process. The primary HDU is a 2-dimensional array holding the original CCD Image (FITS), or extracted

File Type	Description
im files	These files are the first step in the reduction process, where the bad pixels are marked and the overscan region removed.
ex files	These files contain the extracted intensity information. The array included in the primary HDU has 400 rows with 4096 pixels, with each row representing a distinct spectrum.
red files	These files contain the extracted and wavelength calibrated data.
tlm files	These files hold the tramline map.
combined files	These files are the combination of multiple reduced files.
combined BIAS files	These files are a combination of multiple BIAS files.

Table 4.1: Intermediate and output file types created by 2drdf.

spectral data organised in 400 rows of 4096 pixels each. The secondary extension is a binary table containing detailed information about the targets (see Table 4.2).

4.1.2 Reduction Process

2dfdr follows the standard data reduction procedure presented in Figure 4.1. What follows is a description of the internal steps taken by the main processes of the reduction. We place a special focus on the sections that affect the final wavelength calibration, which is key for precision radial velocity measurements.

Tramline Determination

A Tank Tracking Algorithm (Reid, 1979) is used to find a list of fibre traces traversing approximately across the spectral direction (see Section 4.1.3). These coordinates are fitted with quadratics to define full paths across the image (see Figure 4.3). A secondary fit is then applied to the initially calculated quadratic paths, using the nearest peak points in order to derive a smooth path. In this step, an initial FWHM of the PSF is determined. The traces are matched to the fibres by using the gaps produced by the missing traces (due to guide and known missing fibres) as anchors.

ARC and SCIENCE Flux Extraction

Using the tramlines, the flux from each fibre is extracted and an initial estimation of the wavelength corresponding to each pixel is added to the file. This estimate is based on the optical model of the spectrograph and is only temporary. The background scattered light is

Name	Type	Description
NAME	String	Object name from the configure .fld file
RA	Real	Right Ascension from the configure .fld file
DEC	Real	Declination from the configure .fld file
X	Integer	2dF field plate X co-ordinate (in microns)
Y	Integer	2dF field plate Y co-ordinate (in microns)
XERR	Integer	Reported error in X in final fibre placement
YERR	Integer	Reported error in Y in final fibre placement
THETA	Real	Angle of fibre on field plate
TYPE	Character	Fibre type: F-guide, N-broken, P-program, S-Sky, U-Unused
PIVOT	Integer	2dF fibre pivot number
MAGNITUDE	Real	Object magnitude from the configure .fld file
PID	Integer	Program ID from the configure .fld file
COMMENT	String	Comment from the configure .fld file
RETRACTOR	Integer	2dF retractor number
WLEN	Real	Wavelength from the configure .fld file
EXPOSURE	Integer	The exposure time in seconds for the fibre

Table 4.2: 2dfdr target table definition, included as a binary table in the secondary HDU extension.

modelled via a linear fit across the "dead" (guide and known missing) fibres and subtracted from the image if requested.

Wavelength Modelling

For each extracted arc fibre, the pixel positions of the peaks of the measured emission lines are recorded. This forms a sequential data set used by the Tank Tracking algorithm (see Section 4.1.3). This algorithm aims to find a list of tracks along the spatial direction of the CCD. By effectively comparing the changes in emission peaks between fibres, the persistent emission lines are used to calculate the relative shifts across fibres (in the spatial direction) with respect to the central fibre , where distortions are expected to be at a minimum. These transformations are recorded via several quadratic functions that parametrise the shift and distortions across the CCD. This is then used to collapse all arc spectra into a single array of high SNR creating a master spectrum.

Using the temporary estimate of the wavelength solution and the peaks of the master spectrum, and comparing them to the known wavelengths of the emission lines from the arc lamp, a polynomial is calculated. This is achieved in several steps. Using the master spectrum produced in the previous step, a Whale Shark algorithm (see Section 4.1.3) is used to match the emission features with an artificially constructed spectrum generated from the known line list. This step produces a polynomial that characterises the spectral correction necessary to label the detected emission lines. This is representative of the central (reference) fibre. The solution found is then transformed using the shift and distortion polynomials calculated on the previous step to create a wavelength solution for each fibre. This approach imposes a simplified description of the wavelength solution to all fibres, affecting the precision of the results.

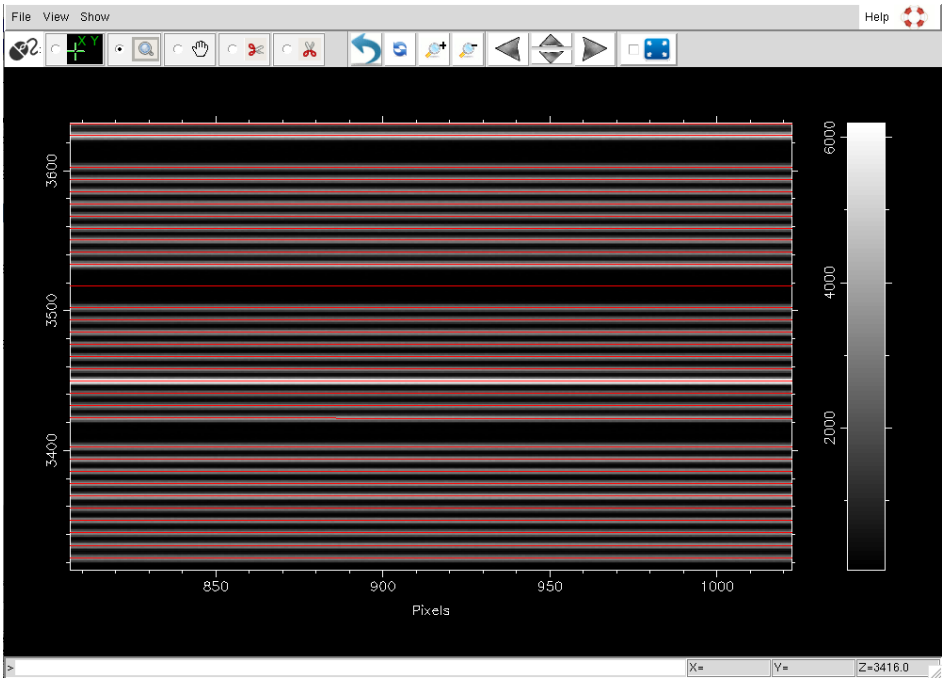

Figure 4.3: Tramline identification in 2dfdr shown in red. The quartz flat exposure is used to identify the traces of the fibres across the CCD and can be seen behind the traces.

Calibrating ARC and SCIENCE

Having the tramlines, and the wavelength solution for each fibre, the last step in extracting the data is to re-sample the spectra onto a linear wavelength scale that is the same for all fibres. This is a necessary step for the approach taken in 2dfdr, but unavoidably affects the precision of the wavelength solution. The SCIENCE calibration adds a step in which the flux is corrected for the relative fibre throughputs and has sky contamination removed.

4.1.3 Algorithms

Across the reduction pipeline there are several key algorithms that are used in several parts of the process. What follows is a description of the most frequently used ones.

Combination of Science Exposures

Observations of the same targets can be performed in several exposures, ensuring the right flux levels for the instrument's sensitivity, while allowing for an increase in SNR. 2dfdr can combine these observations, while accounting for the different levels of flux between targets and exposures. This is primarily achieved using 3 steps:

Initially, the median of each pixel for all the frames is taken to eliminate cosmic rays. If there are only 2 exposures, the minimum value is taken. Cosmic rays are flagged by sigma clipping. Statistics show that 1-2% of pixels per hour are removed. Pixels surrounding these areas are also marked to avoid unwanted spills of excess electrons. The removed values are replaced by the mean of the remaining pixel values weighted by the inverse variance, effectively covering the gap created by the removed pixels.

Flux weighting is an option that can be applied to individual spectra or to the entire frame at once. It is used to account for the relative brightness of the targets and exposure times. The sum of heavily smoothed versions of the spectra is compared to the nominal magnitudes of the targets to find a "zero-point" level. The scaling of weights is derived from the top 5% brightest stars, to avoid inaccuracy from low signal-to-noise ratio targets. The resulting weights are used in the different steps of the combining process, including the final combination.

A final step in the combination process is to ensure that different exposures are checked for having the same configuration. If that's not the case, the combining algorithm uses the target names to ensure that the final output is the sum of the fluxes of the same target, even if it was observed with different fibre configurations. This means that the final, combined, FITS file may have more than 400 rows.

Extraction

There are several extraction algorithms, all aiming to identify an area of the CCD that holds the flux corresponding to a given fibre for a given wavelength range. The values of the identified pixels, or a fraction of them, are summed and stored in an array.

The simplest way to do this sum is to use the precomputed tramline to traverse the CCD. A number of pixels on either side of the tramline is considered part of the target's flux. Each group of pixels is added and linked to a wavelength pre-computed by the wavelength scale model. Alternatively, the sum can be done assuming a Gaussian distribution of flux centred at the tramlines. This ensures less contamination, in particular in the pixels that are furthest from the centre of the tramline.

The set of fibres that carries the light from the focal plane is tightly packed in front of the CCD. This produces an overlap in the illumination produced by the fibres on the CCD, known as cross-talk. In the previous examples, this effect was ignored. Optimal extraction aims to account for this effect by assuming a known shape of the flux distribution from each fibre, the local PSF. This assumption is used to treat the flux on each pixel as a linear combination of the PSFs of all fibres, effectively considering the total pixel count as the result of a weighted contribution from all fibres.

Scrunching

The process of re-sampling the extracted data into new wavelength ranges is defined as frame "scrunching". This step is applied after the data from individual fibres has been identified and a wavelength scale model has been calculated, overriding the initial wavelength solution from the standard instrument model. Each bin is labelled by its central wavelength, and linear or quadratic interpolation is used to re-sample the original data into the new bins.

Whale Shark Pattern Matching Algorithm

In its initial implementation, the goal of this algorithm was to identify star patterns against a known catalogue, the Groth algorithm (Groth, 1986). This was adapted to identify whale shark skin patterns by adding warping transformations allowing for changes in the distance between features (Arzoumanian et al., 2005). 2dfdr uses this algorithm to match the list of known emission lines from a given arc lamp (Thorium-Xenon in the case of HERMES) to the lines that are observed in an arc exposure. This produces a wavelength solution.

The parametrisation of the wavelength related parameters is based on the 2 gaps between any 3 spectral emission lines and the relative intensities, both normalised by their sums. This approach produces 5 parameters that are used in the algorithm to look for matching patterns in the wavelength distribution. Once the identification has been achieved, a wavelength scale model is used to calculate the wavelength value at the centre of each pixel.

Tank Track Tracing Algorithm

This algorithm is used in both the tracing of tramlines on the spectral direction and also for the tracing of spectral lines in the spatial direction, i.e., across different fibres. The basic algorithm comes from the identification of the paths produced by several similar moving targets, originally tanks, using only limited snapshots of the process at different points in time. The feature that makes this algorithm useful for 2dfdr is that it accounts for the fact that the moving targets look similar, hence no individual features can be used for identification, and that not all snapshots will necessarily show all targets.

In the core of the algorithm is the matching of individual targets to the particular coordinates, in 2 dimensions, in the sequence of exposures. In order to achieve this, the shortest Euclidean distance is assigned to identify a given target on sequential exposures. In this case the targets are the emission lines and the exposures, the fibres; hence the information gathered is only 1-dimensional.

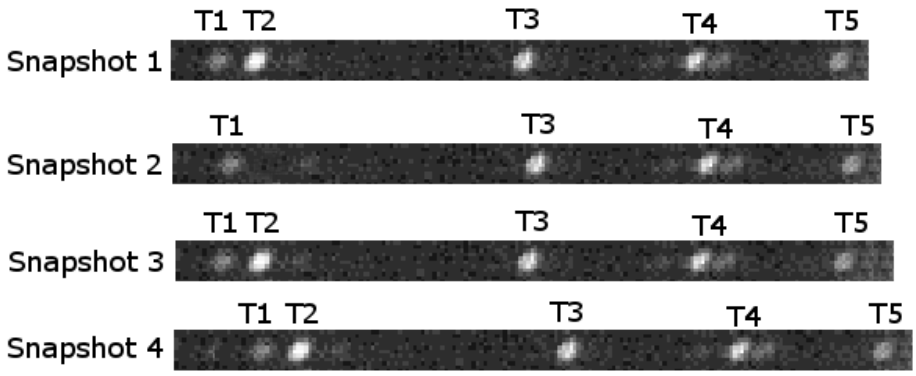

Figure 4.4: Schematic example of how the tank tracking algorithm uses different snapshots of the same collection of items. It aims to match the initially identified members in subsequent exposures, assuming that positions may change and not all items will be present in all snapshots. When used to identify emission lines, each fibre is considered a snapshot and the different emission lines are the items to identify and track.

Emergence Peak Finding Algorithm

This algorithm is designed to count the number of fibres by identifying all peaks produced by tramlines in a given column. A difficulty arises when not all tramlines have the same intensity, generally due to uneven illumination and variations in individual fibre throughput. This algorithm overcomes the problem by using a flux segmentation process combined with

a “watershed" method. Here, the segmentation is carried out for every column in the CCD image. The “water level” at a maximum is the intensity of the image where no peaks (corresponding to fibre traces) are seen. As the water levels decrease, features will emerge as islands, hence the name emergence. If we count the number of islands as a function of water level we’ll start with one, the tallest feature. The number of features will increase, then remain constant for a while, until it finally drops back to one when we expose the underlying connecting structure (floor). This plateau-shaped histogram is the case of a single column of a flat exposure frame. The number of peaks noted over a wide range of "water levels" gives us the total number of fibres (or "islands") in that column (see Figure 4.5).

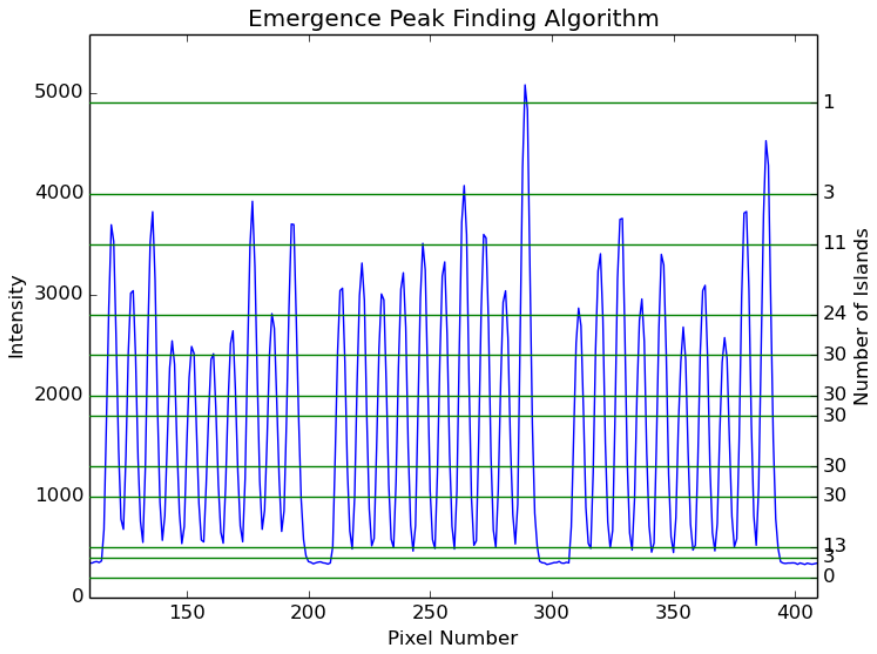

Figure 4.5: Example of the Emergence Peak Finding Algorithm. It calculates the number of “islands” found as a function of intensity levels, producing a curve that flattens when the maximum number of fibres is found, 30 islands in this case. This method avoids inaccurate results due to localised maxima as it looks for a stable solution for a wide range of intensity values.

Throughput Calibration

This algorithm attempts to estimate the relative throughput of the fibres in the system. There are several methods to achieve this. One of them is by using a twilight sky flat in which the sky is assumed to be a fairly flat source in spatial distribution, and no starlight is expected to be collected by the fibres. These fields are reduced as regular science fields and the total output from each fibre should be the same in a perfect instrument. Any variation between fibres is then recorded as a throughput map.

Alternatively, the relative throughputs can be calculated from the data itself. Embedded within the target spectra, there are sky emission lines. As with the twilight sky fields, these lines are expected to have almost equal counts, and thus any deviation of this is accounted as throughput variations.

Sky Subtraction

A key step in the extraction of target data is the subtraction of sky features. In order to have a good sample of the sky spectrum at the time of observation, generally at least 10 to 20 fibres are assigned to parts of the sky away from any known targets. These spectra are median combined after being corrected for their relative throughput, in the process also removing cosmic rays or spikes. This combined sky spectrum is subtracted from all fibres, scaled by the relative fibre throughput. The effectiveness of this method has been measured to leave a 2-3% residual, mainly due to its sensitivity to throughput estimation. A good test of the effectiveness of the sky subtraction is given by examining the residuals after this process is applied to the sky fibres themselves.

Participating in the further development of 2dfdr, during the early stages of its adaptation for HERMES data reduction, helped us understand the limitations we found in the radial velocity calculations. As 2dfdr is a package that services so many instruments and is not optimised for precision radial velocity measurements, there were many lessons learned on how to improve the reduction process beyond 2dfdr's built-in capabilities. The result of this process led to the development of HARPY.

4.2 HARPY

After a comparison between the different data reduction software options, it became clear that the pre-existing software could only approximate the level of radial velocity precision required for exoplanet search from HERMES data. Despite having produced results with other data reduction software, particularly with 2dfdr, it was worth exploring the development of our own reduction software customised for higher radial velocity precision. It is with this background in mind that we set out to write our own reduction software.

HARPY was fully developed in the Python programming language. This allowed us to have full control of the reduction process and gave us flexibility to monitor each step. In addition, Python has been widely adopted by the astronomical community, allowing us to take advantage of a large number of freely available standardised tools and libraries.

The core structure within the data reduction process is the array. This is managed by the Python module numpy. Each file that is used for the reduction is read into a numpy array. All image arrays have rows in the spatial direction, i.e., new fibres are found by travelling from row to row, and columns in the spectral direction, i.e., new wavelengths are found as we navigate from column to column (see Figure 4.6).

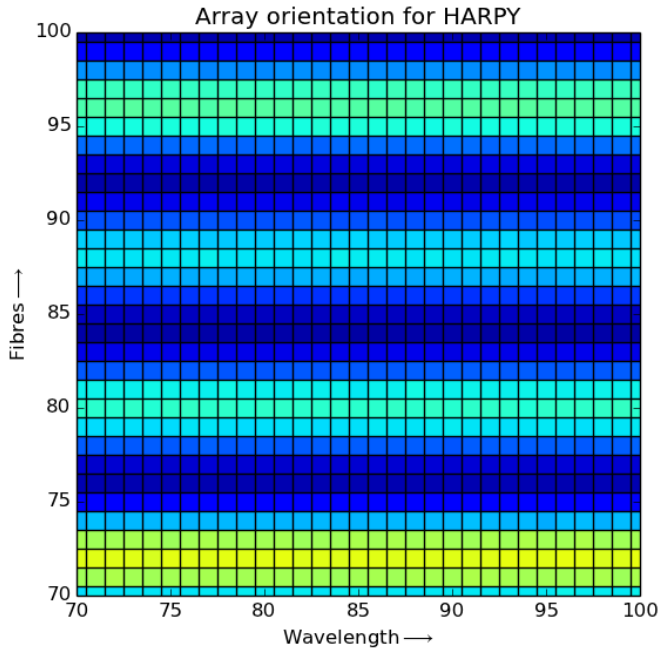

Figure 4.6: Section of a flat exposure from HERMES showing the standardised array orientation used in HARPY. Wavelength values increase with column (X) pixel values and fibres are found as a function of row (Y) pixel values. Brightness levels indicate pixel intensity.

Below we present the detailed descriptions of the custom designed reduction process, outlined in Figure 4.7.

An overview of the reduction steps can be summarised as:

- Bias subtraction
- Flat fielding
- Tramline determination from flats
- Tramline modification for arcs
- Flux extraction
- Wavelength scale solution

4.2.1 Bias Subtraction

Due to the type of detectors used in HERMES, all image output arrays are 4112 rows by 4146 columns. The last 51 columns are dedicated to the overscan region, and consequently receive no flux from the telescope. This overscan area is a reference for the underlying bias level to be removed from the rest of the image.

The readout process in the HERMES detectors is performed though 2 different simultaneous readout registers by default. This design decision was made during HERMES commissioning, as it takes only half the time to perform the readout process without increasing associated noise. This method of performing the readout process leads to 2 different sections in the CCD in terms of its bias level (see Figure 4.8). This effect is accounted for in the overscan subtraction step.

The bias level of each of the CCD sections is calculated by separating the overscan region in 2 halves, corresponding to each readout sections. For each half, the median of the pixel count is calculated, ignoring the last 3 pixels of the each of the sides to avoid windowing effects.

The range of pixels in the overscan region for which the median is calculated are 3:2052,4099:4143 and 2059:4109,4099:4143 for the top and bottom part of the CCD respectively. The overscan subtraction process is applied to all arcs, flats and science frames. Each of these files are used by the rest of the reduction process, as bias-subtracted arrays of 4112 rows by 4095 columns. Dark noise is negligible and hot pixels are subtracted by sigma clipping from the extracted spectrum.

4.2.2 Flat Fielding

Flat exposures are used in two ways by HARPY. They are used to identify the differences in illumination that the CCD receives. They are also used to find the traces of each fibre on the CCD, called tramlines. The tramlines are key to extracting the flux from arc and science frames as they provide a description of the light path produced by each fibre across the CCD.

Before parametrising the location of the tramlines, a series of operations are performed on the flat file array to ensure that the correct paths are identified. Potential sources of error in the path determination are cosmic rays, dead pixels, ghosts, etc.

Saturated pixels are removed using a 2-dimensional moving median over a 3 by 9 pixel window. The array, now assumed free of saturated pixels, is summed in the vertical direction to produce 1-dimensional array containing the combined flux and corresponding variations

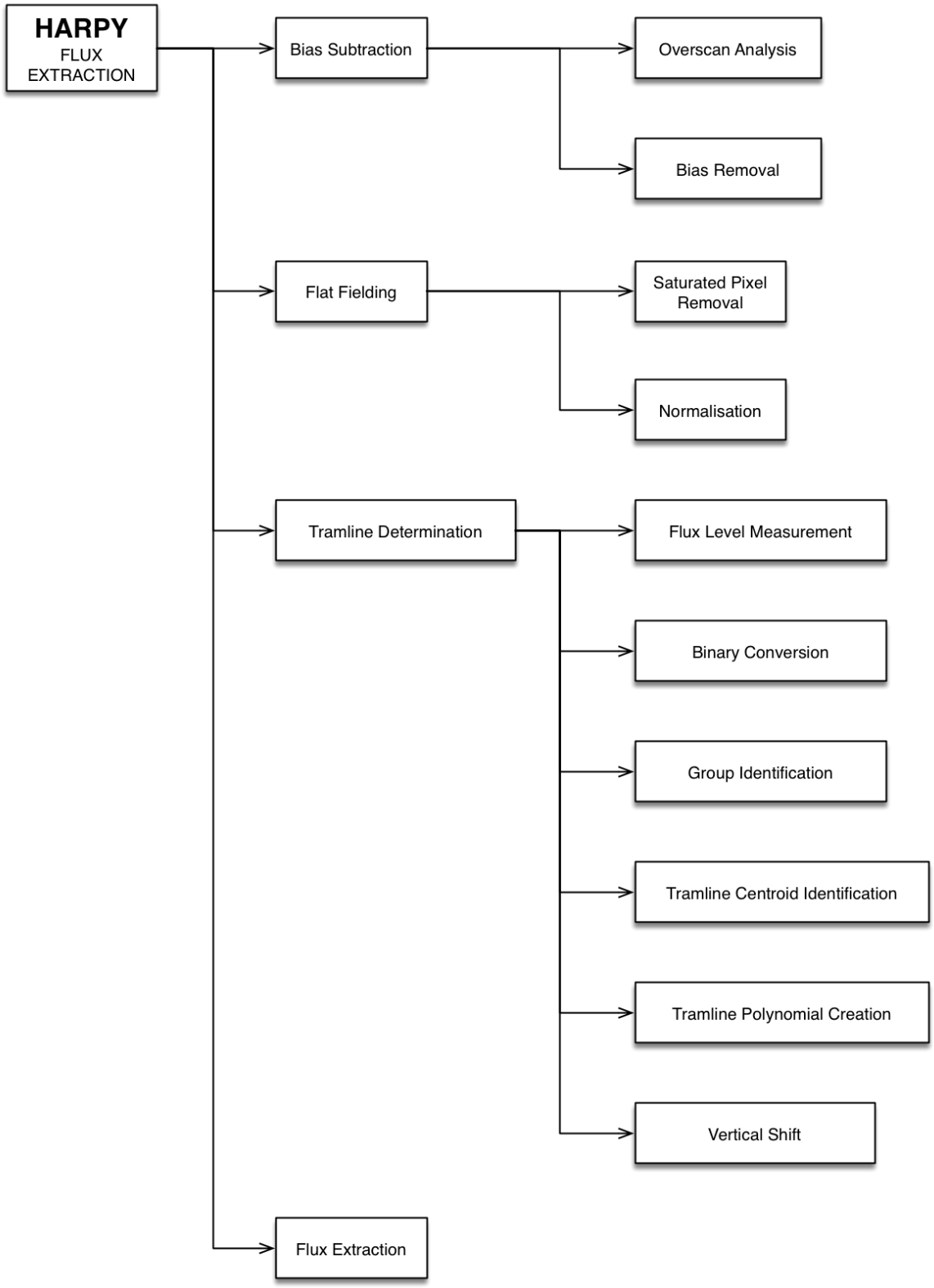

Figure 4.7: Functionality chart of the flux extraction process in HARPY.

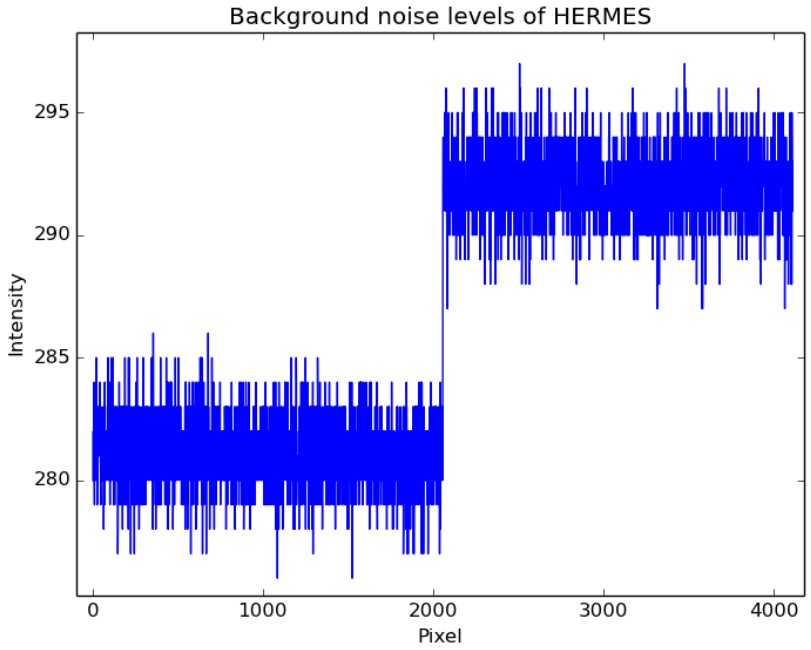

Figure 4.8: Different bias levels in HERMES due to a double register readout method. Readout speed is doubled at the cost of different background levels.

as a function of wavelength. This array is then normalised by the 90th percentile value and the result used to normalise each row of the original median filtered array. The resulting 2-dimensional array is internally named flat_flat and it is used in several steps in the rest of the process.

4.2.3 Tramline determination

Initial parameters from flat

Tramline determination in HARPY uses the reduced flat exposures. The array created in the previous step, Section 4.2.2, is a map of the traces produced by the fibres on the CCD. This step turns these traces into polynomials that can be used to extract the flux from the arc and science frames.

This first step in this process is to turn the flat_flat array into a binary map, where 1 indicates the pixels that are illuminated by fibres and 0 the ones that are not.

We measure the flux between the fibres as an indication of the level of inter-fibre crosstalk. This is found by creating a smoothed minimum filter over a range of 15 pixels. For each column, the flux value is subtracted, effectively bringing the inter-fibre regions to 0.

Similarly, the peak of the fibres is identified with a smoothed maximum filter over a 15 pixel range. In some cases the distance between the peaks is large enough to produce a gap in the smoothed array of maxima (e.g., in the case of a dead fibre). This effect is removed by using a "fixer" array produced by smoothing the array of maxima over a range of 200 pixels. The values of the maxima array are compared to the "fixer", and when their ratio is lower than 0.5, they are replaced by the latter.

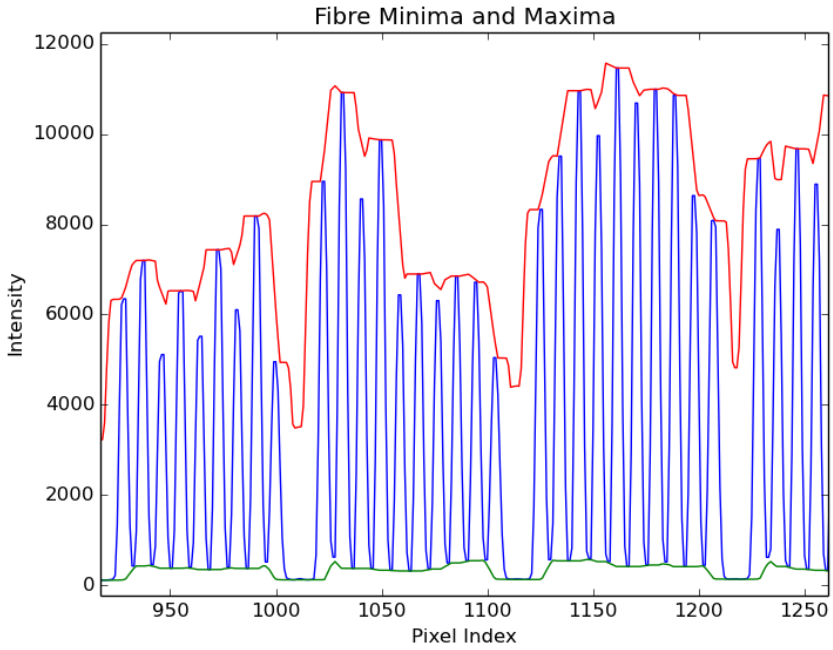

Figure 4.9: Example of the HARPY approach to identify tramlines. A smoothed envelope of the minima and maxima of each column is used to normalise the flux and prepare the array for binary masking, leading to the identification of the fibre traces.

Having identified the maxima and minima of each column (see Figure 4.9), we take the ratio between them, producing an envelope around each fibre. Finally we choose an arbitrary threshold value at 0.3. Any pixels with values above the threshold become 1, and 0 otherwise (see Figure 4.10), thereby creating a binary mask.

In the binary version of the flat array, groups of adjacent pixels with the value 1 represent each fibre. The algorithm that identifies the groups works by travelling along the array until a pixel with value 1 is found. From that pixel, it will travel in all possible directions until it finds a gap in the pixel values. The allowable shape of the gap is determined by a configurable 2-dimensional mask, supplied to the function. For HERMES a 3×3 mask proved the most effective size given the space between fibres. If gaps were reached in all directions, a region is assumed identified and all pixels within the region are marked with an index value that identifies it. The function returns the number of groups found and a 2-dimensional array of the same size as the input array, containing the values 1 to n to identify the groups.

The next step is to travel along the returned 2-dimensional array one column at the time. For each fibre and each column, the average pixel index is recorded. This produces an array of n x 4096, where n is the number of fibres. As an example, the n^{th}, m^{th} element of the array contains the row index of the centre of the tramline for fibre n in column m.

For each row of the newly created array, a 5^{th} degree polynomial is fitted thorough the pixel indices of each fibre. We choose a 5^{th} degree polynomial because it empirically produces the best fit for the data given the range of distortions produced by HERMES. This then becomes the parametrisation of each fibre trace, and the

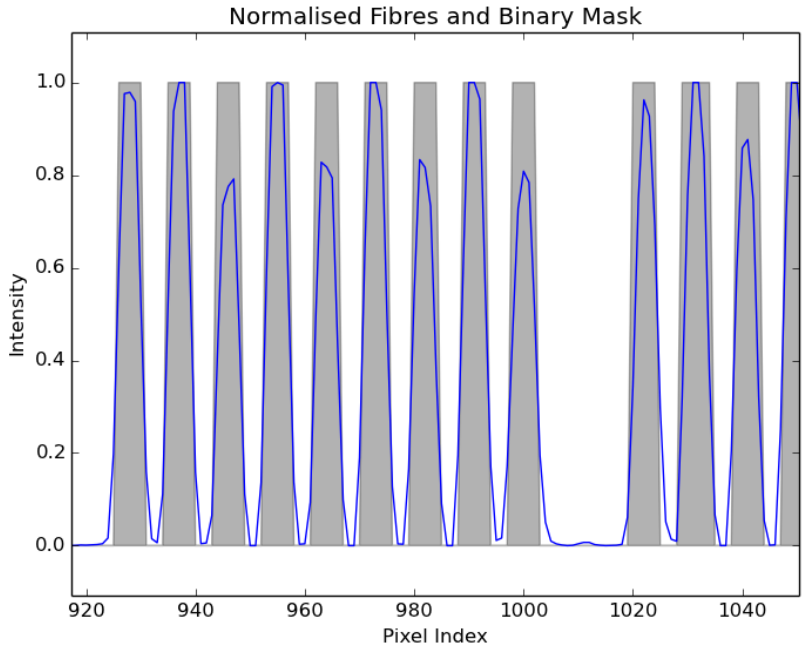

Figure 4.10: Example of the binary mask calculated by HARPY. The ratio between minima and maxima is used to identify the areas assigned to fibre traces. The grey areas are labelled as 1 and the rest as 0.

evaluated value of the 5^{th} degree polynomial for every fibre and column becomes the fibre centroid at that point.

Vertical shifts from arcs

The alignment in the vertical (spatial) direction between the flat and arc exposures is not perfect if left uncorrected. This may lead to a misalignment between the tramlines calculated and the actual location of the fibres in the arc frames. The source of this shift is not clear and it is initially attributed to thermal fluctuations. To avoid having to resample the arc file, we decided to use the arc as a reference. This step brings the tram lines generated from the flat to the reference frame of the arc.

We calculate the vertical shift between the flat and the arc exposures by cross-correlating each column of the flat against the corresponding column of the arc. The resulting curves are added such that we generate a 1-dimensional array representing the vertical relative displacement between the 2 frames. A Gaussian curve is fitted to the profile and the offset from the centre is the the vertical displacement in pixels. This value is subtracted from the tram line centroids, making the flat centroids match the arc.

4.2.4 Extracting flux

Having calculated the tramlines in reference to the arc, we extract the flux from the arc and the science arrays. For each fibre and column, we sum the value of a 4 pixel column centred on the centroid.

This creates an array containing the flux for each fibre, separated in bins. The correct identification of the range of wavelengths that are grouped in a bin or pixel is only found by calculating the accurate wavelength scale model.

4.2.5 Wavelength scale solution

The assignment of a wavelength value to each part of the extracted spectrum is the task of the wavelength calibration process. In the core of this process, the arc exposures are used to link known reference emission lines to pixel values. The accuracy of this process dramatically impacts the resulting radial velocity measurements.

Several factors contribute to the final accuracy of the calculated wavelength solution. In particular, the level of precision of the known wavelength values used as a reference, and the precision and accuracy of the identification of the emission peaks in the extracted arc, will set a limit to the capacity to effectively link both. The wavelength values of known emission lines for a given source are usually provided by measurement institutes and have been calculated to different levels of precision. The location and availability of known lines in the arc exposure depend on the element used for calibration and the wavelength range observed as a result of the spectrograph design. These are only some of the factors that determine the underlying conditions that affect the accuracy of the wavelength solution.

Achieving high relative radial velocity precision was the primary motivation for the development of a custom reduction pipeline. The approach taken in HARPY aims to ensure that the wavelength scale solution is consistent across all epochs. This is the overarching philosophy throughout the development of the package. The key components of HARPY's wavelength scale model are outlined in Figures 4.11 and 4.12.

Initial Wavelength Solution

The starting reference point of the wavelength scale to be used across all reduced spectra is an initial wavelength solution that allows us to assign a tentative wavelength value to each pixel of the extracted flux. The initial version of this solution is based on the optical design of the system.

The approximate wavelength range of each channel in HERMES is known, and so is the number of pixels in the CCD. These values are also quoted in the header of each fits file produced by the spectrograph. The information is provided as the value of the wavelength at the central pixel and the corresponding dispersion. The values are expressed in Angstroms (Å). In the case of the blue channel, the quoted central wavelength is 4833Å and the dispersion is 0.045 Å/px. These values are only an approximation but they still enable us to construct a linear equation as an initial wavelength solution (WS1) of the form

$$wl = 0.045 \times px + 4740.885\,\text{Å} \tag{4.1}$$

where wl and px represent the wavelength and pixel, respectively. This equation aims to provide a linear approximation to assign a pixel value in the next step.

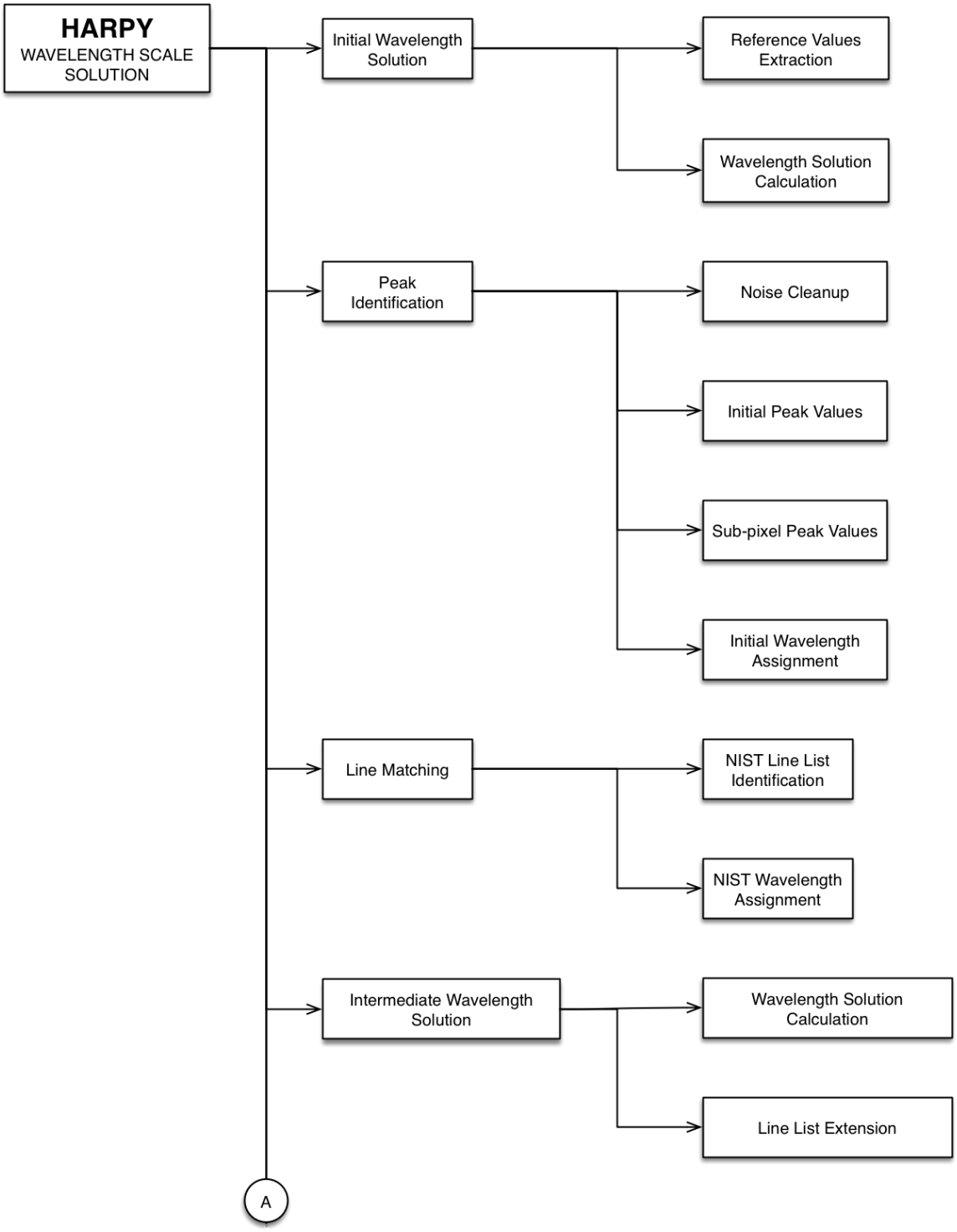

Figure 4.11: Functionality chart for the wavelength scale solution section of HARPY (Part 1 of 2).

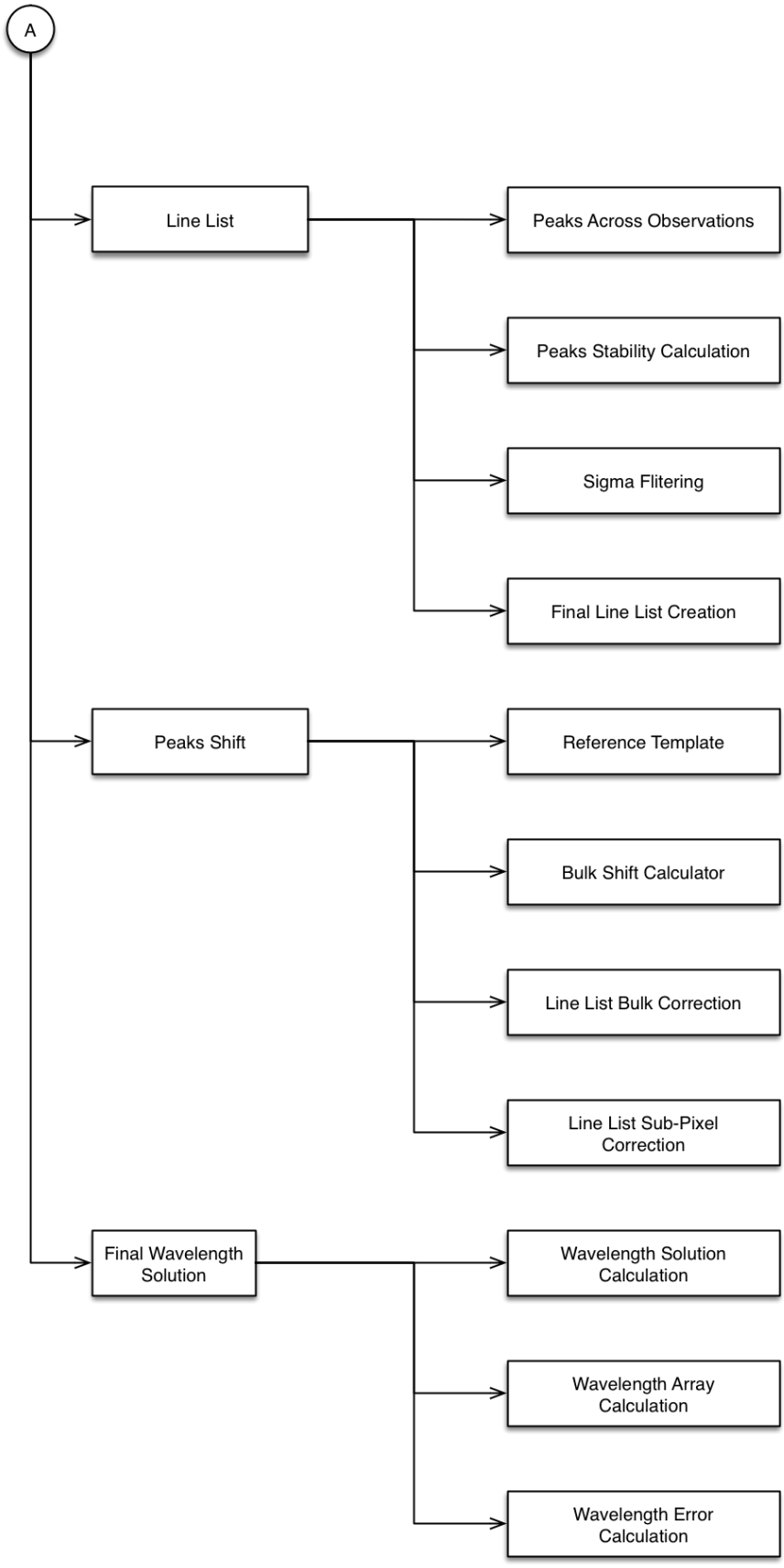

Figure 4.12: Functionality chart for the wavelength scale solution section of HARPY (Part 2 of 2).

Peak identification

The identification of the peaks produced by the arc emission lamps is done using the central fibre of the first epoch as a reference. Initially a level of noise is estimated by eliminating the lower 10^{th} percentile of the intensity levels. These values are set to 0.

Using the virtually noise-free version of the arc, the peaks are found using the python internal function `find_peaks_cwt` of the `scipy` [1] python package. This function returns a list of indices of the identified peaks. In order to improve the accuracy of the peak values to a sub-pixel level, a generalised error distribution curve is fitted to each of the peaks (see Equation 4.3). The choice of curve is an important decision to account for the variations in the spectral PSF of HERMES, particularly near the edges of the CCD. A slice of 5 pixels on each side of each peak is used for fitting via a least-squares method. The centre of each peak is recorded in an array with the corresponding approximate wavelength using Equation 4.2.5.

Line matching

As noted previously, HERMES uses a set of Thorium and Xenon lamps as calibration sources. This design choice was made based on the position of the combined emission lines within the instrument's wavelength range. HARPY uses the values measured by National Institute of Standards and Technology (NIST)[2] as the starting point of the line matching process. These values quote uncertainties that range from 3×10^{-3} nm to 3×10^{-6} nm, which translate to $\approx$1900 m s^{-1} and $\approx$1.9 m s^{-1} respectively for HERMES blue channel. This uncertainty is primarily an inverse function of brightness. Since only the brighter lines can be identified on the reduced arcs, the precision limit introduced is closer to the lower value. Overall, the wavelength precision of the lines, their stability and their distribution across the spectrum are determining factors for the rest of the process. Using the line list from NIST and the line position list created in the previous step, the NIST wavelength is assigned to each peak. This is done by using the brightest lines and matching to the closest known emission lines, a similar process to the equivalent step in 2dfdr.

Improvement of the wavelength solution

Using the line position list of the brightest peaks allows us to build a more accurate wavelength solution (WS2). We achieve this by creating a 3rd order polynomial linking pixel index to wavelength value using the NIST values assigned in the previous step. tests showed that a lower order polynomial failed to capture the variations, in particular where there were few lines to anchor the solution to, and higher order did not increase the accuracy of the solution. We use this new wavelength solution (WS2) to identify the wavelength corresponding to all identified peaks, including the ones used to create WS2. This is an important step because it creates a consistent solution that, despite not matching the values quoted by the literature, results in a parametrisation that can be conserved across epochs and eliminates the uncertainty effects produced by using an independent wavelength solution from each arc. This is an important point that contrasts with 2dfdr and is one of the key aspects of HARPY designed to achieve a consistent wavelength solution.

[1] https://docs.scipy.org/
[2] https://www.nist.gov/

Line list across the dataset

The gradient produced by the emission peaks provide anchors to lock the wavelength scale solution at each point in time. This is a key way to capture the changes in the spectrograph. The stability of these emission lines and the correct measurement of their position from each arc exposure determine the validity of the wavelength solution and minimise the errors introduced by it.

In order to ensure that the emission lines remain reliable across all observations, HARPY compares the behaviour of all the identified peaks across all epochs. We measure changes in position, intensity and line width. Using these measurements we apply a sigma filter that eliminates any peak that shows changes larger than $1\,\sigma$ in any of the measured values. This ensures that the line list adopted for the final wavelength solution uses the same set of peaks at all epochs, minimising the errors introduced by adding or removing points. Only the lines that are consistent across all epochs are used. This is a point of contrast with 2dfdr and ensures a wavelength solution consistent across all epochs. Note that the wavelength values assigned to the final line list not necessarily match the reference wavelength value from the original NIST line list but will be consistent with the final wavelength solution.

Peaks shift across the dataset

Using a line list that has been confirmed to be consistent across all epochs, we model how the position of each peak changes across the dataset. The first step in approximating the solution is to create an artificial template from the line list. This is done by creating an array of zeros of equal length to the array containing the extracted arc and setting to 1 the pixels where the lines are expected to be. The arc corresponding to each epoch is cross-correlated with the template arc in velocity space, producing a measurement of the relative shift for each epoch.

Having an approximate pixel shift for each epoch, we add these values to the original list to create a new pixel position for each epoch. Using the new (shifted) line list positions for each epoch as a starting point, we measure the exact position of each peak, fitting a generalised error distribution curve (see Equation 4.3), for each peak and epoch. This creates one line list per epoch. All of them have the same wavelength values, but differ in the pixel position of each peak at each epoch.

Wavelength solutions across the dataset

The pixel position of each line across the dataset allows us to create independent wavelength solutions, wavelength arrays and measure residuals for each epoch. In this case we have as many versions of each of these we have epochs of observation in the data set.

We use 5^{th} order polynomials for the wavelength solutions. By evaluating the wavelength solutions at each pixel, we build a wavelength array for each epoch that carries the range of wavelength values associated with each extracted spectra. Finally, we evaluate the corresponding polynomial on the differences between the same line at different epochs to determine the errors in our solutions.

The strength of this process lies in the validity of the wavelength solution across epochs for a given target. After a good initial approximation, it focuses on changes of the original wavelength solution rather than the independent calculation of wavelength solutions through the identification of the emission lines. This process is repeated for each fibre and each camera.

4.3 The HARPY Radial Velocity Method

As mentioned previously, the original goal of the software written for this thesis was to utilise the existing HERMES data reduction software, 2dfdr, in an automated pipeline capable of processing large volumes of data with minimal intervention. In addition, the pipeline would derive radial velocities from the extracted data. The shortcomings of 2dfdr with respect to the radial velocity precision required for exoplanet detection prompted us to modify it in an attempt to stabilise the wavelength solution. Finding that this option was still not suitable for the intended purpose, we set out to write our own reduction pipeline, HARPY.

The data presented in this thesis are organised in three independent methods, sketched in Figure 4.13.

- 2dfdr standard
- 2dfdr single-arc
- HARPY

The **2dfdr standard** reduction method produces a wavelength scale model for every epoch. This is calculated using Thorium-Xenon arc exposures taken for that purpose, at a point close in time to the science observations. The timing of these exposures is decided by the observer based on the science being investigated. This is the method used by the software provided by the AAO and is the approach most commonly used by HERMES observers (see Section 4.1).

In contrast, the **2dfdr single-arc** method keeps the wavelength scale model calculated for the first observation as the standard throughout all subsequent observations. This produces an increasingly inaccurate solution as the time between the calculated model and the observations increases. The deviation is also evident when the initial arc exposure is compared to later arc images. In both cases, the science and the arcs, these deviations can be measured as radial velocity shifts.

The goal of the single arc method is to remove the uncertainties introduced by having different wavelength solutions associated with different science exposures. In order to still capture the instrumental shift during the acquisition of the different images, an extra step is added to the RV calculations: the shift measured in the arcs is subtracted from the science results.

A third option was pursued when it became clear that the standardised approach of 2dfdr was not adequate for reaching the instrumental radial velocity precision limits. As mentioned in Section 4.2, the **HARPY** reduction method was written with precision radial velocity measurements in mind. The flux extracted from the 2dfdr vs. HARPY was the first testable result that allowed us to compare the different methods (see Figure 4.14).

In order to provide a fair comparison between the three approaches, the radial velocity calculation method was standardised, i.e., the steps that used the extracted flux and wavelengths to calculate radial velocities were the same for all three methods. This decision not only allowed us to use the lessons learned from the development of the HARPY cross-correlation method (see Section 4.3.3) but also to have a systematic approach to comparing the results from the three methods.

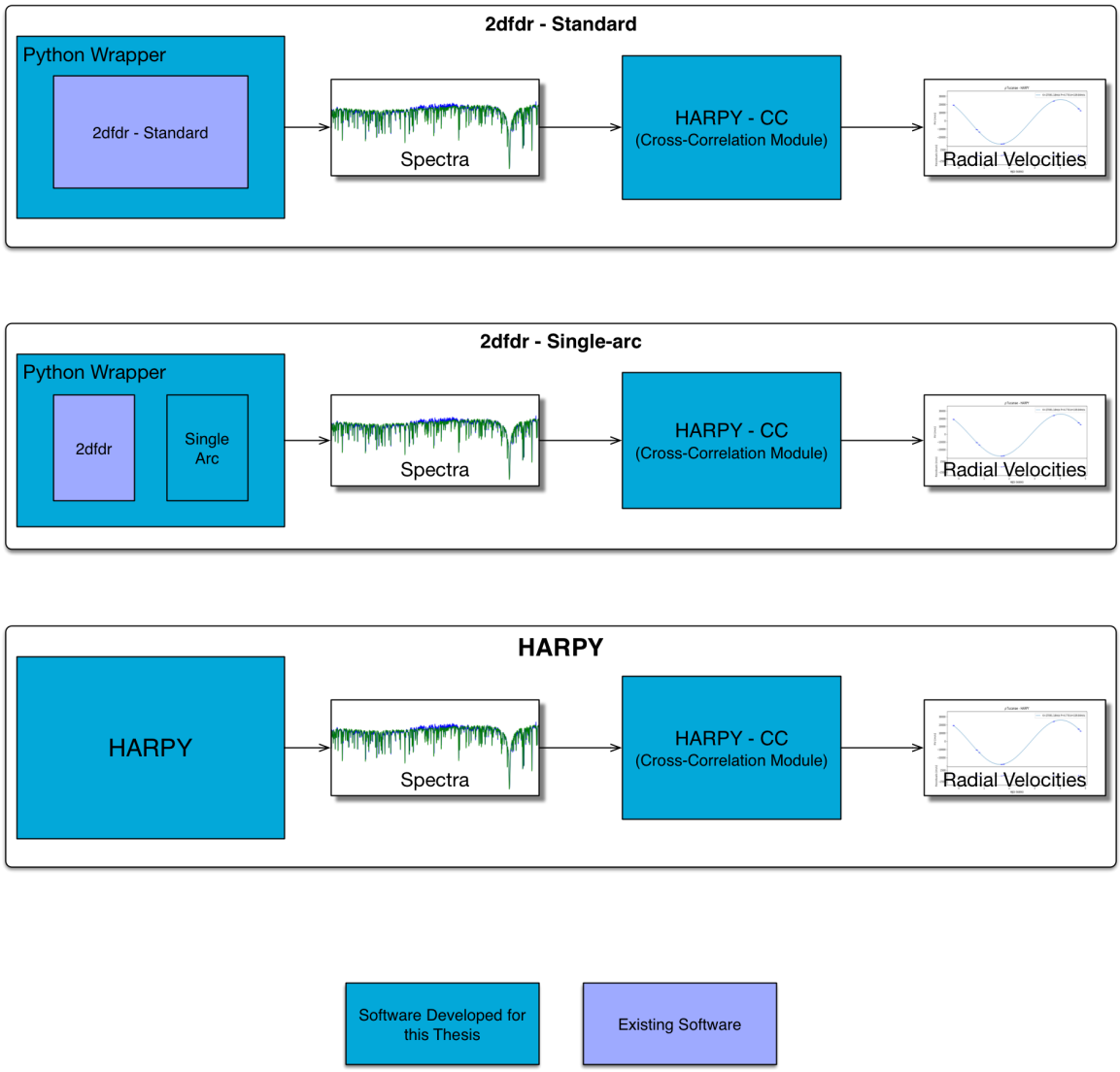

Figure 4.13: Schematic diagram of the 3 reduction methods used for this thesis. A wrapper code was developed to automate 2dfdr and to modify the standard 2dfdr operations for the single-arc mode. In parallel, the HARPY method of data reduction was developed from scratch. Each version of the reduced and extracted spectra was analysed using HARPY CC, the cross-correlation module developed for this thesis.

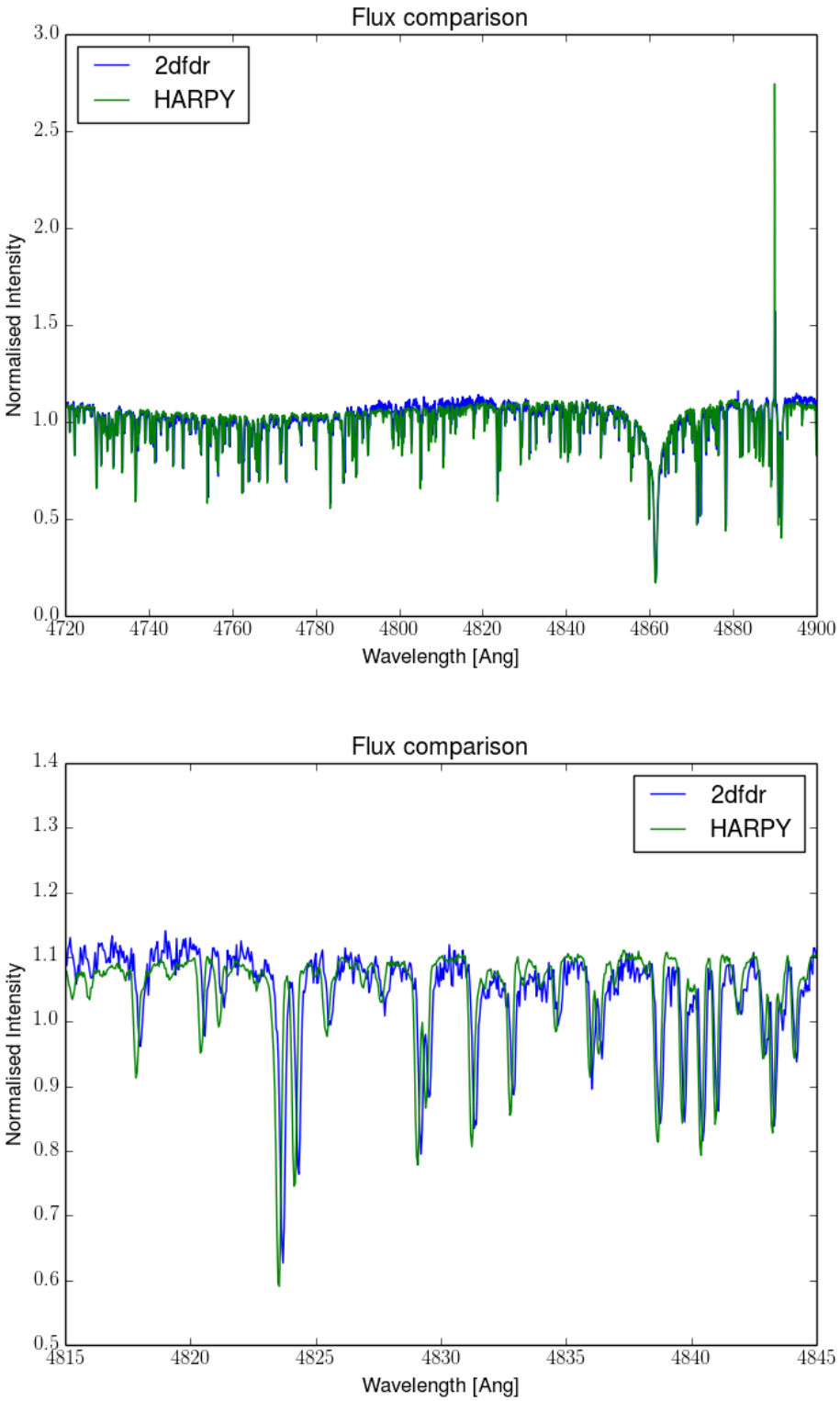

Figure 4.14: The flux of HD1581 extracted with 2dfdr and HARPY. The 2dfdr version of the spectrum (cleaned of cosmic rays) shows more noise than HARPY. The difference in the wavelength solutions can be noted as a shift in spectral features between the two spectra.

4.3.1 Radial Velocity Calculations

The relative line of sight velocity between two points, translates into a shift in the perceived wavelength of the emissions detected. This shift is a function of the velocity between the objects and is the physical principle that radial velocity calculations rely on. The relative shift in wavelength can be converted to radial velocity using

$$RV = \frac{\lambda_2 - \lambda_1}{\lambda_1} \times c \tag{4.2}$$

where λ_2 and λ_1 are the wavelengths of the same spectral feature at 2 different points in time and c is the speed of light.

Using spectroscopic data, the intrinsic features of the source can be used as a fixed pattern to identify the shift between exposures. The cross-correlation method uses these features to identify the shift between two similar spectra. It has the advantage that it uses the patterns across the full spectrum to measure the shift. The result produces a characteristic curve that peaks when both patterns match, or are the closest to matching. The deviation between the resulting peak and the centre of the cross-correlation curve is the measurement of the shift between the compared spectra.

The measured radial velocity is a combination of the motion of the source and the target. Without further reference, either object could be considered stationary. When observed from Earth, several vectors need to be calculated and their combined radial component subtracted in order to anchor the observations on a suitable reference frame. The reference frame used is the centre of gravity of the solar system, or barycentre; by applying a barycentric correction, we place the observer at the centre of gravity of the solar system, removing motion introduced as the Earth spins and orbits around the Sun. It also removes the Sun's own velocity variations due to the planets in the solar system, an effect that would still remain if a heliocentric reference frame was chosen.

The precision in the radial velocity of spectra produced in ideal conditions, that is using a spectrograph without readout noise or throughput loss, as well as without any effects from cosmic rays, atmospheric absorption or reddening, would still be limited by intrinsic stellar properties (see Section 4.3.2). The stars chosen for this thesis belong to stellar types with low associated RV "noise"; thus it is the contamination from other sources that limits the precision attainable, rather than the star's intrinsic features. This puts extra emphasis on the clean-up step of the data reduction (see Section 4.3.3).

We performed our initial tests using the earliest spectrum in the set as a reference. There are alternatives on the choice of reference. The spectrum of any epoch would produce the same radial velocity curve, with a velocity offset. A somewhat different approach is to use a mean spectrum, averaging all spectra, or an artificial template spectrum. These 2 options add uncertainties to the radial velocity calculations, as they use a reference spectrum that is substantially different to the cross correlated data, effectively widening the resulting cross-correlation curve and increasing the uncertainty of the fitted curve towards the O $\mathrm{m\,s^{-1}}$. The final choice was to use a summed version of all the spectra for a given target as a reference. Empirical tests showed that the higher SNR of the combined spectra improves the results of the cross-correlation.

The radial velocity calculations of the data reduced by 2dfdr, showed a variation that exceeded the ranges expected from the instrument design. This effect was later attributed to the wavelength scale model, which, being individually calculated for each observation,

introduced shifts larger than the expected target RV variations. For the purpose of isolating the components of this uncertainty introduced by the existing reduction method, we developed two alternative radial velocity pipelines. Each of the three methods, written in Python for this thesis, are explained in Section 4.3.

4.3.2 Data Quality

A large number of factors affect the precision and accuracy of radial velocity calculations. An extracted spectrum represents a combination of the stellar flux and any modifications it may undergo until it is recorded by the detector. These modifications introduce noise into the data and it is one of the objectives of the instrument design and data reduction pipeline to identify their effects and eliminate them.

Sources of radial velocity uncertainty can be classified into several groups. The lower limit is set by the stellar spectral type, due to fewer or broader spectral lines (see comments on Figure 4.16). The uncertainty cannot be reduced below this limit with a longer exposure baseline or higher SNR. Further modifications to regions of the spectrum are produced by absorption or emission sources such as molecular clouds, cosmic rays or the Earth's atmosphere. Finally, the spectrograph introduces a limitation on the capacity to discern 2 neighbouring wavelengths, quantified by the spectrograph resolution, in addition to the detector electronic noise and intrinsic photon noise.

Temporal variations of the spectrograph are ideally captured by the wavelength model, eliminating any potential influence that these variations can have on the captured data. In reality, the wavelength scale model can't fully capture the changes in the spectrograph and in addition can introduce its own variations; this problem is what led to a comprehensive re-design of the reduction pipeline for this thesis, as has been mentioned in previous sections.

The last step in the radial velocity calculation process requires the measurement of the position of the peak of the cross-correlation curve. This is done by fitting a generalised error distribution curve of the form

$$y = Ae^{-(\frac{|(x-\mu)|\sqrt{2\log 2}}{\sigma})^{\beta}} \tag{4.3}$$

where A is the amplitude, x is the pixel range, μ is the displacement, σ is the width and β the shape.

The shape of the peak of the Cross-Correlation Curve (CCC) is the result of the characteristics of the compared spectra. Achieving an optimal fit has an effect on the measured uncertainty, and the flexibility of the fitted curve shape allows the algorithm to produce a better fit when the cross-correlation peak is non-Gaussian.

A useful approach to identifying the amount of radial velocity information in a stellar spectrum is the Q factor (Connes, 1985; Bouchy et al., 2001). This Q factor is independent of the observed flux, as it represents the intrinsic spectral line richness of the spectrum. It is defined as

$$Q = \frac{\sqrt{\Sigma W(i)}}{\sqrt{\Sigma A_0(i)}} \tag{4.4}$$

where $W(i)$ is the weight assigned to each pixel based on its slope and $A_0(i)$ is the noise free spectrum value at every pixel. The Q factor is specific to each spectrum and allows for the calculation of the minimum uncertainty achievable, δV_{RMS}, by the formula

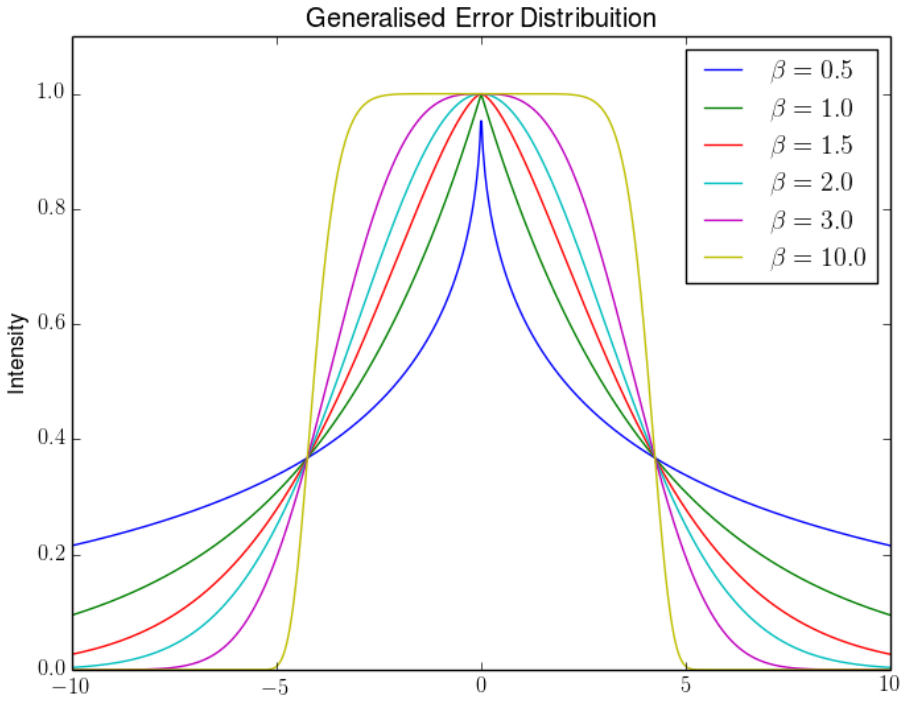

Figure 4.15: Effect of varying the β parameter on the Generalised Error Distribution curve. This parameter modifies the shape, such that it is a normal distribution when $\beta = 2$, a Laplacian when $\beta = 1$ and it converges to a peak when $\beta \to \infty$.

$$\delta V_{RMS} = \frac{c}{Q \times \sqrt{Ne^{-}}} \tag{4.5}$$

where Ne^{-} is the number of photoelectrons. This formula assumes a noise free detector.

The stellar line profile places a limit on the precision attainable. The spectrograph resolution will increase that uncertainty only if its resolution is below the minimum needed to resolve the spectral lines. Bouchy et al. (2001) shows the resulting quality factor Q as a function between spectral resolution, line broadening and spectrograph resolution. Figure 4.16 shows that the Q factor curve flattens at some point, making any increase in the spectral resolution of the spectrograph unnecessary. This is a key aspect to consider during spectrograph design when the target science is known.

All observations in this thesis were carried out using HERMES at a nominal resolution of R $\approx$ 28000. The SNR achieved in each case was dependent on the brightness of the star, exposure time and the extraction method. Measured SNR values in the data range from over 300 to below 10.

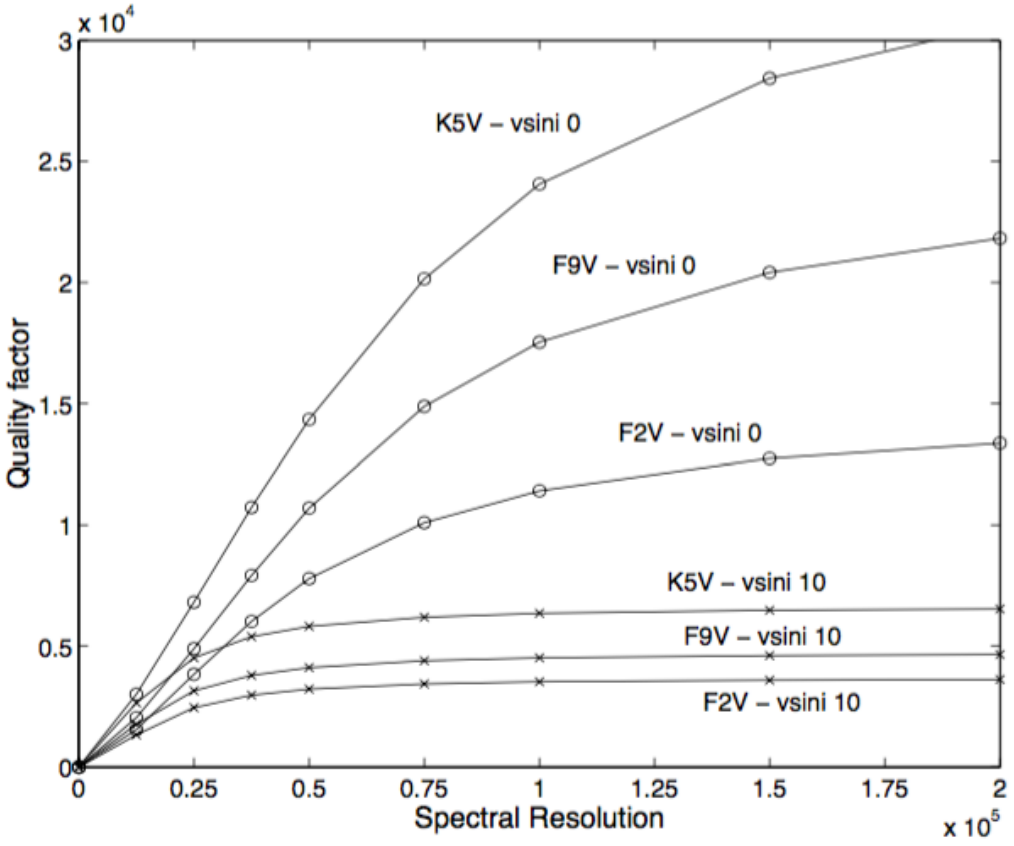

Figure 4.16: Quality factor of a spectrum as a function of spectral resolution and stellar type. An increase in spectral resolution leads to an increase in quality factor. This is true until the uncertainty level imposed by a combination of stellar type and rotational broadening is reached. This figure illustrates these limits. (Bouchy et al., 2001)

4.3.3 The HARPY Cross-Correlation Module

As described previously, the shift between two spectra can be measured using the cross-correlation method. This method measures the common area between two signals at increasingly overlapping intervals to find the position at which they have a best match. It produces a characteristic curve called the Cross-Correlation Curve (CCC). If the shift between the two signals is zero, the peak of the CCC would be at its centre. Any deviation from this point indicates a shift between the two spectra.

In the method developed for this thesis, the radial velocity shift is measured individually for each camera. In the initial step, the SNR for all fluxes is calculated. For each pixel, the SNR based on the photon noise is

$$SNR = \frac{N}{\sqrt{N}} = \sqrt{N} \tag{4.6}$$

were N is the intensity value. The median SNR is quoted for each spectrum.

The next step is to remove the barycentric velocities from each spectra. In order to minimise the number of operations performed on the flux, the barycentric correction is used to modify the wavelength axis, rather than shifting the flux array.

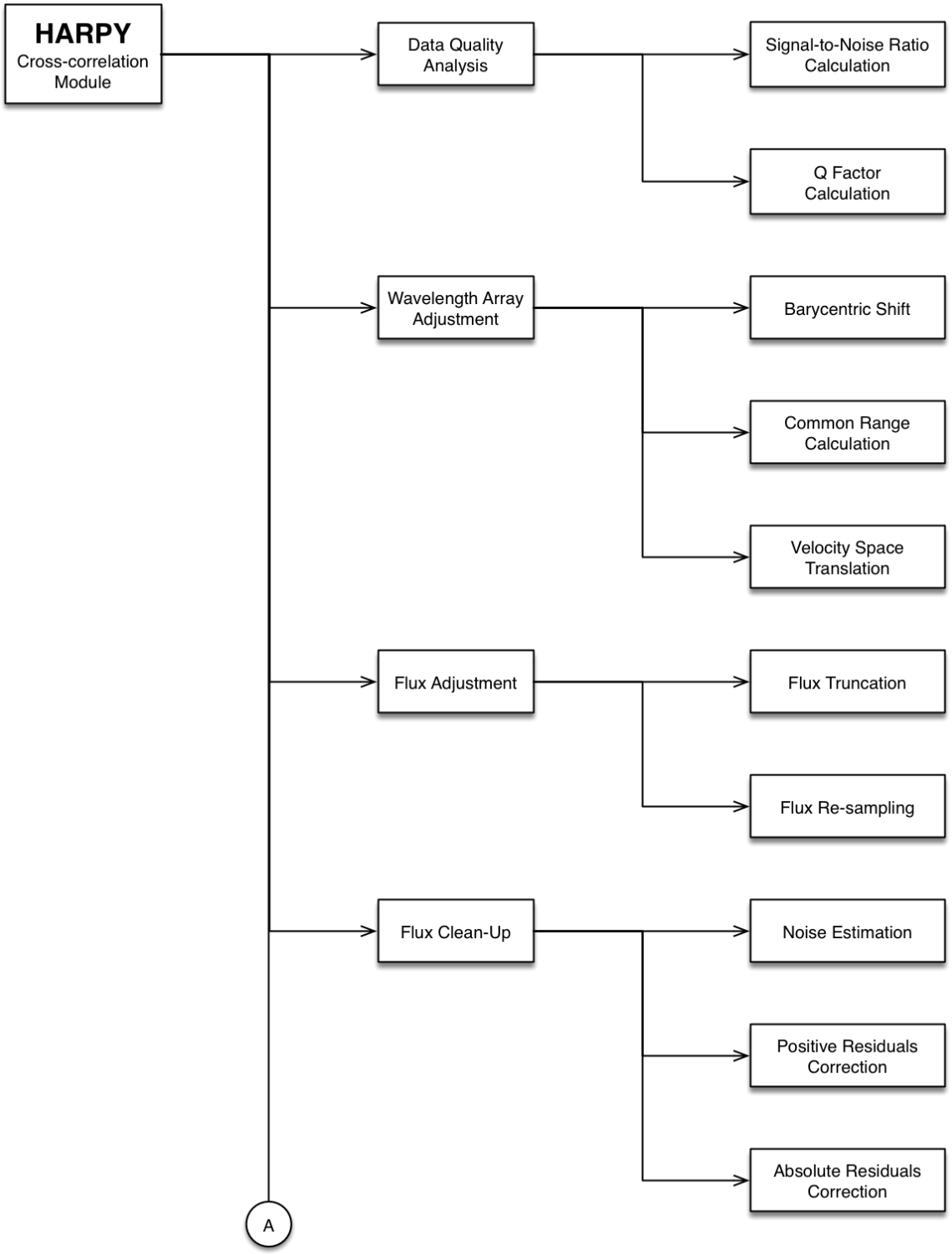

Figure 4.17: Functionality of the HARPY Cross-Correlation Module (Part 1 of 2).

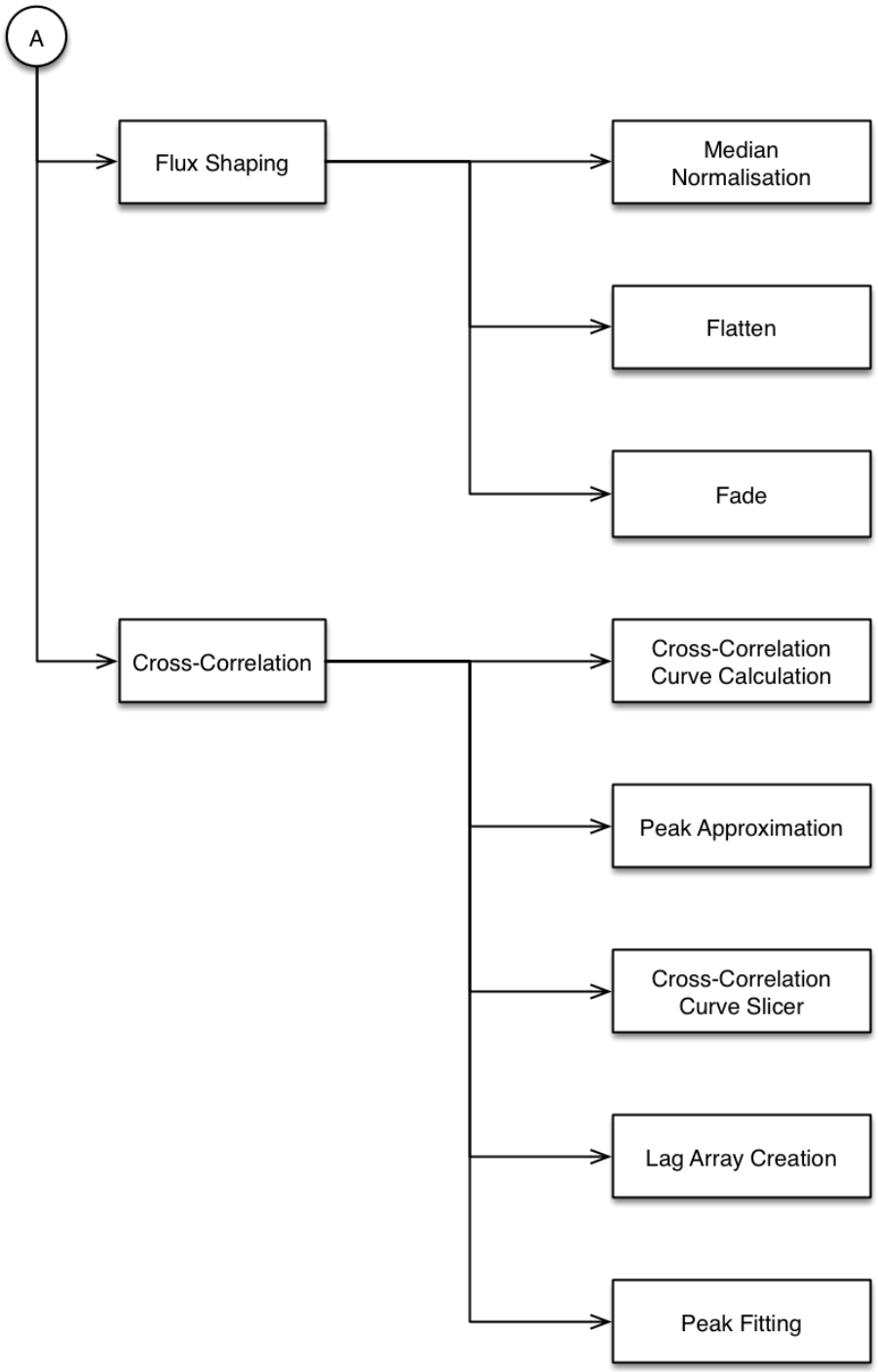

Figure 4.18: Functionality of the HARPY Cross-Correlation Module (Part 2 of 2).

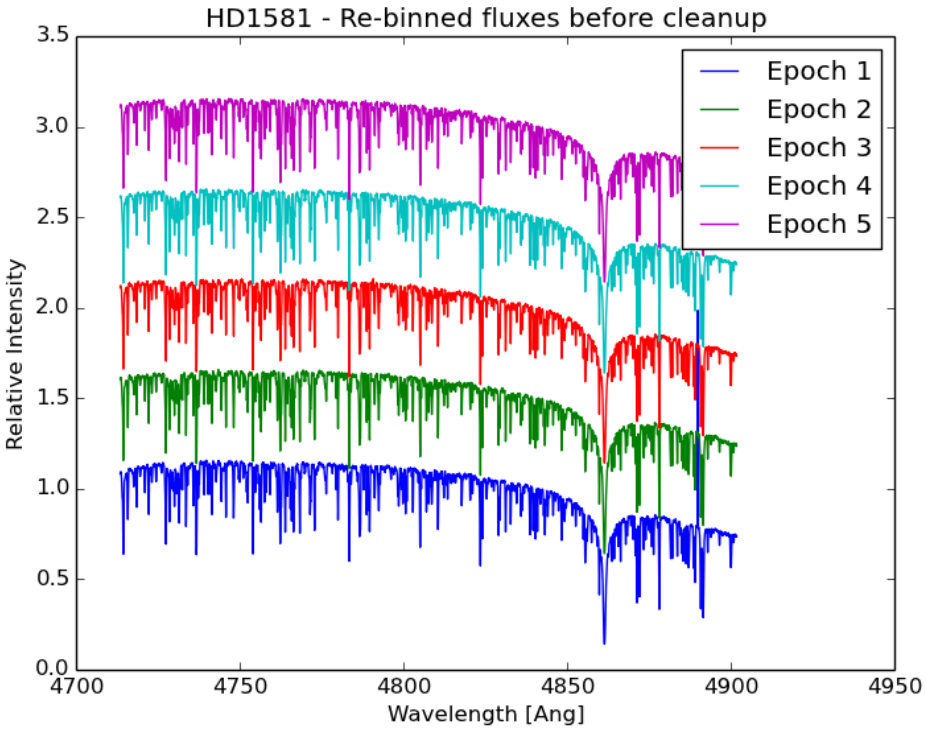

Figure 4.19: Flux from all observations of HD1581 (blue channel). The wavelength axis is shared by all observations and has been barycentre corrected.

Before attempting to build the CCC, each spectrum is organised in order to make the flux of all epochs fit the same wavelength bins. We achieve this by calculating the common wavelength range for all observations. A new axis is created and shared between all observations.

The relation between wavelength shift and velocity change is not linear. A shift of a given $\Delta\lambda$ will correspond to a different velocity change depending on the region of the spectrum used for the measurement. As an example, a shift of 1 pixel in the blue camera can correspond to a value between $\approx$2845 m s^{-1} and $\approx$2740 m s^{-1} depending on the location of the measured pixel. In order to make effective use of the cross-correlation method, each pixel has to measure the same velocity change. This is achieved by expressing the new (common) axis in velocity space by using the natural logarithm of the wavelength. The actual limits of the new axis are the natural logarithm of the minimum and maximum common wavelength values. In addition, the steps of each pixel in the new array are $5{\times}10^{-6}\ln(\lambda)$. This corresponds to approximately 1.5 km s^{-1} per pixel, effectively allowing us to up-sample our data to double the original resolution. It's important to note that the data themselves won't gain resolution by this process, but the cross correlation curve will be able to use more intermediate points, simplifying the fitting process applied later.

Using the newly created axis, we interpolate the extracted flux from each epoch into the corresponding bins. This produces a 2D array where the first axis corresponds to the epochs and the second axis is the natural logarithm of the wavelength. All epochs share the same $\ln(\lambda)$ axis and have been barycentric corrected at this point of the reduction.

The re-binned flux remains the result of the raw extraction, lacking any clean-up. Cosmic rays, invalid values (NaNs) and electronic noise need to be removed from the interpolated

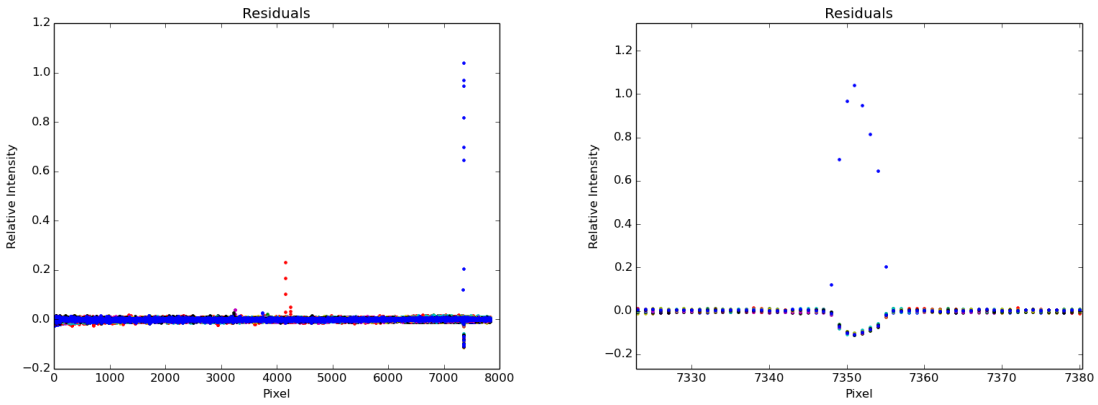

Figure 4.20: Residuals in the flux of HD1581. Positive outliers are from cosmic rays and should be flagged. In contrast, the points in the negative side are a consequence of the bias in the reference curve created by the positive points. Cleaning both sides at the same cut-off level would eliminate useful data that is now shifted towards the negative. This effect is avoided by cleaning the data recursively.

data before cross-correlation (see Figure 4.19).

Data clean-up starts with the measurement of the residuals at each point of each of the spectra. The data are median normalised. A single spectrum is then created from the sum of the non-normalised data, and the resulting array is also normalised. The difference between the flux of each epoch and the combined flux forms the 2-dimensional array of residuals, of the same shape as the flux array.

The clean-up algorithm in HARPY uses a recursive approach. This addresses the effect of outliers, usually cosmic rays or hot pixels. Outliers affect the reference curve by producing a bias in the affected region of the spectra. Figure 4.20 shows the residuals produced by the cosmic rays (the positive points) and the negative deviation produced in all other epochs that weren't affected by cosmic rays. The algorithm was written using a recursive method to address this effect. In the initial iteration, HARPY flags the positive points above a cut-off value to create a mask. In the current pipeline version, the noise values for this step are calculated but require manual verification to confirm the suitable noise level for clipping (see Figure 4.21 and Section 6.4).

The patching algorithm cleans the spectra in regions where invalid data are present. The flux regions flagged in the previous step are replaced by interpolation. This allows us to re-calculate the summed reference curve and subsequently the residuals. Effects like the one seen in Figure 4.20 are eliminated and a new cleaning iteration can start. With the extreme positive values eliminated, we can assume a reference curve unbiased enough to attempt a clean-up on both the positive and negative sides (see Figure 4.22). The challenge at this step is to find the right noise level. Visual inspection was used to determine this level. The key features to look for are groups of outliers that belong to a single exposure. The noise level chosen should approximate the regions where the individual groups become harder to identify.

To prepare the data for cross-correlation, individual fluxes need to be shaped to maximise the effectiveness of the process. In particular, each spectrum is mean subtracted and a tapering envelope is applied to the 5% of pixels at the ends of the spectrum in order to avoid producing

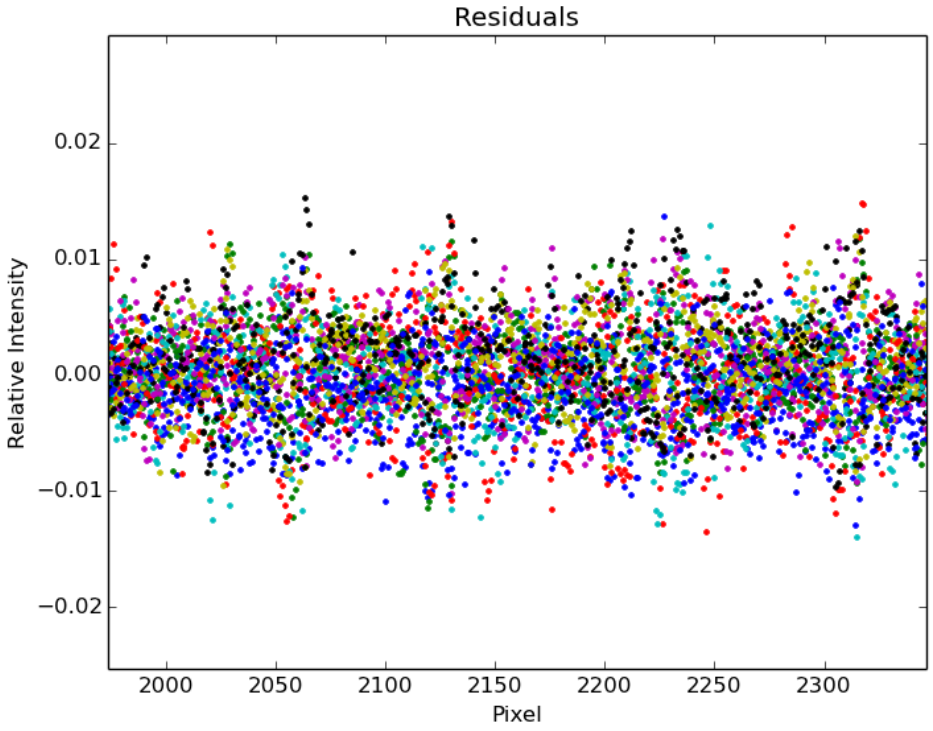

Figure 4.21: A subset of the residuals for all epochs and pixels for HD1581. Unlike the cosmic rays, the electronic noise level cut-off value is much harder to identify.

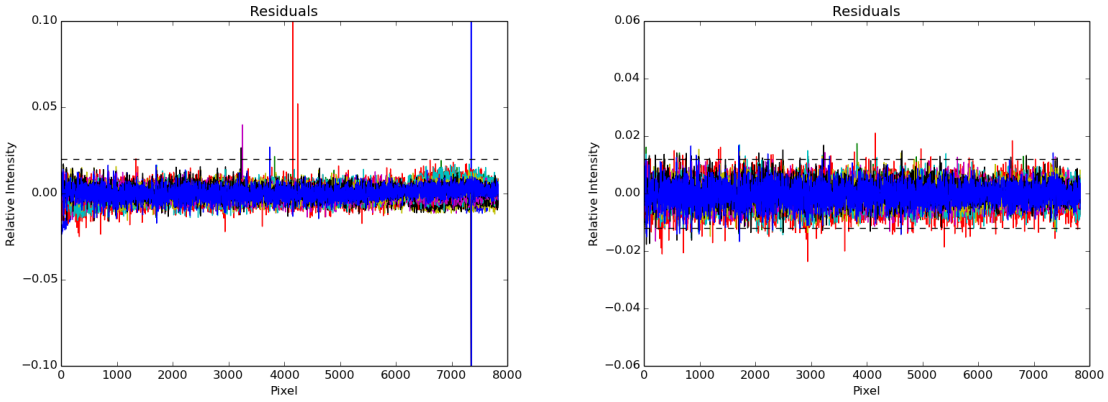

Figure 4.22: The residuals from the summed median flux in the two step clean-up for HD1581. In the first step, the positive outliers are removed and the residuals re-calculated. The new residuals, now referenced from a less biased median flux, can be filtered based on their absolute standard deviation.

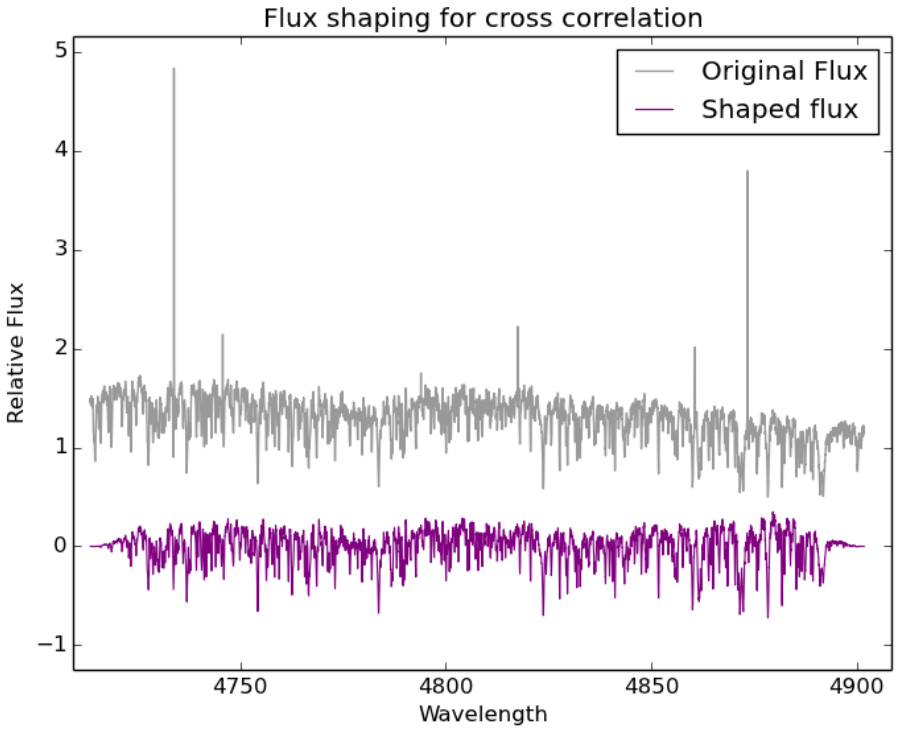

Figure 4.23: An example of the flux of HD1581 as extracted from the image, and the flux after being cleaned and shaped for cross correlation. Cosmic rays and hot pixels are removed, and the spectrum is flattened, normalised and tapered on the ends.

sharp edges into the CCC (see Figure 4.23).

Once the CCC is produced, the index of the array element that contains the peak is identified. In order to increase the precision of the peak identification to a sub-element (sub-pixel) level, a curve must be fitted. For this purpose, a region at both sides of the peak is used. The width of this section depends on the radial velocities expected. In general we used 25 elements on each side. This would allow us to detect a shift of up to $\approx \pm 37\,\mathrm{km\,s^{-1}}$ per epoch. A generalised error distribution curve (see Equation 4.3 and Figure 4.15) is fitted using a least-squares method. The parameters for the best fit include the position of the peak and the width of the curve, which is a measurement of the precision of the fit. The offset between the peak and the centre of the array is recorded as the radial velocity shift between the compared spectra. It is worth noting that the cross-correlation method outlined above is a computationally fast and effective method to compute the radial velocity of a target, and that the basic steps described represent a generally accepted method within the literature of high-precision Doppler velocity studies.

5

Radial Velocity Results

This chapter describes the results obtained with the different reduction methods. The initial three targets were chosen with the purpose of calculating the radial velocity precision of HERMES, and each of the three reduction methods were applied to each target. The spectra were extracted using the 2dfdr standard and 2dfdr single-arc methods, with a purpose-built pipeline, and were also extracted using the HARPY package, specifically developed for this thesis. All radial velocities were calculated from the reduced spectra using HARPY (see Section 4.3).

Each observation was carried out in a similar way. Several science frames were combined with an arc and a flat exposure for calibration. The number of observations associated with each set of calibration frames was usually 3, but it reached as many as 6 observations in some cases. Each group of science observations and calibration frames is referred to as an epoch in this thesis.

The purpose of this reduced dataset was to test the results achievable with each of the methods from the same observations. It became clear from the results that the HARPY pipeline – applied all the way from reduction of the raw data to measurement of the final radial velocity values – yields the highest precision, due to its focus on wavelength consistency across observations. Based on these conclusions we applied the complete HARPY pipeline to further targets in the second part of this chapter.

The radial velocities quoted in the observation tables of each target are the values calculated by the HARPY cross-correlation step from the spectra extracted by the three different reduction methods. The radial velocity value presented for each reduction method and epoch is the average of all the observations associated with it. There have been cases where low SNR has yielded obviously spurious results, and in those cases the individual observations have been eliminated from the calculations on a sigma clipping basis. The error bars presented for each epoch are calculated from the spread in the radial velocities in the associated observations.

We applied two different types of sine fit on these results. The “literature” sine fit has been calculated from the values published in the literature for each target. The period (P) and semi-amplitude (K) were taken from the relevant publications, allowing for a ±10% uncertainty, as they did not include any error values. The phase (ph) and offset (Off) were

allowed to take any values. The second type of sine fit was an unconstrained sine fit. In this mode we allowed all parameters to vary freely. The results produced by this method included a 1-sigma confidence bound associated with each parameter. The sigma value is calculated by the inverse R factor from QR decomposition of the Jacobian, the degrees of freedom for error and the root mean square error. We present these confidence values with the corresponding results in Table 5.5.

Both sine fit optimisation methods aim to minimise the residuals between the radial velocity values calculated via each reduction method and a sine function of the form

$$f(x) = K \times \sin(\frac{2\pi}{P} + 2\pi ph) + \text{Off} \tag{5.1}$$

where K is the semi-amplitude, P is the period, ph is the phase and Off is the offset.

The residuals shown in the lower part of each figure are calculated as the difference between the individual data points and the literature sine curve fit. This does not apply to the stable star (HD1581) as there is no variation expected. The error bars in the residuals are the same as the errors in the data points (i.e., the spread within measurements in a given epoch). The residuals show a comparatively smaller axis range, allowing us to see the relative errors in more detail than in the radial velocity results. The standard deviation of the residuals (σ_{res}) presented in the two tables at the end of the chapter, Tables 5.4 and 5.5, are calculated from the differences between the radial velocities and the corresponding sine fit.

Some of the targets presented in this chapter were chosen because they had a known periodic radial velocity signal(ρ Tucanae and HD285507) or were known to be stable stars (HD1581). Other targets were selected from the rest of the data sources (see Chapter 3) because their radial velocities were indicative of periodic behaviour. In these cases, an unconstrained sine curve fit was attempted by a least-squares method. In the cases of systems with known parameters, the values found using the HARPY pipeline are in agreement with the values from the literature.

The discussion in this chapter includes the results from ρ Tucanae, HD285507 and HD1581, in addition to selected targets from 47 Tucanae, NGC2477 and M67. The chapter concludes with a summary of results from the targets used for radial velocity precision calculations.

5.1 ρ Tucanae

This bright single-lined spectroscopic binary, a main sequence F6V-type star, shows a large radial velocity variation over the 5 days of observation due to an unseen companion. This characteristic makes ρ Tucanae an excellent target to test the functionality of the core modules of the pipeline, as it presents none of the challenges that low signal or low radial velocity amplitude targets would add to the development and testing of the complete pipeline.

Binary star systems show similar radial velocity variations to the ones found in exoplanet hosts, but typically with much larger amplitudes. The spectral signature measured depends on the relative brightnesses of the orbiting stars. Spectroscopic binaries share the characteristic that they are only detected by their effect on the observed spectra; their angular separation is too small to be observed astrometrically. When the relative luminosities of the members of

the system are different, only the spectral features of the brightest member can be detected, but it is still affected by the Doppler wobble induced by its companion's presence. For this observation a single-lined spectroscopic binary was chosen, as it eliminates the difficulties associated with separating the superimposed spectra of both stars.

Observations were carried out over a period of 5 days. The first observed epoch consisted of 8 observations taken with the purpose of testing the SNR achievable with different exposure times. The rest of the epochs were done with 3 to 5 science observations. Exposure times varied from 120 seconds to 600 seconds, to compensate for temporary high clouds.

ρ Tucanae is the "safest" target in terms of the relative uncertainties that each method would produce, due to the relatively large expected radial velocity amplitude. Nonetheless, individual methods still carry the absolute uncertainties produced by their corresponding algorithms, primarily influenced by the effect of the approaches taken in the wavelength calibration steps.

ρ Tucanae is a bright target and, for the 2dfdr standard method, the SNR ranges from $\approx$20 to $\approx$220. An unconstrained sine fit produced a semi-amplitude of 25730$\pm$380 m s^{-1} with a period of 4.813$\pm$0.021 days, and a standard deviation of the residuals of 280 m s^{-1}, with a median uncertainty per epoch of 129.5 m s^{-1}. In comparison, the literature fit produced a semi-amplitude of 25660 m s^{-1} and a period of 4.8 days with a standard deviation of the residuals of 260 m s^{-1}. These parameters agree with previously published results (Pourbaix et al., 2004) (see Table 5.4).

The 2dfdr single-arc method (see Section 4.3) produced the lowest SNR after extraction, which decreases as a function of epoch. This, in general, is due to an increasingly outdated tramline map as the time between the reference epoch and a given observation increases. The 2dfdr single-arc method has the largest uncertainties in the unconstrained sine fit parameters.

The HARPY method results produce a 27130$\pm$140 m s^{-1} semi-amplitude with a period of 4.766$\pm$0.018 days, and a standard deviation in the residuals of 99 m s^{-1} with a typical uncertainty of 77.1 m s^{-1}. It produced the highest overall SNR in comparison with the other methods. This is due to an exposure-specific tramline parametrisation that analysed a single fibre at a time. A key indication of the advantage of HARPY is shown in the uncertainties of the unconstrained sine fit parameters and the corresponding residuals of the radial velocity values (see Figure 5.1 and Table 5.1).

In summary, for our unconstrained sine fit, all three methods produce results that are close to those in the literature for ρ Tucanae. This is expected because of ρ Tucanae's large radial velocity amplitude. We note that the median error bars for the standard method and the HARPY method are similar, $\approx$65 m s^{-1}, but the 2dfdr single-arc method has a large median uncertainty of 339 m s^{-1}. However, we find that the literature fit parameters, which are allowed to vary within 10% of the quoted values, produce excellent matches to the 2dfdr standard and HARPY methods, with a standard deviation of the residuals of 260 m s^{-1} and 110 m s^{-1}, respectively. The lower residuals to the fit shown by HARPY support our conclusion that the HARPY radial velocities are more precise.

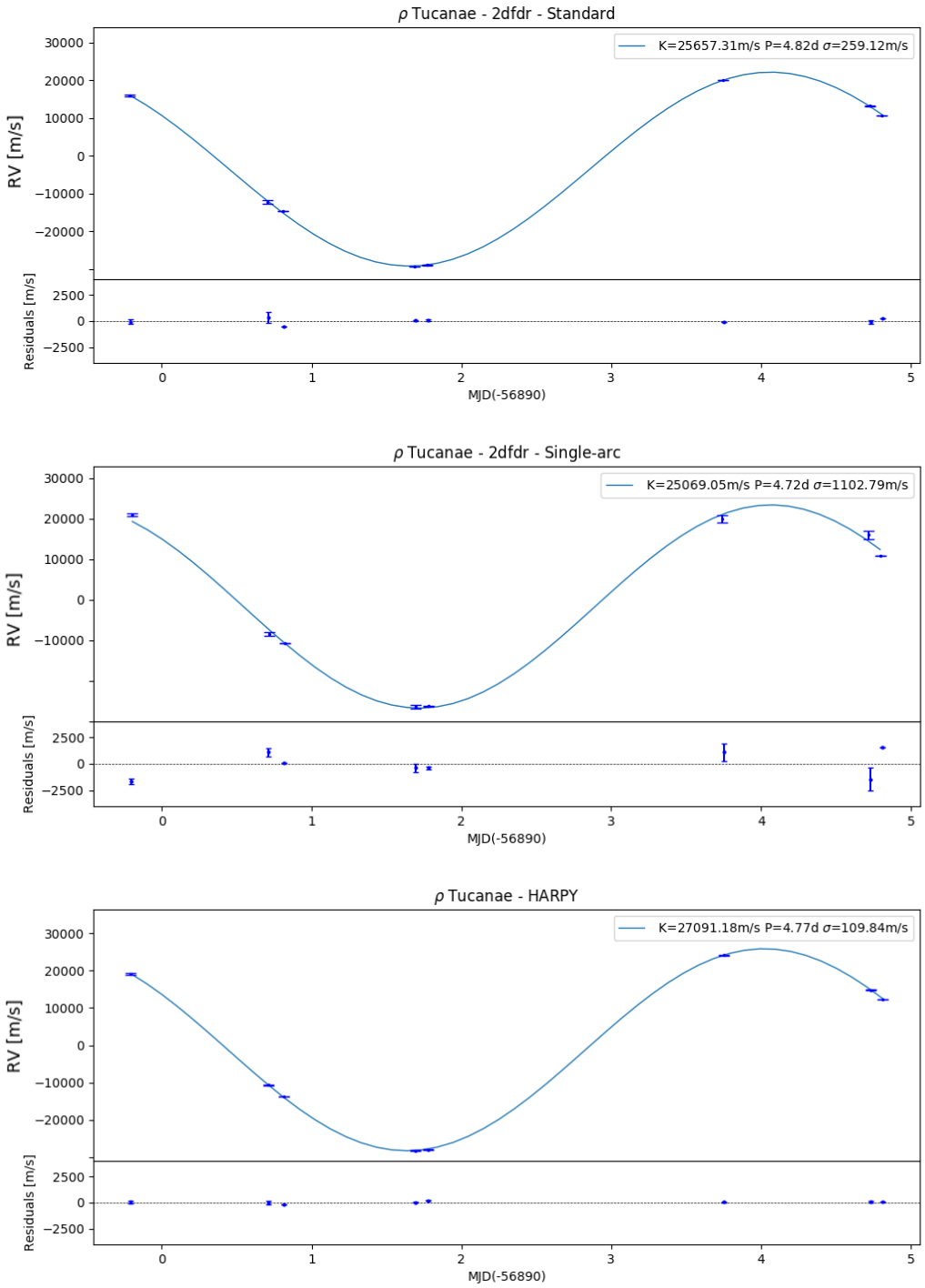

Figure 5.1: Radial velocity curves and residuals of ρ Tucanae constructed from the results of the 3 methods. Residuals are calculated from fitted curve-observed. The error bars in the 2dfdr standard and HARPY methods are on the order of $\approx 100\,\mathrm{m\,s^{-1}}$, noticeable in the residuals figure. The 2dfdr single-arc method produces a similar fit to the 2dfdr standard method; however, the residuals are substantially larger. Error bars are calculated from the standard deviation of the results. The HARPY method produces results that match the values from the literature with error bars that range from $\approx 180\,\mathrm{m\,s^{-1}}$ to $\approx 32\,\mathrm{m\,s^{-1}}$ and with smaller residuals than the other 2 methods.

		2dfdr - Standard		2dfdr - Single-arc		HARPY	
Obs	MJD	SNR	RV [m/s]	SNR	RV [m/s]	SNR	RV [m/s]
0	56889.783	149.96	16180.97	149.96	21195.25	167.77	19416.13
1	56889.788	167.75	16265.88	167.75	21284.82	187.76	19306.73
2	56889.792	97.44	15825.46	97.44	20677.55	108.10	19093.86
3	56889.794	93.53	16286.69	93.53	21360.73	103.92	19098.26
4	56889.796	97.39	15577.50	97.39	20549.40	108.61	19077.05
5	56889.799	95.09	16029.28	95.09	20805.98	105.78	19071.48
6	56889.801	95.18	16105.83	95.18	20794.91	106.39	18985.69
7	56889.803	97.90	16169.00	97.90	20968.14	109.80	18893.96
8	56890.704	95.65	-11555.79	84.91	-7948.20	107.46	-10454.11
9	56890.711	155.57	-12447.03	135.64	-8404.63	176.33	-10643.23
10	56890.719	179.02	-12779.49	155.29	-8948.52	203.96	-10901.65
11	56890.817	21.38	-14592.50	20.34	-10812.04	22.21	-13863.77
12	56891.691	188.47	-29201.99	136.19	-26153.24	212.65	-28319.70
13	56891.696	185.31	-29217.01	133.38	-26901.11	209.33	-28195.00
14	56891.701	182.67	-29150.50	131.06	-25974.89	206.56	-28193.18
15	56891.778	209.76	-28997.67	146.29	-26418.49	234.45	-28036.97
16	56891.783	208.30	-28797.26	144.67	-26098.73	233.46	-27972.42
17	56893.747	220.38	20104.73	78.01	19809.93	223.85	24079.84
18	56893.753	186.59	20123.97	66.05	21145.81	190.39	24126.72
19	56893.759	184.85	20080.18	65.13	19084.08	188.78	24251.38
20	56894.725	155.37	13446.57	11.07	15044.50	159.75	14954.97
21	56894.730	180.67	13079.80	12.84	15459.92	187.79	14835.05
22	56894.735	179.84	13150.94	12.77	17541.49	187.52	14756.02
23	56894.811	131.72	10730.36	9.23	10886.05	134.94	12412.40

Table 5.1: Radial velocity and SNR results of the observations of ρ Tucanae extracted by the 3 methods. Horizontal lines separate epochs. As expected, the 2dfdr - single-arc method shows the lowest SNR values. It decreases as the elapsed time between the reference tramline and a given observation increases. The SNRs of the observations extracted with the HARPY method show the highest values. The resulting radial velocity measurements from HARPY are within the expected values from the literature and carry the lowest uncertainties.

5.2 HD285507

HD285507 is an exoplanet host. This star was chosen as it exhibits a level of radial velocity variability that sits at the limit of the spectral resolution theoretically predicted for HERMES. With a published semi-amplitude of 125 m s^{-1} and a period of 6.09 days (Quinn et al., 2014), the attempt to detect this planet provides a key test of the radial velocity precision attainable with HERMES.

Planets produce a periodic variation in the radial velocity observed in their host star. Due to the differences in their masses, this signature is considerably smaller than the one expected from binary stars. Most exoplanets discovered by the radial velocity method exhibit a host star radial velocity amplitude smaller than 200 m s^{-1} (see Figure 1.4). It is for this reason that the radial velocity precision attainable with an instrument is a key characteristic limiting the potential detection of exoplanets.

HD285507 was observed over 5 days. At V=10.5, this target required exposures between 5 and 15 minutes to reach the desired SNR. Each epoch had 3 observations of varying exposure times depending on cloud cover.

The results obtained from HD285507 were a crucial test of the capacity of HERMES to detect exoplanets. The 2dfdr standard method was originally assumed to be able to detect velocity variations on the order of those expected for this target. HARPY's radial velocity precision was challenged for the first time with this target, as these measurements were made right after the successful results with ρ Tucanae.

The 2dfdr standard method literature sine fit produced a σ_{res}=95 m s^{-1}, found a period of 5.5 days and a radial velocity semi-amplitude of 132 m s^{-1}. The HARPY method with a literature sine fit found the same period and a semi-amplitude of 126 m s^{-1} but with a σ_{res} of only 29 m s^{-1}. As shown in Figure 5.3, the HARPY radial velocities phase up closely with those found in (Quinn et al., 2014).

The results of the 2dfdr - single-arc method obtained at this stage highlighted the intrinsic challenges of this approach. There is a clear decrease in the SNR as we move further from the reference epoch, reaching as low as ≈1.5 at the last epoch. This drop in the SNR strongly affected the resulting radial velocity precision, as evidenced by the large σ_{res} shown in both the free parameters fit and the literature fit (see Tables 5.4 and 5.5).

HARPY produces the highest SNR and the most accurate results. As noted above, the literature fitted sine curve produces a radial velocity semi-amplitude of 126 m s^{-1} and a period of 5.5 days with a residual standard deviation of 29 m s^{-1}. In comparison, the unconstrained fitted sine curve shows a radial velocity semi-amplitude of 129.5±315.1 m s^{-1} and a period of 6.07±12.3 days with a residual standard deviation of 40 m s^{-1}.

These results give us confidence that the variations detected by the HARPY method are astrophysical in nature, which is not the case for the 2dfdr methods, as evidenced by their residuals to the literature fit. While these may not be conclusive results for an exoplanet detection, a radial velocity variation of this amplitude using HARPY could be considered trustworthy enough to warrant additional observations. It opens up the possibility of using HERMES as a planet-finding instrument. These results could potentially be improved with better bracketing of science exposures with arc calibration frames, and with higher SNR observations (see Section 6.2.1).

In conclusion, the 2dfdr single-arc results were poor due to their low SNRs. The 2dfdr standard and HARPY methods had similar uncertainties per epoch, but the residuals to the

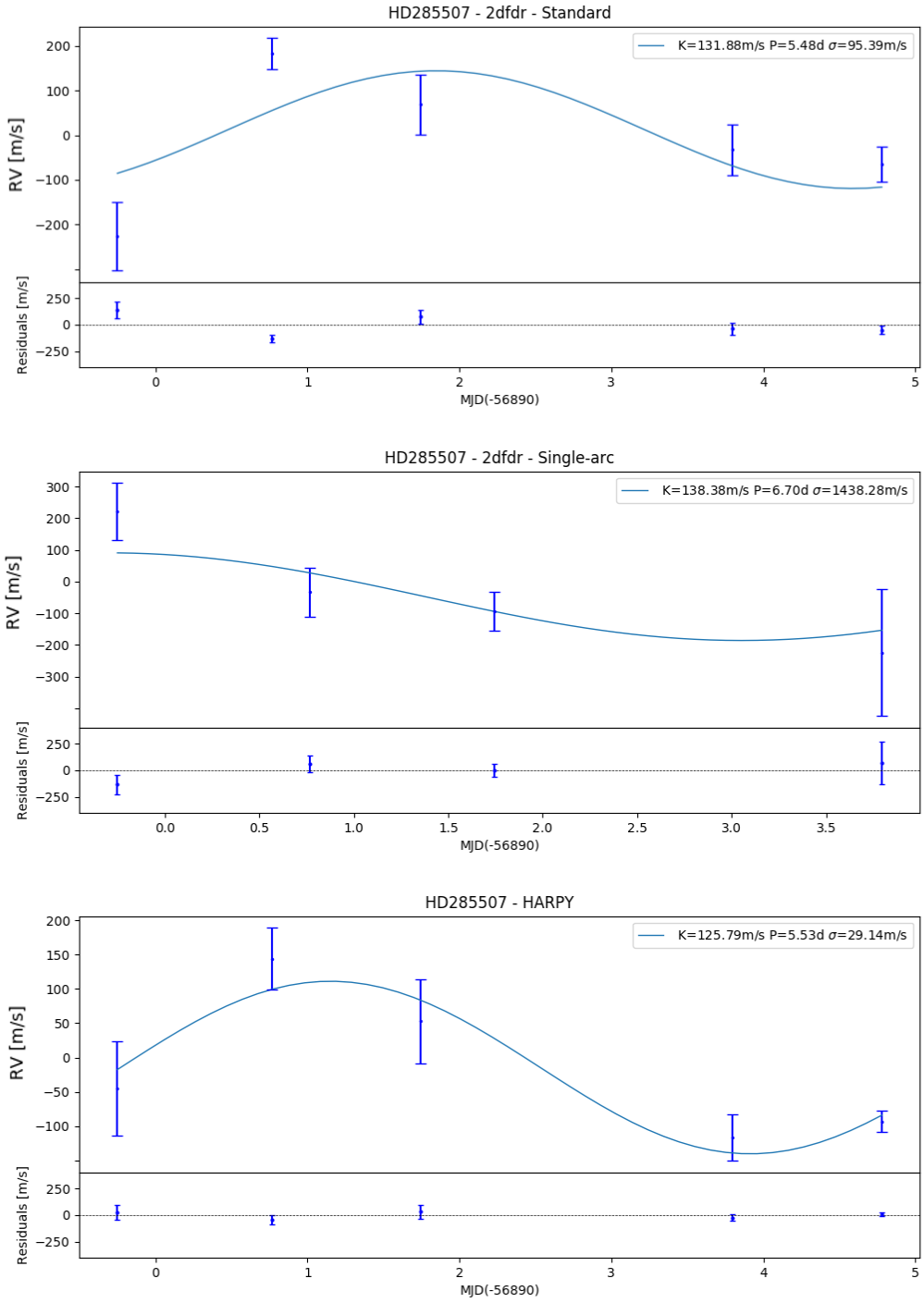

Figure 5.2: Radial velocity curves of HD285507 constructed from the results of the three methods. Residuals are calculated from fitted curve-observed. 2dfdr standard results show relatively small error bars, yet the fit to the data is quite poor. The 2dfdr - single-arc results are clearly noise dominated. Only four points are shown in the figure, as there was a fifth point that had very low SNR and yielded a radial velocity value far outside the expected range; It was omitted from this figure. HARPY produces results that are consistent with a planet candidate detection, which is also supported by the small residuals.

		2dfdr - Standard		2dfdr - Single-arc		HARPY	
Obs	MJD	SNR	RV [m/s]	SNR	RV [m/s]	SNR	RV [m/s]
0	56889.735	20.41	-119.99	20.41	348.30	21.12	148.08
1	56889.748	27.47	-256.67	27.47	169.59	28.80	-121.59
2	56889.763	27.43	-301.35	27.43	146.10	28.93	-160.56
3	56890.745	28.18	232.10	26.88	68.53	29.98	206.82
4	56890.767	34.63	155.30	32.70	-117.92	37.48	122.73
5	56890.788	34.87	161.32	32.92	-51.75	37.71	102.39
6	56891.728	33.05	162.16	27.58	-15.42	35.37	155.77
7	56891.743	29.51	37.76	24.95	-167.43	31.33	62.26
8	56891.758	29.02	7.38	24.60	-96.42	30.73	-58.48
9	56893.781	33.72	23.48	16.53	-128.64	36.81	-129.77
10	56893.796	32.85	-109.63	16.20	-502.62	35.66	-150.11
11	56893.808	23.30	-10.98	12.54	-40.61	24.77	-70.70
12	56894.765	34.19	-97.07	1.14	5381.36	37.12	-108.03
13	56894.780	34.80	-87.99	1.79	3144.70	37.72	-100.63
14	56894.795	31.11	-9.90	1.43	2616.94	33.24	-71.65

Table 5.2: Radial velocity and SNR results for the observations of HD285507 obtained with the 3 methods. Horizontal lines separate epochs. The 2dfdr standard method and HARPY show consistent SNR values. The gradual degradation of the tramline mapping with time can be seen in the extreme decrease in SNR in the later epochs for 2dfdr single-arc method.

literature sine fit and the unconstrained sine fit were considerable smaller for HARPY. This is strong evidence that the epoch to epoch wavelength solution for HARPY is more consistent, despite the fact that within a given epoch the two methods produce a similar amount of scatter in the observations.

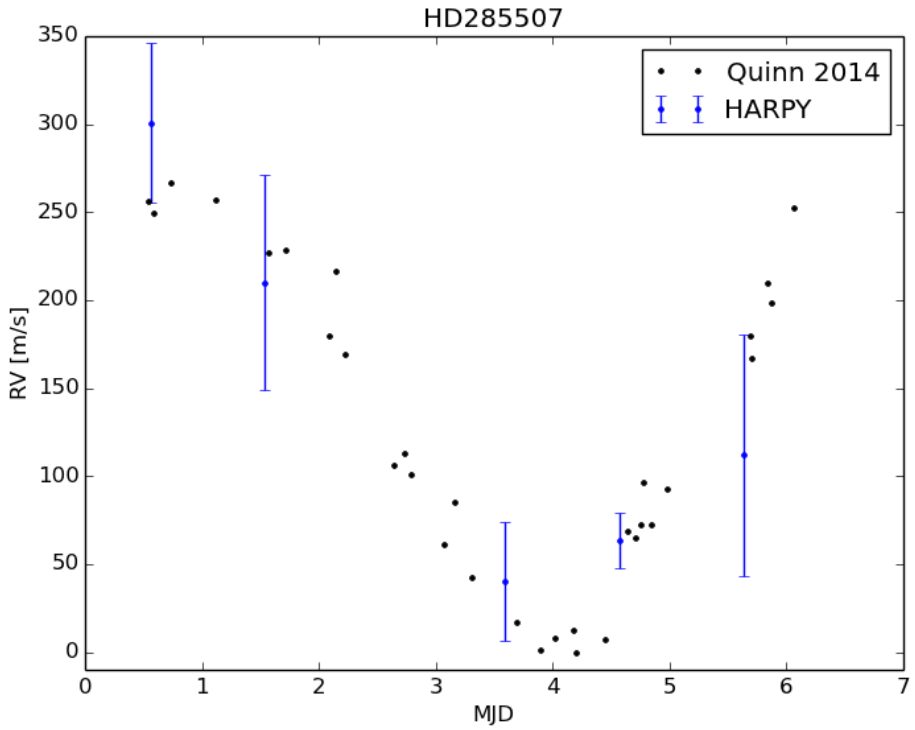

Figure 5.3: Data from Quinn et al. (2014) with the HARPY results added. HARPY data have been period folded and the values shifted to fit the approach taken in the literature. Error bars are as per Figure 5.2 (HARPY)

5.3 HD1581

This star has been observed extensively using the HARPS spectrograph. While ρ Tucanae was chosen as a reference target due to its large radial velocity amplitude, HD1581 was chosen for the opposite reason, namely its radial velocity stability. Observations over 2566 days with a radial velocity scatter of $1.26\,\mathrm{m\,s^{-1}}$ (Pepe et al., 2011) make this star an ideal radial velocity calibrator. Expecting it to show no detectable radial velocity variations makes any measured deviation from constant radial velocity an accurate indicator of an instruments overall stability, and allows us to quantify the limits of the data reduction and analysis process.

The absolute limiting factor in radial velocity measurements is set by the star itself. Granulation and rotation impose a minimum value on the radial velocity precision attainable from a star (see Section 4.3.2). Granulation represents localised convective motion on the photosphere of a star that includes a line-of-sight component of motion, adding noise to the measurements. In addition, the rotation of a star blurs spectral features by shifting their rest wavelength by an amount related to the radius of the star and the phase of rotation during an exposure period. This effect translates to a broadening of the spectral features, decreasing the attainable precision. Different stellar types are associated with different combinations of these two effects. However, a star that has been observed to be stable provides an empirically tested reference that can be used as a calibrator, relatively independent of stellar type.

The observations of HD1581 were carried out as by placing one of the central fibres on a single target, namely the star. The observations span 5 days, and the observing times were short, between 30 seconds and 2 minutes, due to the star's brightness (V= 4.23). The time

		2dfdr - Standard		2dfdr - Single-arc		HARPY	
Obs	MJD	SNR	RV [m/s]	SNR	RV [m/s]	SNR	RV [m/s]
0	56889.811	211.72	-253.78	211.72	568.09	244.78	-0.75
1	56890.804	166.24	86.43	144.09	-19.14	185.83	114.60
2	56890.807	98.25	80.52	86.37	16.42	109.35	102.56
3	56890.809	144.14	99.99	124.69	27.95	161.75	109.26
4	56891.707	193.18	-74.79	138.94	-326.39	219.21	39.15
5	56891.709	189.58	-38.37	136.20	-224.61	214.68	72.91
6	56891.711	190.10	-100.53	136.66	-380.57	215.28	76.98
7	56893.765	267.47	-276.15	85.46	-993.94	323.94	-32.99
8	56893.767	220.19	-279.51	71.00	-996.53	266.60	-41.48
9	56893.768	135.83	-257.23	45.11	-685.12	163.12	-36.22
10	56893.769	136.03	-262.40	45.29	-468.31	164.52	-68.67
11	56893.771	129.15	-255.13	43.04	-491.50	155.34	-45.25
12	56894.743	159.48	851.98	9.51	1109.25	189.23	-66.87
13	56894.745	155.40	789.83	9.23	1502.32	185.04	-74.64
14	56894.746	166.80	837.53	9.77	635.21	199.59	-82.32

Table 5.3: Radial velocity and SNR results of the observations of HD1581 for the three methods. Horizontal lines separate epochs. As a known consequence of the 2dfdr single-arc method, the SNR decreases towards the end of the observing run. This effect leads to an increasingly inaccurate wavelength solution, as seen in the increase in the size of the error bars and particularly in the offset of the final epoch. HARPY shows a high SNR across all observations and shows the lowest radial velocity dispersion of the set.

variations are the result of adjustments in the SNR and temporary clouds.

The observations of a stable star provide the possibility of a useful empirical method to test the stability of the observations and reduction methods. Each of the three reduction methods used in this thesis were tested on the stable star. In particular, the concept behind the 2dfdr single-arc method aims to reduce the uncertainty introduced by an inconsistent wavelength scale model, while maintaining the functionality of 2dfdr (see Section 4.3). This was of particular interest in the context of these observations.

The standard 2dfdr reduction of HD1581 yielded a good SNR as expected for a V=4.23 magnitude star, ranging from ≈100 to ≈220. This method produced what we expected to be the best possible performance for HERMES radial velocity precision at the time. Despite a small median uncertainty per epoch, $17.7\,\mathrm{m\,s^{-1}}$, these results showed a large standard deviation on the residuals, $\pm 400\,\mathrm{m\,s^{-1}}$. These results helped trigger the decision to attempt new data reduction methods, initially led by the 2dfdr single-arc method and later followed by HARPY.

2dfdr single-arc shows several effects in the data. The decrease in SNR, from 211.72 to 9.77, as the time interval between a given observation and the beginning of the set increases. This effect creates an increasingly larger spread on the results of each individual epoch. This is an effect carried from the low SNR in the arc extraction. It is particularly noticeable in the last group of data points that shows the lowest SNR in the dataset, leading to a radial velocity result over $1500\,\mathrm{m\,s^{-1}}$ above the expected value. In particular, the last epoch shows an issue

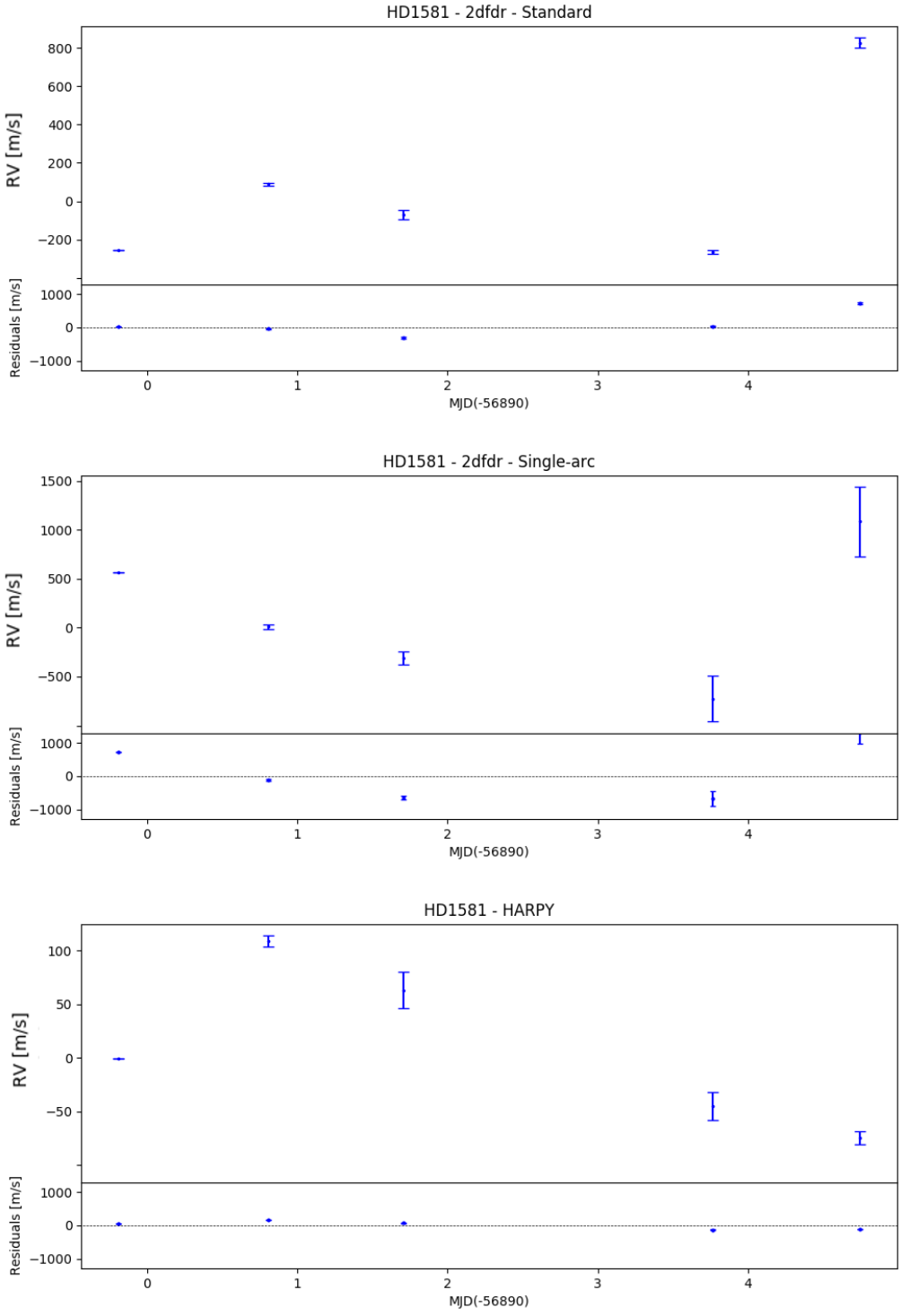

Figure 5.4: Radial velocity curves of HD1581 constructed from the results of the three methods. Residuals are calculated from fitted curve-observed. As with the previous stars, the HARPY method shows smaller residuals than both the 2dfdr standard and the 2dfdr single-arc methods. HARPY shows a standard deviation of $\approx$70 m s^{-1}. These represent the most precise radial velocity result achieved with HERMES to date.

with the wavelength scale model due to an unusually low SNR in the arc. The origin of this issue is not clear; perhaps there might have been a technical malfunction during the observing process. The proposed live monitoring feature addition to the pipeline would detect these type of issues (see Section 6.4).

The complete HARPY reduction method shows the most promising radial velocity results. The use of HD1581 as a calibration star, with an expected stability below the precision limits of the instrument, makes any result different from $\approx 0\,\mathrm{m\,s^{-1}}$ a measurement of the instrument's instability and the effectiveness of the data reduction pipeline. The standard deviation of the HARPY radial velocities is the smallest of the three methods.

2dfdr standard shows an uncertainty per epoch of 17.7 $\mathrm{m\,s^{-1}}$ but a much larger epoch to epoch scatter of $400\,\mathrm{m\,s^{-1}}$. Similarly, HARPY shows an uncertainty per epoch of $9.5\,\mathrm{m\,s^{-1}}$ and an σ_{res} of $71\,\mathrm{m\,s^{-1}}$. These two results indicate that both methods are successful at tracking the changes in the instrument within an epoch. However, they do not track the changes from epoch to epoch as well as their uncertainties suggest. The development of a wavelength solution for HARPY with a focus on calibration consistency across epochs is reflected in the lower scatter in the radial velocity values. Nonetheless, further refinements to improve the tracking of these instrumental changes are suggested in Section 6.4.

5.4 Other Targets

Having tested the velocity precision attainable with HARPY, we decided to go back and apply it to the dataset observed in January 2014 and the selected GALAH data (see Section 3.1). To obtain preliminary velocities, HARPY was run with a standard parametrisation on the complete dataset. This included the extraction of the spectra from the raw images, the radial velocity determination, and a sine fit to the velocities.

We examined the entire dataset for stars observed with consistent observing parameters and produced results for each target. The importance in keeping the observing parameters consistent, was to avoid additional variability due to extra instrumental effects like position on the field, plate number or fibre throughput (see Section 6.2.1).

We visually inspected each target looking for clear radial velocity variability with relatively low radial velocity scatter within each epoch. There were several targets that were flagged for follow up. We selected one interesting target for each dataset and we then re-reduced those targets with a special focus on the individual reduction parameters using the complete HARPY method.

The following three datasets are examples of targets that show interesting features and caught our attention. Some were known binaries or variables and some others were certainly interesting targets for science follow-up, either with a different observing strategy (see Section 6.4) or with a different instrument.

5.4.1 47 Tucanae

The core of the globular cluster 47 Tucanae is too densely populated to be able to target individual stars on a single fibre. This dataset was generated at a distance from the core where crowding was still likely, but aimed at the brightest stars to minimise the effects of the fainter companions.

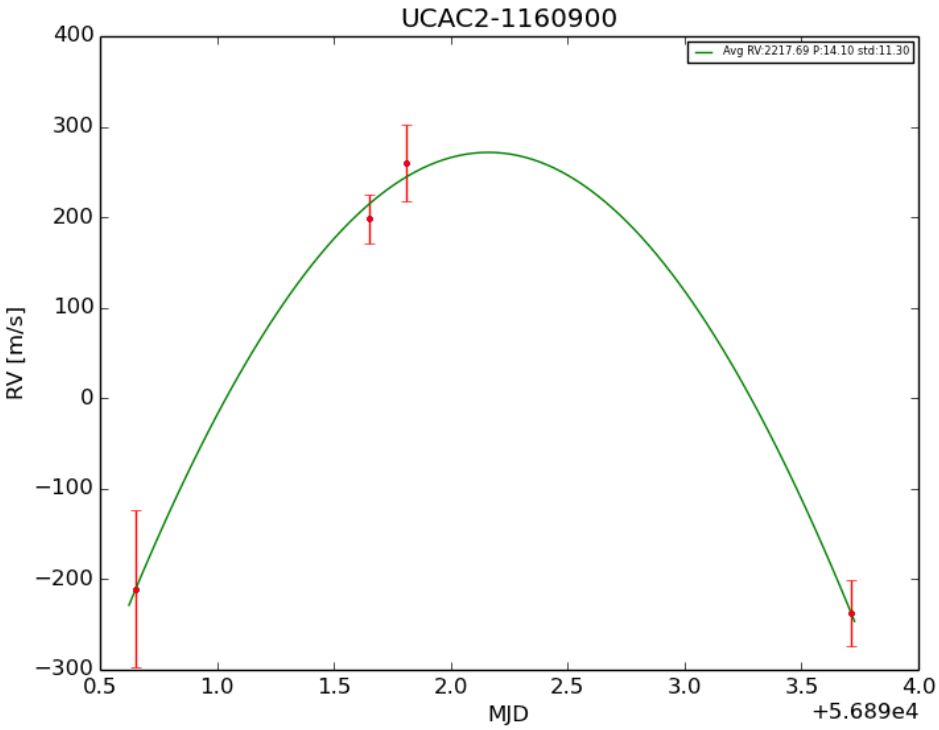

Figure 5.5: Radial velocity curve measured for the star UCAC2-1160900 (Bright67). The small uncertainty of each epoch compared to the magnitude of the change in radial velocity, suggests intrinsic stellar radial velocity variability.

We chose the star UCAC2-1160900 (Bright67) as an object of interest. It shows a typical uncertainty in its radial velocities of $\approx$100 m s^{-1} and we see a clear variation over the period of observation of $\approx$400 m s^{-1} (see Figure 5.5).

Lebzelter et al. (2005) shows this star's photometric and radial velocity variability studied over several years. The period and amplitude quoted in Lebzelter et al. (2005) is 52 days and 4$\pm$1 km s^{-1}. However, this published work lacks the spectroscopic and temporal resolution to be able to compare their results with the scale of variability detected in this thesis.

5.4.2 NGC2477

This member of NGC2477 open cluster, 253-020236 in the UCAC4 catalogue, shows a large radial velocity variation over the $\approx$2 days of observation (see Figure 5.6). The results are distributed in only 2 groups, not enough data points for constraining a sine curve. However the amplitude of the variation may indicate that it is a single-lined spectroscopic binary.

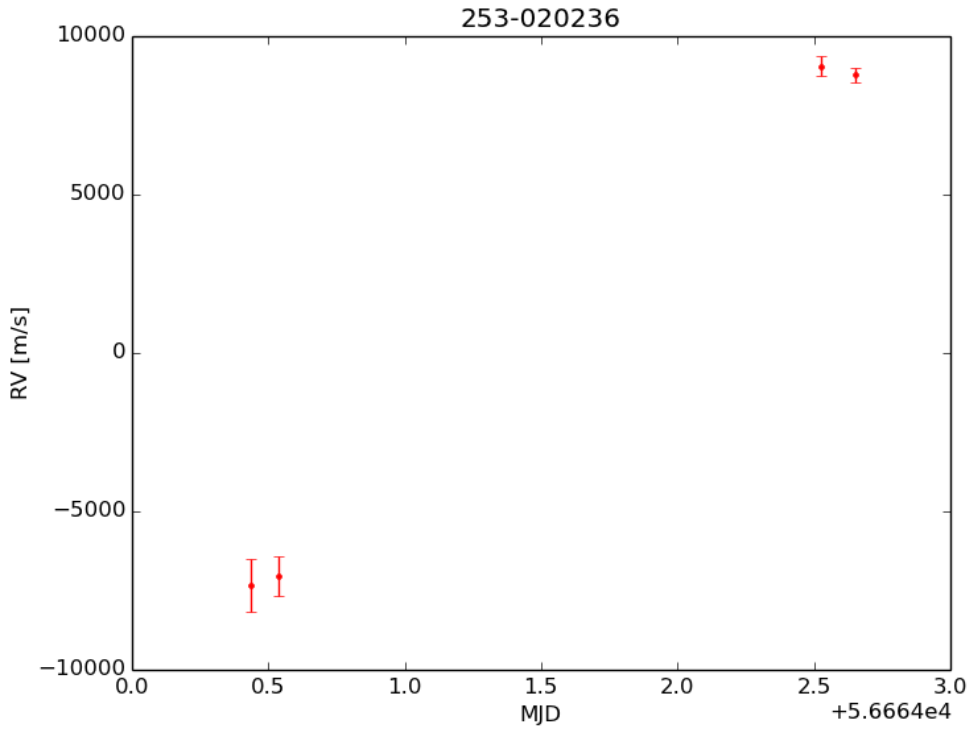

Figure 5.6: Radial velocity curve measured for the star 253-020236. There are not enough points to constrain a sine curve. It is worth noting that there is a significant change in radial velocity during the observing period.

5.4.3 M67

The open cluster M67 was targeted as part of the HERMES commissioning calibration, the GALAH survey and in our own observations. The star s654 (Sanders, 1977), shows a large radial velocity amplitude and low spread within the individual epochs. A sine curve was fitted suggesting a 12.6 km s^{-1} amplitude over a 4.54 day period. However, this result is based on a limited number of data points and therefore the parameters have significant uncertainty. Geller et al. (2015) includes this star as a single-lined spectroscopic binary, which is consistent with our observations.

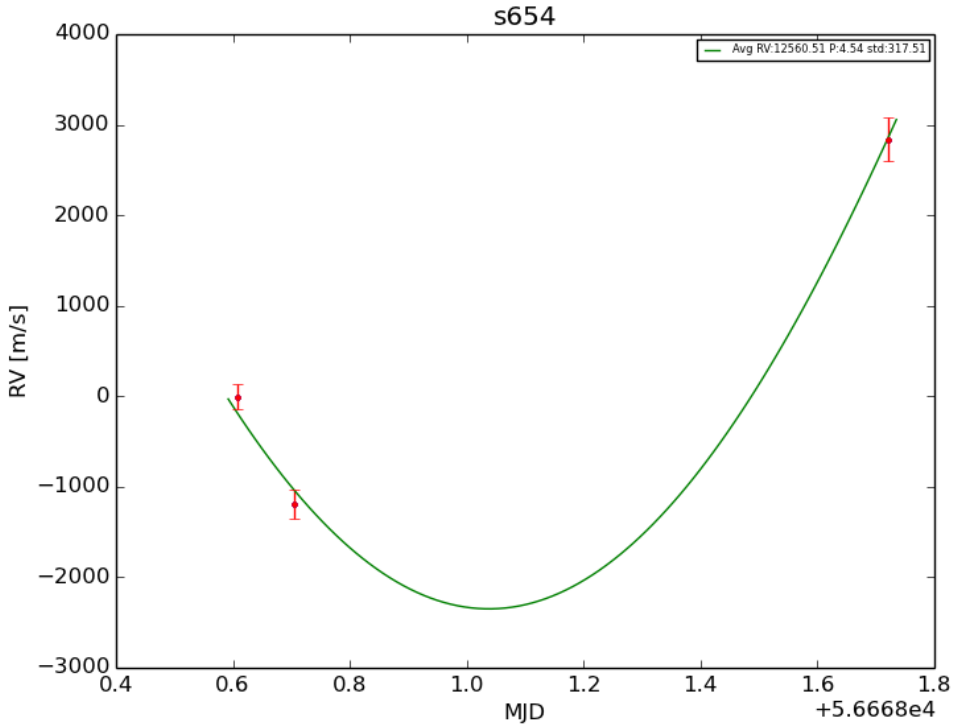

Figure 5.7: The star S654 in M67 exhibits a large radial velocity amplitude, with each epoch exhibiting a small uncertainty. Despite the small number of points, this suggests a single line spectroscopic binary which is consistent with Geller et al. (2015).

5.5 Summary of Results

In this chapter we have described the radial velocity results obtained with the three methods of analysis used for the chosen calibrator stars. Throughout the analyses, HARPY produced spectra with higher SNR and velocities with smaller uncertainties than the other two methods.

Our first calibrator target was ρ Tucanae, a single-lined spectroscopic binary. The median error bars for the 2dfdr standard method and the HARPY method are similar, $\approx$129 m s^{-1} and $\approx$77 m s^{-1} respectively, but those for the 2dfdr single-arc method are $\approx$5 times larger. The literature fit parameters produced excellent matches to the 2dfdr standard and HARPY results, with lower residuals shown by the HARPY fits.

Our next calibration target was the exoplanet host HD285507. The 2dfdr single-arc results were particularly poor for this target due to low SNR. The 2dfdr standard and HARPY methods had similar uncertainties per epoch, but the residuals to both the unconstrained and literature sine fit were considerably smaller for HARPY.

Our final calibration target was the radial velocity stable star HD1581. 2dfdr standard results showed a small median uncertainty per epoch, $\approx$17.7 m s^{-1} but a large scatter across epochs $\approx$400 m s^{-1}. Similarly, HARPY showed a small median uncertainty per epoch $\approx$9.5 m s^{-1} but a smaller scatter than 2dfdr standard across epochs $\approx$71 m s^{-1}.

In addition we showed that, using HARPY, we were able to detect several likely spectroscopic binary stars from our larger sample of star cluster data: UCAC2-1160900, 253-020236 and s654.

Star	Method	Literature Fit K [m/s]	Literature Fit P [days]	σ_{res} [m/s]
ρ Tucanae	2dfdr standard	25660	4.8	260
	2dfdr single-arc	25100	4.7	1100
	HARPY	27090	4.7	110
HD285507	2dfdr standard	132	5.5	95
	2dfdr single-arc	138	6.7	1400
	HARPY	126	5.5	29
HD1581	2dfdr standard	0	0	400
	2dfdr single-arc	0	0	700
	HARPY	0	0	71

Table 5.4: Literature fit results for each target and method. The fit values were allowed to vary within 10% of the literature values. The HARPY residuals are considerably smaller than the residuals from the other methods.

Star	Method	Calculated Sine Fit K [m/s]	Calculated Sine Fit P [days]	σ_{res} [m/s]
ρ Tucanae	2dfdr standard	25730±380	4.813±0.021	280
	2dfdr single-arc	25800±1700	4.69±0.21	1400
	HARPY	27130±140	4.766±0.018	99
HD285507	2dfdr standard	149.3±1505.5	5.17±22.0	110
	2dfdr single-arc	413.4±13595	1.78±21.9	1500
	HARPY	129.5±315.1	6.07±12.3	40

Table 5.5: Unconstrained sine curve fit results of the data calculated by each method. The HARPY methods produced residuals that are smaller than the other 2 methods and the fit parameters matched the literature values.

In conclusion we have demonstrated that HARPY yielded an improvement on the radial velocity precision of HERMES data relative to the 2dfdr methods used for comparison. We were able to identify the radial velocity signature from a planet and quantify the new measurable radial velocity limit of HERMES using HARPY at $\approx 70\,\mathrm{m\,s^{-1}}$.

6
Conclusions

The initial aims of this thesis were to determine the radial velocity precision attainable with the HERMES spectrograph and, depending on the results, to apply this new instrument to fields ranging from exoplanet detection and characterisation to asteroseismology. Delays in the commissioning of the instrument and calibration issues with the existing data reduction pipeline led to a change in focus, namely to develop a wavelength solution that improves the precision achievable with the HERMES spectrograph and apply it to a range of science applications.

We achieved this goal in several steps. We first used the design of the RHEA spectrograph to build a physically driven forward model for the instrument. By optimising the model parameters iteratively we matched the observed spectrum produced by the spectrograph. This provided insight into the behaviour of the instrument under changing conditions.

We carried this experience and understanding into our work with the HERMES spectrograph, where our aim was to maximise the radial velocity precision attainable. We found that the complex intrinsic variability of HERMES led us toward an empirical calibration, more similar to a traditional analysis than the model-driven approach we used with RHEA. With this decided, and after determining that existing HERMES data reduction software was not adequate for our needs, we set out to write our own extraction and calibration pipeline that focussed on wavelength stability across time. The most significant change from the traditional approach was to examine the position and stability of emission lines in calibration spectra across all epochs.

In order to benchmark our software against existing options we chose 3 calibrator stars with decreasing amplitudes of radial velocity variability. By analysing the results we were able to directly compare both the absolute velocity precision attainable as well as the improvement that our technique was able to bring to the HERMES spectrograph data. We successfully demonstrated that our method could improve the radial velocity precision of HERMES to levels previously unattainable; in particular we showed that we could reach the $\approx 70\,\mathrm{m\,s^{-1}}$ level, effectively demonstrating the HERMES spectrograph's capacity for exoplanet searches.

This chapter summarises the goals reached, and the lessons learned from the observing and reduction methods, and proposes new options for applying these methods. Finally, we discuss a range of potential scientific follow-up programs with HERMES that are now

possible with the advances made through this project.

6.1 Summary of Conclusions

In this section we highlight the achievements throughout the thesis, with particular emphasis on the individual milestones reached in each section.

We worked on developing a physically motivated wavelength scale model for the RHEA spectrograph. This exercise entailed writing wavelength scale modelling software for precision radial velocity measurement. It provided hands-on experience in connecting the software with the hardware components and understanding the interdependencies. No on-sky data could be collected with the RHEA spectrograph within the time allocated before the HERMES spectrograph became available for the remainder of this thesis, but we applied the knowledge gained in this effort toward the early stages of the development of HARPY.

Analysing the performance of HERMES helped us gain an understanding of what could be expected from the instrument. Instrumental characteristics with a high impact, such as the variations of the PSF across the CCD, and less complex (but still important) effects, like the numbering system for the fibres, have an major influence on the approach taken in the software. The need for many of these measurements was not always clear at the early stages of the project, yet the collection of these data proved extremely useful for producing the final version of the software.

After a comparison between the different data reduction software options, it became clear that the available software could at best only approach the level of radial velocity precision required for exoplanet searches in HERMES data. Having assessed the results with 2dfdr and the modified version of 2dfdr using a single arc, we began developing our own HERMES data reduction software customised for higher radial velocity precision, which we called HARPY.

HARPY was fully developed in the Python programming language. This allowed us to have full control of the reduction process and gave us flexibility to monitor each step. In addition, Python has been widely adopted by the astronomical community, allowing us to take advantage of a large number of freely available standardised tools and libraries. We then developed HARPY CC, a radial velocity calculation pipeline based on the cross-correlation method, a computationally fast, effective and widely used method for measuring the radial velocity of a target.

Having developed and tested HARPY to our satisfaction, we empirically assessed the differences between HARPY, the standard 2dfdr pipeline and the modified single-arc 2dfdr pipeline on a variety of selected targets.

Our first target was ρ Tucanae, a single-lined spectroscopic binary, and for our unconstrained sine functional fit, all three methods produced results that are close to those in the literature. This was to be expected due to the star's large radial velocity amplitude. We noted that the median error bars for the 2dfdr standard method and the HARPY method were similar but those for the 2dfdr single-arc method were ~5 times larger. The literature fit parameters produced excellent matches to the 2dfdr standard and HARPY results, with lower residuals shown by the HARPY fits. These measurements were the initial indication of HARPY outperforming the other 2 methods.

Our next calibration target was the exoplanet host HD285507. The 2dfdr single-arc results were particularly poor due to low SNR. The 2dfdr standard and HARPY methods had similar uncertainties per epoch, but the residuals to both types of sine fit were considerable smaller for HARPY. This was strong evidence for the consistency of wavelength solution for HARPY.

Our final calibration target was the stable star HD1581. 2dfdr standard results showed a small uncertainty per epoch but a large scatter across epochs. Similarly, HARPY showed a small uncertainty per epoch but a smaller scatter than 2dfdr - standard across epochs. We confirmed the suitability of both methods to track the changes in the instrument within an epoch. But, again, we demonstrated that the development of a wavelength solution for HARPY with a focus on calibration consistency across epochs was reflected in the results.

At this point we had demonstrated that HARPY yielded an improvement on the radial velocity precision of HERMES data. We were able to identify the radial velocity signature from a planet and quantify the new measurable radial velocity limit of HERMES. Nonetheless, further refinements to the method to track instrumental changes are suggested in Section 6.4.

6.2 Lessons from the Observational Strategy and Reduction Methods

A core component of this thesis is the maximisation of the science achievable with the HERMES spectrograph. In this context, carefully identifying the lessons learned is a key aspect of the steps towards further improvement of the methods applied. This section summarises the most important lessons learned.

6.2.1 Observational Strategy

One of the consistent challenges found across the dataset was the low SNR, particularly in the arc frames. This translates into an uncertainty in the identification of the position of the emission peaks. The function that relates known wavelength values with pixel positions depends on the correct identification of the position of the emission peaks to a sub-pixel level in order to build a valid wavelength solution. In addition to this effect, the low signal can leave weak emission lines under the detector noise level, effectively reducing the number of anchor points that the wavelength solution can use. Both of these effects lead to inaccuracies in the wavelength solution that, in turn, can reduce the accuracy and precision of the radial velocity calculations. The standard arc exposures times for HERMES are 180 seconds. Increasing the exposure time as a way to increase SNR can lead to problems in the cadence of the science frames. Increasing illumination of the fibres instead, can increase SNR without increasing exposure time, but it requires modifications in the telescope.

When observations are performed using different fibres or plates, the differences in these configurations can be complex and difficult to model. At the moment it is unclear if it is possible to characterise these effects well enough to completely remove, or even reduce, their influence on the data. Until these effects are understood, comparing spectra from the same star when observed on different fibres or plates will add noise above the expected science results, limiting this approach to targets with high radial velocity variability, i.e., those for which the Doppler shift can overcome the noise effects.

An additional consideration for the observation of precision radial targets is the frequency of arc exposures as timestamps of the status of the instrument. The reduction of the arc frames, and consequent calculation of its wavelength scale, allows us to gain understanding of the instrument's stability. An investigation of our data has shown that a drift of several pixels in both the spectral and spatial directions can be expected over a night's observations. This is, in principle, accounted for with the individual calculations of the wavelength scale model using the emission lines in the arcs as anchor points, but the drift introduces distortions that

not only shift but also stretch the wavelength solution. In addition, spectral lines are not abundant or stable enough to allow us to fully map-out this drift in enough detail across multiple observations. This limitation is one of the fundamental limits of the precision of this dataset. A specific improvement to the current observing strategy would be to bracket the observations, or at least the group of observations, to be able to model the instrumental drift during the exposure time.

6.2.2 Reduction Methods

HERMES employs Thorium-Xenon arc lamps as wavelength calibrators, which produce a limited number of emission lines in the wavelength range of the spectrograph. One of the key strengths of the HARPY approach to the wavelength scale model calculation method used for this study is the pre-determination of the stable arc lines across the complete sample for an individual target. The limited number of known wavelengths for the Thorium-Xenon lamps is increased to include all detected peaks, thereby increasing the number of anchors for the wavelength solution beyond the number of identified emission lines. At the same time, the step to verify the stability of these lines across epochs leads, in many cases, to a reduced number of emission lines that can be used to anchor the wavelength scale model in a way that is valid for all observations in the set. As a consequence, certain regions of the spectra carry an inaccurate wavelength value, affecting the position of the cross-correlation peak and consequently the derived radial velocity value.

Cosmic rays introduce sharp streaks across the CCD that translate into peaks in the extracted flux, affecting the cross-correlation curve and the estimation of its peak. There are two basic approaches to the removal of cosmic rays: it is possible to remove them from the 2-dimensional spectrum image, or they can be removed from the 1-dimensional extracted spectrum of the source data. These two options have different consequences and can affect the resulting radial velocity measurements. In particular, the latter is the method used in this thesis. The detection of cosmic ray spikes is done by estimating a continuum and measuring the deviation of each point from it. This allows us to identify and eliminate outliers based on a reference value. By using this method, we address the cosmic ray issue, as well as a fraction of the detector noise.

6.2.3 Instrumental Effects

HERMES has known limitations to its image quality due to distortions in the PSF. These distortions increase as one approaches the edges of the CCD and are noticeable in both the spatial and spectral directions, see Figure 2.11. This characteristic of the spectrograph has two distinct consequences.

The spatial PSF distortion leads to fibre cross-talk, i.e. the contamination of neighbouring fibres, see Figure 2.12. The result is that the extracted flux will contain a fraction of the flux that belongs to a neighbouring fibre, adding unwanted flux to the spectrum.

In contrast, the spectral PSF distortion will either merge adjacent spectral lines, or stretch existing lines. The effect reduces the precision with which the pixel position of emission peaks can be identified. This affects the way the wavelength solution is constructed, and consequently adds uncertainty to the radial velocity measurements.

HERMES detectors require thermal stabilisation to minimise the amount of electronic noise transferred into the image (Sheinis et al., 2015). All detectors are housed in a sealed thermally stable environment. At present, the blue channel is the only camera holding its

vacuum seal over long periods, while the other 3 channels need to be pumped down every few days. This is not an issue for individual observations, but over long baseline observations, as it is the case with radial velocity variability measurements, the changes in pressure introduce additional uncertainty to the measurements. This was the reason for focusing this thesis on blue channel data. In addition, the detector focal position is re-adjusted every night, creating differences in the fields produced that are not monitored during the night.

The wavelength calibration of HERMES is calculated from arc frames that are illuminated by Thorium-Xenon lamps. As has been pointed out, these images are observed at a different point in time than the science frames. There are differences in the instrument between the exposures. Some of these differences can be modelled and removed. The residuals become noise in the final data and a source of uncertainty. One way to eliminate this effect from an instrumental design angle is to add a simultaneous wavelength reference source. There are several options currently in use elsewhere that take this approach. The addition of a reference source in the light path, commonly an iodine cell (Butler et al., 1996), accomplishes this result at the cost of reduced throughput. Alternatively, some systems use dedicated fibres, usually within each bundle, to carry a reference source that is used during the reduction process.

6.3 Further reduction options

What follows is a description of the tests that, in addition to the work done for this thesis, could further improve the results from the current dataset. These are specific tests that would require relatively straighforward changes to the HARPY pipeline.

The cross-correlation produces a curve that peaks when the two compared spectra reach their best match. This process reflects how each individual part of one spectrum matches the corresponding section of the other spectrum; however, not all parts of the spectrum are equally useful for radial velocity estimation. Typical reasons for a section of spectrum to be less useful can include the imperfect removal of cosmic rays, an inaccurate wavelength solution or a region dominated by noise.

A method that could address these issues is the cross-correlation by sections. In this approach each spectrum is divided into several portions, and the corresponding sections cross-correlated. This method produces several radial velocity values per epoch. The advantage is that the outliers can be identified, pointing to any problem regions. A closely related method consists of mapping out regions of the spectrum that are known to be less accurate (e.g., intrinsically variable absorption lines) in order to reduce noise and increase precision.

The current dataset has relatively low SNR in most of the subsets. This issue could potentially be resolved by co-adding the flux of individual observations that are close in time to each other. This was part of the original goal of the observations: to reach $\sim$ 100 SNR one would need approximately 60 minutes total integration time for a 14^{th} magnitude star. We followed that guideline by doing 3 exposures of 20 minutes each. However, the results presented here were calculated by using individual exposures and then combining the results.

Certain emission lines from an arc lamp can be weak in intensity, yet stable as a wavelength reference. Our ability to measure their position in the spectrum is dependent on the SNR of the arc lines. These weaker lines could be potentially used as anchors for the wavelength scale model but they would require longer exposures to be useful. At the same time, the stronger emission lines could potentially saturate with longer exposure times. The suggested exposure times currently used for HERMES arc lamps are based on the saturation of the strongest

lines. A possible improvement would to find the "sweet spot" in exposure time that would maximise the number of available lines, even if some to the strongest lines would then need to be ignored due to saturation. Based on a preliminary analysis of the fainter emission line intensities of HERMES arc lamps, a much longer exposure time may be needed, and hence this issue might be better addressed by increasing the brightness of the arc lamps (e.g., by adding additional lamps), rather than by simply increasing the exposure times to potentially impractical levels.

6.4 Large-scale pipeline development

While writing the reduction code for this thesis we adopted an iterative approach; the improvements that were gathered during the development and testing of a given version were collected for later implementations. This process led to the final version used to reduce the data included in this thesis. Nonetheless, some features were not included in the final pipeline version. In addition, several other potential improvements became clear during the implementation of the pipeline. This section describes the most relevant items from the development list that could be included in future versions.

Some of the shortcomings in the data used in this thesis could have been detected during the observing run, see section 6.2.1. Having a live analysis of the data, as they are taken, would permit the adjustment of parameters and updates of the observing plans accordingly. A key example of this is the estimation of the signal levels. Early detection of a low signal level would allow us to reach a target SNR by increasing the exposure times, see Figure 6.1.

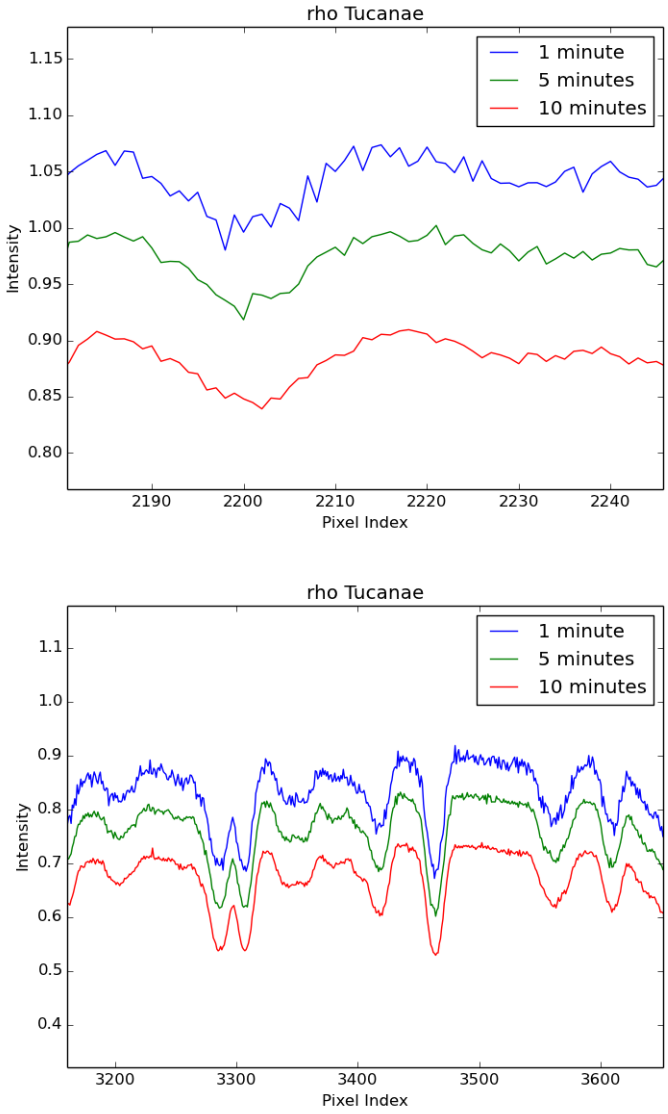

Figure 6.1: The normalised spectrum from ρ Tucanae, taken with 3 different exposure times. Each spectrum is offset for clarity. The relative effects of electronic noise affecting the target's signal become clear in the shortest exposure.

Understanding the stability of the instrument and being able to model the changes is a key step in precision radial velocity measurements. In order to increase the accuracy of the model, arc lamp images need to be taken more often than was done for the current dataset. A single arc associated with a set of science exposures is not enough to capture the instrumental changes to the level required for precise radial velocity determination. Above, we proposed bracketing each exposure or at a minimum each epoch with a set of arc images. The software could also be significantly improved with the addition of an algorithm that interpolates the instrumental drift to build a wavelength solution that is valid at the exact time of a given observation. In addition, the statistical information produced from the understanding and monitoring of the drifts over time can give insight on instrumental limitations that could potentially be resolved (e.g., the time-varying impact of the cameras' faulty vacuum seals).

The differences in throughput across different fibres and wavelengths introduce complexities in the analysis of reduced data. A throughput map that produces a scaling coefficient as a function of fibre, wavelength and plate position would allow us to, in principle, compare exposures from different fibres and plates, see Simpson et al. (2016). This would increase the range of targets in the final dataset by allowing us to compare observations of the same target through different fibres or plates.

The spatial PSF becomes increasingly distorted as we approach the edge of the CCD. This creates a contamination effect known as cross-talk, where the light from a given fibre is compromised by unwanted light from a neighbouring fibre. The cross talk between fibres can be at least partially removed if the neighbour spectrum is known. Currently up to $\sim 5\%$ of the flux can belong to a neighbour fibre near the edges of the CCD. Potential software improvements could include a cross-talk elimination algorithm. An example of an approach that aims to eliminate cross-talk is the more complex extraction method known as spectro-perfectionism (Bolton and Schlegel, 2010). This approach completely reconstructs the image from a full description of the 2-dimensional PSF as a function of position in the detectors. It has been proven to effectively extract the flux from adjacent fibres, almost eliminating cross-talk. However its implementation is complex and requires long processing times. For the purposes of this thesis, this issue has been addressed in most cases by avoiding configuring adjacent fibres.

The wavelength solution calculation is the single most important part of the reduction process. Attempting to detect shifts in spectra of the order of 0.02 pixels relies primarily on an accurate wavelength solution. There are several changes that could potentially improve the calculation of the wavelength solution. The addition of a star with known absolute radial velocity can provide a calibrator that not only can help to test the data reduction methods, but also can help to calibrate the wavelength solution across channels. At the moment, the red, green and Infra Red (IR) channels are producing inconsistent radial velocity results. A wavelength solution that includes the 4 channels, and that produces consistent results, would require extensive testing with a radial velocity calibrator.

In order to clean-up the spectra from the effects of cosmic rays, a recursive approach is taken. The process looks for outliers in the extracted 1-dimensional spectra. Cosmic rays are usually easy to identify as their flux levels are much higher than the continuum. Whilst our approach is effective at finding outliers, the resulting interpolation over the cosmic rays can be better implemented in the 2-dimensional image domain, prior to spectral extraction. Several algorithms are available in the literature that would be suitable for this purpose (Pych, 2004; Hirst et al., 2014; Hill et al., 1997).

6.5 Follow-up

There were over 1000 targets in the complete dataset attained as part of this thesis. These objects are a combination of a few targets selected due to their known characteristics, and a large collection of background targets included either by virtue of their position in the field or because of their membership to a given cluster. The radial velocity curves for all of the targets were individually calculated.

The combined dataset allows for a range of analytical methods with higher complexity than is possible with a single star. Further pipeline developments can aim towards this kind of research. A particular emphasis should be placed on obtaining a wavelength calibration which is stable across fibres and detectors, in addition to the current multi-epoch stability. Having a consistent dataset, calibrated for differences in CCD position, fibre throughput, plate position, etc. would allow us to pursue additional science, such as can be derived from the statistical properties of several samples taken from the same group.

As an example, the members of a given star cluster, with measured radial velocity curves, can be combined to form a complex parameter space that includes isochrone fits, asteroseismologically derived parameters and chemical tagging to constrain the uncertainties in stellar parameters. In addition, any potential discovery of binary systems or exoplanets can reduce the uncertainty in the companion's derived parameters through a better understanding of the host's properties.

6.6 Closing Comments

The extended period of time occupied by a doctoral thesis project is usually associated with, and is perhaps unavoidably accompanied by, changes in one's life circumstances.

In a similar fashion, this thesis has changed focus since its original course was laid out, which is by no means an unusual story. The important lesson was learning to deal with constraints and limitations, and to overcome – or, when necessary, work around – them.

With the goal of precisely measuring the radial velocities of large numbers of targets simultaneously, we found ourselves facing a challenge, but also an opportunity. We have made great progress and opened new possibilities. It is this author's wish to see the ramifications of this work expand and evolve, to find the obstacles and continue to push through them.

A
Acronyms

2dfdr Two Degree Field Data Reduction

AAO Australian Astronomical Observatory

AAT Anglo-Australian Telescope

ATAC Australian Telescope Allocation Committee

CCC Cross-Correlation Curve

CCD Charged Coupled Device

DRAMA Distributed Real-time AAO Monitor for Astronomy

FITS Flexible image Transport System

FLAMES Fibre Large Array Multi Element Spectrograph

FWHM Full Width Half-Maximum

GALAH Galactic Archaeology with HERMES

HARPS High Accuracy Radial velocity Planet Searcher

HARPY HERMES Automated Radial velocities in PYthon

HDU Header Display Unit

HERMES High-Efficiency and Resolution Multi-Element Spectrograph

IR Infra Red

IRAF Image Reduction and Analysis Facility

KOALA Kilofibre Optical AAT Lenslet Array

NIST National Institute of Standards and Technology

NOAO National Optical Astronomy Observatories

PSF Point Spread Function

RHEA Replicable High-Resolution Exoplanets and Asteroseismology

SAMI Sydney-Australian-Astronomical-Observatory Multi-object Integral-Field Spectrograph

SNR Signal-to-Noise Ratio

VLT Very Large Telescope

VPH Volume Phase Holographic

WSM Wavelength Scale Model

B

Radial Velocity Equation

This appendix focuses on the derivation of the radial velocity equation from first principles. It is based on work presented in my Honours thesis (Bacigalupo, 2013). It assumes 2 bodies of masses m_1 and m_2 orbiting at a maximum distance a.

Initially, the two-body analysis can be reduced to a single body by adjusting the semi-major axis using the reduced mass formula

$$a_1 = \left(\frac{m_2}{m_1 + m_2}\right) a \tag{B.1}$$

where a_1 is the semi-major axis of the body analysed and $a = a_1 + a_2$ is the maximum distance between the objects. The distance from any point on the orbit to the centre of mass of the system can be written as

$$r = \frac{a_1(1 - e^2)}{1 + e\cos f} \tag{B.2}$$

where e is the eccentricity and f is the true anomaly[1], or substituting a_1,

$$r = \left(\frac{m_2}{m_1 + m_2}\right) \frac{a(1 - e^2)}{1 + e\cos f}. \tag{B.3}$$

Adopting a Cartesian set of coordinates concentric to the system's barycentre with the $\hat{\mathbf{x}}$-axis pointing in the direction of periastron, the position and velocity vectors are

$$\mathbf{r} = \begin{pmatrix} r\cos f \\ r\sin f \end{pmatrix} \tag{B.4}$$

,

and

[1]The angle formed by the position of the object, the centre of mass and the point in the orbit where the body is further from the centre of mass, or periapse

$$\frac{\mathbf{dr}}{\mathbf{dt}} = \begin{pmatrix} \frac{dr}{dt}\cos f - r\frac{df}{dt}\sin f \\ \frac{dr}{dt}\sin f + r\frac{df}{dt}\cos f \end{pmatrix}, \tag{B.5}$$

respectively.

Keeping in mind that the goal is to find the velocity as a function of f, $\frac{dr}{dt}$ and $\frac{df}{dt}$ need to be expressed as a function of f.

Differentiating Equation B.2 we obtain

$$\frac{dr}{dt} = \frac{a_1 e(1-e^2)}{(1+e\cos f)^2}. \tag{B.6}$$

Simplifying with

$$1 + e\cos f = \frac{a_1(1-e^2)}{r} \tag{B.7}$$

from Equation B.2, we find

$$\frac{dr}{dt} = \frac{er^2\frac{df}{dt}\sin f}{a_1(1-e^2)}. \tag{B.8}$$

by replacing in Equation B.5 we obtain

$$\frac{\mathbf{dr}}{\mathbf{dt}} = \begin{pmatrix} \frac{e\,r^2\frac{df}{dt}\sin f}{a_1(1-e^2)}\cos f - r\frac{df}{dt}\sin f \\ \frac{e\,r^2\frac{df}{dt}\sin f}{a_1(1-e^2)}\sin f + r\frac{df}{dt}\cos f \end{pmatrix}. \tag{B.9}$$

The following steps are a simplification of the last expression.

$$\frac{\mathbf{dr}}{\mathbf{dt}} = r\frac{df}{dt}\begin{pmatrix} \frac{e\,r\sin f}{a_1(1-e^2)}\cos f - \sin f \\ \frac{e\,r\sin f}{a_1(1-e^2)}\sin f + \cos f \end{pmatrix} \tag{B.10}$$

$$\frac{\mathbf{dr}}{\mathbf{dt}} = r\frac{df}{dt}\begin{pmatrix} \frac{e\,r\sin f}{a_1(1-e^2)}\cos f - \frac{r(1+e\cos f)\sin f}{a_1(1-e^2)} \\ \frac{e\,r\sin f}{a_1(1-e^2)}\sin f + \frac{r(\cos f + e\cos^2 f)}{a_1(1-e^2)} \end{pmatrix} \tag{B.11}$$

$$\frac{\mathbf{dr}}{\mathbf{dt}} = \frac{r^2\frac{df}{dt}}{a_1(1-e^2)}\begin{pmatrix} e\sin f\cos f - (1+e\cos f)\sin f \\ e\sin f\sin f + \cos f + e\cos^2 f \end{pmatrix} \tag{B.12}$$

$$\frac{\mathbf{dr}}{\mathbf{dt}} = \frac{r^2 \frac{df}{dt}}{a_1(1-e^2)} \begin{pmatrix} -\sin f \\ \cos f + e \end{pmatrix} \tag{B.13}$$

Energy and angular momentum are constants of motion of the system. Using $h_1 = m_1 r^2 \frac{df}{dt}$ as the angular momentum, Equation B.13 can be rewritten as

$$\frac{\mathbf{dr}}{\mathbf{dt}} = \frac{h_1}{m_1 a_1(1-e^2)} \begin{pmatrix} -\sin f \\ \cos f + e \end{pmatrix} \tag{B.14}$$

.

The expression of the angular momentum of the system in terms of the semi-major axis, a, and the eccentricity, e, is

$$h = \sqrt{G(m_1 + m_2)a(1-e^2)}. \tag{B.15}$$

h_1 can then be expressed in terms of h by using the reduced mass equation, yielding

$$h_1 = \left(\frac{m_2}{m_1 + m_2}\right) h = \sqrt{\frac{G m_1^2 m_2^4 a(1-e^2)}{(m_1+m_2)^3}}. \tag{B.16}$$

Replacing back in Equation B.14 we find the general expression for the velocity as a function of f,

$$\frac{\mathbf{dr}}{\mathbf{dt}} = \sqrt{\frac{G m_2^2}{(m_1+m_2)a(1-e^2)}} \begin{pmatrix} -\sin f \\ \cos f + e \end{pmatrix} \tag{B.17}$$

This equation is expressed in the frame of reference centred in the centre of mass of the system with the $\hat{\mathbf{x}}$-axis pointing in the direction of periastron. To transform it into an equation that can be used to interpret observations from Earth, we need to find the projection of the velocity vector into the line of sight.

The vector $\mathbf{k}$ can be described in terms of the frame of reference of the system, with the reminder that the $\hat{\mathbf{z}}$ is perpendicular to the other 2 vectors conforming to a right-hand convention. In such reference frame the $\mathbf{k}$ vector can be expressed as

$$\mathbf{k} = \begin{pmatrix} \sin\phi \sin\theta \\ \cos\phi \sin\theta \\ \cos\theta \end{pmatrix} \tag{B.18}$$

where θ and ϕ are the polar and azimuthal angles respectively in the reference frame of the system. Then

$$\begin{aligned}\frac{\mathbf{dr}}{\mathbf{dt}} \cdot \mathbf{k} &= \sqrt{\frac{G}{(m_1+m_2)a(1-e^2)}} m_2 \sin\theta(\sin f \sin\phi + \cos f \cos\phi + e\cos\phi) \\ &= \sqrt{\frac{G}{(m_1+m_2)a(1-e^2)}} m_2 \sin\theta(\cos(\phi+f) + e\cos\phi)\end{aligned} \tag{B.19}$$

We are interested in the radial velocity semi-amplitude,

$$RV = \left((\frac{\mathbf{dr}}{\mathbf{dt}} \cdot \mathbf{k})_{max} - (\frac{\mathbf{dr}}{\mathbf{dt}} \cdot \mathbf{k})_{min} \right) /2 \tag{B.20}$$

, so

$$RV = \sqrt{\frac{G}{(m_1+m_2)a(1-e^2)}} m_2 \sin\theta. \tag{B.21}$$

This equation allows us to link the observations of radial velocity variations with the mass and separation of the observed system. As it is mentioned in the thesis, the angle between the line of sight and the system can't be measured by the radial velocity method, so the coefficient $\sin\theta$ remains unknown until measurements from a different method are incorporated.

C Targets Observed

This appendix contains the complete list of targets observed.

C.1 ρ Tucanae - Binary System

Name	Kmag	RA(hms)	DEC(dms)
Field01	8.13	0h42m29.90s	-65d23m03.8s
Field02	6.58	0h42m41.30s	-65d36m30.8s
Field03	6.73	0h44m31.00s	-65d26m32.7s
Field04	8.34	0h42m36.50s	-65d12m33.1s
Field05	4.95	0h44m39.30s	-65d38m58.2s
Field07	8.27	0h43m22.80s	-65d04m14.2s
Field08	6.78	0h40m50.30s	-65d51m26.7s
Field09	8.83	0h40m14.50s	-65d49m30.6s
Field10	7.68	0h43m30.50s	-65d03m14.8s
Field11	7.45	0h42m43.60s	-64d58m44.8s
Field13	8.91	0h36m58.00s	-65d11m49.6s
Field14	6.0	0h48m41.00s	-65d34m10.4s
Field15	5.48	0h43m16.70s	-64d49m10.1s
Field17	8.98	0h39m18.80s	-66d04m14.7s
Field18	8.99	0h45m 3.00s	-64d49m32.7s
Field19	5.92	0h38m 8.40s	-66d02m34.2s
Field20	8.71	0h48m30.80s	-65d05m47.4s
Field21	8.24	0h36m 6.50s	-65d48m17.1s
Field22	8.74	0h49m22.90s	-65d40m13.9s
Field23	8.92	0h49m16.70s	-65d50m55.7s
Field24	8.37	0h38m52.80s	-64d45m08.4s
Field25	8.63	0h36m35.20s	-64d55m37.6s
Field26	8.43	0h36m55.00s	-64d52m00.9s
Field27	7.58	0h49m27.90s	-65d00m16.3s
Field28	7.74	0h36m52.10s	-64d49m40.5s

Name	Kmag	RA(hms)	DEC(dms)
Field29	5.4	0h36m22.60s	-64d46m45.2s
Field30	8.7	0h43m55.00s	-64d31m27.9s
Field31	8.18	0h41m42.40s	-64d30m30s
Field32	8.77	0h36m45.00s	-66d14m33.7s
Field33	8.98	0h51m34.50s	-65d14m35.9s
Field34	6.69	0h40m19.90s	-66d25m31.1s
ρ-Tucanae	4.17	0h42m28.40s	-65d28m05s
Giant02	8.85	0h43m57.50s	-65d14m33.7s
Giant03	7.69	0h38m23.40s	-65d31m17.2s
Giant04	7.94	0h47m23.20s	-65d33m22.4s
Giant05	3.51	0h36m37.70s	-65d07m28s
Giant06	8.85	0h48m20.40s	-65d06m49.1s
Giant07	8.19	0h39m15.80s	-66d09m32.9s
Giant08	8.11	0h50m 9.80s	-65d18m05.1s
Giant09	8.22	0h48m59.70s	-64d58m27.4s
Giant10	7.75	0h41m37.60s	-66d23m04.8s
Giant11	8.52	0h33m36.50s	-65d08m35.1s
Giant12	6.21	0h51m59.50s	-65d20m07.2s

Table C.1: ρ Tucanae - All observed targets.

C.2 HD285507 - Exoplanet Host

Name	Kmag	RA(hms)	DEC(dms)
Field32	6.24	4h10m40.9s	15d14m13.4s
Giant35	8.1	4h10m54.6s	15d15m45.8s
Giant28	8.4	4h10m26.3s	15d06m16.1s
Giant12	7.36	4h9m16.9s	15d12m03.1s
Giant16	8.99	4h9m42.9s	15d10m55.7s
Giant08	8.97	4h8m44.7s	15d06m47.9s
Field05	5.03	4h7m42.0s	15d09m45.8s
Field16	4.81	4h8m28.7s	14d53m38.7s
Giant02	6.44	4h7m32.5s	15d11m45s
Field34	8.41	4h8m52.7s	14d32m48.2s
Field24	4.14	4h8m47.4s	14d42m03.8s
Giant10	7.03	4h7m42.2s	14d50m34.3s
Field28	8.03	4h8m16.2s	14d33m05.9s
Giant36	6.64	4h8m25.8s	14d27m26.3s
Field08	7.56	4h7m34.2s	14d59m12.1s
Giant13	6.42	4h7m20.8s	14d44m22.4s
Field36	5.99	4h6m22.9s	14d24m07.9s
Field38	7.73	4h6m33.0s	14d22m10.2s
Field39	7.99	4h6m35.6s	14d22m00s
Field11	8.56	4h6m47.2s	14d51m56.5s
Giant24	6.54	4h6m3.5s	14d33m19.5s

Name	Kmag	RA(hms)	DEC(dms)
Giant03	8.96	4h6m54.1s	15d08m29.3s
Giant33	8.32	4h6m13.4s	14d25m26s
Field02	7.37	4h6m45.3s	15d12m36.8s
Giant18	8.85	4h5m57.0s	14d41m41.9s
Giant29	8.3	4h5m43.7s	14d31m50.5s
Field06	6.02	4h6m25.4s	15d07m36.1s
Field15	7.99	4h5m24.3s	14d56m07.3s
Giant31	8.96	4h3m58.8s	14d48m32.1s
Giant26	8.83	4h3m54.0s	14d56m57.5s
Giant38	8.58	4h3m32.2s	14d49m39s
Field03	8.23	4h6m20.2s	15d13m56.9s
Giant27	7.88	4h3m40.8s	15d03m11.7s
Field23	5.2	4h4m13.0s	15d01m36.8s
Field21	8.28	4h4m1.8s	15d10m38s
Field40	8.35	4h3m4.2s	15d06m07.4s
Field25	7.91	4h3m39.2s	15d14m12.7s
Giant25	7.77	4h3m36.5s	15d26m10.4s
Giant30	8.91	4h3m34.1s	15d36m14.8s
Giant37	8.26	4h3m13.0s	15d37m29.8s
Giant14	8.67	4h4m34.8s	15d29m36.5s
Giant04	8.05	4h6m8.4s	15d26m21.7s
Giant05	6.5	4h5m34.7s	15d30m13.3s
Field14	8.9	4h5m2.8s	15d33m46.4s
HD285507	7.67	4h7m1.2s	15d20m06.2s
Giant34	8.11	4h3m48.4s	15d51m27.3s
Field07	6.81	4h5m55.4s	15d29m56.3s
Field13	4.82	4h5m24.2s	15d41m06.9s
Giant17	8.8	4h4m48.2s	15d45m40.9s
Field18	4.38	4h5m26.4s	15d49m49.7s
Giant09	5.38	4h5m42.4s	15d44m17s
Giant06	8.77	4h5m56.6s	15d37m57s
Field09	6.45	4h6m16.1s	15d41m53.2s
Giant32	8.75	4h5m14.8s	16d09m13s
Field17	8.91	4h5m58.7s	15d54m07s
Field30	8.98	4h6m17.9s	16d11m01.8s
Field12	7.51	4h6m28.7s	15d49m17.5s
Field27	8.88	4h6m6.2s	16d08m36.2s
Giant22	8.46	4h7m5.0s	16d07m57.8s
Giant15	8.93	4h7m3.4s	15d59m10.6s
Field04	6.55	4h6m55.5s	15d33m10.3s
Giant11	7.47	4h7m43.0s	15d50m38.9s
Giant19	6.12	4h8m7.8s	16d01m29.1s
Field19	6.56	4h7m50.0s	16d01m11.7s
Field33	5.38	4h8m45.0s	16d07m23.3s
Field22	8.87	4h8m12.2s	16d01m05.6s
Field37	5.79	4h8m32.9s	16d14m02s
Giant21	7.09	4h8m11.6s	16d03m28.9s
Field41	8.94	4h9m20.6s	16d09m33s
Giant23	7.04	4h9m3.4s	15d57m53.7s

Name	Kmag	RA(hms)	DEC(dms)
Field31	8.11	4h9m56.3s	15d52m05.4s
Field35	8.77	4h10m2.3s	15d54m49s
Field42	7.28	4h10m11.2s	15d58m37.9s
Giant20	8.09	4h9m49.1s	15d43m12.4s

Table C.2: HD285507 - All observed targets.

C.3 47 Tucanae - Globular Cluster

Name	Kmag	RA(hms)	DEC(dms)
Brght01	12.01	0h20m22.80s	-72d01m13.6s
Brght02	10.56	0h20m45.60s	-72d04m39.1s
Brght03	11.8	0h21m43.70s	-72d05m16.3s
Brght04	11.27	0h22m 1.40s	-72d13m18.3s
Brght05	10.35	0h22m 5.70s	-72d03m56.6s
Brght06	9.95	0h22m 5.90s	-72d07m48.9s
Brght07	11.36	0h22m 7.20s	-72d00m32.9s
Brght08	11.48	0h22m10.00s	-72d03m19.5s
Brght09	11.4	0h22m19.60s	-71d54m38.4s
Brght10	10.49	0h22m23.00s	-72d07m05s
Brght11	10.76	0h22m40.40s	-72d08m54.8s
Brght12	12.99	0h22m43.00s	-71d59m36.2s
Brght13	10.85	0h22m51.80s	-72d14m37.7s
Brght14	11.57	0h22m54.10s	-72d05m17s
Brght15	11.38	0h23m 7.90s	-72d00m57.2s
Brght16	10.93	0h23m12.90s	-72d10m19s
Brght17	11.71	0h23m16.20s	-72d07m48s
Brght18	11.67	0h23m20.90s	-72d05m18.4s
Brght19	11.39	0h23m21.80s	-71d55m57.1s
Brght20	10.16	0h23m22.80s	-72d01m03.8s
Brght22	11.95	0h23m25.50s	-72d13m55.1s
Brght23	11.1	0h23m26.50s	-72d06m16.6s
Brght24	11.46	0h23m29.30s	-72d04m48.3s
Brght25	11.33	0h23m33.90s	-72d03m28.5s
Brght27	10.55	0h23m35.10s	-72d01m28.9s
Brght28	11.81	0h23m37.20s	-72d06m37.6s
Brght31	10.58	0h23m41.80s	-72d04m17.9s
Brght32	11.7	0h23m42.80s	-72d06m10.8s
Brght33	11.86	0h23m46.00s	-71d57m37.3s
Brght35	8.84	0h23m47.40s	-72d06m52.7s
Brght36	11.78	0h23m48.90s	-72d07m33.8s
Brght37	9.49	0h23m49.00s	-72d03m13s
Brght39	9.32	0h23m51.20s	-72d03m49.1s
Brght40	10.79	0h23m54.40s	-71d58m35.6s
Brght42	9.31	0h23m55.60s	-71d57m28.4s

Name	Kmag	RA(hms)	DEC(dms)
Brght44	10.76	0h23m58.70s	-71d54m10.4s
Brght45	9.81	0h24m 3.40s	-71d55m47.4s
Brght48	10.1	0h24m 5.10s	-72d00m03.3s
Brght50	9.93	0h24m10.50s	-72d11m16.5s
Brght51	11.82	0h24m12.50s	-71d55m15.8s
Brght53	10.84	0h24m16.90s	-72d11m49.6s
Brght54	12.24	0h24m19.10s	-72d08m36s
Brght55	8.98	0h24m22.50s	-71d53m28.7s
Brght56	11.96	0h24m35.60s	-72d14m45.2s
Brght57	11.1	0h24m45.10s	-72d08m25.2s
Brght58	11.44	0h24m45.80s	-72d09m10.4s
Brght59	13.17	0h24m54.50s	-72d00m06.2s
Brght60	10.62	0h25m 0.60s	-71d55m58.6s
Brght61	11.75	0h25m 1.00s	-72d02m22.1s
Brght62	10.72	0h25m 3.60s	-72d05m32s
Brght64	11.76	0h25m 7.20s	-72d00m41.6s
Brght65	11.01	0h25m10.30s	-71d58m28.5s
Brght67	8.9	0h25m20.60s	-72d06m39.9s
Brght69	11.99	0h25m23.70s	-72d12m07.7s
Brght71	11.32	0h25m23.00s	-71d54m36.6s
Brght72	11.72	0h25m27.30s	-72d15m06.6s
Brght73	11.63	0h25m29.90s	-72d02m18s
Brght74	12.35	0h25m31.50s	-72d14m37.8s
Brght75	11.76	0h25m34.30s	-71d57m35.3s
Brght76	10.11	0h25m35.70s	-72d04m08.1s
Brght77	9.21	0h25m44.00s	-72d06m50.7s
Brght78	11.42	0h25m54.50s	-72d01m49.1s
Brght79	11.58	0h25m57.50s	-72d07m52.8s
Brght80	10.77	0h25m59.60s	-72d04m31s
Brght81	11.44	0h24m25.00s	-72d02m45.8s
Brght83	11.14	0h24m42.00s	-72d03m13.6s
Brght85	11.17	0h23m43.20s	-72d02m41.7s
Brght86	11.36	0h23m57.60s	-72d10m38.9s
Brght87	11.09	0h24m15.80s	-72d00m41.4s
Brght88	11.39	0h24m31.40s	-72d01m25.3s
Brght89	12.07	0h25m16.10s	-72d01m35.9s
Brght90	11.36	0h20m53.70s	-72d13m36.1s

Table C.3: 47 Tucanae - All observed targets.

C.4 NGC2477 - Open Cluster

Name	Kmag	RA(hms)	DEC(dms)
1008.0	12.36	7h52m18.91s	-38d31m36.35s
1044.0	11.83	7h52m26.64s	-38d29m45.18s

Name	Kmag	RA(hms)	DEC(dms)
1069.0	9.81	7h52m18.90s	-38d28m22.9s
1252.0	11.48	7h52m30.70s	-38d27m57.79s
2009.0	11.01	7h52m22.51s	-38d31m43.16s
2036.0	12.14	7h52m26.90s	-38d31m47.5s
2061.0	12.72	7h52m41.83s	-38d32m13.18s
2117.0	10.04	7h52m44.00s	-38d30m42.2s
253-020236	12.88	7h50m13.46s	-39d24m20.98s
253-020308	12.33	7h50m31.54s	-39d28m05.94s
253-020973	13.55	7h53m24.59s	-39d27m06.19s
253-021045	14.47	7h53m46.29s	-39d27m25.55s
254-019633	13.9	7h49m 4.76s	-39d18m35.91s
254-019648	12.41	7h49m10.26s	-39d16m24.47s
254-019764	14.2	7h49m46.54s	-39d21m33.19s
254-019914	13.11	7h50m35.70s	-39d16m04.5s
254-019929	10.52	7h50m43.54s	-39d14m52.88s
254-019951	12.83	7h50m53.08s	-39d19m29.13s
254-020037	12.72	7h51m18.11s	-39d20m24.9s
254-020046	12.78	7h51m21.15s	-39d15m35.74s
254-020105	13.89	7h51m38.05s	-39d20m25.29s
254-020113	13.65	7h51m40.29s	-39d23m11.27s
254-020212	14.43	7h52m12.88s	-39d13m25.8s
254-020421	14.27	7h53m29.12s	-39d13m48.52s
254-020475	14.45	7h53m48.94s	-39d19m44.29s
254-020486	13.22	7h53m52.84s	-39d19m00.03s
254-020552	13.49	7h54m16.88s	-39d17m18.41s
254-020638	13.95	7h54m40.35s	-39d15m34.84s
254-020645	12.91	7h54m41.51s	-39d20m05.87s
254-020670	13.82	7h54m50.80s	-39d15m58.53s
254-020821	12.85	7h55m24.09s	-39d12m48.87s
255-020157	13.33	7h48m32.19s	-39d00m05.7s
255-020197	14.15	7h48m47.33s	-39d09m08.87s
255-020232	12.44	7h49m 0.57s	-39d00m53.39s
255-020474	14.1	7h50m15.42s	-39d06m06.9s
255-020475	13.37	7h50m15.54s	-39d00m27.66s
255-020481	13.97	7h50m18.30s	-39d06m59.05s
255-020492	12.89	7h50m21.55s	-39d02m32.47s
255-020536	13.34	7h50m37.19s	-39d10m53.25s
255-020634	13.57	7h51m 8.83s	-39d04m49.25s
255-020659	14.33	7h51m17.80s	-39d01m46.13s
255-020666	13.98	7h51m19.29s	-39d05m14.44s
255-020691	13.04	7h51m27.40s	-39d10m00.06s
255-020720	14.48	7h51m32.76s	-39d02m15.85s
255-020814	12.1	7h51m52.26s	-39d08m32.89s
255-020818	13.94	7h51m54.22s	-39d11m06s
255-020848	14.15	7h52m 8.87s	-39d08m24.35s
255-020874	14.3	7h52m19.24s	-39d02m15.96s
255-020886	14.1	7h52m22.23s	-39d11m07.1s
255-020944	13.11	7h52m40.59s	-39d06m06.4s
255-020981	11.93	7h52m50.65s	-39d03m08.98s

Name	Kmag	RA(hms)	DEC(dms)
255-021048	11.4	7h53m 9.86s	-39d05m27.13s
255-021052	14.16	7h53m10.79s	-39d03m16.78s
255-021062	13.83	7h53m13.91s	-39d07m15.45s
255-021086	10.91	7h53m22.95s	-39d02m23.73s
255-021144	13.82	7h53m41.11s	-39d02m41.1s
255-021230	12.74	7h54m 9.23s	-39d01m10.02s
255-021240	14.31	7h54m11.37s	-39d09m06.3s
255-021258	14.21	7h54m17.48s	-39d01m29.82s
255-021381	12.03	7h54m54.41s	-39d09m31.98s
255-021417	13.94	7h55m 1.95s	-39d00m02s
255-021493	14.12	7h55m19.73s	-39d03m29.86s
255-021573	14.03	7h55m34.03s	-39d08m43.64s
255-021705	12.32	7h56m 2.28s	-39d03m25.5s
256-020361	11.88	7h47m30.96s	-38d51m07.36s
256-020431	13.88	7h47m54.83s	-38d51m08.36s
256-020444	13.89	7h47m58.23s	-38d54m52.03s
256-020480	13.3	7h48m10.68s	-38d57m08.16s
256-020535	13.18	7h48m26.01s	-38d57m48.25s
256-020559	14.48	7h48m31.12s	-38d51m31.1s
256-020644	12.86	7h48m56.58s	-38d55m05.86s
256-020662	11.77	7h49m 2.52s	-38d48m57.84s
256-020685	14.08	7h49m10.20s	-38d49m37.33s
256-020706	14.31	7h49m16.70s	-38d55m43.62s
256-020709	14.04	7h49m17.84s	-38d57m20.15s
256-020775	11.93	7h49m44.10s	-38d49m02.25s
256-020787	13.96	7h49m48.81s	-38d51m28.27s
256-020821	13.24	7h50m 0.98s	-38d59m19.89s
256-020867	13.35	7h50m23.59s	-38d56m36.7s
256-020874	11.79	7h50m25.13s	-38d57m24.47s
256-020906	13.35	7h50m33.08s	-38d57m28.3s
256-020911	13.2	7h50m34.04s	-38d50m53.46s
256-020955	11.33	7h50m46.78s	-38d58m52.33s
256-021054	13.93	7h51m22.90s	-38d54m40.82s
256-021093	14.03	7h51m32.40s	-38d48m12.4s
256-021111	12.31	7h51m41.10s	-38d56m24.82s
256-021225	14.07	7h52m14.36s	-38d53m39.61s
256-021249	14.43	7h52m22.70s	-38d56m38.63s
256-021269	13.76	7h52m29.08s	-38d53m44.3s
256-021313	13.58	7h52m43.49s	-38d48m31.89s
256-021323	12.12	7h52m47.77s	-38d50m07.01s
256-021355	13.16	7h52m58.27s	-38d55m36.24s
256-021476	13.28	7h53m29.43s	-38d55m18.11s
256-021513	13.67	7h53m39.72s	-38d51m36.91s
256-021641	13.9	7h54m18.82s	-38d59m18.36s
256-021666	14.23	7h54m25.43s	-38d48m31.09s
256-021747	13.78	7h54m59.97s	-38d56m48.56s
256-021839	14.19	7h55m27.63s	-38d52m08.75s
256-021840	13.38	7h55m27.79s	-38d56m42.94s
256-021843	13.86	7h55m27.97s	-38d55m28.28s

Name	Kmag	RA(hms)	DEC(dms)
256-021890	14.23	7h55m40.38s	-38d57m44.7s
256-021910	11.4	7h55m45.42s	-38d49m08.08s
256-022005	14.43	7h56m15.51s	-38d59m12.96s
256-022032	14.35	7h56m21.68s	-38d53m49.41s
256-022064	14.41	7h56m33.48s	-38d48m16.38s
256-022090	13.06	7h56m40.89s	-38d54m49.39s
256-022099	14.16	7h56m43.13s	-38d54m09.16s
257-020259	14.3	7h47m 9.32s	-38d41m57.89s
257-020324	13.4	7h47m31.77s	-38d40m45.02s
257-020408	14.18	7h48m 2.10s	-38d46m22.81s
257-020468	13.35	7h48m18.12s	-38d40m29.64s
257-020473	13.68	7h48m19.96s	-38d37m17.71s
257-020534	13.98	7h48m37.02s	-38d40m37.33s
257-020652	13.93	7h49m15.00s	-38d45m49.08s
257-020670	13.83	7h49m24.61s	-38d43m52.68s
257-020748	13.83	7h50m 0.03s	-38d44m21.85s
257-020759	13.99	7h50m 3.64s	-38d38m19.41s
257-020811	13.39	7h50m24.18s	-38d47m08.6s
257-020845	13.01	7h50m36.52s	-38d39m45.95s
257-020852	14.35	7h50m38.67s	-38d38m24.15s
257-020874	14.18	7h50m43.47s	-38d43m47.71s
257-020907	13.59	7h50m52.02s	-38d44m53.27s
257-020909	13.37	7h50m53.12s	-38d40m26.08s
257-020915	13.09	7h50m54.22s	-38d41m21.32s
257-020978	10.86	7h51m 9.48s	-38d36m54.45s
257-020979	13.47	7h51m 9.82s	-38d40m53.96s
257-020982	14.06	7h51m10.19s	-38d47m46.65s
257-020985	13.47	7h51m10.94s	-38d42m31.1s
257-020997	12.83	7h51m13.34s	-38d45m12.17s
257-021018	12.9	7h51m18.36s	-38d42m39.79s
257-021060	14.29	7h51m26.85s	-38d38m40.31s
257-021066	14.11	7h51m27.40s	-38d40m44.98s
257-021114	14.13	7h51m34.24s	-38d44m11.5s
257-021140	13.95	7h51m38.41s	-38d36m03.08s
257-021145	13.9	7h51m39.77s	-38d39m11.33s
257-021153	13.2	7h51m41.19s	-38d37m22.75s
257-021186	12.91	7h51m49.29s	-38d39m04.09s
257-021195	12.36	7h51m51.40s	-38d46m38.02s
257-021208	13.69	7h51m53.15s	-38d46m59.94s
257-021212	14.22	7h51m54.12s	-38d42m47.66s
257-021248	14.17	7h52m 0.30s	-38d42m34.02s
257-021250	13.69	7h52m 0.43s	-38d39m04.02s
257-021278	14.37	7h52m 4.61s	-38d40m56.18s
257-021298	14.11	7h52m 6.47s	-38d46m26.11s
257-021319	12.11	7h52m 8.59s	-38d36m54.07s
257-021325	13.44	7h52m 9.05s	-38d38m41.57s
257-021345	13.83	7h52m11.57s	-38d43m31.82s
257-021363	13.36	7h52m13.86s	-38d41m50.39s
257-021388	14.24	7h52m17.18s	-38d38m22.65s

Name	Kmag	RA(hms)	DEC(dms)
257-021422	13.4	7h52m22.36s	-38d40m49.6s
257-021456	12.34	7h52m26.18s	-38d39m15.71s
257-021467	12.66	7h52m28.39s	-38d41m27.73s
257-021480	14.36	7h52m30.40s	-38d44m22.96s
257-021490	13.48	7h52m30.93s	-38d40m18.67s
257-021516	14.19	7h52m36.20s	-38d46m10.96s
257-021532	13.99	7h52m38.58s	-38d38m29.98s
257-021537	13.05	7h52m39.95s	-38d36m29.44s
257-021547	11.0	7h52m42.31s	-38d36m43.55s
257-021593	12.25	7h52m48.91s	-38d40m32.63s
257-021618	14.42	7h52m51.65s	-38d45m41.42s
257-021619	11.71	7h52m51.67s	-38d43m15.17s
257-021623	14.2	7h52m52.07s	-38d38m29.2s
257-021663	13.39	7h53m 0.24s	-38d42m12.08s
257-021665	12.59	7h53m 0.38s	-38d38m35.37s
257-021680	13.11	7h53m 4.77s	-38d42m15.14s
257-021719	13.5	7h53m13.91s	-38d42m49.11s
257-021743	13.44	7h53m18.09s	-38d36m17.86s
257-021784	10.39	7h53m32.75s	-38d36m22.23s
257-021795	13.59	7h53m36.50s	-38d43m19.11s
257-021860	14.08	7h53m55.16s	-38d44m56.47s
257-021877	13.13	7h54m 1.70s	-38d42m02.59s
257-021888	14.18	7h54m 4.10s	-38d41m25.37s
257-021905	14.22	7h54m 9.15s	-38d40m06.46s
257-021907	12.68	7h54m 9.75s	-38d36m30.39s
257-021921	13.98	7h54m14.33s	-38d39m29.86s
257-022013	12.77	7h54m55.10s	-38d45m49.26s
257-022084	13.6	7h55m20.13s	-38d36m39.56s
257-022220	14.24	7h55m59.88s	-38d47m18.04s
258-020416	14.32	7h47m31.30s	-38d35m21.36s
258-020421	13.51	7h47m33.22s	-38d26m06.44s
258-020605	13.54	7h48m32.07s	-38d27m43.18s
258-020614	14.44	7h48m35.17s	-38d27m02.53s
258-020658	13.55	7h48m44.20s	-38d26m14.59s
258-020663	12.26	7h48m47.03s	-38d24m50.93s
258-020689	13.12	7h48m54.50s	-38d24m56.18s
258-020714	13.0	7h49m 2.45s	-38d30m26.74s
258-020774	12.1	7h49m22.07s	-38d29m42.67s
258-020777	13.18	7h49m22.35s	-38d33m28.65s
258-020937	14.26	7h50m12.75s	-38d31m01.1s
258-020938	14.5	7h50m12.93s	-38d32m45.58s
258-020946	14.4	7h50m14.97s	-38d33m45.15s
258-020971	14.37	7h50m21.80s	-38d31m40.7s
258-020977	12.48	7h50m22.37s	-38d31m09.63s
258-021018	14.48	7h50m29.91s	-38d35m27.25s
258-021033	12.85	7h50m31.62s	-38d24m28.17s
258-021080	14.13	7h50m40.37s	-38d32m10.72s
258-021096	13.34	7h50m43.17s	-38d26m08.11s
258-021147	13.53	7h50m52.83s	-38d28m56.84s

Name	Kmag	RA(hms)	DEC(dms)
258-021150	14.4	7h50m53.43s	-38d29m42.26s
258-021161	13.09	7h50m55.26s	-38d30m24.23s
258-021202	12.71	7h51m 2.31s	-38d34m50.97s
258-021217	13.48	7h51m 5.04s	-38d32m35.6s
258-021227	13.36	7h51m 6.90s	-38d24m13.93s
258-021253	14.04	7h51m11.79s	-38d27m03.95s
258-021268	12.76	7h51m14.46s	-38d25m13.7s
258-021291	13.68	7h51m17.30s	-38d35m13.75s
258-021309	12.82	7h51m19.18s	-38d24m57.22s
258-021322	12.46	7h51m21.65s	-38d34m04.14s
258-021331	12.83	7h51m22.99s	-38d33m30.75s
258-021339	12.93	7h51m24.11s	-38d25m11.27s
258-021343	12.53	7h51m24.89s	-38d35m33.04s
258-021365	13.2	7h51m28.08s	-38d28m13.94s
258-021367	14.12	7h51m28.39s	-38d29m04.25s
258-021370	13.3	7h51m28.72s	-38d31m06.2s
258-021380	12.91	7h51m30.00s	-38d26m53.24s
258-021404	12.12	7h51m32.64s	-38d26m53.13s
258-021412	12.41	7h51m33.58s	-38d34m37.17s
258-021420	12.84	7h51m34.37s	-38d32m12.56s
258-021433	13.69	7h51m35.76s	-38d35m59.61s
258-021498	13.84	7h51m41.88s	-38d26m26.47s
258-021516	14.39	7h51m43.93s	-38d29m22.56s
258-021527	14.46	7h51m45.25s	-38d31m14.38s
258-021530	13.15	7h51m45.39s	-38d27m51.61s
258-021536	13.48	7h51m45.92s	-38d32m50.24s
258-021548	11.04	7h51m47.05s	-38d33m53.38s
258-021557	13.06	7h51m47.82s	-38d25m25.04s
258-021594	11.78	7h51m50.68s	-38d32m09.81s
258-021601	13.46	7h51m51.40s	-38d35m36.59s
258-021604	14.25	7h51m51.68s	-38d27m34.49s
258-021803	11.73	7h52m 4.90s	-38d30m11.85s
258-021818	13.04	7h52m 5.72s	-38d29m39.64s
258-021828	13.68	7h52m 6.53s	-38d30m56.77s
258-021835	13.24	7h52m 6.86s	-38d27m51.39s
258-021853	12.21	7h52m 7.85s	-38d31m34.18s
258-021963	12.36	7h52m14.12s	-38d29m39.56s
258-022036	13.24	7h52m17.86s	-38d30m20.05s
258-022041	13.71	7h52m17.98s	-38d24m48.57s
258-022098	11.51	7h52m21.68s	-38d32m44.19s
258-022112	14.12	7h52m22.70s	-38d30m34.57s
258-022115	13.29	7h52m23.00s	-38d26m58.17s
258-022145	12.84	7h52m24.61s	-38d24m26.69s
258-022160	14.08	7h52m25.62s	-38d27m20.31s
258-022200	13.51	7h52m29.37s	-38d30m52.31s
258-022201	12.55	7h52m29.39s	-38d25m41.5s
258-022249	14.38	7h52m33.15s	-38d32m32.54s
258-022257	12.65	7h52m33.61s	-38d35m37.49s
258-022288	12.67	7h52m37.15s	-38d29m06.54s

Name	Kmag	RA(hms)	DEC(dms)
258-022311	13.36	7h52m38.95s	-38d31m15.12s
258-022319	11.99	7h52m39.73s	-38d29m50.75s
258-022372	13.9	7h52m45.91s	-38d29m00.93s
258-022419	14.09	7h52m52.37s	-38d35m23.11s
258-022429	12.76	7h52m53.75s	-38d32m49.58s
258-022435	12.41	7h52m54.63s	-38d31m17.81s
258-022439	14.26	7h52m55.32s	-38d24m16.8s
258-022453	14.3	7h52m57.09s	-38d27m25.45s
258-022459	14.23	7h52m57.34s	-38d25m09.66s
258-022483	13.3	7h52m59.87s	-38d32m34.2s
258-022487	12.42	7h53m 0.47s	-38d29m41.98s
258-022533	12.76	7h53m 7.41s	-38d31m29.35s
258-022538	12.52	7h53m 8.29s	-38d29m35.91s
258-022541	13.37	7h53m 8.75s	-38d27m26.38s
258-022545	13.8	7h53m 9.84s	-38d28m45.89s
258-022578	13.88	7h53m14.19s	-38d34m48.24s
258-022600	14.45	7h53m19.15s	-38d33m38.88s
258-022603	12.74	7h53m19.62s	-38d34m31.13s
258-022658	14.12	7h53m30.14s	-38d25m10.49s
258-022671	14.28	7h53m34.15s	-38d27m46.72s
258-022672	12.94	7h53m34.41s	-38d31m38.17s
258-022677	12.27	7h53m35.18s	-38d26m31.86s
258-022742	13.83	7h53m51.92s	-38d31m19.31s
258-022869	13.71	7h54m37.21s	-38d25m19.74s
258-022885	11.86	7h54m43.07s	-38d31m55.64s
258-022904	13.31	7h54m50.81s	-38d26m28.66s
258-022930	13.58	7h55m 1.85s	-38d32m50.13s
258-022959	13.43	7h55m10.42s	-38d26m48.32s
258-023005	12.43	7h55m23.38s	-38d29m12.75s
258-023081	14.03	7h55m41.92s	-38d24m39.45s
258-023304	14.25	7h56m33.71s	-38d26m42.09s
258-023311	14.3	7h56m35.43s	-38d32m02.3s
258-023391	12.79	7h56m54.66s	-38d25m41.93s
258-023434	13.19	7h57m 4.24s	-38d31m52.14s
259-019657	14.03	7h47m14.75s	-38d19m13.91s
259-019698	14.48	7h47m27.55s	-38d16m09.05s
259-019778	13.39	7h47m56.24s	-38d13m12s
259-019803	14.18	7h48m 2.65s	-38d17m44.41s
259-019849	13.19	7h48m11.95s	-38d14m46.44s
259-019914	14.39	7h48m28.43s	-38d21m09.38s
259-019924	12.67	7h48m31.51s	-38d16m26.54s
259-020084	12.21	7h49m10.88s	-38d15m25.5s
259-020111	12.71	7h49m17.60s	-38d13m25.12s
259-020117	11.13	7h49m18.72s	-38d17m46.92s
259-020269	11.66	7h50m 7.81s	-38d19m16.99s
259-020270	13.99	7h50m 8.52s	-38d12m09.51s
259-020488	12.14	7h50m55.58s	-38d14m22.9s
259-020586	12.92	7h51m13.01s	-38d23m31.49s
259-020603	13.47	7h51m14.72s	-38d17m55.53s

Name	Kmag	RA(hms)	DEC(dms)
259-020746	12.88	7h51m43.26s	-38d13m07.17s
259-020751	13.28	7h51m44.43s	-38d23m09.58s
259-020767	13.65	7h51m47.90s	-38d18m08.55s
259-020782	14.41	7h51m49.66s	-38d15m35.93s
259-020815	12.89	7h51m55.27s	-38d14m37.06s
259-020830	13.45	7h51m57.49s	-38d16m16.55s
259-020864	12.92	7h52m 3.74s	-38d20m53.12s
259-020871	13.47	7h52m 5.74s	-38d19m30.04s
259-020881	14.26	7h52m 8.66s	-38d21m44.75s
259-020912	13.16	7h52m13.16s	-38d23m14.07s
259-020916	14.07	7h52m13.49s	-38d20m03.69s
259-020935	13.86	7h52m16.95s	-38d19m00.59s
259-020949	13.28	7h52m19.93s	-38d14m54.32s
259-020970	13.21	7h52m24.10s	-38d13m33.22s
259-020995	13.41	7h52m29.82s	-38d23m22.79s
259-020998	14.37	7h52m30.21s	-38d16m56.01s
259-021021	13.54	7h52m36.52s	-38d21m31.51s
259-021051	12.02	7h52m44.86s	-38d16m26.19s
259-021052	14.43	7h52m44.88s	-38d19m29.11s
259-021119	13.47	7h53m 1.49s	-38d17m05.41s
259-021245	14.18	7h53m35.79s	-38d22m19.62s
259-021252	12.45	7h53m38.50s	-38d22m01.81s
259-021320	14.07	7h53m57.24s	-38d23m52.66s
259-021331	14.46	7h53m59.78s	-38d17m07.57s
259-021388	14.03	7h54m16.39s	-38d16m14.27s
259-021589	14.1	7h55m19.83s	-38d12m03.17s
259-021663	13.42	7h55m39.52s	-38d13m22.91s
259-021722	12.97	7h55m53.91s	-38d23m39.77s
259-021756	14.13	7h56m 3.79s	-38d20m56.46s
259-021837	11.67	7h56m24.78s	-38d23m37.22s
259-021879	12.89	7h56m36.00s	-38d18m09.13s
259-021893	13.74	7h56m38.47s	-38d16m03.87s
259-021979	14.34	7h56m59.23s	-38d23m23.66s
260-020706	13.15	7h47m57.95s	-38d00m03.09s
260-020708	13.73	7h47m58.51s	-38d09m46.06s
260-020740	14.42	7h48m 4.99s	-38d08m38.71s
260-020823	13.06	7h48m20.89s	-38d07m18.67s
260-020963	14.16	7h48m55.13s	-38d09m41.54s
260-021018	12.85	7h49m 7.76s	-38d09m04.46s
260-021032	13.24	7h49m11.52s	-38d02m17.19s
260-021137	12.82	7h49m41.15s	-38d09m09.53s
260-021234	14.0	7h50m17.29s	-38d05m02.04s
260-021387	14.01	7h50m44.06s	-38d10m57.76s
260-021391	14.5	7h50m45.73s	-38d02m14.73s
260-021405	13.82	7h50m47.17s	-38d10m13.85s
260-021560	13.83	7h51m16.08s	-38d08m45.07s
260-021612	12.54	7h51m29.37s	-38d00m45.57s
260-021646	12.45	7h51m40.32s	-38d02m21.51s
260-021658	14.22	7h51m42.31s	-38d06m51.13s

Name	Kmag	RA(hms)	DEC(dms)
260-021694	12.89	7h51m52.37s	-38d10m00.1s
260-021698	13.63	7h51m53.53s	-38d02m27.35s
260-021722	14.43	7h52m 0.51s	-38d03m08.01s
260-021796	14.15	7h52m23.41s	-38d10m21.27s
260-021806	12.29	7h52m25.58s	-38d01m58.47s
260-021818	11.42	7h52m28.18s	-38d04m11.06s
260-021830	13.24	7h52m32.34s	-38d07m46.42s
260-021910	12.89	7h52m58.08s	-38d05m07.39s
260-021969	13.87	7h53m13.22s	-38d09m10.49s
260-022071	14.34	7h53m43.88s	-38d06m12.34s
260-022142	13.85	7h54m 4.67s	-38d06m35.02s
260-022145	14.3	7h54m 5.32s	-38d04m07.38s
260-022167	12.07	7h54m10.33s	-38d10m30.02s
260-022252	14.08	7h54m35.11s	-38d01m45.11s
260-022389	13.4	7h55m16.61s	-38d05m32.1s
260-022392	14.37	7h55m17.54s	-38d02m06.26s
260-022460	13.31	7h55m35.20s	-38d02m31.31s
260-022516	13.73	7h55m50.48s	-38d00m02.93s
260-022521	13.82	7h55m51.56s	-38d06m24.76s
260-022535	12.78	7h55m54.69s	-38d01m00.68s
260-022571	12.3	7h56m 7.04s	-38d09m49.54s
260-022572	13.16	7h56m 7.59s	-38d06m00.74s
260-022593	13.96	7h56m13.30s	-38d07m56.11s
260-022605	14.21	7h56m16.58s	-38d06m35.26s
260-022673	13.33	7h56m39.97s	-38d05m49.61s
260-022692	13.5	7h56m48.82s	-38d08m54.37s
260-022696	13.24	7h56m50.48s	-38d07m57.76s
261-020931	13.28	7h48m 1.23s	-37d57m29.64s
261-021178	14.35	7h48m56.86s	-37d57m14.32s
261-021202	14.31	7h49m 5.03s	-37d55m54.26s
261-021230	12.08	7h49m12.74s	-37d55m57.51s
261-021558	12.62	7h50m42.51s	-37d48m02.04s
261-021656	14.05	7h51m 5.23s	-37d56m47.18s
261-021670	12.23	7h51m 7.97s	-37d59m39.77s
261-021740	13.82	7h51m24.78s	-37d54m16.9s
261-021749	13.31	7h51m27.10s	-37d58m14.02s
261-021796	14.34	7h51m38.08s	-37d49m01.57s
261-021810	14.28	7h51m41.38s	-37d54m29.73s
261-022013	13.97	7h52m38.39s	-37d55m33.22s
261-022057	12.63	7h52m51.22s	-37d49m20.03s
261-022076	13.4	7h52m56.90s	-37d52m33.2s
261-022138	14.35	7h53m 7.53s	-37d54m19.45s
261-022171	13.26	7h53m13.47s	-37d51m42.3s
261-022362	13.99	7h54m 4.52s	-37d55m30.39s
261-022424	14.27	7h54m21.81s	-37d58m07.39s
261-022617	14.28	7h55m33.73s	-37d51m18.33s
261-022626	12.93	7h55m38.81s	-37d49m11.67s
262-020716	14.5	7h49m23.33s	-37d45m33.37s
262-020735	14.44	7h49m27.45s	-37d41m38.44s

Name	Kmag	RA(hms)	DEC(dms)
262-020761	13.32	7h49m34.88s	-37d46m29.96s
262-020789	13.85	7h49m43.03s	-37d42m44.3s
262-020800	13.65	7h49m46.16s	-37d46m18.17s
262-020880	14.36	7h50m 9.10s	-37d41m02.46s
262-020885	14.33	7h50m10.50s	-37d39m07.04s
262-020912	13.18	7h50m20.34s	-37d38m45.96s
262-020945	12.66	7h50m27.96s	-37d45m08.61s
262-020986	13.66	7h50m38.75s	-37d39m40.02s
262-021008	13.21	7h50m44.04s	-37d40m14.08s
262-021104	13.04	7h51m10.09s	-37d39m52.08s
262-021155	12.96	7h51m26.05s	-37d38m09.72s
262-021207	14.12	7h51m38.33s	-37d39m57.45s
262-021215	13.65	7h51m40.48s	-37d38m06.69s
262-021377	13.34	7h52m20.76s	-37d43m15.14s
262-021438	14.14	7h52m43.43s	-37d36m49.04s
262-021493	13.6	7h52m55.32s	-37d46m35.56s
262-021689	14.12	7h53m45.66s	-37d39m28.24s
262-021840	13.79	7h54m47.43s	-37d47m19.46s
262-021928	12.42	7h55m23.58s	-37d46m49.12s
262-021954	12.4	7h55m32.70s	-37d47m18.98s
263-022156	9.81	7h50m58.86s	-37d34m36.48s
263-022417	12.91	7h51m59.01s	-37d32m21.22s
263-022502	12.5	7h52m26.44s	-37d35m19.41s
263-022696	12.85	7h53m25.53s	-37d33m43.24s
3170.0	12.35	7h52m45.14s	-38d33m50.27s
3176.0	12.63	7h52m43.35s	-38d35m10.02s
4004.0	10.81	7h52m17.80s	-38d33m25.5s
4027.0	12.15	7h52m21.07s	-38d34m38.08s
4046.0	12.09	7h52m24.60s	-38d36m19.1s
4221.0	12.27	7h52m36.53s	-38d37m54.5s
4248.0	12.66	7h52m32.02s	-38d39m53.7s
4301.0	12.94	7h52m46.78s	-38d38m58.08s
4327.0	12.65	7h52m48.01s	-38d41m31.81s
5043.0	12.16	7h52m 9.71s	-38d35m54.02s
5047.0	11.7	7h52m 6.50s	-38d35m25.15s
5073.0	12.29	7h52m14.30s	-38d37m14.8s
5207.0	12.82	7h52m18.91s	-38d40m05.66s
5223.0	11.39	7h52m14.80s	-38d38m49.4s
5345.0	12.58	7h51m58.98s	-38d40m03.12s
6005.0	12.51	7h52m 7.82s	-38d32m38.68s
6020.0	12.43	7h51m56.98s	-38d32m37.87s
6040.0	11.89	7h51m54.02s	-38d34m22.97s
6053.0	10.91	7h52m 7.32s	-38d33m21.9s
6058.0	12.55	7h52m10.70s	-38d33m17.97s
6088.0	12.38	7h51m59.06s	-38d35m51.95s
6251.0	12.48	7h51m55.17s	-38d36m14.52s
7012.0	12.43	7h52m10.71s	-38d31m37.87s
7206.0	12.79	7h51m54.41s	-38d28m51.5s
7311.0	11.76	7h51m49.80s	-38d27m26.4s

Name	Kmag	RA(hms)	DEC(dms)
7334.0	12.88	7h51m40.72s	-38d28m43.4s
7349.0	12.47	7h51m40.21s	-38d30m30.21s
7367.0	11.79	7h51m40.79s	-38d31m47.47s
8019.0	12.15	7h52m16.06s	-38d30m23.43s
8033.0	12.46	7h52m 7.87s	-38d30m12.58s

Table C.4: NGC2477 - All observed targets.

C.5 M67 - Open Cluster

Name	Kmag	RA(hms)	DEC(dms)
M67-375	15.81	8h50m45.62s	11d55m36s
M67-378	14.788	8h50m46.86s	11d52m57.85s
M67-381	13.9	8h50m47.62s	11d45m23.2s
M67-383	13.59	8h50m47.69s	11d47m52.9s
M67-385	14.526	8h50m48.02s	11d49m41.49s
M67-386	14.085	8h50m48.11s	11d54m47.66s
M67-389	17.23	8h50m50.56s	11d41m17s
M67-392	16.93	8h50m52.97s	11d43m14.2s
M67-393	14.39	8h50m53.34s	11d43m40.05s
M67-395	15.06	8h50m54.30s	11d55m15.3s
M67-396	13.512	8h50m54.74s	11d51m09.31s
M67-399	13.62	8h50m56.03s	11d53m52.3s
M67-402	15.795	8h50m59.43s	11d54m52.45s
M67-403	13.5	8h51m 1.58s	11d47m50.5s
M67-409	14.533	8h51m 3.99s	11d42m23.87s
M67-410	13.83	8h51m 4.95s	11d52m26.4s
M67-413	14.03	8h51m 5.78s	11d43m47.2s
M67-414	15.599	8h51m 6.96s	11d41m49.01s
M67-417	15.54	8h51m 8.18s	11d49m44.9s
M67-418	14.55	8h51m 9.14s	11d57m00.31s
M67-419	14.547	8h51m 9.91s	11d46m16.95s
M67-424	14.622	8h51m10.78s	11d39m50.9s
M67-425	13.764	8h51m11.64s	11d48m50.55s
M67-429	16.69	8h51m12.69s	11d48m06.7s
M67-432	15.891	8h51m13.39s	11d39m37.55s
M67-433	15.208	8h51m13.98s	11d57m34.15s
M67-437	13.54	8h51m16.60s	11d54m15.4s
M67-439	13.91	8h51m17.39s	11d46m03.5s
M67-443	14.023	8h51m18.68s	11d40m36.77s
M67-444	12.3	8h51m18.99s	11d58m11.3s
M67-445	13.85	8h51m20.16s	11d52m48s
M67-449	14.11	8h51m21.52s	11d59m05.1s
M67-450	15.214	8h51m21.62s	11d49m02.51s
M67-451	14.172	8h51m21.77s	11d44m05.09s

Name	Kmag	RA(hms)	DEC(dms)
M67-457	15.837	8h51m26.71s	11d56m12.05s
M67-464	14.369	8h51m29.88s	11d50m22.86s
M67-470	13.702	8h51m31.20s	11d53m17.92s
M67-474	15.481	8h51m31.75s	11d45m08.83s
M67-475	13.64	8h51m32.09s	11d55m08.9s
M67-481	15.164	8h51m32.84s	11d53m44.67s
M67-482	15.763	8h51m32.95s	11d54m47.47s
M67-484	13.8	8h51m33.27s	11d59m41.5s
M67-489	14.57	8h51m34.50s	11d43m49.46s
M67-490	15.491	8h51m34.55s	11d49m06.8s
M67-496	14.343	8h51m35.54s	11d39m47s
M67-499	13.96	8h51m36.41s	11d56m51.1s
M67-506	14.109	8h51m38.74s	11d42m37.37s
M67-507	13.697	8h51m39.05s	11d47m55.34s
M67-512	15.656	8h51m39.59s	11d42m10.83s
M67-523	15.52	8h51m42.58s	11d45m59.1s
M67-524	17.72	8h51m43.15s	11d51m02.4s
M67-525	16.36	8h51m43.37s	11d40m13.3s
M67-530	13.51	8h51m44.95s	11d38m59.3s
M67-531	13.54	8h51m45.22s	11d56m55.29s
M67-538	14.679	8h51m47.40s	11d44m42.31s
M67-539	14.307	8h51m47.42s	11d47m09.63s
M67-546	15.272	8h51m48.98s	11d43m39.84s
M67-549	15.721	8h51m50.58s	11d51m31.21s
M67-556	14.51	8h51m53.34s	11d56m17.4s
M67-557	14.327	8h51m55.16s	11d39m40.19s
M67-558	13.88	8h51m55.61s	11d48m38.5s
M67-560	15.038	8h51m56.21s	11d53m35.75s
M67-562	15.548	8h51m58.79s	11d48m14.83s
M67-564	15.158	8h51m58.99s	11d51m14.15s
M67-570	14.77	8h52m 2.50s	11d55m34.5s
M67-573	14.0	8h52m 3.32s	11d58m04.9s
M67-577	12.62	8h52m 4.77s	11d58m29.4s
M67-580	14.735	8h52m 7.30s	11d47m09.02s
M67-582	13.821	8h52m 7.86s	11d49m49.92s
M67-590	12.83	8h52m11.37s	11d45m38.3s
M67-F-108	9.68	8h51m17.51s	11d45m23s
M67-F-117	12.58	8h51m18.71s	11d47m03s
M67-F-130	12.875	8h51m20.57s	11d46m16.37s
M67-F-132	13.085	8h51m20.81s	11d45m02.47s
M67-F-135	11.43	8h51m21.59s	11d46m06.5s
M67-F-149	12.53	8h51m25.40s	11d47m34.6s
M67-F-170	9.64	8h51m29.93s	11d47m17.1s
M67-F-81	9.985	8h51m11.78s	11d45m22.13s
M67-I-198	13.14	8h51m20.35s	11d45m52.8s
M67-I-242bl	11.06	8h51m14.35s	11d45m00.54s
M67-I-242ble	11.06	8h51m14.38s	11d45m00.8s
M67-I-51	14.103	8h51m24.99s	11d45m42.95s
M67-I-9	13.178	8h51m22.05s	11d46m40.99s

Name	Kmag	RA(hms)	DEC(dms)
M67-IV-202	8.84	8h50m12.31s	11d51m24.49s
M67-S1	12.77	8h51m35.43s	11d57m56.8s
M67-S10	12.82	8h51m29.43s	11d54m14.2s
M67-S100	13.36	8h51m46.44s	11d46m27s
M67-S104	12.64	8h51m 3.28s	11d45m47.7s
M67-S108	10.73	8h51m50.22s	11d46m07.2s
M67-S109	12.61	8h51m31.26s	11d45m50.9s
M67-S11	10.48	8h51m26.21s	11d53m52.3s
M67-S110	13.14	8h52m 2.78s	11d46m04.2s
M67-S113	12.9	8h51m29.38s	11d45m27.9s
M67-S114	11.3	8h51m 3.54s	11d45m03.1s
M67-S115	12.68	8h50m47.68s	11d44m51.7s
M67-S116	13.07	8h51m43.77s	11d45m15.1s
M67-S12	12.26	8h51m35.80s	11d53m35s
M67-S120	12.84	8h51m46.67s	11d44m58.4s
M67-S121	13.44	8h51m16.31s	11d44m33.2s
M67-S122	10.76	8h51m43.57s	11d44m26.8s
M67-S123	13.36	8h51m45.99s	11d44m09.6s
M67-S124	11.238	8h51m26.43s	11d43m50.71s
M67-S125	13.12	8h51m30.15s	11d43m50.2s
M67-S126	12.69	8h51m41.97s	11d43m37.5s
M67-S127	13.41	8h51m18.36s	11d43m25.5s
M67-S128	13.093	8h50m46.09s	11d43m08.28s
M67-S129	13.26	8h51m18.10s	11d42m54.75s
M67-S131	13.48	8h51m 1.33s	11d41m59.1s
M67-S132	12.77	8h51m 9.53s	11d41m45.3s
M67-S133	13.18	8h51m44.67s	11d41m51.3s
M67-S135	13.37	8h51m 3.66s	11d40m31.3s
M67-S136	13.33	8h51m53.11s	11d40m54s
M67-S139	13.046	8h50m59.73s	11d39m52.51s
M67-S14	12.74	8h51m27.45s	11d53m26.9s
M67-S141	12.97	8h50m59.78s	11d39m22.5s
M67-S15	12.6	8h51m 7.25s	11d53m02.2s
M67-S16	13.06	8h51m31.97s	11d53m12s
M67-S167	15.69	8h50m44.04s	11d42m49.8s
M67-S17	12.81	8h51m15.78s	11d52m59.1s
M67-S171	14.99	8h50m46.42s	11d52m17.1s
M67-S172	15.331	8h50m46.86s	11d53m52.65s
M67-S174	14.137	8h50m47.13s	11d42m54.84s
M67-S175	16.15	8h50m48.15s	11d40m23.7s
M67-S18	10.51	8h51m12.72s	11d52m42.7s
M67-S180	13.992	8h50m49.76s	11d54m24.36s
M67-S187	12.72	8h50m51.85s	11d56m56.2s
M67-S19	12.79	8h51m59.66s	11d52m58s
M67-S191	13.59	8h50m53.46s	11d44m34.9s
M67-S194	15.32	8h50m54.17s	11d41m30.4s
M67-S196	15.015	8h50m55.72s	11d52m55.65s
M67-S2	13.21	8h50m59.26s	11d56m37.1s
M67-S20	11.28	8h51m21.78s	11d52m38.2s

Name	Kmag	RA(hms)	DEC(dms)
M67-S200	14.965	8h51m 2.05s	11d45m19.12s
M67-S202	15.77	8h51m 2.49s	11d55m22.5s
M67-S203	14.549	8h51m 2.79s	11d51m25.48s
M67-S21	13.25	8h51m25.55s	11d52m39.1s
M67-S210	16.4	8h51m 6.46s	11d47m30.9s
M67-S214	15.364	8h51m 7.36s	11d46m27.94s
M67-S216	15.594	8h51m 7.74s	11d56m30.64s
M67-S217	15.784	8h51m 7.83s	11d59m35.38s
M67-S218	14.749	8h51m 7.95s	11d58m53.27s
M67-S219	13.77	8h51m 8.59s	11d50m53.3s
M67-S22	12.85	8h50m58.18s	11d52m22.6s
M67-S224	15.404	8h51m11.76s	11d50m01.85s
M67-S23	11.96	8h50m55.72s	11d52m15s
M67-S230	14.47	8h51m14.34s	11d41m09.18s
M67-S232	14.129	8h51m15.05s	11d49m21.1s
M67-S233	13.88	8h51m15.25s	11d58m38s
M67-S234	15.004	8h51m15.44s	11d51m57.98s
M67-S24	12.794	8h51m28.30s	11d52m17.51s
M67-S241	14.118	8h51m18.72s	11d55m49.67s
M67-S245	14.048	8h51m21.75s	11d51m42.04s
M67-S247	15.278	8h51m21.94s	11d53m08.91s
M67-S248	15.706	8h51m22.15s	11d48m27.96s
M67-S25	12.66	8h51m28.83s	11d52m00.3s
M67-S252	14.9	8h51m23.21s	11d39m15.1s
M67-S254	14.686	8h51m24.68s	11d43m06.22s
M67-S26	10.922	8h51m27.01s	11d51m52.55s
M67-S266	15.456	8h51m28.91s	11d43m08.73s
M67-S267	15.73	8h51m28.97s	11d47m42.98s
M67-S27	13.18	8h51m33.68s	11d51m45.3s
M67-S271	13.97	8h51m30.13s	11d58m24.9s
M67-S272	15.391	8h51m30.18s	11d59m21.29s
M67-S279	14.561	8h51m32.58s	11d42m05.25s
M67-S280	14.167	8h51m34.12s	11d46m55.72s
M67-S283	13.88	8h51m36.18s	11d38m56.6s
M67-S285	10.91	8h51m37.18s	11d59m02.8s
M67-S288	12.86	8h51m37.97s	11d58m49.5s
M67-S29	13.28	8h51m22.43s	11d51m29.5s
M67-S293	16.64	8h51m38.83s	11d39m02.2s
M67-S295	15.512	8h51m39.06s	11d53m05.22s
M67-S296	15.31	8h51m39.56s	11d45m01.6s
M67-S297	14.338	8h51m39.80s	11d42m54.72s
M67-S298	13.78	8h51m40.84s	11d49m05.9s
M67-S299	15.898	8h51m40.90s	11d57m44.38s
M67-S3	12.75	8h50m54.41s	11d56m29.3s
M67-S30	13.282	8h51m29.86s	11d51m29.93s
M67-S301	14.94	8h51m41.90s	11d49m37.66s
M67-S303	15.939	8h51m42.59s	11d56m05s
M67-S304	14.026	8h51m42.79s	11d59m31.01s
M67-S305	15.118	8h51m43.00s	11d40m59.57s

Name	Kmag	RA(hms)	DEC(dms)
M67-S307	10.5	8h51m43.91s	11d56m42.8s
M67-S317	15.277	8h51m47.10s	11d42m29.81s
M67-S318	14.009	8h51m48.47s	11d42m22.86s
M67-S319	14.778	8h51m48.67s	11d47m35.56s
M67-S32	13.31	8h51m 5.98s	11d51m10.2s
M67-S322	12.77	8h51m51.48s	11d57m50s
M67-S326	14.573	8h51m53.30s	11d54m19.45s
M67-S327	15.767	8h51m54.96s	11d53m05.98s
M67-S328	14.021	8h51m55.04s	11d40m50.31s
M67-S33	11.24	8h51m42.39s	11d51m23.4s
M67-S336	14.304	8h51m58.78s	11d50m02.47s
M67-S337	15.62	8h51m58.95s	11d59m56.3s
M67-S338	14.7	8h51m59.03s	11d41m49.5s
M67-S339	10.48	8h51m59.54s	11d55m05.1s
M67-S34	10.528	8h51m56.01s	11d51m26.47s
M67-S341	14.345	8h52m 0.42s	11d56m07.03s
M67-S342	15.237	8h52m 0.53s	11d52m29.12s
M67-S345	16.5	8h52m 2.02s	11d59m56.6s
M67-S347	14.56	8h52m 3.52s	11d47m48.4s
M67-S35	10.894	8h51m34.32s	11d51m10.48s
M67-S36	12.977	8h51m15.64s	11d50m56.18s
M67-S360	13.07	8h52m 8.54s	11d55m40.7s
M67-S364	14.0	8h52m 9.64s	11d46m46.5s
M67-S37	12.51	8h51m48.35s	11d51m12.2s
M67-S39	11.13	8h51m17.06s	11d50m46.8s
M67-S4	12.88	8h51m48.86s	11d56m51.5s
M67-S42	12.209	8h51m32.58s	11d50m40.61s
M67-S43	10.53	8h51m29.01s	11d50m33.4s
M67-S44	12.72	8h51m 1.08s	11d50m11.2s
M67-S45	12.779	8h51m15.34s	11d50m14.33s
M67-S452	14.098	8h50m43.90s	11d44m31.19s
M67-S457	16.38	8h50m44.87s	11d40m08.6s
M67-S461	13.61	8h50m46.37s	11d54m31.3s
M67-S47	12.53	8h51m19.04s	11d50m06s
M67-S474	14.623	8h50m52.30s	11d45m03.57s
M67-S479	15.816	8h50m54.99s	11d56m50.3s
M67-S48	13.2	8h52m 7.44s	11d50m22.5s
M67-S484	14.643	8h50m56.66s	11d49m54.66s
M67-S485	14.953	8h50m57.07s	11d56m50.72s
M67-S488	15.594	8h50m58.51s	11d48m44s
M67-S49	12.61	8h51m32.17s	11d50m03.9s
M67-S491	13.77	8h50m58.93s	11d48m19.6s
M67-S496	15.334	8h51m 0.68s	11d40m41.28s
M67-S5	13.3	8h51m27.91s	11d55m41.2s
M67-S50	12.89	8h51m56.14s	11d50m15.1s
M67-S516	14.246	8h51m 8.85s	11d57m53.7s
M67-S52	11.62	8h51m42.37s	11d50m08s
M67-S522	15.993	8h51m10.90s	11d48m58.87s
M67-S523	15.74	8h51m11.31s	11d57m21.26s

Name	Kmag	RA(hms)	DEC(dms)
M67-S525	15.119	8h51m12.22s	11d47m14.89s
M67-S526	14.149	8h51m12.29s	11d54m22.96s
M67-S529	13.59	8h51m13.64s	11d51m18.6s
M67-S53	12.22	8h51m39.26s	11d50m04.1s
M67-S538	14.145	8h51m16.82s	11d45m41.69s
M67-S539	13.53	8h51m17.62s	11d39m36.3s
M67-S54	11.49	8h51m23.80s	11d49m49.6s
M67-S542	13.67	8h51m19.21s	11d47m55s
M67-S55	12.64	8h51m 1.57s	11d49m34.6s
M67-S557	14.934	8h51m24.30s	11d47m28.37s
M67-S56	12.53	8h51m42.48s	11d49m52.3s
M67-S560	15.553	8h51m25.61s	11d53m15.79s
M67-S565	15.764	8h51m27.68s	11d57m30.02s
M67-S569	15.805	8h51m28.52s	11d45m33.84s
M67-S57	12.83	8h51m34.30s	11d49m44.1s
M67-S572	15.711	8h51m29.20s	11d42m11.89s
M67-S58	12.669	8h51m49.14s	11d49m43.56s
M67-S581	14.941	8h51m34.25s	11d45m53.52s
M67-S588	15.189	8h51m36.54s	11d54m27.21s
M67-S59	12.9	8h50m49.97s	11d49m13s
M67-S591	14.407	8h51m37.58s	11d56m44.52s
M67-S6	13.36	8h50m57.64s	11d55m15s
M67-S60	12.77	8h51m28.17s	11d49m27.8s
M67-S600	13.78	8h51m40.10s	11d52m43.7s
M67-S607	15.731	8h51m43.46s	11d48m52.1s
M67-S61	12.63	8h51m18.57s	11d49m21.8s
M67-S617	15.896	8h51m49.92s	11d56m45.13s
M67-S622	14.836	8h51m51.61s	11d44m50.34s
M67-S626	15.648	8h51m52.89s	11d44m07.76s
M67-S627	14.47	8h51m53.91s	11d39m05.2s
M67-S632	16.91	8h51m55.59s	11d54m10.9s
M67-S64	12.6	8h51m49.97s	11d49m31.5s
M67-S642	15.265	8h51m58.60s	11d52m15.25s
M67-S65	13.25	8h51m22.99s	11d49m13.4s
M67-S654	14.769	8h52m 5.11s	11d46m21.4s
M67-S67	12.68	8h51m30.60s	11d49m13.5s
M67-S68	13.22	8h51m25.95s	11d49m08.92s
M67-S69	13.38	8h52m 7.17s	11d49m25.8s
M67-S7	13.18	8h51m37.14s	11d55m00.3s
M67-S70	10.866	8h51m48.64s	11d49m15.6s
M67-S72	12.68	8h51m22.91s	11d48m49.39s
M67-S73	13.33	8h52m 2.18s	11d49m08.7s
M67-S74	11.037	8h51m32.59s	11d48m52.05s
M67-S76	13.36	8h51m 9.27s	11d48m20.9s
M67-S78	10.28	8h51m17.12s	11d48m16.5s
M67-S79	11.53	8h51m 7.84s	11d48m09.6s
M67-S8	12.74	8h51m 0.20s	11d54m32.4s
M67-S81	12.7	8h51m53.38s	11d48m21.2s
M67-S82	10.45	8h51m22.83s	11d48m02.1s

Name	Kmag	RA(hms)	DEC(dms)
M67-S83	13.29	8h50m53.19s	11d47m34.5s
M67-S84	12.65	8h51m15.47s	11d47m31.8s
M67-S85	11.49	8h51m45.10s	11d47m46.3s
M67-S87	12.806	8h51m14.76s	11d47m23.99s
M67-S88	12.38	8h51m 8.41s	11d47m12.4s
M67-S9	12.76	8h51m41.25s	11d54m29.3s
M67-S93	12.43	8h51m58.54s	11d46m53.3s
M67-S95	12.67	8h51m36.03s	11d46m33.9s
M67-S96	12.39	8h51m42.70s	11d46m36.9s
M67-S97	13.19	8h51m12.32s	11d46m21.6s
M67-S98	13.44	8h50m59.25s	11d46m13.3s
M67-S99	13.411	8h51m 8.64s	11d46m11.8s
M67-T626	9.36	8h51m20.10s	12d18m10.41s

Table C.5: M67 - All observed targets.

References

AAO software Team (2015). 2dfdr: Data reduction software. *Astrophysics Source Code Library*, page ascl:1505.015.

Appenzeller, I., Fricke, K., FÃijrtig, W., GÃďssler, W., HÃďfner, R., Harke, R., Hess, H.-J., Hummel, W., JÃijrgens, P., Kudritzki, R.-P., Mantel, K.-H., Meisl, W., Muschielok, B., Nicklas, H., Rupprecht, G., Seifert, W., Stahl, O., Szeifert, T., and Tarantik, K. (1998). Successful commissioning of FORS1 - the first optical instrument on the VLT. *The Messenger*, 94:1–6.

Arzoumanian, Z., Holmberg, J., and Norman, B. (2005). An astronomical pattern-matching algorithm for computer-aided identification of whale sharks Rhincodon typus. *Journal of Applied Ecology*, 42(6):999–1011.

Bacigalupo, C. (2013). A Compact Spectrograph to Search for Extrasolar Planets. *ArXiv e-prints*, 1308:arXiv:1308.2971.

Bailey, J. A., Farrell, T. J., and Shortridge, K. (1995). DRAMA: an environment for distributed instrumentation software. volume 2479, pages 62–68.

Bakos, G. Ã., Csubry, Z., Penev, K., Bayliss, D., JordÃąn, A., Afonso, C., Hartman, J. D., Henning, T., KovÃącs, G., Noyes, R. W., BÃľky, B., Suc, V., CsÃąk, B., Rabus, M., LÃązÃąr, J., Papp, I., SÃąri, P., Conroy, P., Zhou, G., Sackett, P. D., Schmidt, B., Mancini, L., Sasselov, D. D., and Ueltzhoeffer, K. (2013). HATSouth: A Global Network of Fully Automated Identical Wide-Field Telescopes. *Publications of the Astronomical Society of the Pacific*, 125:154.

Baranne, A., Mayor, M., and Poncet, J. L. (1979). CORAVEL - A new tool for radial velocity measurements. *Vistas in Astronomy*, 23:279–316.

Baranne, A., Queloz, D., Mayor, M., Adrianzyk, G., Knispel, G., Kohler, D., Lacroix, D., Meunier, J.-P., Rimbaud, G., and Vin, A. (1996). ELODIE: A spectrograph for accurate radial velocity measurements. *Astronomy and Astrophysics Supplement Series*, 119:373–390.

Barden, S. C., Ramsey, L. W., Huenemoerder, D. P., and Buzasi, D. (1987). Performance of the Penn State Fiber Optic Echelle at KPNO. volume 19, page 1099.

Benomar, O., Bedding, T. R., Stello, D., Deheuvels, S., White, T. R., and Christensen-Dalsgaard, J. (2012). Masses of Subgiant Stars from Asteroseismology Using the Coupling Strengths of Mixed Modes. *The Astrophysical Journal Letters*, 745:L33.

Bento, J., Ireland, M., Feger, T., Bacigalupo, C., Bedding, T., and Parker, Q. (2013). The Replicable High-resolution Exoplanet and Asteroseismology (RHEA) spectrograph. page 2.

Bolton, A. S. and Schlegel, D. J. (2010). Spectro-Perfectionism: An Algorithmic Framework for Photon Noise-Limited Extraction of Optical Fiber Spectroscopy. *Publications of the Astronomical Society of the Pacific*, 122:248.

Borucki, W. J., Koch, D., Basri, G., Batalha, N., Brown, T., Caldwell, D., Caldwell, J., Christensen-Dalsgaard, J., Cochran, W. D., DeVore, E., Dunham, E. W., Dupree, A. K., Gautier, T. N., Geary, J. C., Gilliland, R., Gould, A., Howell, S. B., Jenkins, J. M., Kondo, Y., Latham, D. W., Marcy, G. W., Meibom, S., Kjeldsen, H., Lissauer, J. J., Monet, D. G., Morrison, D., Sasselov, D., Tarter, J., Boss, A., Brownlee, D., Owen, T., Buzasi, D., Charbonneau, D., Doyle, L., Fortney, J., Ford, E. B., Holman, M. J., Seager, S., Steffen, J. H., Welsh, W. F., Rowe, J., Anderson, H., Buchhave, L., Ciardi, D., Walkowicz, L., Sherry, W., Horch, E., Isaacson, H., Everett, M. E., Fischer, D., Torres, G., Johnson, J. A., Endl, M., MacQueen, P., Bryson, S. T., Dotson, J., Haas, M., Kolodziejczak, J., Van Cleve, J., Chandrasekaran, H., Twicken, J. D., Quintana, E. V., Clarke, B. D., Allen, C., Li, J., Wu, H., Tenenbaum, P., Verner, E., Bruhweiler, F., Barnes, J., and Prsa, A. (2010). Kepler Planet-Detection Mission: Introduction and First Results. *Science*, 327:977.

Bouchy, F., Pepe, F., and Queloz, D. (2001). Fundamental photon noise limit to radial velocity measurements. *Astronomy and Astrophysics*, 374:733–739.

Bragaglia, A., Sestito, P., Villanova, S., Carretta, E., Randich, S., and Tosi, M. (2008). Old open clusters as key tracers of Galactic chemical evolution. II. Iron and elemental abundances in NGC 2324, NGC 2477 NGC 2660, NGC 3960, and Berkeley 32. *Astronomy and Astrophysics*, 480:79–90.

Breger, M., Handler, G., Nather, R. E., Winget, D. E., Kleinman, S. J., Sullivan, D. J., Li, Z.-P., Solheim, J. E., Jiang, S.-Y., Liu, Z.-L., Wood, M. A., Watson, T. K., Dziembowski, W. A., Serkowitsch, E., Mendelson, H., Clemens, J. C., Krzesinski, J., and Pajdosz, G. (1995). The Îť Scuti star FG Virginis. I. Multiple pulsation frequencies determined with a combined DSN/WET campaign. *Astronomy and Astrophysics*, 297:473.

Bryant, J. J., Owers, M. S., Robotham, A. S. G., Croom, S. M., Driver, S. P., Drinkwater, M. J., Lorente, N. P. F., Cortese, L., Scott, N., Colless, M., Schaefer, A., Taylor, E. N., Konstantopoulos, I. S., Allen, J. T., Baldry, I., Barnes, L., Bauer, A. E., Bland-Hawthorn, J., Bloom, J. V., Brooks, A. M., Brough, S., Cecil, G., Couch, W., Croton, D., Davies, R., Ellis, S., Fogarty, L. M. R., Foster, C., Glazebrook, K., Goodwin, M., Green, A., Gunawardhana, M. L., Hampton, E., Ho, I.-T., Hopkins, A. M., Kewley, L., Lawrence, J. S., Leon-Saval, S. G., Leslie, S., McElroy, R., Lewis, G., Liske, J., LÃşpez-SÃąnchez, Ã. R., Mahajan, S., Medling, A. M., Metcalfe, N., Meyer, M., Mould, J., Obreschkow, D., O'Toole, S., Pracy, M., Richards, S. N., Shanks, T., Sharp, R., Sweet, S. M., Thomas, A. D., Tonini, C., and Walcher, C. J. (2015). The SAMI Galaxy Survey: instrument specification and target selection. *Monthly Notices of the Royal Astronomical Society*, 447:2857–2879.

Brzeski, J., Case, S., and Gers, L. (2011). Design and development of the fibre cable and fore optics of the HERMES Spectrograph for the Anglo-Australian Telescope (AAT). volume 8125, pages 812504–812504–6.

Brzeski, J., Gers, L., Smith, G., and Staszak, N. (2012). Hermes: the engineering challenges. volume 8446, page 84464N.

Butler, R. P., Marcy, G. W., Williams, E., McCarthy, C., Dosanjh, P., and Vogt, S. S. (1996). Attaining Doppler Precision of 3 M s-1. *Publications of the Astronomical Society of the Pacific*, 108:500.

Catelan, M. and Smith, H. A. (2015). *Pulsating Stars*.

Charpinet, S., Fontaine, G., and Brassard, P. (2001). A Theoretical Exploration of the Pulsational Stability of Subdwarf B Stars. *Publications of the Astronomical Society of the Pacific*, 113:775–788.

Chatterjee, S., Ford, E. B., Geller, A. M., and Rasio, F. A. (2012). Planets in open clusters detectable by Kepler. *Monthly Notices of the Royal Astronomical Society*, 427:1587–1602.

Connes, P. (1985). Absolute astronomical accelerometry. *Astrophysics and Space Science*, 110:211–255.

de Jong, R. S., Barden, S. C., Bellido-Tirado, O., Brynnel, J. G., Frey, S., Giannone, D., Haynes, R., Johl, D., Phillips, D., Schnurr, O., Walcher, J. C., Winkler, R., Ansorge, W. R., Feltzing, S., McMahon, R. G., Baker, G., Caillier, P., Dwelly, T., Gaessler, W., Iwert, O., Mandel, H. G., Piskunov, N. A., Pragt, J. H., Walton, N. A., Bensby, T., Bergemann, M., Chiappini, C., Christlieb, N., Cioni, M.-R. L., Driver, S., Finoguenov, A., Helmi, A., Irwin, M. J., Kitaura, F.-S., Kneib, J.-P., Liske, J., Merloni, A., Minchev, I., Richard, J., and Starkenburg, E. (2016). 4most: the 4-metre Multi-Object Spectroscopic Telescope project at preliminary design review. volume 9908, page 99081O.

de Juan Ovelar, M., Kruijssen, J. M. D., Bressert, E., Testi, L., Bastian, N., and CÃąnovas, H. (2012). Can habitable planets form in clustered environments?

de Medeiros, J. R. and Mayor, M. (1999). A catalog of rotational and radial velocities for evolved stars. *Astronomy and Astrophysics Supplement Series*, 139:433–460.

De Silva, G. M., Freeman, K. C., Bland-Hawthorn, J., Martell, S., de Boer, E. W., Asplund, M., Keller, S., Sharma, S., Zucker, D. B., Zwitter, T., Anguiano, B., Bacigalupo, C., Bayliss, D., Beavis, M. A., Bergemann, M., Campbell, S., Cannon, R., Carollo, D., Casagrande, L., Casey, A. R., Da Costa, G., D'Orazi, V., Dotter, A., Duong, L., Heger, A., Ireland, M. J., Kafle, P. R., Kos, J., Lattanzio, J., Lewis, G. F., Lin, J., Lind, K., Munari, U., Nataf, D. M., O'Toole, S., Parker, Q., Reid, W., Schlesinger, K. J., Sheinis, A., Simpson, J. D., Stello, D., Ting, Y.-S., Traven, G., Watson, F., Wittenmyer, R., Yong, D., and Å¡erjal, M. (2015). The GALAH survey: scientific motivation. *Monthly Notices of the Royal Astronomical Society*, 449:2604–2617.

Diego, F., Charalambous, A., Fish, A. C., and Walker, D. D. (1990). Final tests and commissioning of the UCL Echelle Spectrograph. volume 1235, pages 562–576.

Dumusque, X., Glenday, A., Phillips, D. F., Buchschacher, N., Collier Cameron, A., Cecconi, M., Charbonneau, D., Cosentino, R., Ghedina, A., Latham, D. W., Li, C.-H., Lodi, M., Lovis, C., Molinari, E., Pepe, F., Udry, S., Sasselov, D., Szentgyorgyi, A., and Walsworth, R. (2015). HARPS-N Observes the Sun as a Star. *The Astrophysical Journal Letters*, 814:L21.

Dumusque, X., Pepe, F., Lovis, C., SÃľgransan, D., Sahlmann, J., Benz, W., Bouchy, F., Mayor, M., Queloz, D., Santos, N., and Udry, S. (2012). An Earth-mass planet orbiting Îś Centauri B. *Nature*.

Dunham, E. W., Mandushev, G. I., Taylor, B. W., and Oetiker, B. (2004). PSST: The Planet Search Survey Telescope. *Publications of the Astronomical Society of the Pacific*, 116(825):1072.

Feger, T., Bacigalupo, C., Bedding, T. R., Bento, J., Coutts, D. W., Ireland, M. J., Parker, Q. A., Rizzuto, A., and Spaleniak, I. (2014). RHEA: the ultra-compact replicable high-resolution exoplanet and Asteroseismology spectrograph. volume 9147, page 91477I.

Feger, T., Ireland, M. J., Schwab, C., Bento, J., Bacigalupo, C., and Coutts, D. W. (2016). Attaining m s-1 level intrinsic Doppler precision with RHEA, a low-cost single-mode spectrograph. *Experimental Astronomy*, 42:285–300.

Fraunhofer, J. (1817). Bestimmung des Brechungs- und des Farbenzerstreungs-VermÃűgens verschiedener Glasarten, in Bezug auf die Vervollkommnung achromatischer FernrÃűhre. *Annalen der Physik*, 56:264–313.

Freeman, K. and Bland-Hawthorn, J. (2002). The New Galaxy: Signatures of Its Formation. *Annual Review of Astronomy and Astrophysics*, 40:487–537.

Geller, A. M., Latham, D. W., and Mathieu, R. D. (2015). STELLAR RADIAL VELOCITIES IN THE OLD OPEN CLUSTER M67 (NGC 2682). I. MEMBERSHIPS, BINARIES, AND KINEMATICSWIYN Open Cluster Study. LXVII. *The Astronomical Journal*, 150(3):97.

Gray, P. M. (1984). Fibre optic coupled aperture plate (FOCAP) system at the AAO. volume 445, pages 57–64.

Groth, E. J. (1986). A pattern-matching algorithm for two-dimensional coordinate lists. *The Astronomical Journal*, 91:1244–1248.

Han, E., Wang, S. X., Wright, J. T., Feng, Y. K., Zhao, M., Fakhouri, O., Brown, J. I., and Hancock, C. (2014). Exoplanet Orbit Database. II. Updates to Exoplanets.org. *Publications of the Astronomical Society of the Pacific*, 126:827.

Handler, G. (2013). Asteroseismology. *arXiv:1205.6407 [astro-ph]*, pages 207–241. arXiv: 1205.6407.

Handler, G., Balona, L. A., Shobbrook, R. R., Koen, C., Bruch, A., Romero-Colmenero, E., Pamyatnykh, A. A., Willems, B., Eyer, L., James, D. J., and Maas, T. (2002). Discovery and analysis of p-mode and g-mode oscillations in the A-type primary of the eccentric binary HD 209295. *Monthly Notices of the Royal Astronomical Society*, 333(2):262–278. arXiv: astro-ph/0202214.

Harrison, G. R. (1949). The production of diffraction gratings: II. Design of eschelle gratings and spectrographs - (1949). *Journal of the Optical Society of America (1917-1983)*, 39:522.

Hartwick, F. D. A., Hesser, J. E., and McClure, R. D. (1972). A photometric study of the open cluster NGC 2477. *The Astrophysical Journal*, 174:557.

Hatzes, A. P. and Cochran, W. D. (1998). Stellar Oscillations in K Giant Stars. volume 154, page 311.

Hearnshaw, J. (2009). *Astronomical Spectrographs and Their History*. Cambridge University Press. Google-Books-ID: raFv_wT_2QkC.

Heijmans, J. A. C., Gers, L., and Faught, B. (2011). Design and development of the high-resolution spectrograph HERMES and the unique volume phase holographic gratings. page 81671A.

Heller, R., Williams, D., Kipping, D., Limbach, M. A., Turner, E., Greenberg, R., Sasaki, T., Bolmont, Ã., Grasset, O., Lewis, K., Barnes, R., and Zuluaga, J. I. (2014). Formation, Habitability, and Detection of Extrasolar Moons. *Astrobiology*, 14:798–835.

Hill, J. M., Angel, J. R. P., Scott, J. S., Lindley, D., and Hintzen, P. (1980). Multiple object spectroscopy - The Medusa spectrograph. *The Astrophysical Journal Letters*, 242:L69–L72.

Hill, R. S., Landsman, W. B., Lindler, D., and Shaw, R. (1997). Cosmic ray and hot pixel removal from STIS CCD images. page 120.

Hirst, P., Slocum, C., Turner, J., Sienkiewicz, M., Greenfield, P., Hogan, E., Simpson, M., and Labrie, K. (2014). Ureka: A Distribution of Python and IRAF Software for Astronomy. volume 485, page 335.

Hubbard, W. B., Burrows, A., and Lunine, J. I. (2002). Theory of Giant Planets. *Annual Review of Astronomy and Astrophysics*, 40:103–136.

Istrate, A. G., Fontaine, G., Gianninas, A., Grassitelli, L., Marchant, P., Tauris, T. M., and Langer, N. (2016). Asteroseismic test of rotational mixing in low-mass white dwarfs. *Astronomy and Astrophysics*, 595:L12.

Johnson, J. A., Aller, K. M., Howard, A. W., and Crepp, J. R. (2010). Giant Planet Occurrence in the Stellar Mass-Metallicity Plane. *Publications of the Astronomical Society of the Pacific*, 122:905–915.

Kipping, D. M., Bakos, G. Ã., Buchhave, L., NesvornÃ¡, D., and Schmitt, A. (2012). The Hunt for Exomoons with Kepler (HEK). I. Description of a New Observational project. *The Astrophysical Journal*, 750:115.

Kos, J., Lin, J., Zwitter, T., Å¡erjal, M., Sharma, S., Bland-Hawthorn, J., Asplund, M., Casey, A. R., De Silva, G. M., Freeman, K. C., Martell, S. L., Simpson, J. D., Schlesinger, K. J., Zucker, D., Anguiano, B., Bacigalupo, C., Bedding, T. R., Betters, C., Da Costa, G., Duong, L., Hyde, E., Ireland, M., Kafle, P. R., Leon-Saval, S., Lewis, G. F., Munari, U., Nataf, D., Stello, D., Tinney, C. G., Traven, G., Watson, F., and Wittenmyer, R. A. (2017). The GALAH survey: the data reduction pipeline. *Monthly Notices of the Royal Astronomical Society*, 464:1259–1281.

Kuehn, K., Lawrence, J., Brown, D. M., Case, S., Colless, M., Content, R., Gers, L., Gilbert, J., Goodwin, M., Hopkins, A. M., Ireland, M., Lorente, N. P. F., Muller, R., Nichani, V., Rakman, A., Richards, S. N., Saunders, W., Staszak, N. F., Tims, J., and Waller, L. G. (2014). TAIPAN: optical spectroscopy with StarBugs. volume 9147, page 914710.

Lebzelter, T., Wood, P. R., Hinkle, K. H., Joyce, R. R., and Fekel, F. C. (2005). Long period variables in the globular cluster 47 Tuc: Radial velocity variations. *Astronomy and Astrophysics*, 432:207–217.

Lemke, U. and Reiners, A. (2016). The G\"ottingen Solar Radial Velocity Project: Sub-m/s Doppler precision from FTS observations of the Sun as a star.

Liu, Y.-J., Sato, B., Zhao, G., Noguchi, K., Wang, H., Kambe, E., Ando, H., Izumiura, H., Chen, Y.-Q., Okada, N., Toyota, E., Omiya, M., Masuda, S., Takeda, Y., Murata, D., Itoh, Y., Yoshida, M., Kokubo, E., and Ida, S. (2008). A Substellar Companion to the Intermediate-Mass Giant 11 Comae. *The Astrophysical Journal*, 672:553–557.

Lorente, N. P. F., Vuong, M. V., Shortridge, K., Farrell, T. J., Smedley, S., Hong, S. E., Bacigalupo, C., Goodwin, M., Kuehn, K., and Satorre, C. (2016). AAO Starbugs: software control and associated algorithms. volume 9913, page 99130U, eprint: arXiv:1608.02645.

Lucretius (99BCE). On the Nature of Things.

Magic, Z., Serenelli, A., Weiss, A., and Chaboyer, B. (2010). On using the CMD morphology of M67 to test solar abundances. *The Astrophysical Journal*, 718(2):1378–1387. arXiv: 1004.3308.

Martell, S. L., Sharma, S., Buder, S., Duong, L., Schlesinger, K. J., Simpson, J., Lind, K., Ness, M., Marshall, J. P., Asplund, M., Bland-Hawthorn, J., Casey, A. R., De Silva, G., Freeman, K. C., Kos, J., Lin, J., Zucker, D. B., Zwitter, T., Anguiano, B., Bacigalupo, C., Carollo, D., Casagrande, L., Da Costa, G. S., Horner, J., Huber, D., Hyde, E. A., Kafle, P. R., Lewis, G. F., Nataf, D., Navin, C. A., Stello, D., Tinney, C. G., Watson, F. G., and Wittenmyer, R. (2017). The GALAH survey: observational overview and Gaia DR1 companion. *Monthly Notices of the Royal Astronomical Society*, 465:3203–3219.

Mayor, M. and Queloz, D. (1995). A Jupiter-mass companion to a solar-type star. *Nature*, 378:355–359.

McLaughlin, D. E., Anderson, J., Meylan, G., Gebhardt, K., Pryor, C., Minniti, D., and Phinney, S. (2006). Hubble Space Telescope Proper Motions and Stellar Dynamics in the Core of the Globular Cluster 47 Tucanae. *The Astrophysical Journal Supplement Series*, 166:249–297.

Morgan, J. G. and Eggleton, P. P. (1978). A reappraisal of the gap in the HR diagram of M67. *Monthly Notices of the Royal Astronomical Society*, 182:219–231.

Newton, S. I. (1730). *Opticks:: Or, A Treatise of the Reflections, Refractions, Inflections and Colours of Light*. William Innys at the West-End of St. Paul's. Google-Books-ID: GnAFAAAAQAAJ.

Niemela, V. S., Massey, P., Testor, G., and Benitez, S. G. (2002). The Massive Wolf-Rayet Binary SMC WR7. *Monthly Notices of the Royal Astronomical Society*, 333(2):347–352. arXiv: astro-ph/0202203.

Pasquini, L., Avila, G., Blecha, A., Cacciari, C., Cayatte, V., Colless, M., Damiani, F., de Propris, R., Dekker, H., di Marcantonio, P., Farrell, T., Gillingham, P., Guinouard, I., Hammer, F., Kaufer, A., Hill, V., Marteaud, M., Modigliani, A., Mulas, G., North,

P., Popovic, D., Rossetti, E., Royer, F., Santin, P., Schmutzer, R., Simond, G., Vola, P., Waller, L., and Zoccali, M. (2002). Installation and commissioning of FLAMES, the VLT Multifibre Facility. *The Messenger*, 110:1–9.

Pepe, F., Lovis, C., SÃľgransan, D., Benz, W., Bouchy, F., Dumusque, X., Mayor, M., Queloz, D., Santos, N. C., and Udry, S. (2011). The HARPS search for Earth-like planets in the habitable zone. I. Very low-mass planets around HD 20794, HD 85512, and HD 192310. *Astronomy and Astrophysics*, 534:58.

Pepe, F., Mayor, M., Rupprecht, G., Avila, G., Ballester, P., Beckers, J.-L., Benz, W., Bertaux, J.-L., Bouchy, F., Buzzoni, B., Cavadore, C., Deiries, S., Dekker, H., Delabre, B., D'Odorico, S., Eckert, W., Fischer, J., Fleury, M., George, M., Gilliotte, A., Gojak, D., Guzman, J.-C., Koch, F., Kohler, D., Kotzlowski, H., Lacroix, D., Le Merrer, J., Lizon, J.-L., Lo Curto, G., Longinotti, A., Megevand, D., Pasquini, L., Petitpas, P., Pichard, M., Queloz, D., Reyes, J., Richaud, P., Sivan, J.-P., Sosnowska, D., Soto, R., Udry, S., Ureta, E., van Kesteren, A., Weber, L., Weilenmann, U., Wicenec, A., Wieland, G., Christensen-Dalsgaard, J., Dravins, D., Hatzes, A., KÃijrster, M., Paresce, F., and Penny, A. (2002). HARPS: ESO's coming planet searcher. Chasing exoplanets with the La Silla 3.6-m telescope. *The Messenger*, 110:9–14.

Perryman, M. A. C., Brown, A. G. A., Lebreton, Y., Gomez, A., Turon, C., Cayrel de Strobel, G., Mermilliod, J. C., Robichon, N., Kovalevsky, J., and Crifo, F. (1998). The Hyades: distance, structure, dynamics, and age. *Astronomy and Astrophysics*, 331:81–120.

Pollacco, D. L., Skillen, I., Collier Cameron, A., Christian, D. J., Hellier, C., Irwin, J., Lister, T. A., Street, R. A., West, R. G., Anderson, D. R., Clarkson, W. I., Deeg, H., Enoch, B., Evans, A., Fitzsimmons, A., Haswell, C. A., Hodgkin, S., Horne, K., Kane, S. R., Keenan, F. P., Maxted, P. F. L., Norton, A. J., Osborne, J., Parley, N. R., Ryans, R. S. I., Smalley, B., Wheatley, P. J., and Wilson, D. M. (2006). The WASP Project and the SuperWASP Cameras. *Publications of the Astronomical Society of the Pacific*, 118:1407–1418.

Pourbaix, D., Tokovinin, A. A., Batten, A. H., Fekel, F. C., Hartkopf, W. I., Levato, H., Morrell, N. I., Torres, G., and Udry, S. (2004). SB9: The ninth catalogue of spectroscopic binary orbits. *Astronomy and Astrophysics*, 424:727–732.

Pych, W. (2004). A Fast Algorithm for Cosmic Rays Removal from Single Images. *Publications of the Astronomical Society of the Pacific*, 116(816):148–153. arXiv: astro-ph/0311290.

Queloz, D., Henry, G. W., Sivan, J. P., Baliunas, S. L., Beuzit, J. L., Donahue, R. A., Mayor, M., Naef, D., Perrier, C., and Udry, S. (2001). No planet for HD 166435. *Astronomy and Astrophysics*, 379:279–287.

Quinn, S. N., White, R. J., Latham, D. W., Buchhave, L. A., Torres, G., Stefanik, R. P., Berlind, P., Bieryla, A., Calkins, M. C., Esquerdo, G. A., FÅśrÃľsz, G., Geary, J. C., and Szentgyorgyi, A. H. (2014). HD 285507b: An Eccentric Hot Jupiter in the Hyades Open Cluster. *The Astrophysical Journal*, 787:27.

Rajpaul, V., Aigrain, S., and Roberts, S. (2016). Ghost in the time series: no planet for Alpha Cen B. *Monthly Notices of the Royal Astronomical Society*, 456:L6–L10.

Rauer, H., Catala, C., Aerts, C., Appourchaux, T., Benz, W., Brandeker, A., Christensen-Dalsgaard, J., Deleuil, M., Gizon, L., Goupil, M.-J., GÃijdel, M., Janot-Pacheco, E., Mas-Hesse, M., Pagano, I., Piotto, G., Pollacco, D., Santos, Ä., Smith, A., SuÃąrez, J.-C., SzabÃş, R., Udry, S., Adibekyan, V., Alibert, Y., Almenara, J.-M., Amaro-Seoane, P., Eiff, M. A.-v., Asplund, M., Antonello, E., Barnes, S., Baudin, F., Belkacem, K., Bergemann, M., Bihain, G., Birch, A. C., Bonfils, X., Boisse, I., Bonomo, A. S., Borsa, F., BrandÃčo, I. M., Brocato, E., Brun, S., Burleigh, M., Burston, R., Cabrera, J., Cassisi, S., Chaplin, W., Charpinet, S., Chiappini, C., Church, R. P., Csizmadia, S., Cunha, M., Damasso, M., Davies, M. B., Deeg, H. J., DÃŋaz, R. F., Dreizler, S., Dreyer, C., Eggenberger, P., Ehrenreich, D., EigmÃijller, P., Erikson, A., Farmer, R., Feltzing, S., de Oliveira Fialho, F., Figueira, P., Forveille, T., Fridlund, M., GarcÃŋa, R. A., Giommi, P., Giuffrida, G., Godolt, M., Gomes da Silva, J., Granzer, T., Grenfell, J. L., Grotsch-Noels, A., GÃijnther, E., Haswell, C. A., Hatzes, A. P., HÃľbrard, G., Hekker, S., Helled, R., Heng, K., Jenkins, J. M., Johansen, A., Khodachenko, M. L., Kislyakova, K. G., Kley, W., Kolb, U., Krivova, N., Kupka, F., Lammer, H., Lanza, A. F., Lebreton, Y., Magrin, D., Marcos-Arenal, P., Marrese, P. M., Marques, J. P., Martins, J., Mathis, S., Mathur, S., Messina, S., Miglio, A., Montalban, J., Montalto, M., Monteiro, M. J. P. F. G., Moradi, H., Moravveji, E., Mordasini, C., Morel, T., Mortier, A., Nascimbeni, V., Nelson, R. P., Nielsen, M. B., Noack, L., Norton, A. J., Ofir, A., Oshagh, M., Ouazzani, R.-M., PÃąpics, P., Parro, V. C., Petit, P., Plez, B., Poretti, E., Quirrenbach, A., Ragazzoni, R., Raimondo, G., Rainer, M., Reese, D. R., Redmer, R., Reffert, S., Rojas-Ayala, B., Roxburgh, I. W., Salmon, S., Santerne, A., Schneider, J., Schou, J., Schuh, S., Schunker, H., Silva-Valio, A., Silvotti, R., Skillen, I., Snellen, I., Sohl, F., Sousa, S. G., Sozzetti, A., Stello, D., Strassmeier, K. G., Åăvanda, M., SzabÃş, G. M., Tkachenko, A., Valencia, D., Van Grootel, V., Vauclair, S. D., Ventura, P., Wagner, F. W., Walton, N. A., Weingrill, J., Werner, S. C., Wheatley, P. J., and Zwintz, K. (2014). The PLATO 2.0 mission. *Experimental Astronomy*, 38:249–330.

Reid, D. (1979). An algorithm for tracking multiple targets. *IEEE Transactions on Automatic Control*, 24(6):843–854.

Ricker, G. R., Winn, J. N., Vanderspek, R., Latham, D. W., Bakos, G. Ã., Bean, J. L., Berta-Thompson, Z. K., Brown, T. M., Buchhave, L., Butler, N. R., Butler, R. P., Chaplin, W. J., Charbonneau, D., Christensen-Dalsgaard, J., Clampin, M., Deming, D., Doty, J., De Lee, N., Dressing, C., Dunham, E. W., Endl, M., Fressin, F., Ge, J., Henning, T., Holman, M. J., Howard, A. W., Ida, S., Jenkins, J., Jernigan, G., Johnson, J. A., Kaltenegger, L., Kawai, N., Kjeldsen, H., Laughlin, G., Levine, A. M., Lin, D., Lissauer, J. J., MacQueen, P., Marcy, G., McCullough, P. R., Morton, T. D., Narita, N., Paegert, M., Palle, E., Pepe, F., Pepper, J., Quirrenbach, A., Rinehart, S. A., Sasselov, D., Sato, B., Seager, S., Sozzetti, A., Stassun, K. G., Sullivan, P., Szentgyorgyi, A., Torres, G., Udry, S., and Villasenor, J. (2014). Transiting Exoplanet Survey Satellite (TESS). volume 9143, page 914320, eprint: arXiv:1406.0151.

Rogers, L. A. (2015). Most 1.6 Earth-radius Planets are Not Rocky. *The Astrophysical Journal*, 801:41.

Sandage, A. and Eggen, O. J. (1969). Isochrones, Ages, Curves of Evolutionary Deviation, and the Composite C-M Diagram for Old Galactic Clusters. *The Astrophysical Journal*, 158:685.

Sanders, W. L. (1977). Membership of the open cluster M67. *Astronomy and Astrophysics Supplement Series*, 27:89–116.

Santos, N. C., Israelian, G., and Mayor, M. (2004). Spectroscopic [Fe/H] for 98 extra-solar planet-host stars. Exploring the probability of planet formation. *Astronomy and Astrophysics*, 415:1153–1166.

Santos, N. C., Lovis, C., Pace, G., Melendez, J., and Naef, D. (2009). Metallicities for 13 nearby open clusters from high-resolution spectroscopy of dwarf and giant stars. Stellar metallicity, stellar mass, and giant planets. *Astronomy and Astrophysics*, 493:309–316.

Sato, B., Omiya, M., Liu, Y., Harakawa, H., Izumiura, H., Kambe, E., Toyota, E., Murata, D., Lee, B.-C., Masuda, S., Takeda, Y., Yoshida, M., Itoh, Y., Ando, H., Kokubo, E., Ida, S., Zhao, G., and Han, I. (2010). Substellar Companions to Evolved Intermediate-Mass Stars: HD 145457 and HD 180314. *Publications of the Astronomical Society of Japan*, 62:1063–1069.

Shafter, A. W. (1983). Radial velocity studies of cataclysmic binaries. I - KR Aurigae. *The Astrophysical Journal*, 267:222–231.

Sheinis, A., Anguiano, B., Asplund, M., Bacigalupo, C., Barden, S., Birchall, M., Bland-Hawthorn, J., Brzeski, J., Cannon, R., Carollo, D., Case, S., Casey, A., Churilov, V., Warrick, C., Dean, R., De Silva, G., D'Orazi, V., Duong, L., Farrell, T., Fiegert, K., Freeman, K., Gabriella, F., Gers, L., Goodwin, M., Gray, D., Green, A., Heald, R., Heijmans, J., Ireland, M., Jones, D., Kafle, P., Keller, S., Klauser, U., Kondrat, Y., Kos, J., Lawrence, J., Lee, S., Mali, S., Martell, S., Mathews, D., Mayfield, D., Miziarski, S., Muller, R., Pai, N., Patterson, R., Penny, E., Orr, D., Schlesinger, K., Sharma, S., Shortridge, K., Simpson, J., Smedley, S., Smith, G., Stafford, D., Staszak, N., Vuong, M., Waller, L., de Boer, E. W., Xavier, P., Zheng, J., Zhelem, R., Zucker, D., and Zwitter, T. (2015). First Light Results from the Hermes Spectrograph at the AAT. *Journal of Astronomical Telescopes, Instruments, and Systems*, 1(3):035002. arXiv: 1509.00129.

Shortridge, K., Farrell, T. J., Bailey, J. A., and Waller, L. G. (2004a). The data flow system for the AAO2 controllers. volume 5496, pages 463–468.

Shortridge, K., Meyerdierks, H., Currie, M., Clayton, C., Lockley, J., Charles, A., Davenhall, C., Taylor, M., Ash, T., Wilkins, T., Axon, D., Palmer, J., Holloway, A., Graffagnino, V., Bridger, A., and Fuller, N. M. (2004b). FIGARO – A general data reduction system. *Starlink User Note*, 86.

Simms, W. (1840). On the Optical Glass prepared by the late Dr. Ritchie. *Memoirs of the Royal Astronomical Society*, 11:165.

Simpson, J. D., De Silva, G. M., Bland-Hawthorn, J., Freeman, K. C., Martell, S. L., Schlesinger, K. J., Sharma, S., Zucker, D. B., Zwitter, T., Kos, J., Anguiano, B., Nataf, D. M., Reid, W., and Wittenmyer, R. A. (2016). The GALAH survey: relative throughputs of the 2df fibre positioner and the HERMES spectrograph from stellar targets. *Monthly Notices of the Royal Astronomical Society*, 459:1069–1081.

Skrutskie, M. F., Cutri, R. M., Stiening, R., Weinberg, M. D., Schneider, S., Carpenter, J. M., Beichman, C., Capps, R., Chester, T., Elias, J., Huchra, J., Liebert, J., Lonsdale, C., Monet,

D. G., Price, S., Seitzer, P., Jarrett, T., Kirkpatrick, J. D., Gizis, J. E., Howard, E., Evans, T., Fowler, J., Fullmer, L., Hurt, R., Light, R., Kopan, E. L., Marsh, K. A., McCallon, H. L., Tam, R., Van Dyk, S., and Wheelock, S. (2006). The Two Micron All Sky Survey (2mass). *The Astronomical Journal*, 131:1163–1183.

Thompson, T. A. (2013). Gas giants in hot water: inhibiting giant planet formation and planet habitability in dense star clusters through cosmic time. *Monthly Notices of the Royal Astronomical Society*.

Tinney, C. G., Butler, R. P., Marcy, G. W., Jones, H. R. A., Penny, A. J., Vogt, S. S., Apps, K., and Henry, G. W. (2001). First Results from the Anglo-Australian Planet Search: A Brown Dwarf Candidate and a 51 Peg-like Planet. *The Astrophysical Journal*, 551:507–511.

Tody, D. (1993). IRAF in the Nineties. volume 52, page 173.

Udry, S., Mayor, M., Maurice, E., Andersen, J., Imbert, M., Lindgren, H., Mermilliod, J.-C., NordstrÃűm, B., and PrÃľvot, L. (1999). 20 Years of CORAVEL Monitoring of Radial-Velocity Standard Stars. volume 185, page 383.

Uytterhoeven, K., Moya, A., GrigahcÃĺne, A., Guzik, J. A., GutiÃľrrez-Soto, J., Smalley, B., Handler, G., Balona, L. A., Niemczura, E., Fox Machado, L., Benatti, S., Chapellier, E., Tkachenko, A., SzabÃş, R., SuÃąrez, J. C., Ripepi, V., Pascual, J., Mathias, P., MartÃŋn-RuÃŋz, S., Lehmann, H., Jackiewicz, J., Hekker, S., Gruberbauer, M., GarcÃŋa, R. A., Dumusque, X., DÃŋaz-Fraile, D., Bradley, P., Antoci, V., Roth, M., Leroy, B., Murphy, S. J., De Cat, P., Cuypers, J., Kjeldsen, H., Christensen-Dalsgaard, J., Breger, M., Pigulski, A., Kiss, L. L., Still, M., Thompson, S. E., and van Cleve, J. (2011). The Kepler characterization of the variability among A- and F-type stars. I. General overview. *Astronomy and Astrophysics*, 534:A125.

Warmels, R. H. (1992). The ESO–MIDAS System. volume 25, page 115.

Wolszczan, A. and Frail, D. A. (1992). A planetary system around the millisecond pulsar PSR1257 + 12. *Nature*, 355:145–147.

Wright, J. T., Marcy, G. W., Howard, A. W., Johnson, J. A., Morton, T. D., and Fischer, D. A. (2012). The Frequency of Hot Jupiters Orbiting nearby Solar-type Stars. *The Astrophysical Journal*, 753:160.

Zacharias, N., Finch, C. T., Girard, T. M., Henden, A., Bartlett, J. L., Monet, D. G., and Zacharias, M. I. (2013). The Fourth US Naval Observatory CCD Astrograph Catalog (UCAC4). *The Astronomical Journal*, 145:44.